UNIVERSITY OF STRATHCLYDE
Department of Physics

Gallium nitride light–emitting diode enabled visible light communications

by

Ricardo Xavier da Graça Ferreira

A thesis presented in fulfilment of the
requirements for the degree of
Doctor of Philosophy

October 2017

This thesis is the result of the author's original research. It has been composed by the author and has not been previously submitted for examination which has led to the award of a degree.

Signed: ____

Date: ____

Frontispiece

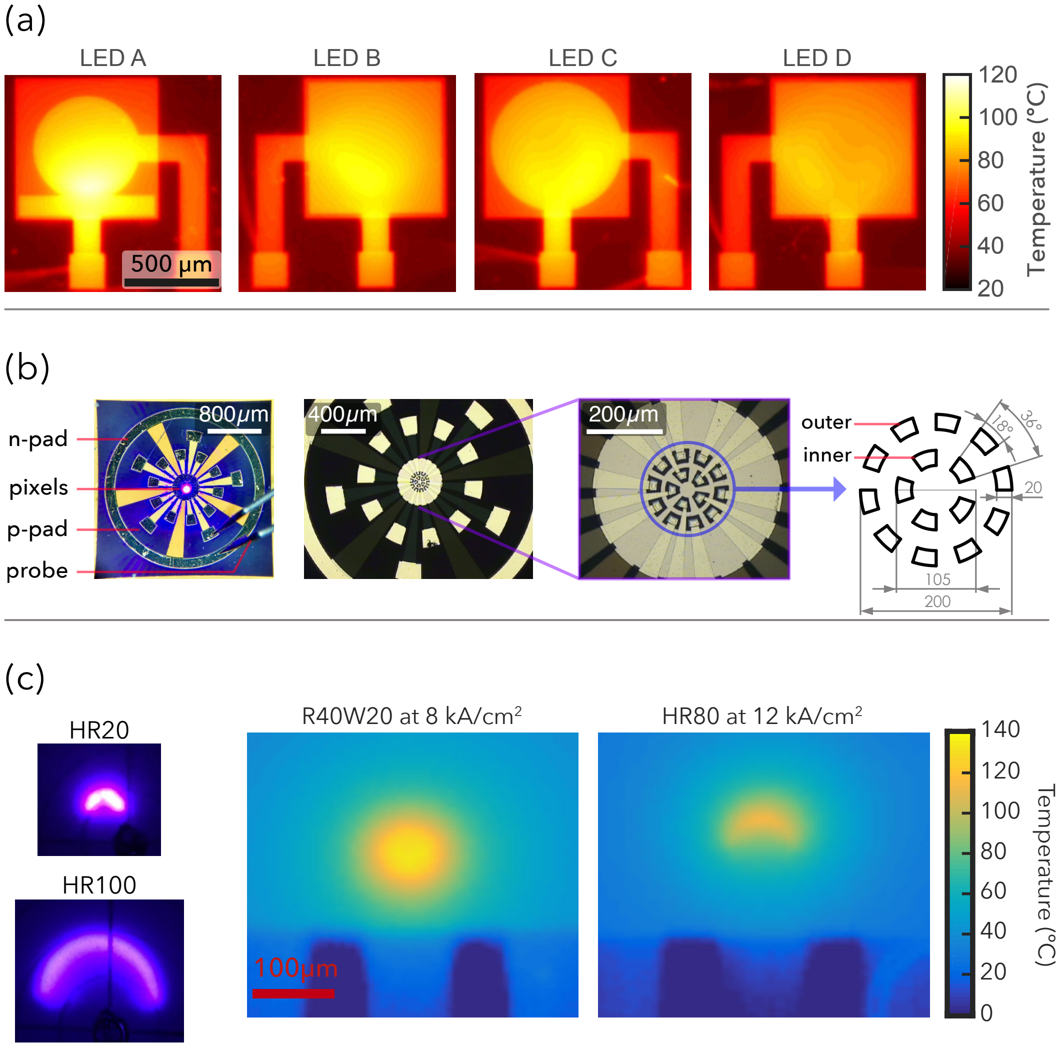

In (a) a thermal image of four broad area LEDs used to study current crowding and heat dissipation. In (b) photographs of a circular segmented micro-LED array. In (c) micrographs of half-ring micro-LEDs and thermal images of micro-LEDs in ring and half-ring designs.

Acknowledgements

First of all, I would like to thank my supervisor, Professor Martin Dawson, for the excellent guidance and patience throughout this journey. The fantastic opportunity that was given to me will change the course of my life for the better, for that I am truly grateful.

The course of my research involved amazing people that in one way or another pushed me forward and away from cliffs. From the Institute of Photonics I would like to thank Dr. Enyuan Xie for the so much support and teachings; Dr. Jonathan McKendry for all the training, patience and guidance over the last 3 years; Dr. Johannes Hendersorhf for the interesting and productive discussions on device physics and life lessons; last but not least the former Dr. António Trindade for the great work we did together and the positive energy (“mostra-lhes como é”). To Dr. Carol Trager-Cowan and Dr. Paul Edwards for pushing forward to learn SEM and discover a little more of the world of small things. From the University of Glasgow, I would like to thank Dr. Anthony Kelly for pushing me forward, helping me to see through; Dr. Scott Watson for his patience and various contributions in measurements. From the University of Edinburgh, first of all I would like to thank Professor Harald Haas for constant positive and super optimistic attitude. Dr. Stefan Videt, Dr. Dobroslav Tsonev and Mohamed Islim for the great work we did together, the learning in OFDM and discussions on the meaning of the “number race” and the boundaries between physics and communications, we managed it, you guys rock. From the University of Cambridge, I would like to thank to Xin Li and Nikos Bamiedakis for close collaboration on new ideas integrating device to system that lead us to record breaking results. From the University of Oxford, I would like to thank to Dr. Sujan Rajbhandari, Dr. Hyunchae Chun and Dr. Ariel Gomez for their dedications and perseverance. Together we have beaten our own records multiple times. I cannot forget Professor Dominic O’Brien for the senior advice regarding the IEEE standards and the industry during the time time–off at the 2015 Summer Topicals conference.

One very special form of gratitude to Hyunsu Nam for enduring the time, distance and sometimes lack of patience. The tip on the RF interference made me and Mohamed feel so stupid. Thinks are about to change, again!

Dedico este trabalho à minha família.

Abstract

This thesis focuses on the development, measurement and application of novel micrometre-sized light emitting diodes (micro–LEDs) based on Gallium Nitride (GaN) for visible light communications (VLC) in both free-space and guided wave configurations. The goal is to set benchmarks for LED-based wireless optical communications. An overview of the field integrating research, industry and standards is presented.

A top–down approach is taken with application requirements driving development of new micro–LEDs with simultaneously increased optical power and modulation bandwidth. This was achieved by mitigating two limitations, namely current crowding and mutual device heating. Two novel techniques were developed to access pixel performance: spatially–resolved mapping of modulation bandwidth and spectral characteristics, and thermal imaging. On this basis, broad-area LEDs were used to understand the independent benefits, providing insight for the design of novel micro-LEDs. Circular segmented micro-LEDs emitting at 450nm achieved modulation bandwidths in excess of 800MHz, the highest reported for LEDs, while maintaining optical power above 2mW. In data transmission using systems with 1.8GHz bandwidth, the devices achieved 8Gbps in free-space and guided-wave operation at wavelengths of 400nm, 450nm and 520nm. Ring and half-ring micro-LEDs introduced here have shown modulation bandwidths that scale with the increase of active area and consequently optical power. Bandwidths in excess of of 600MHz were achieved at optical powers over 5mW. In data transmission using a system limited to 1GHz bandwidth, these devices achieved 7Gbps in free-space operation.

Contents

List of Figures

List of Tables

Abbreviations

3GPP	3rd Generation Partnership Project
AlInGaN	aluminium indium gallium nitride
AP	access point
APD	avalanche photodiode
AR	augmented reality
AWG	arbitrary waveform generator
Au	gold
BER	bit error rate
CQD	colloidal quantum dot
CRI	colour rendering index
CSP	chip scale package
DAC	digital-to-analogue converter
DC	direct current
DCO-OFDM	DC–biased (or offset) OFDM
DoS	density of states
DSP	digital signal processing
ECC	error–correcting code
E_g	bandgap energy
ε	emissvity
EQE	external quantum efficiency
E_{peak}	emission peak
FEC	forward error correction
FWHM	full width at half maximum
GaN	gallium nitride
GLONASS	globalnaya navigazionnaya sputnikovaya sistema
GPS	global positioning system
ICP	inductively coupled plasma
IEEE	Institute of Electrical and Electronics Engineers
IMDD	intensity-modulation direct-detection
InSb	Indium Antimonide
iFFT	inverse fast Fourier transform
IoT	internet–of–things
IQE	internal quantum efficiency
IrDA	infra–red data association

IR	infra-red
ISP	internet service provider
ITU	International Telecommunication Union
I–V	current–voltage
K	thermal conductivity
λ	wavelength
λ_{peak}	peak emission wavelength
LED	light-emitting diode
LD	laser diode
LiFi	light fidelity
L–I	electroluminescence (power)–current
L–V	electroluminescence (power)–voltage
LoS	line-of-sight
LTE	long-term evolution
MAC	media access control
MOVPE	Metalorganic Vapour Phase Epitaxy
MQW	multiple quantum well
n_{ideal}	ideality factor
OFDM	orthogonal frequency division multiplexing
OOK	on–off keying
OWC	optical wireless communications
PAM	pulse amplitude modulation
PC-LED	phosphor-converted light-emitting diode
PCB	printed circuit board
Pd	palladium
PD	photodiode
POF	polymer optical fibre
PMMA	poly(methyl methacrylate)
PWM	pulse width modulation
QAM	quadrature amplitude modulation
RC-LED	resonant-cavity light-emission diode
RF	radio frequency
ρ	resistivity
R_p	parallel resistance
R_s	series resistance
SiO_2	silicon dioxide
SiPM	Silicon photon multiplier
SNR	signal-to-noise ratio
SPAD	single photon avalanche photodiode
SRH	Shockley-Read-Hall
SSL	solid state lighting
Ti	titanium
TIA	transimpedance amplifier

T_j	junction temperature
micro–LED	micron-sized light-emitting diode
UPnP	universal plug-and-play
UP-VLC	Ultra–Parallel Visible Light Communications
V2V	vehicle-to-vehicle
V2X	vehicle-to-infrastructure
VLC	visible light communication
VLCA	Visible Light Communications Association
V_{th}	threshold voltage
VR	virtual reality
WDM	wavelength division multiplexing
WiFi	wireless fidelity

Chapter 1

Introduction

This thesis was developed in the context of the EPSRC-funded project Ultra–Parallel Visible Light Communications (UP-VLC). This project aimed to explore the potential of semiconductor-based light sources for new forms of high-speed optical data communications based on visible light, offering novel technology for wireless, mobile and personal communications, high-performance computing and data centres. The UP-VLC programme involved a partnership between the Universities of Strathclyde, St. Andrews, Edinburgh, Oxford and Cambridge. The associative collaborative work involved the author in multiple visits to the above institutions, in particular the Universities of Edinburgh, Oxford and Cambridge. As such, the main focus of this thesis is the application of micro–LEDs for visible light communication (VLC), in particular data transmission in free–space and guided-wave configurations. Results obtained from a direct collaboration with these other research groups are pointed out throughout this thesis, in particular in chapter 5.

This thesis follows a natural progression from the development of devices to their final application in optical communications with high level data encoding modulation schemes. The various chapters contain work that resulted in a number of publications.

Chapter 1 introduces the concept of VLC and light fidelity (LiFi), giving a short historical overview, the current state of norms to be adopted by industry and the directions taken in research. With these concepts in mind, motivation for the use of micro–LEDs within this field is also defined.

Chapter 2 presents a brief historical overview of LED light sources, in particular those LEDs based on aluminium indium gallium nitride (AlInGaN) epitaxial material. This is followed by a description of the physics, operating principles and recombination mechanisms of gallium nitride (GaN)-based LEDs. Typical electrical, optical, spectral and thermal characteristics and methods to measure them are presented. In addition, issues and problems specifically affecting micro–LEDs are also mentioned.

Chapter 3 begins with the fast response to direct intensity modulation of GaN-based micron-sized light-emitting diodes (micro–LEDs), the point of major interest for VLC applications. Benefits and limitations are also presented, accompanied with by respective impact for communications.

Chapter 4 begins with a summary of the basic limitations of micro–LEDs, as raised in chapters 2 and 3. New ideas to mitigate the thermal management and current crowding problems are formulated and studied with broad area LEDs and two novel techniques. As a result, two novel micro–LED designs are presented, namely segmented pixels and ring–shaped pixels tailored for guided–wave and free–space VLC, respectively.

Chapter 5 focuses on modulation schemes, communications systems and data transmission using the new pixel designs introduced in chapter 4. Major data rate results are presented here obtained in collaboration with our partner research groups using state of the art systems and modulation techniques.

Chapter 6 closes this thesis with a summary of key findings identified, future research to be pursued and makes a few recommendations for future practice.

1.1 Historical view of visible light communications

Communication of information using visible light dates back to at least 800 BC when fire beacons were used to transmit simple signals over long distances, in particular for guiding military operations. Pharos of Alexandria was the first notable lighthouse dating back to 247 BC. Constructed by the Ptolemaic Kingdom as a symbol of the Empire, it was used to aid sailors and as a defensive monument. Lighthouses were originally used to signal the location of reefs and promontories to vessels approaching the coast. Nowadays, lighthouses are still in use.

In 1880 Alexander Graham Bell and Charles Sumner Tainter invented the photophone. Figure 1.1 illustrates the operation principle of the device. Sunlight is collected and focused into a diaphragm-coupled mirror. Human speech generates sound waves that modulate the diaphragm with pressure changes, thus varying the intensity of reflected light. On the receiver side, the modulated sunlight is collected and focused in to a photo sensitive membrane generating an electrical signal proportional to the received intensity. Then, the signal is amplified and played back on a speaker. The photophone was the first demonstration of a device with wireless voice communications, but unfortunately it was never used for real applications.

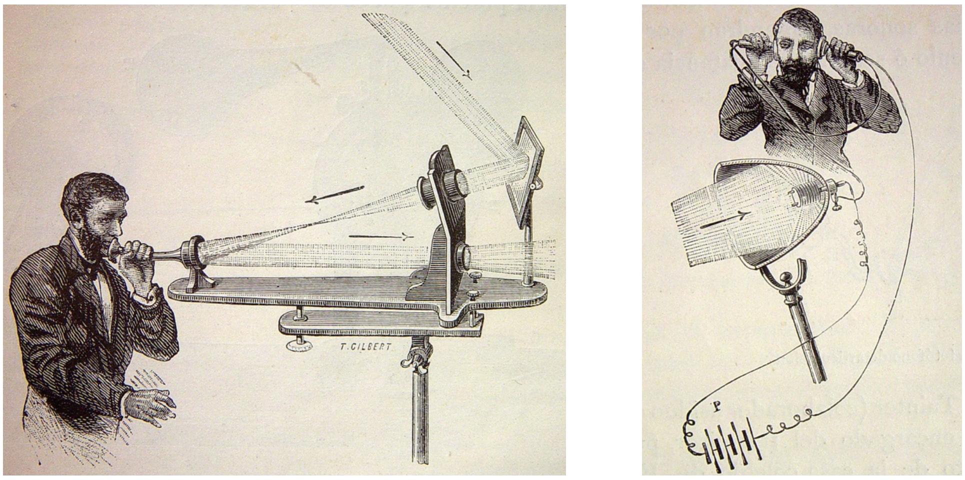

(a) (b)

Figure 1.1: Principle of operation of the photophone, (a) transmitter and (b) receiver. From Wikimedia with free licence.

The heliograph, shown in figure 1.2, was widely used during the 19th and 20th centuries, playing an important role during World War I. This device consists of a mirror and an shutter that signals by flashing sunlight with Morse code. Ship-to-ship communications emerged using kerosene lamps with a lens to transmit light signals over long distances. Signal lamps are still in use by navies across the world when radio communications needs to be silent. Their main advantage is security as the signal is directional (line-of-sight) and the communication is only compromised when precisely intercepted.

These early stage technological advancements using visible light were a major step forward transmitting information in a format now known as free–space and/or line-of-sight (LoS) communications.

(a) (b)

Figure 1.2: Examples of heliographs: (a) German built system and (b) Ottoman heliograph crew at Huj during World War I, 1917. From Wikimedia with free licence.

Remote control

With the advent of LEDs and the need for cord-less control of systems, light communication appears as a means of transmitting digitised information over short distances. The primary example is the infra-red remote control operating at wavelengths (λs) of 850 – 900 nm. A standard driven by a group of ∼50 companies in the 1990s, the infra–red data association (IrDA), established the first implementation of light communications using point-and-shoot principles. The main reason behind the development of the IrDA remote control was to take the last few metres of controlling a device from a cable to a wireless data transfer. The underpinning technology was the already mature GaAs-based LEDs for the transmitter and Si-based PIN diodes for the receiver. Figure 1.3 (a) presents examples of IrDA remote controls for domestic use. IrDA is invisible to the human eye, but can be detected by image sensors, for example as shown in Figure 1.3 (b).

IrDA offers advantages such as: security, given that data being transmitted via infrared is


(a) (b)

Figure 1.3: Examples of IrDA transmitting devices, (a) domestic remote controls and (b) emission from a remote control detected by an image sensor. From Wikimedia with free licence.

very difficult to intercept as it is directional; relative freedom from spectrum regulations; low cost, given that components cost pennies; freedom from radio frequency (RF) interference or signal conflicts; very low BER, thus being very efficient; using small and low power components permitting a variety of form factors. Home appliances and portables devices have made wide use of IrDA, being the first wireless communication protocol able to connect devices of different types. Examples are mobile phones sending a job to a printer via IrDA, direct file sharing between devices and universal remote control of TVs and DVD players without the need for a router or network. These applications marked the initial concepts of what is now known as the internet–of–things (IoT). Limitations such as the lack of encryption and unique identification, low data rates, short connection times and devices being unaware of the existence of other devices left open room for competing technologies. Nowadays, IrDA capability is being replaced by RF technologies such as wireless fidelity (WiFi) and Bluetooth operating in the 2.4 GHz and 5 GHz bands.

1.2 Modern concepts in wireless communications

1.2.1 Supply versus demand

Raise of mobile data consumption

Radio frequency (RF) is the unpinning technology for the modern wireless communications we use today, from mobile phones to satellites. According to Cisco's visual networking index

(VNI) global mobile data traffic forecast 2016, mobile data traffic will grow at a rate around 53% from 2015 to 2020, as show in figure 1.4. Mobile data communication is expected to increase eightfold in the next five years, four-fifths of which is to come from smartphones alone [1]. The average connection speed is expected to triple in the same period. According to figure 1.4, the largest market share by 2020 is expected to be Asia Pacific with the largest market growths in Middle East and Africa.

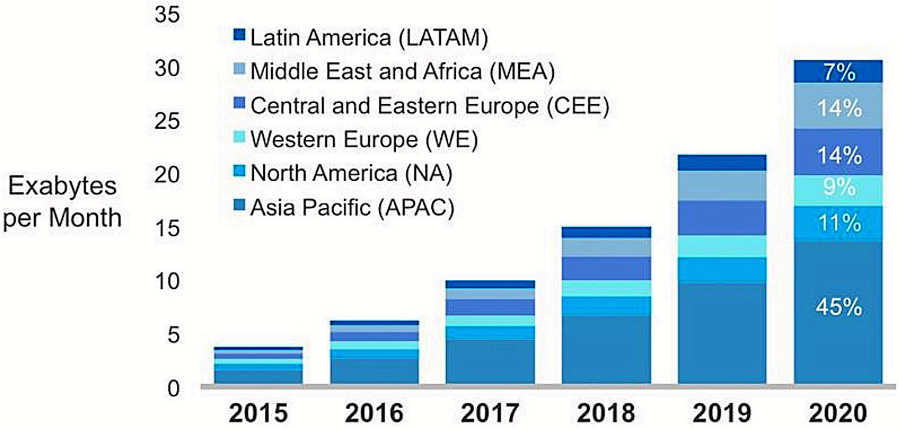

Figure 1.4: Global mobile data traffic forecast by region. From [1] with public license.

The number of connected and interconnect devices per user is increasing at an exponential rate, and by 2020 the number of connected devices is expect to reach 1.5 per capita globally. This exponential growth places a large stress on the current RF technologies and infrastructure, with the risk of not meeting demand in coming years [1].

Spectrum crunch

Future development of RF technologies is highly dependent on the availability of electromagnetic spectrum. This spectrum is referred to as a global resource by the International Telecommunication Union (ITU) [12]. Figure 1.5 presents the electromagnetic spectrum allocation in the United States as of 2011. As spectrum is a scarce resource, the exponential rise in consumption of mobile data is leading to what is known as the '*spectrum crunch*'.

The next generation of RF wireless mobile communications is the so-called 5G (fifth generation). It is set to use frequency bands at 28, 38, 60, 72-73 and up to 90 GHz. These high frequencies allow increased data rates (>1 Gbps) with replies to queries between a mobile device and the network at $\sim 1\ ms$, an order of magnitude lower than the current 4G technology, this is commonly known as latency. The debate regarding potential problems such as signal penetration, clash with satellite frequency bands, human health implications, deployment costs and energy efficiency (Watt per unit data) is still ongoing. The terrestrial infrastructure behind the wireless communication must also be considered. This refers to the long physical links (100s km) between the access point (AP) to the internet providers and servers. As of today, this is mostly based on optical fibre placed underground connecting cities and countries, and placed on the seabed connecting continents. Typically, fibre is deployed up to the main streets with the optical signal being modulated/demodulated from/to an electrical signal sent via copper wires to the final client. Such systems are limited in bandwidth by frequency-dependent losses beyond 10 MHz for long cables [13]. Currently a large scale deployment of high-speed fibre-optics directly to the final client is not commercially viable due to the cost of components and safety concerns over clients' potential exposure to high intensity infrared laser beams [13].

Limitations of future radio-frequency communications

Regulations impose strict frequency allocation bands for each application, as shown in Figure 1.5. This leads to an increase in licensing costs per frequency band for the service providers. The high costs, impose long periods for return of investment, increasing prices for the services for the end users. Furthermore, as each new RF technology depends the deployment of new hardware (base stations, repeaters, switches) there is a high risk of technology obsolescence before profitability.

A direct effect of the '*spectrum crunch*' is the balance between data rate and latency. As the available spectrum is scarce, so it is the available bandwidth. In a crowded RF band with many connected devices, transmitted signals suffer from additional distortion created by interference. These can significantly decrease the signal quality leading to limited coverage and blind spots i.e. low signal within buildings. One way to mitigate distortions is to increase the overhead per transmitted frame, e.g. better estimation of the available channel, at the

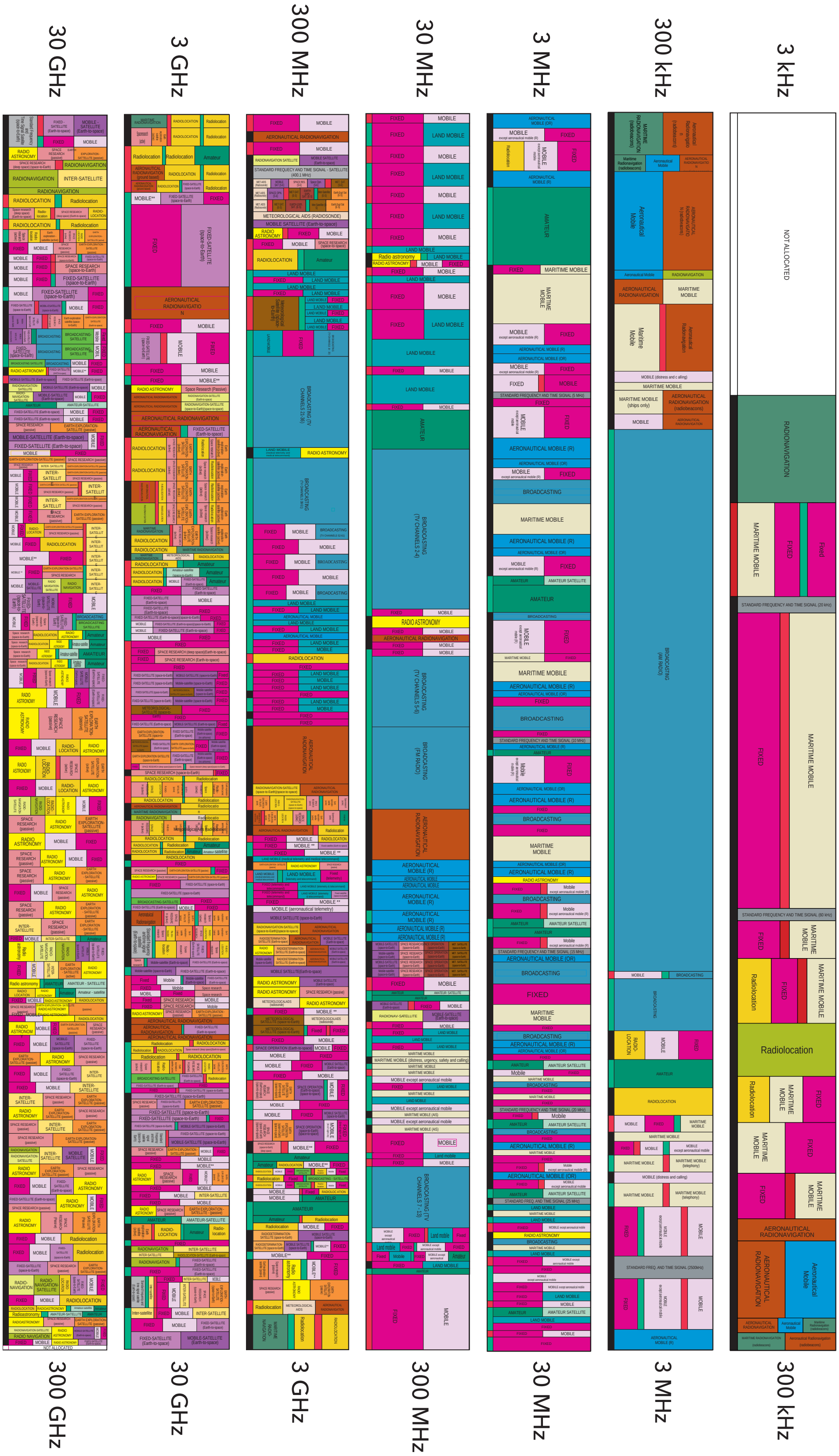

Figure 1.5: United States frequency allocation chart in 2011. Adapted from [2].

expense of throughput (bitrate). Distortions are a major issue for the IoT as the number of connected devices per unit area is expected to increase exponentially. Technologies such as beam forming can reduce interference and increase data rates at the expense of coverage, number of connected devices at a given time and increased cost of access points (APs). The 5G technology seeks to solve the above problems by using larger bandwidths at carrier frequencies in the range of 30–90 GHz. Increasing the base frequency decreases the penetration depth of the electromagnetic waves due an increased absorption by the atmosphere (path loss) and materials (buildings). In the general case, the received power on a fixed area can be approximated by the loss in the electric field for a given frequency, material properties and distance given by [14]:

$$Power \propto |E_0|^2 \, \frac{2\pi f}{v_p\sqrt{\frac{\mu}{\varepsilon}}} \, e^{-\frac{4\pi f}{v_p}\,x} \tag{1.1}$$

where $|E_0|^2$ is the initial electric field intensity, f the frequency, v_p the propagation velocity, μ the magnetic permeability, ε the electric permittivity and x the path distance. From equation 1.1, a linear increase in the path distance or the frequency leads to an exponential decrease in the received power. Solving equation 1.1 to distance assuming free-space transmission (air only) with $|E_0|^2 = 1$, $Power = 1$, $v_p = 3 \times 10^8$, yields that to achieve the same received power from a 800 MHz 4G cell, the distance from 30 GHz 5G cell has to decrease by a factor of 27. This means if in a typical 4G deployment one can be ≈ 1 :km from the a cell to receive good signal quality, in a 5G deployment one must be ≈ 37 :m from a cell to receive similar signal quality. In order words, in a 5G deployment the distance between cells would $\approx 50\,m$, a similar distance to the separation between street lights. In addition, the when the signal passes through various materials, e.g. walls and windows, the changes in μ and ε will further attenuate the signal, which may indicate that indoor usage of 5G technologies may not be possible. As such, for pervasive coverage in 5G technology many more cells are required, leading to significant challenges for the infrastructure deployment and cost. These aspects open the question for the real benefit of the new technology versus the current solution given the drawbacks and the significant increase in investment required.

1.2.2 Visible light communications (VLC)

Concept

Acknowledging the issues mentioned in section 1.2.1, VLC appears as one possible solution to answer the communications needs of our fast-paced society [15].

The main idea behind VLC is to use the unlicensed visible wavelength spectrum ($\lambda = 380-780$ nm) for communications. This is closely related with novel developments in Gallium Nitride-based semiconductor technology. A VLC data stream is achieved by modulating the intensity of the light to signal binary data or bits. A high speed communication link requires sending and receiving a large amount of data per second, measured in Mbps (10^6 bit per second) or Gbps (10^9 bit per second). Such links require fast modulation solid state light sources such as LEDs and laser diodes (LDs). The nature of VLC applications raises concerns over users being exposed to modulated light, imposing significant challenges on the use of LDs in particular, due to eye safety [16].

The strong need for VLC emerges from the increasing usage of mobile devices by end users that consume large amounts of data with expensive and limited amount of bandwidth [15].

In section 1.2.1 we introduced the spectrum limitations of current RF technologies. Current commercial systems have the following bandwidths: from 20 MHz to 100 MHz for 4G by the 3rd Generation Partnership Project (3GPP) [17], the current standard for the fourth generation mobile communications; and from 80 MHz to 160 MHz for 802.11.ac WiFi by the Institute of Electrical and Electronics Engineers (IEEE) [18], the current generation of wireless local area network. This compares to a theoretical $\sim 300\ THz$ of license-free bandwidth in the visible spectrum, which is also license-free. This is nearly ten thousand times greater than the RF spectrum [15].

Advantage

VLC is a subset of a larger field known as optical wireless communications (OWC), which also includes infrared and ultraviolet spectrum for the purpose of communications. Infrared is already a mature technology in optical communications with emitters and receiver devices

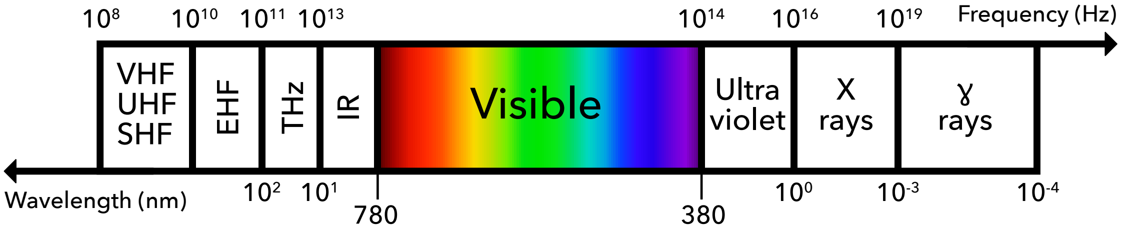

Figure 1.6: Electromagnetic spectrum in logarithmic scale for frequency and wavelength. The visible range is enlarged and is not to scale.

highly optimised. The main advantage of using the visible range the possibility to couple it with existing infrastructure. This opposes to infrared systems that require deployment of new infrastructure for optical communications only.

VLC can in principle be implemented at any place where a light source already exists, and it can be divided into two major types, namely free–space and guided wave. Free–space embodiments means that light travels through an existing medium (air) between the emitter and the receiver, mostly (but not only) by line of sight (LoS). The typical case of free–space is the LED-based lighting. Guided–wave embodiments mean that light is contained within an optimised medium offering low loss, and in this thesis it refers to polymer optical fibre (POF). This type of VLC also includes applications for optoelectronic interconnects with waveguides.

Figure 1.7 presents two application scenarios for VLC: (a) indoors and (b) outdoors. These can be multiplexed with free–space for clients and guided wave for APs. Other applications scenarios exist such as underwater and in-flight. Indoor applications are based on the use of LED-based lighting infrastructure to provide illumination and communications to devices such as computers and mobile phones. Outdoor applications include for example street and traffic lights to serve as APs to a person carrying a mobile device as well as road vehicles equipped with LED lights. This is also known as vehicle-to-vehicle (V2V) and vehicle-to-infrastructure (V2X), where vehicles can *talk* to each other in a daisy chain enabling self-driving, and to the infrastructure enabling smart traffic management.

High-speed free-space data communications is not complete without a high-speed access to the existing network. The large scale infrastructure of national network grids is composed of high-speed laser-based fibre optics made of silica and with guide-waving cores of a few microns, technologies that have been in continuous development since the first transatlantic

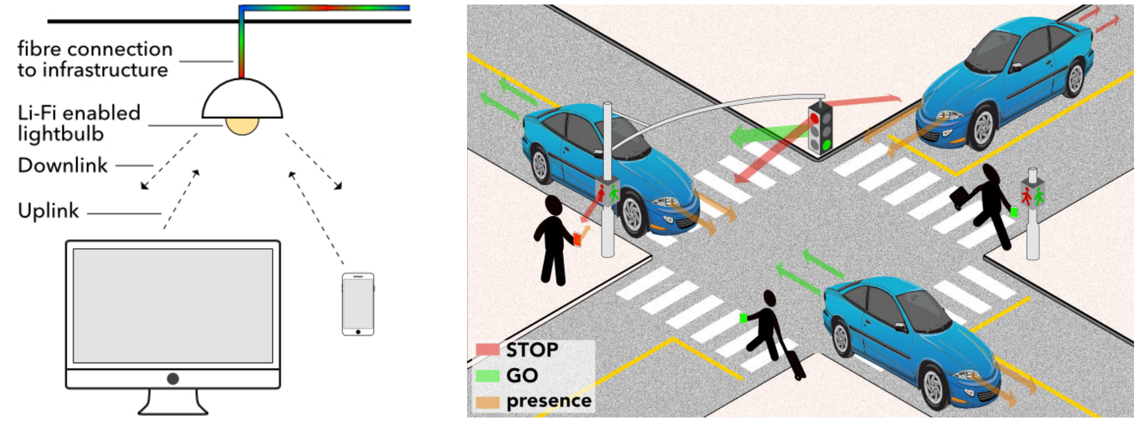

(a) (b)

Figure 1.7: VLC usage scenarios: (a) indoors for device-to-infrastructure and device-to-device communication; (b) outdoors for device-to-infrastructure, vehicle-to-infrastructure and vehicle-to-vehicle.

fibre-optic cable 1988 [19]. This type of optical communication is not practical for the final delivery from the main switch on a street to the clients in houses or apartments due to the cost of equipment and installation, and due to eye safety risks of exposing users to high-intensity laser beams at infrared wavelengths (1310 nm, 1550 nm) [3]. Today, this final delivery, also known as '*the last km*', is in the majority of the cases installed in copper cables, limiting the maximum throughput to about 100 Mbps [3]. One possible solution is the use of polymer-based optic fibre (POF) coupled with LED technology to deliver a low-cost alternative that is also optically safer. In figure 1.8 presents the attenuation of a typical step-index POFs with about 1 mm diameter core. The low loss windows are situated in the blue, green and red regions of the optical spectrum. This shows a good match with the wavelengths available in GaN-based LEDs. The major limitation of such a system is the modulation bandwidth of traditional LEDs. This represents an opportunity for micro-LEDs to improve performance by enabling larger modulation bandwidths and eventually achieve the limit imposed by dispersion of such large core fibres [3].

An example of an application is shown in figure 1.7 (a) where a POF link provides high-speed network access to a VLC-enabled light bulb, complementing the free-space connections. This represents a full light-based system from large-scale infrastructure to the final client. It is estimated that for residences the total costs of a POF-based network during its economic

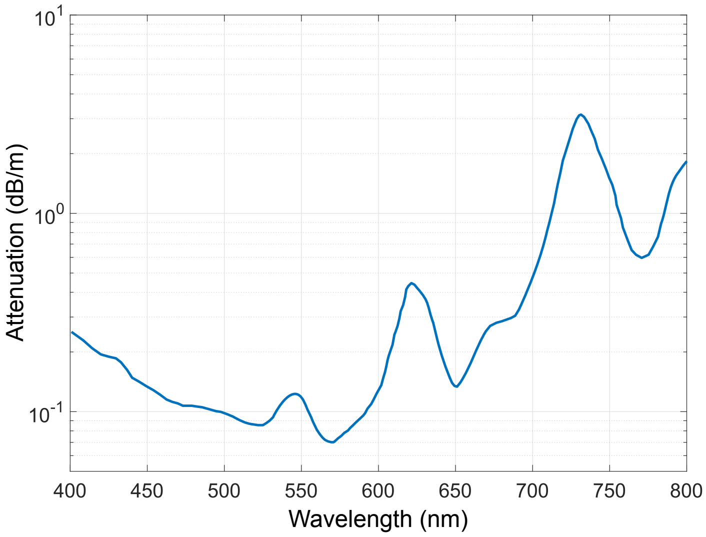

Figure 1.8: Attenuation of step-index polymer optical fibre versus wavelength. Adapted from [3].

lifetime are lower than traditional copper cable infrastructure [20]. In addition, this allows similar LED technology to be used for both landlines and free–space, minimising development costs and simplifying standards. POF could be used in both the final delivery, '*the last km*', from a fibre station to buildings or homes, and for the intranet inside buildings.

In VLC, the major technology barrier is the emitter. The major properties required of an emitter device for VLC are optical power and fast response (modulation bandwidth). Being semiconductor-based, LEDs can be controlled directly by electronics allow fast modulation required for VLC. LEDs are inexpensive and are available at various wavelengths in the visible range, making them an ideal candidate for VLC. In addition, LED-based solid state lighting (SSL) provides high quality of white light [21], as determined by the colour rendering index (CRI). Details on VLC systems will be presented in chapter 5.

1.2.3 LiFi

Light-fidelity (LiFi) is a term coined by Professor Harald Haas from the University of Edinburgh during a talk Technology, Entertainment, Design (TED) conference in 2011 [22]. LiFi combines the existing illumination infrastructure with LED lightbulbs prepared for optical communications. Commercial systems with this capability are starting to emerge and, by the way of example, figure 1.9 presents the Li-1st, a commercial product from the UK company pureLiFi, demonstrating a luminaire as an access point (AP) and a receiver streaming high-definition video in indirect lighting conditions, also known as non-line-of-sight. Other companies, such as Oledcomm and Luciom in France also commercialise LiFi systems, and the latter was recently acquired by Philips Lighting [23].

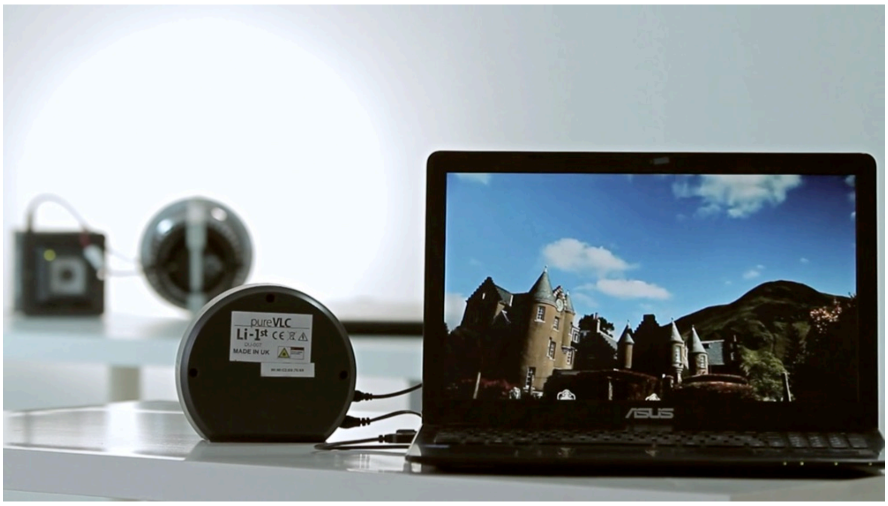

Figure 1.9: First LiFi commercial system by the UK company pureLiFi, the Li-1st, a full–duplex VLC system. A videio is being communicated wirelessly over free-space between source and detector using reflected light. Picture taken from [4].

LiFi can be described by two separate parts: the physical layers and the network layers [24]. The physical layers is where the VLC sits with front-end subsystems (devices and components) for free–space, and is the carrier of information between the AP and receiving device. These layers also include the all digital signal processing (DSP) associated with data transmission. The network layers can be described by the following sublayers: channel model, link level algorithms, media access control (MAC) protocols, interference mitigation, security, networking and communication protocol interface. It is responsible for integration of the APs and the connected device to the existing infrastructure and connecting these to the internet service provider (ISP).

LiFi is tailored for both indoor and outdoor (street lamps) usage, going beyond current capabilities of RF-based technologies. It supports higher data rates per unit area; the network layer supports hundreds to thousands APs (e.g. lightbulbs); installation is easy and inexpensive with universal plug-and-play (UPnP); it is immune to electromagnetic interference; it is secure within each room; it is energy efficient. It can be installed in places where electromagnetic radiation is considered a hazard such as aircraft, hospitals, power stations, and petrol stations.

LiFi is not a direct substitute for wireless fidelity or WiFi. LiFi is visioned as a complement to WiFi to create a hybrid LiFi/WiFi network capable of providing higher performance and better service for end users [24]. LiFi differs from WiFi in the implementation of roaming between access points and capability to accommodate a large number of users without any performance degradation. LiFi is also not a direct substitute for mobile networks. As penetration and performance of high-frequency RF are limited for indoor use, LiFi may complement mobile communication systems to maintain a good quality of service indoors. Figure 1.10 illustrates the implementation of LiFi with other communication networks as envisioned by the UK company pureLiFi. The handover from mobile cellular to WiFi, and to LiFi can be integrated such as the user only experience a unified network access. In addition, the nature of lighting creates an ideal opportunity to for roaming between the LiFi APs (luminaires) without major interference from adjacent luminaires.

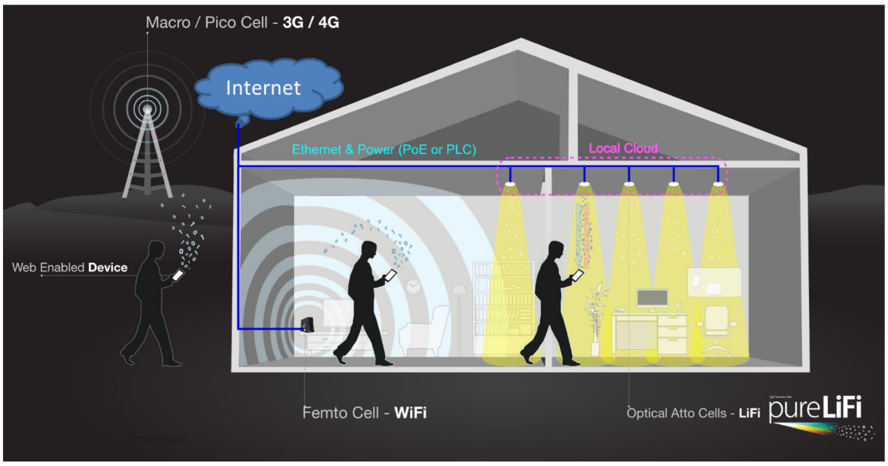

Figure 1.10: Illustration of the communication handover between services (mobile to WiFi to LiFi). From [4].

Energy consumption has distinct aspects in LiFi compared to other communication technologies. As the system is superimposed on the lighting infrastructure, in the majority of the use cases LiFi does not require separate hardware and consumes minimal additional power. The first idea of transporting information and energy simultaneously have emerged for RF technologies [25]. The extension for optical wireless communication is the use of photovoltaic solar panels as optical receivers for VLC [26]. In addition, this allows a number of intelligent services running on the lighting infrastructure, also known as smart lighting. In a TED talk in 2015 professor Harald Haas presented a LiFi system operating with solar panel as a reeiver [24] as shown in figure 1.11. The system allows to harvest energy (DC power) and receive communication signals (AC modulation) at the same time, an important step towards a energy-neutral communication system. Benefits of a large scale deployment of a LiFi network include: APs with unique identifier separated by a metre or so can provide very accurate positioning for mapping services indoors and outdoors; lighting infrastructure can easily include sensors to be aware of the presence of people, allowing buildings and rooms to automatically adjust light colour to the needs of a each user or to signal emergency situations such as a cardiac arrest, a fire or a person trapped in a lift.

Figure 1.11: A public demonstration of a solar panel as a optical receiver for LiFi by professor Harald Haas in a TED talk in 2015. From [5] with Creative Commons licence.

1.3 State of the art

1.3.1 Solid-state lighting and visible light communications

The developments of SSL and VLC are at different stages. Research in SSL – that is, lighting based on semiconductor electroluminescent devices, especially LEDs – started in 1990s [27].

It is a mature technology with commercial LED-based light bulbs being available now for about eight years. Research in VLC started in early 2000s with applications for POF [28], and by the late 2000s VLC was considered for a standard by the IEEE [29].

SSL started with the combination of two technologies, namely III-Nitride LEDs and wavelength down-conversion [30]. In early 1990s groups in Japan developed Gallium Nitride crystal growth by Metalorganic Vapour Phase Epitaxy (MOVPE), including buffering on sapphire substrates, p-doping and double heterojunctions for LEDs [27]. The idea of wavelength down-conversion has existed since late 1960s, and consists of using high energy photons to pump a lower energy bandgap material to achieve a combined spectrum with specific wavelength characteristics. White light is achieved using energy efficient GaN-based LEDs emitting in the blue and selecting phosphors that emit in the green, yellow and/or red regions packaged in a single chip, this being known as the phosphor-converted light-emitting diode (PC-LED) architecture and was first filled for patent in 1996 by a team of scientists at the German company OSRAM Opto Semiconductors [31]. Current SSL has proven very efficient in comparison with traditional lighting technologies. As of 2016 the highest luminous efficacy for a commercial LED is 210 lm/W by Nichia and in research is 303 lm/W by Cree [32]. This compares to 16 lm/W for the historical Thomas Edison filament-based bulbs. Luminous efficacy is a measure of light efficiency given the colour response of the human eye. Typical sub-efficiencies of a PC-LED are: blue LED (40%), phosphor plus package (70%), and spectral match to the human eye response (80%). Thus, the overall wall plug efficiency is $\approx 22\%$ [33]. Current developments are concentrated on increasing the output optical power – thus improving surface brightness of the LED, packaging technology, chip design, power handling and colour rendering capabilities. The two major applications of SSL today are indoor/outdoor illumination and automotive lighting.

LED-based VLC as we know it today was, as mentioned above, pioneered in Japan in the early 2000s [34]. It is currently under very active research with a few commercial products available from spinoff/startup companies. There are two main approaches to the development of VLC, namely top-down and bottom-up. The top-down approach consists of firstly start with the communication system that provides a number of services and secondly looking to implement it with existing off-the-shelf high-power PC-LEDs. This is the approach usually adopted by communication systems groups and data rates achieved are up to 1 Gbps in free–space, limited by the bandwidth of the LEDs ($\sim$ 20 MHz) and the recombination lifetime of the phosphors [35, 36]. The bottom-up approach, as presented in this thesis, consists of designing LEDs specifically for optical communications, prioritising fast response (high bandwidth) and taking into account the technicalities of communication systems for free–space and guided–wave modes of operation. The most effective way to increase the communication performance is to increase the total available bandwidth of the system.

Major sources of limitations are the emitters and receivers, and in the case of guided–wave operation the POF material also limits bandwidth for long reach, see chapter 5. As the focus of this thesis is on the emitters, this means increasing the response speed of the LED. This can be achieved by reducing the pixel size during fabrication, making the LED smaller. This comes with penalties in optical power however, described in chapter 3. Small-size LEDs or micro–LEDs, originally dating back to the 1970s [37, 38], have significantly faster response than large area LEDs (commercial high-power). Investigation of GaN-based micro–LEDs started in the early 2000s [39, 40, 41, 42, 43], although studies of micro–LEDs for VLC applications only started in the early 2010s with devices of typical response times in sub-nanosecond regime [44], and bandwidths up to 450 MHz [45]. Having available bandwidths in the scale of 100s instead of 10s of MHz – achieved conveniently with the micro-LED approach – is one of the major advantages of VLC over RF. A baseline communication performance is achieved with simple modulation schemes such on–off keying (OOK) in short range free–space, described in more detail in chapter 5, and blue-emitting micro–LEDs were in this way able to achieve data rates up to 1 Gbps in free–space [46]. Higher level modulation schemes such as orthogonal frequency division multiplexing (OFDM), also described in detail later, were able to increase data rates up to 3 Gbps with a single pixel [47]. Obtaining data rates at the Gbps scale with visible LEDs is major achievement for future mobile communications.

VLC applications are not limited to free–space, guided–wave operation is also explored for terrestrial POF-based links. Typical ranges of interest are 10 to 500 m, the necessary distances for street to residence connections and in-building networks. At the moment, research is focused on ranges from 10 to 50 m , mostly due to the bandwidth limitation of the poly(methyl methacrylate) (PMMA) material of the POF for long reach. Guided-wave applications do not required any colour rendering capabilities, there is instead, a need for light emission in the low absorption spectrum windows of the POF, see figure 1.8. For this reason, red resonant-cavity light-emission diodes (RC-LEDs) have typically been used in order to select the low-loss spectrum window and maximise bandwidth. As previously shown in figure 1.8, POF also presents low-loss windows at the blue and green wavelengths. Data transmission with a single commercial RC-LEDs in POF achieves 3 to 5 Gbps over 25 m [48, 49] and 1.5 Gbps over 50 m [50, 51]. Regular GaN LEDs achieved 5.5 Gbps over 1 m [52], 3 Gbps over 10 m[53] and 1 Gbps over 50 m [54]. A single micro-LED has shown to achieve data rates of 1 Gbps over 1 m [55], 5 Gbps over 10 and 25 m [56, 49], and 1 Gbps at 50 m [57]. Although RC-LEDs at long reach (25–50 m) are able to achieve higher data rates than typical LED or micro-LEDs due to the higher optical power, they present drawbacks such as cost and restricted wavelengths.

In both cases, free–space and guided–wave operations, higher data rates per channel/link are possible by using multiple LEDs or micro-LEDs at different wavelengths simultaneously, a technique known as wavelength division multiplexing (WDM) [58, 59], or by clustering multiple pixels to increase the optical power [60].

1.3.2 IEEE standard

The IEEE is responsible for the standardisation of VLC with inputs from industry and academia. The VLC standardisation process started in 2008 with the first public domain documentation available in 2009 [29]. The process was and is conducted within the IEEE Wireless Personal Area Networks working group (802.15) [61]. The specific codename for VLC is 802.15.7, which stands for “Short-Range Wireless Optical Communication Using Visible Light”, and the standard document is available at [9]. As of 2017, IEEE 802.15.7 remains a draft. “Considerations for VLC using LED displays” considers dynamic displays and addressed displays for the purpose of data transmission, and guidelines for broadcast topologies are also given. This closely follows on from work done by Japanese research funded by private industries within the framework of the Visible Light Communications Association (VLCA).

In table 1.1 are presented spectrum bands as defined by the standard. Each band can have a direct match with a III–V semiconductor alloy. Spectral widths are in line with typical emission observed from LEDs and colloidal quantum dot (CQD) colour converting materials. Regarding high-speed data transmission, the physical layers (PHY) II and III defines data rates up to 96 Mbps at a clock rate of 120 MHz.

Table 1.1: IEEE visible light wavelength band plan. From [9].

Wavelength (nm)	Spectral width (nm)	Code
380 - 478	98	000
478 - 540	62	001
540 - 588	48	010
588 - 633	45	011
633 - 679	46	100
679 - 726	47	101
726 - 780	54	110

Further developments in the IEEE 802.15.7 standard appeared in 2012 with various modulation schemes and dimming support [15]. In 2013 and 2014, the standardisation process acknowledged new services enabled by VLC such as: safety automotive lighting, RF-free toys, fashion and fabrics, light control networks, indoor positioning, among others [62, 63]. As of 2017, the standard 802.15.7 is being revised [29] and the the topic of LiFi / OWC is added as a workgroup to the standard 802.11 for WiFi.

1.3.3 Opportunities

As of 2017, VLC is a growing area in research and in industry with new companies appearing every year. There are still, however, a number of important challenges to overcome for the VLC/LiFi technology to reach maturity. Each one of these provides an opportunity for further research.

Integration with existing network systems

The world of telecommunications is complex and new investments are large. As such, VLC needs to simultaneously offer its benefits and integrate within the constrains of existing system. LiFi provides networking topologies to support a large number of APs, clients and the inherent roaming between them maintaining security, high performance and quality of service. The range of LiFi applications is broader than previous RF-based technologies [24]. As such, it becomes increasingly important for LiFi to be integrated well with current WiFi and 4G long-term evolution (LTE). This is particular important as the clients need to roam between the different services smoothly. Integration with such large networking topologies is a significant challenge, in particular regarding standards.

Device integration

The main headline capability of VLC is its high-speed. Throughout this thesis performance levels of micro-LEDs are demonstrated under laboratory conditions. In order to increase the technology readiness level one must solve a number problems. First, the modulation speed of micro-LEDs straight from the chip is at least an order of magnitude higher than commercial PC-LEDs. Commercialising high-power micro-LEDs capable of illumination is not as simple as wire bonding a chip with clustered micro-pixels on a package and appling a heatsink. Early tests by ourselves have shown the speed to quickly decrease in such clustered formats. A strong mutual heating dependancy seems to be the cause. Second, high-speed micro-LEDs are GaN-based and present emission from the UV to green wavelengths. For a single white LED chip, this implies the integration of fast wavelength down-conversion materials, typically quantum dots, platelets or nanocrystals in a single package. These materials typically show an inverse relation between conversion efficiency and recombination time. Third, to achieve reliability, light modulation and data transmission requires specific electronic control of current rather than voltage (DC current driver plus AC current modulation). Current drivers suffer from inductance which quick decreases their efficiency in high-speed operation. In addition, the driver needs to be integrated in a tight space inside the lightbulbs. Lastly, a wide penetration of LiFi networks can only be achieved when each lightbulb becomes a transceiver, i.e. a transmitter and receiver of data. This requires suitable detectors to be integrated with hte emitters without optical crosstalk or electrical interference.

Optical wireless communication

Working with visible light that is also used for illumination implies signal conditions that are dependent on the needs of each user regarding the lighting conditions, which may require high and/or low levels of illumination. This means that bandwidth and signal-to-noise ratio (SNR) conditions are broad and need to be considered. Various modulations schemes exist for these situations with their advantages and disadvantages. As standards develop, there is a need for unification which might encompass a tradeoff of performance for features to fulfil a broad range of applications. There is also a need for further optimisation regarding the DSP, bill of materials and power consumption e.g. DSP can overcome non-linearities in the system by using expensive chips and high power consumption. Multi-wavelength emitters enable WDM techniques, which can increase the overall data rates of the link via multichannel operation. Optical integration, particularly at the receiver, is required to discern the different channels. Integrating these in a small cost-effective package is a significant challenge for research and for industry.

Location services

LiFi involves giving each AP an unique identifier. Upon installation, each AP can be mapped within a building or street. This is especially important for indoor as the global positioning system (GPS) and globalnaya navigazionnaya sputnikovaya sistema (GLONASS) are too week to penetrate through buildings. Roaming through APs can provide directions and location-based notification. Combining these with other sensory information enables, for example, localised signalling and evacuation routes on-demand for occupants and emergency teams not familiar with a particular building. All of these can be used even when a user does have clearance to access the LiFi network and can provide feedback through the lighting system, blinking or change of colour. How these services will work together, what they require from the LiFi infrastructure and what they impose on the APs is not yet fully clear. This a field known as smart or digital lighting which is under active research in academia and industry operating beyond the specific context of LiFi.

Open questions

There are a number of questions to which answers are not yet known. One such example is if the combined use of lighting and data communication in a single AP is a better solution than the use of existent SSL alongside a dedicated communications module using techniques such beam steering. There is a growing interest in GaN laser-based phosphor-converted lighting systems due to their increased capability for high-power with a first such product already present in the automotive industry. In addition to power, laser diodes present larger bandwidths than LEDs. These properties might be of interest also for underwater and satellite-to-satellite communications. The question is if the laser approach is feasible for SSL given drawbacks with temperature control, cost, efficiency and eye safety requirements. An area that has seen a strong focus, particularly in Japan, is V2V and V2X communications. One of the main ideas here is to use image sensor and pattern-encoded frames within the LED-based vehicle headlight and traffic lights to transmit data. The signal recovery is then done using an image sensor with low resolution and high speed to recognise and decode the patterns with minimum use of DSP. This approach can extend to other applications such as driving aids and road security. A future need to broadcast large amount of information to vehicles occupants may also arise. In those cases, high-speed LEDs and photodiodes might outperform image sensors. One last aspect is the high-speed computing and board interconnects. This a mature area already with products on the market for a several years, a recent example is the optical Thunderbolt^{TM} interface developed by Intel, Apple and Corning. Optical Thunderbolt uses infra-red laser diodes combined with silica-based fibre supporting up to 40 Gbps (revision 3) up to 60 m reach. This level of performance is current beyond LEDs or micro-LEDs and best suited for large server and high performance computing facilities due to the higher cost. It is not clear if optical Thunderbolt can reduce the cost or if VLC with polymer-based fibre connections would be of higher value for consumers.

1.4 Summary

In this first chapter was presented an historical view of VLC and introduced the current concepts within the optical wireless communications. The fundamentals limitations of RF technologies and the need for VLC were shown. Commercial implementation of VLC such as LiFi and related standards is also presented. The current state of the art of VLC technologies is presented in the context of free–space and guided–wave operation. Opportunities, limitations and open questions are highlighted as they define directions taken in the research, including this thesis.

Chapter 2

Micrometre-sized light-emitting diodes

2.1 Historical developments

2.1.1 Light-emitting diode (LED)

Light emission from a semiconductor was first observed by Henry Round at the Marconi Labs in 1907 [64]. It was not until 1927, however, that the first light-emitting diode was reported by Oleg Vladimirovich Lossev in a Russian journal and 1928 in a British journal [65]. Lossev found that luminescence occurred in some when biased in forward and reverse directions. Lossev was the first to understand the potential of the LED for telecommunications. In the introduction to his patent entitled 'Light Relay' [66] granted in 1929 he writes "*The proposed invention uses the known phenomenon of luminescence of a carborundum detector and consists of the use of such a detector in an optical relay for the purpose of fast telegraphic and telephone communication, transmission of images and other applications when a light luminescence contact point is used as the light source connected directly to a circuit of modulated current.*" In the late 1960s, improvements in the quality of SiC films made possible the fabrication of p-n junctions in that material [67], leading to blue light-emitting diodes which remained commercially available into the 1990s. By the early 1970s, Pankove pioneered the first electroluminescent GaN LED in the blue and violet [68, 69], complemented by the first study of the frequency response of such device [70].

Even after Pankove's work, obtaining p-doping in GaN proved to be very difficult and as result the devices present very low efficiency. It was not until late 1980s and early 1990s that the first true p-type doping and conductivity in GaN was demonstrated by two independent groups of researchers in Japan, Amano and Akasaki at Nagoya University and Nakamura at Nichia Chemical Industries [71, 72]; the first group used low energy electron beam irradiance (LEEBI) and the second group htermal annealing. Further developments lead to efficient UV/blue [73] and high-brightness blue InGaN/AIGaN double-heterostructure LEDs [74, 75].

The idea of using a GaInN/GaN LED for optical excitation was firstly presented by Nakamura in 1995 [76]. The first LED lamp emitting white light based in a phosphor wavelength converter optically excited by a blue GaInN/GaN LED was filed for patent in 1996 by Jürgen Schneider *et al.* [31] and also reported by Bando *et al.* in the same year [77]. The first commercial LED lamp was lunched in the market a year later. Since then, research and development has lead the way to increase luminous efficacy and reduce the price per lumen of LEDs every year. In 2006, the first LEDs with 100 lm/W were produced [78], only outmatched by gas discharge lamps, and as of 2017 luminous efficacies of commercial lighting products are up to 200 lm/W [79]. In research, luminous efficacies up to 303 lm/W have been achieved [32].

For their outstanding work on the development of GaN LEDs and its impact in modern lighting, Isamu Akasaki, Hiroshi Amano and Shuji Nakamura were awarded the 2014 Nobel Prize in Physics [27].

2.1.2 Micrometre-sized light-emitting diodes

The concepts behind micro-size light-emitting diodes, or micro–LEDs, have existed since the late 1970s [37]. Initially known as micro-layer and micro-area devices, since the early stages of development, researchers were aware of of the benefits of reducing the scale of LEDs combined with flip-chip fabrication, referred to as upside-down mounting [80]. LEDs consisting of InGaAsP/InP emitting at $\lambda = 1.3\ \mu m$ with a diameter of $\phi 45\ \mu m$, active area of 1590 μm^2, at the time referred to as a current gate, were reported to sustain 6 kA/cm^2 for

5000 h with a 15% decrease of output power [80].

One possible definition for micro–LEDs is pixellated areas in which the largest features in plane are measured in micrometre (μ) rather than milimetre (mm) or around 100 : μ. Figure 2.1 schematically presents the relative dimensions of micro–LEDs compared to a current commercial LED (Samsung 2016 LM101A [81]) available in chip-scale package CSP. High-power LEDs for SSL are even larger with typical active areas over 1 mm^2.

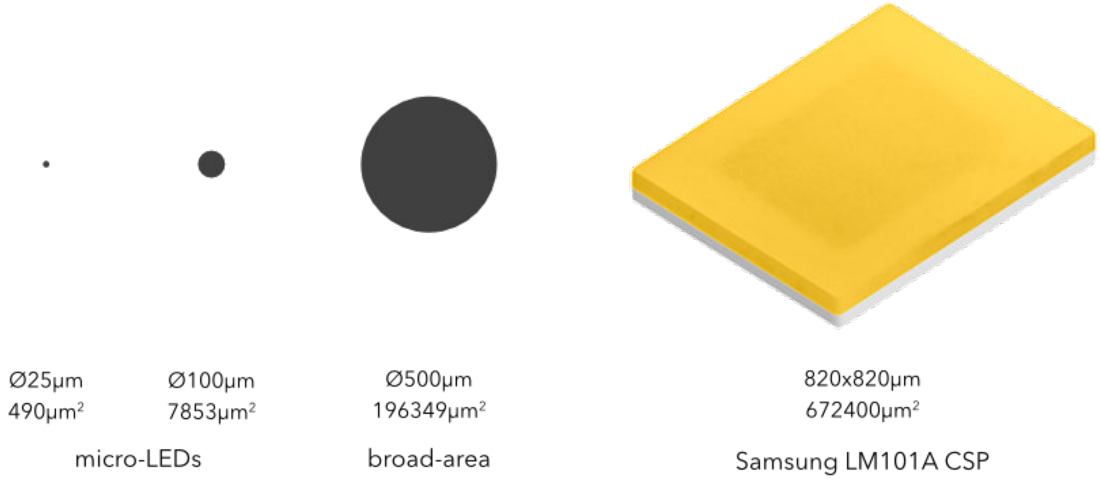

Figure 2.1: Schematic size comparison between typical micro–LEDs and broad-area and current commercial CSP LEDs.

After the success of GaN semiconductor alloys pioneered by Nakamura, Amano and Akasaki in the late 1980s and early 1990s [27], micro–LEDs emerged as one new format of nitride devices. In the early 2000s full micro–LED structures emitting at $\lambda = 450$ nm were developed [39, 40, 41, 42, 43]. The early work focused on demonstrations of fabrication approaches motivated by prospects of future applications based on the size and superior performance of micro–LEDs. At the time, the major benefits identified included: current densities approximately five times higher than broad-area LEDs, indicating an increased quantum efficiency per unit area due to a more efficient use of the injection current [39]; and clustered micro–LEDs showing optical powers two times higher than broad-area LEDs with equivalent area, attributed to increased extraction efficiency [82].

In the next few years, research on GaN micro-LEDs focused on improvements in fabrication techniques [43, 83], size-dependent characteristics [42], light extraction efficiency and optical power density [84], self-heating [85, 86], efficiency droop [87, 88], spectral response [89, 90, 91] and optical modulation bandwidth [45, 46, 92, 93].

As micro–LED technology has matured, applications for optical communications at visible wavelengths have also emerged. The first demonstration of data transmission through POF using LEDs was done by Matsuoka *et al.* in 2000 [28]. In 2004, Komine *et al.* presented the first concept of what is now known as VLC and LiFi, proposing LEDs as sources for both illumination and communication [34].

Along with research reports, patents regarding micro–LED technology and respective applications were awarded [94, 95, 96, 97, 98, 99]. Various spin-off companies specialising in micro–LEDs were formed, including mLED, LuxVue, InfiniLED and X-Celeprint. As of 2017, the largest acquisition in this area was that of LuxVue Technology by Apple Inc in 2014 for $43.78 million dollars (USD) [100], indicating the promise of this technology for virtual reality virtual reality (VR) and augmented reality (AR) applications.

2.2 Fabrication process

This section summarises the fabrication process used by our colleague Dr. Enyuan Xie to produce the GaN micro-LEDs presented in thesis. The recipe described is an improvement over previous fabrication technology for these devices [101, 46], specifically via the introduction of deep etching and a palladium (Pd) p–contact.

The micro-LEDs were fabricated from commercially available epitaxial material. The wafer (Super Nova), grown on c-plane sapphire substrate, is specifically designed for LEDs emitting at 450 nm. Detailed information for this wafer is proprietary but the manufacturer did provide a representative simple structure as illustrated in figure 2.2 (a). In common with other GaN epistructures, the wafer is in p–i–n form, with p-doped (with Magnesium) and n-doped (with Silicon) layers sandwiching an InGaN/GaN multiple quantum well (MQW) light emitting active region. The quantum well characteristics are described in more detail in section 2.3.3. The EBL is an electron blocking layer providing a potential barrier to stop electrons overflowing the active region. A flip–chip LED architecture emits light through the substrate, as is possible with nitrides to where sapphire is used, providing significantly higher power than LEDs with top–emitting (i.e. through the p-contact) architecture. The typical flip–chip LED architecture is illustrated schematically in figure 2.2 (b).

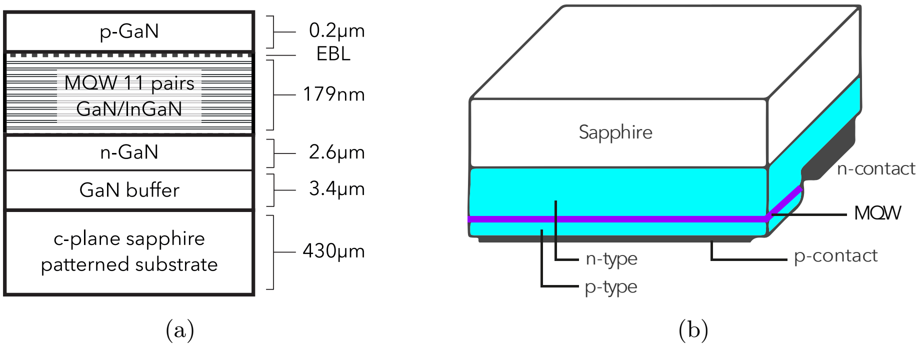

(a) (b)

Figure 2.2: Structure illustrations of (a) Super Nova 450 nm GaN wafer and (b) a typical flip–chip LED.

Fabrication of GaN-on-sapphire LEDs requires three basic steps: defining the p-contact, etching to the n-GaN and defining the n-contact. The middle step is required because sapphire is an electrical insulator. In micro-LEDs the feature size is reduced, requiring additional steps to guarantee optimal performance. Figure 2.3 presents the major steps of the GaN micro-LED fabrication process using standard photolithography.

2.2.1 Process flow

The following paragraphs explain the major steps in the fabrication process as shown in figure 2.3.

p–contact On the bare wafer the top layer is the p–GaN. The first step is to achieve the p–contact. The sample is cleaned and a 100 nm thick layer of *Pd* is deposited using electron–beam evaporation. The *Pd* contact has three functions: it spreads current over the p–GaN, it acts as an electrical contact to the p-GaN material and is the mirror to reflect the light downwards.

patterning The micro–LED design is transferred to the sample through a defined pattern. Pattern definition is a crucial step in the fabrication process, done using industry standard photolithography techniques. A photosensitive material (photoresist), previously

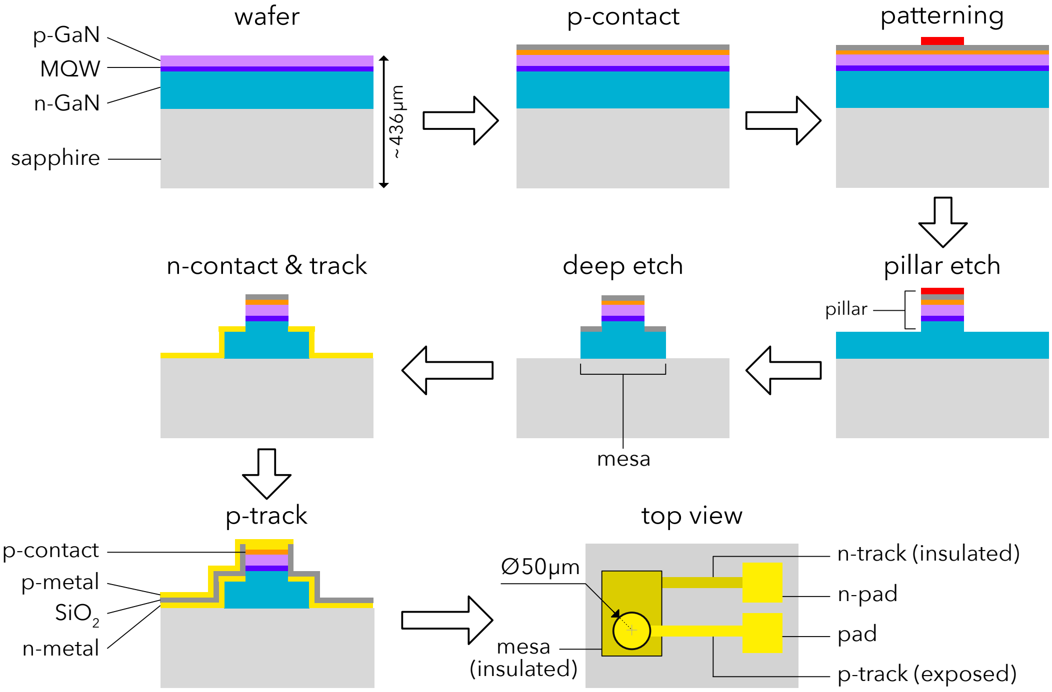

Figure 2.3: Schematic of the major steps in the fabrication process of GaN micro-LEDs. The top-view schematic is an example of the finished device with large pads for probing and wire bonding. Note that the n-metal is insulated with SiO_2. Relative dimensions are not to scale.

spin–coated on the sample, is exposed to light through a photomask that contains the intended design. This is executed in a mask aligner with a UV400 lamp (peaks at 365, 405 and 436 nm respectively), which limits the feature size to ≈2 μm. Once the pattern is defined, the remaining photoresist is removed by a chemical solution.

pillar The transferred pattern defines the pixel pillar by etching the remaining material. This is achieved by dry etch using an inductively coupled plasma (ICP) system. The ICP process is executed in a pressurised chamber ≈7 mTorr using a Choline/Argon plasma achieving an etching rate of ≈430 nm/min. The sample is etched down to the n–GaN layer, followed by an additional 1 μm into the n–GaN. This step exposes the n–GaN to further define the n–contact with crosstalk to the active region.

deep etch The sample is patterned with an area larger than the pillar. Remaining n–GaN area is etched down to the sapphire substrate. This step reduces the overall area of n–GaN feeding electrons to the pixel, effectively reducing the capacitance of the micro–

LEDs. At the end of this step the sample is annealed at 300 °C in a Nitrogen environment to create the Ohmic contact between Pd and the p–GaN.

n–metal After the deep etch the sample is cleaned, left with the p–GaN protected by silicon dioxide (SiO_2) and the n–GaN exposed. A 350 nm thick metallic layer (Ti 50 nm, Au 300 nm) is deposited on the whole sample using a sputter process forming the n–contact. This is followed by lift-off to remove redundant metal and define the n–track and pad.

p–metal In the previous step the n–metal is deposited surrounding the whole pixel to minimise current crowding, details in chapter 4. This forces the use of an additional step for the p–metal. An insulation layer of SiO_2 is deposited on the whole sample. This isolation avoids shorting and allows individual control of the micro–LED pixels which are are too small for direct wire bonding on the p-contact. Subsequently, the SiO_2 layer is patterned to expose the pixel (p–contact). A 350 nm thick layer metallic is deposited followed by lift-off to remove redundant metal and define the p–track and pad.

Once the device is fabricated it sits on a bare die with mechanical support by the sapphire substrate. At this stage the devices are accessible via micro-probes and characterised as such to reduce sources of parasitics as shown in figure 2.4 (a) and (b). In further use for applications in optical communications, the device must be wire-bonded to a printed circuit board (PCB) or a standard integrated circuit package, see figure 2.4 (c) for a case of PCB packaging.

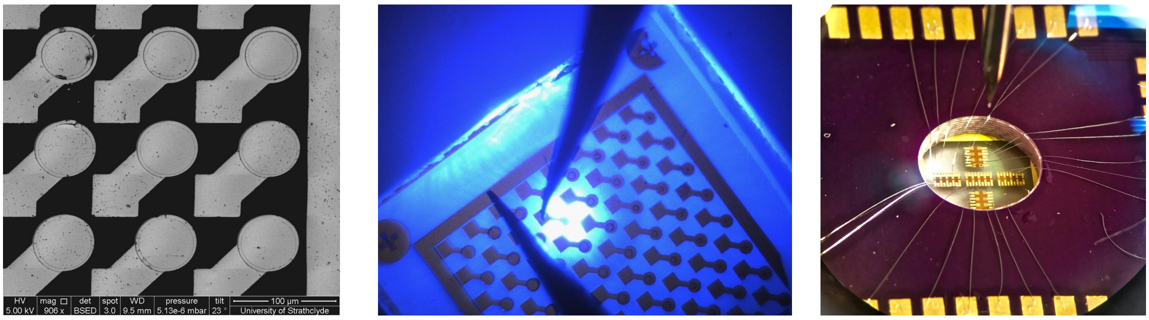

(a) (b) (c)

Figure 2.4: Images of micro-LEDs devices a multiple sizes: (a) a backscattered scanning electron microscope, (b) a micrograph of the same chip in operation and (c) an example of wire bonding the bare chip onto a PCB.

2.3 Operating principles of LEDs

2.3.1 Bandgap

Solid materials are composed of a large ensemble of atoms. Electrons fill the orbitals of each atom, forming discrete energy levels. Each orbital is decomposed into various sub-orbitals according to the ‘Hund’s rules’ of electronic configuration and in a solid these can overlap to form a continuum of energy or a band. This creates a number of bands inside the material in which electronic states are allowed. In conductors, the orbitals are overlap to form a single band where electrons are free to move and the material can conduct electricity. In insulators, the bands are far apart, requiring a large amount of energy (several eV) for an electron to jump between different bands and thus electrons are not free move and the material cannot conduct electricity. In semiconductors, the band separation, or bandgap, lies in between the previous cases, requiring a modest amount of energy for electron jump (1–6 eV), high enough in general to avoid the process occurring spontaneously. In the crystalline solid there are two distinct bands groups as shown in figure 2.5 (a). A low energy group at the bottom is filled with electrons and the highest energy band of this group is called the valence band. The high energy group at the top is empty, the lowest energy band of which is known as the conduction band. The separation between the valance and conduction bands is called the bandgap energy (E_g). In figure 2.5 (a) is also denoted the Fermi level (E_f) at zero temperature

(0 K), defined as $E_f = E_c - E_v = Eg/2$. As shown at zero temperature, the Fermi level does not allow electrons to spontaneously travel to the conduction band, thus the Fermi function is zero. In next section we will see how the Fermi level plays a role for devices.

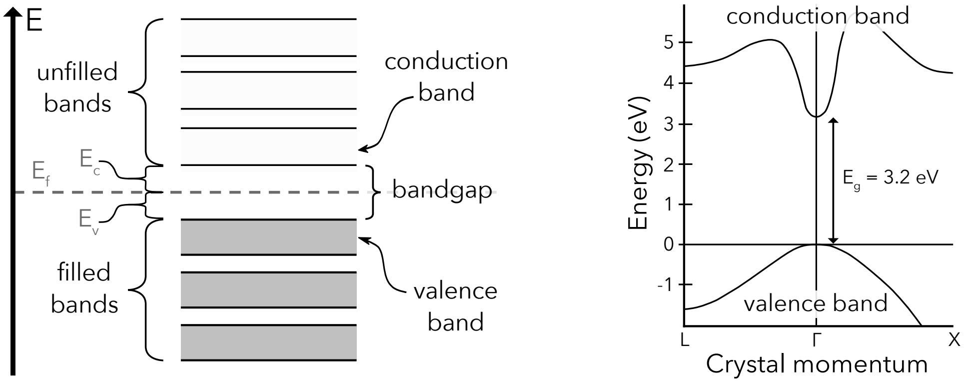

(a) (b)

Figure 2.5: In (a) the theoretical band structure of semiconductors and (b) a simplified band diagram for GaN in k–space.

In bulk semiconductor crystals, the band structure is dependent on the crystal momentum vector or k–space (the Fourier transform of the direct or real space). In figure 2.5 (b) is presented the simplified band diagram for GaN. The maximum of the valence band and the minimum of the conduction band are here aligned in k–space at the Γ point and the semiconductor is then said to be of direct bandgap. When an electron in the valence is excited with energy at least equal to E_g, it jumps to the conduction band leaving a vacancy behind, which behaves as a positively charged hole. The presence of an electron–hole pair leads to an attractive electric field which can lead to the formation of excitons. The carriers recombine and can release the excess energy radiatively as a photon with energy Eg, related to frequency ν or wavelength λ via equation 2.1.

$$Eg = E_{peak} - E_v = E_{photon} = h\nu = \frac{hc}{\lambda} \tag{2.1}$$

where h represents the Planck constant and c is the speed of light.

2.3.2 Gallium Nitride alloy system

Bandgap engineering is possible by creating solid crystalline structures in alloy systems. In the Al/InGaN system, AlN increases the bandgap and InN reduces the bandgap, also resulting in a change of crystal lattice constant a_0. In figure 2.6 we present the bandgap energy as a function of lattice constant for the AlInGaN alloy system. One can easily see from this that InN presents the largest lattice mismatch with GaN, and this lead to crystal defects responsible for non-radiative recombination and consequently low efficiency, especially for green LEDs.

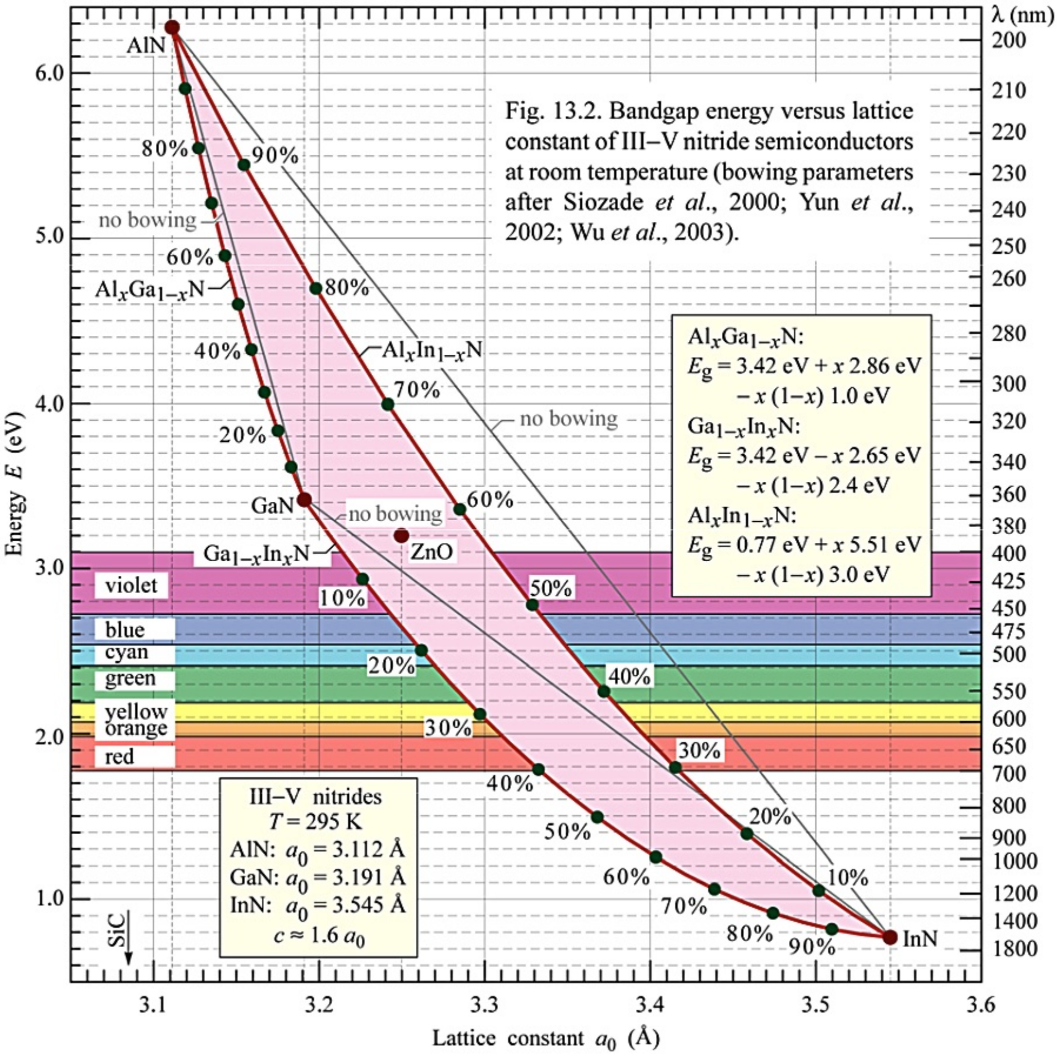

Figure 2.6: Bandgap energy as a function of lattice constant for the AlInGaN system. From [6].

Efficiency is expected to be highly reduced with increase of InN and no high-performance yellow or red GaN-based LEDs have been realised. In the case of the blue LED, containing a moderate amount of InN, In fluctuation leads to carriers being trapped in clusters of high In content [102]. This has beens suggested as the mechanism by which non-radiative recombination at threading dislocation occurs at high density GaN structures, is minimised. As the In content increases the radiative recombination efficiency starts to decrease for longer wavelengths and the as such theres the so called “green-gap”, where neither III–Nitrides or III–Phosphides are of high efficiency.

2.3.3 P–N junction

The simplest structure for an LED is a p–n junction as illustrated in figure 2.7 (a). The p–n junction, also known as a homojunction, is a stack of two layers of material with the same bandgap but different doping levels. Its name is due to the heavy doping used to create excess electrons (n–type) and excess holes (p–type), significantly increasing the the number of charged carriers. At the interface, carriers diffuse from the n–type side to the p–type side and vice versa to maintain charge neutrality. This generates a depletion region with an associated depletion voltage. Applying a forward bias forces the bands to bend and carriers can flow generating recombination. This recombination is dependent on the diffusion length of the charge carriers and requires a wide region leading to low efficiency recombination.

In general, LEDs are not designed with a homojunction but rather with MQWs, illustrated in figure 2.7 (b) for a typical structure of a GaN LED. A MQW device compromises a p–n junction with an intrinsic layer (i–type) in between. This intrinsic layer is composed of a stack of double heterostructures with non-doped material of different bandgaps creating potential barriers where charge carriers are trapped for recombination.

When the double heterostructure width (W_{QW}) is comparable to the de Broglie wavelength for the motion of charge carriers, typically a few nanometre, quantum confinement effects appear. The de Broglie wavelength is given by:

$$\lambda = \frac{h}{p} = \frac{h}{\sqrt{2m^* \cdot kT}} \tag{2.2}$$

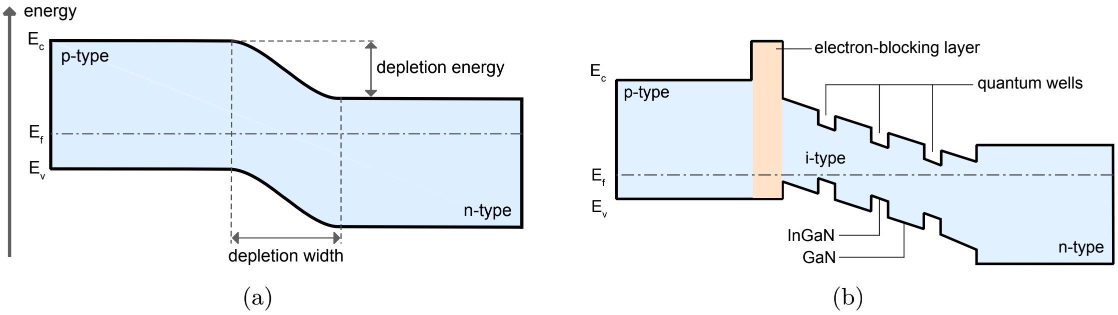

(a) (b)

Figure 2.7: Band diagrams of (a) a p–n junction diode and (b) a typical GaN MQW structure with three quantum wells. Here the horizontal axis represents distance in the growth direction of the crystal. Adapted from [6]

where m^* is the effective mass of the carrier and p the particle momentum. Quantum confinement means charge carriers inside the wells are confined is one crystal direction creating distinct energy levels instead of continuous energy bands, illustrated in figure 2.8. These quantised energy levels can be then associated with a thin one-dimension potential well limited by two carrier-limiting potential barriers. In this case, the permitted energy levels that charge carriers can occupy within the well are given by:

$$E_n = \frac{n^2 h^2}{8m^* W_{DH}^2} \tag{2.3}$$

where n is the integer that can be filled by charge carriers. One can see from equation 2.3 that a thinner well width increases the allowed levels to higher energies – radiative photons with shorter wavelength – and such it is an important parameter for bandgap engineering to tune the spectral emission.

2.3.4 Recombination mechanisms

This section provides a short view on recombination and introduces a semi-classical model initially developed by Roosbroeck and Shockley (1954), known as the *ABC model.* There are two basic types of recombination: radiative and non–radiative.

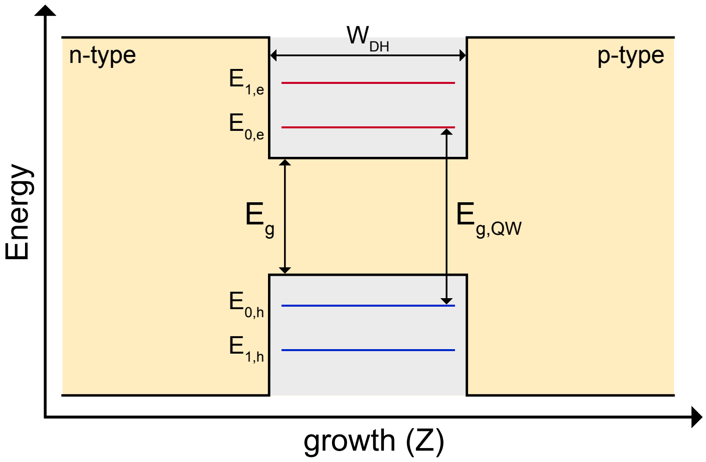

Figure 2.8: Schematic of a quantum well wit gap energy E_g. It is also represented the lowest energy transition $E_{g,QW}$.

Radiative recombination

The probability for an electron–hole pair to recombine radiatively is proportional to the number of free carriers $R \propto np$. The radiative recombination rate (R_r) per unit per unit volume is given by:

$$R_r = -\frac{dn}{dt} = -\frac{dp}{dt} = Bnp \quad (cm^3/s) \tag{2.4}$$

where B is the bimolecular recombination coefficient, n the electron concentration and p the hole concentration. The electron concentration (n) depends on the intrinsic or equilibrium electrons (n_0) and injected electrons Δn such that $n = n_0 + \Delta n$, and for the holes $p = p_0 + \Delta p$. Since electrons and holes are created and annihilated in pairs, the electron and hole concentrations are equal $\Delta n = \Delta p$.

The intensity of luminescence is proportional to the recombination rate and thus carrier concentration. Figure 2.9 illustrates that the carrier decay can be calculated by a short optical excitation and measuring the decay in luminescence. The photo-generated carriers concentration will rapidly decrease once the excitation is terminated. For the case of low excitation the decrease is exponential and in the case of high excitation the decrease is faster than exponential. The characteristic time constant τ of the decay corresponds to the minority carrier lifetime and is summarised for the cases of low and high excitation in equations 2.5a and 2.5b, respectively.

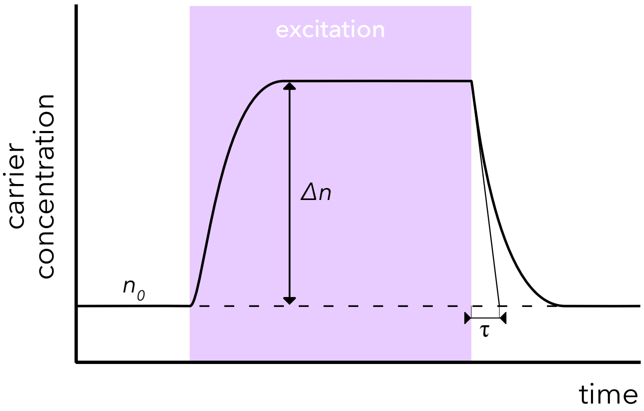

Figure 2.9: Carrier concentration as function of time for a square pulse optical excitation.

$$\tau = \begin{cases} \dfrac{1}{B(n_0 + p_0)} & \text{low excitation } \Delta n << n_0 \quad (2.5a) \\ t + \dfrac{1}{B\Delta n} & \text{high excitation } \Delta n >> n_0 \quad (2.5b) \end{cases}$$

In the case of a quantum well, the confining properties permit higher carrier concentrations per unit volume. The radiative recombination coefficient taking into account the well width L_{QW} is given by:

$$R_r = B\frac{n^{2D}p^{2D}}{L_{QW}} \quad (cm^3/s) \tag{2.6}$$

where n^{2D} and p^{2D} are, respectively, the in-plane carrier concentrations for the electrons and holes. Reducing the well width leads to a short carrier lifetime for the radiative recombination, increasing radiative efficiency, a major advantage of quantum wells over double heterostructures.

Another important factor is the dependency of the radiative coefficient B with increasing temperature. Empirical data shows that when the temperature increases, the carrier concentration increases, but the radiative recombination coefficient decreases. This dependence is weaker at higher injection carrier concentration [88]. This can be summarised by:

$$B \propto \begin{cases} \dfrac{1}{T^4} & \text{low carrier concentration } \Delta n \quad (2.7a) \\ \dfrac{1}{T^{3/2}} & \text{high carrier concentration } \Delta n \quad (2.7b) \end{cases}$$

where T is the temperature. The difference in the temperature dependence is connected with the carrier distribution which is approximately described by Maxwell-Boltzmann statistics at low carrier concentration and by Fermi-Dirac carrier distribution at high carrier concentration [103].

Non-radiative recombination

The transfer of electrical to optical energy is always accompanied by losses, both of electrons and of photons. Losses of electron are due to non-radiative recombination events where the energy of the electron is absorbed by the crystal lattice as vibrations, or phonons, thus generating heat. Defects or traps are the most common source of non-radiative recombination. Traps can form energy levels within the bandgap of the semiconductor, acting as efficient recombination centres, known as *luminescence killers*. This type of non–radiative processes is illustrated in figure 2.10. It was first analysed by Shockley, Read and Hall in the 1950s and is represented by the Shockley-Read-Hall (SRH) recombination coefficient A.

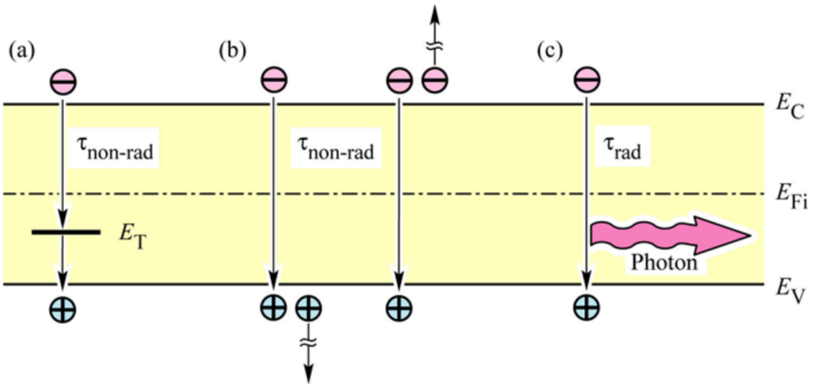

Figure 2.10: Illustration of the band diagram showing recombination: (a) non-radiative via deep level, (b) non-radiative via Auger and (c) radiative. From [6]

.

Surfaces and interfaces create abrupt termination of the crystal leaving a large quantity of electrically active states, and these also contribute to SRH recombination as they contain a large number of recombination centres. The simplest form of the SRH recombination rate is:

$$R_{SRH} = AN \tag{2.8}$$

where N is the carrier density injected into the device. At low carrier density, SRH recombination is dominant and the non-radiative recombination lifetime decreases with increasing temperature [104]. With increasing carrier density, SRH recombination is very small in comparison with other high carrier density loss mechanisms, resulting in a lower temperature dependence.

In case of Auger recombination, the available energy from the electron-hole pair is dissipated by the electron being excited into higher energy levels within the conduction band or by the hole being excited deeper in the valence band. Subsequently, the carriers lose their energy by phonon emission. The simplest form of Auger recombination rate is:

$$R_{Auger} = (C_p + C_n)^3 = CN^3 \tag{2.9}$$

The theoretical probability of this Auger process decreases exponentially with increasing E_g and decreasing operating temperature T, $C \propto exp(-Eg/kB_T)$, where C is the Auger coefficient and k_B is the Boltzmann constant [105]. Experimentally it has been found $C \propto 1/T^2$ at high carrier concentration ($10^{20}\ cm^{-3}$) in micro-LEDs, a quadratic decrease instead of exponential [88].

Hence, the total recombination rate is given by:

$$R = AN + BN^2 + CN^3 \tag{2.10}$$

This means that the recombination rate per unit volume per unit time is dependent on the radiative and non–radiative recombination. As such, the total carrier lifetime is commonly expressed as

$$\tau^{-1} = \tau_r^{-1} + \tau_{nr}^{-1} \tag{2.11}$$

From equation 2.10, this may be represented as:

$$\tau^{-1} = \frac{d}{dN}(AN + BN^2 + CN^3) \tag{2.12}$$

$$= A + 2BN + 3CN^2 \tag{2.13}$$

At low carrier densities SRH is the dominant process for non-radiative recombination. At high carrier density Auger recombination is the dominant non–radiative mechanism leading to efficiency loss. As equation 2.10 predicts, there is a carrier density at which the non-radiative processes overcome the radiative recombination, i.e. there is an inflection point in the output power. More details on these aspects are presented in section 2.5.

2.4 Electrical properties

The micro-LEDs used to take results reported in this section are part of a chip presented in more detail in section 4.4. They are in the form of disc-shaped devices with diameters 20–100 μm used as a baseline reference to compare with advanced shaped pixels.

2.4.1 Current-voltage characteristics (I–V)

The expected theoretical current-voltage (I-V) characteristic os an LED follows the Shockley model, characteristic of p-n junction diodes, and expressed in equation 2.14:

$$I = I_s \left(exp\left(\frac{e\,V}{K_B\,T\,n_{ideal}} \right) - 1 \right) \tag{2.14}$$

Here the I is the current consumed at the applied voltage V, I_s is the saturation current in reverse bias, e is the electron charge, n_{ideal} represents the ideality factor, K_B is the Boltzmann constant and T the temperature in Kelvin; K_BT represents the thermal energy of the junction.

The current-voltage characteristic (I-V) of an LED is a direct result of the semiconductor bandgap energy and the fabrication technology. The ideality factor is an empirical parameter to adjust the theoretical curve to the real device, where $n = 1.0$ for the perfect diode [6]. Nitride LEDs typically present ideality factors between 2 to 8 depending on the alloy and operation regime [106]. The threshold voltage (V_{th}) empirical parameter that defines is the minimum voltage required to turn on the LED to a minimum substantial current or optical power. It can be approximated to the epitaxy material as $V_{th} \approx E_g/e = hc/(\lambda e) = 2.8\ eV$ for a 450 nm emitting wavelength. In real GaN device this value is typically higher due to bandgap discontinuities, non-perfect Ohmic contacts, low p–GaN conductivity and parasitic voltage drops in the GaN buffer.

Figure 2.11 (a) presents the I–V characteristics of 450 nm emitting disc–shaped micro–LEDs of various diameters. The series resistance (R_s) can be extracted from the slope of the linear region of the curves as $dI/dV = 1/R_s$. In this analysis, only the upper 20 % of the I–V curve is used for the fit, following a common practice [6]. This results in significantly lower values of series resistance for these devices in their useful dynamic range. Recording the I–V is a quick measurement ($\sim$ 10 s), however, in direct current (DC) operation over a long period the junction will increase in temperature leading to a decrease in resistance, requiring less driving voltage to achieve a similar current. Due to this effect, LEDs in general work best with current sources rather than voltage sources, a small problem that will be further explored in chapter 5. The R_s fit allows one to determine the V_{th} by looking at the voltage at which the fit curve is at zero current, the region on the I–V curve below this voltage is affected by a parallel resistance (R_p) or shunt resistance. One can see from figure 2.11 (a) that in micro–LEDs R_p is significant, attributed to the mask design and fabrication technology.

Figure 2.11 (b) shows the relationship between the ideality factor (n_{ideal}) and the R_s. These quantities are obtained independently: n_{ideal} is determined by fitting equation 2.14 which derives from a physical model, whereas R_s is determined by an electrical relationship ($V = RI$). Three things are found from this: first, the ideality factor for such devices is very high compared with reported values for broad–area devices (2–8) of the same material family; second, n_{ideal} increases with smaller pixels and decrease in active area; third, the n_{ideal} and

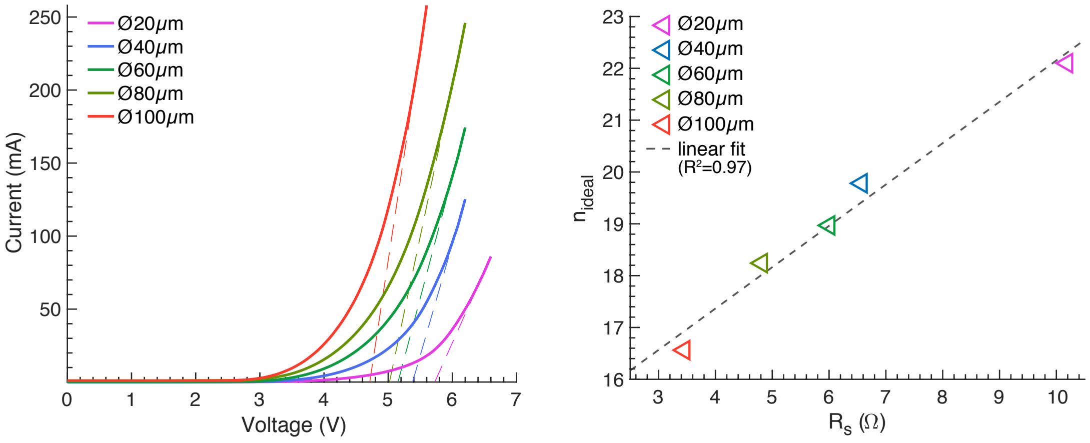

(a) (b)

Figure 2.11: In (a) the I–V characteristics of disc–shaped micro–LEDs of various sizes with the curves fitted to extract the series resistance, in (b) the ideality factor as function of series resistance is shown.

R_s are linearly correlated, indicating that in micro–LEDs the high values of n_{ideal} might be due to the higher overall resistance. The electrical characteristics are summarised in table 2.1 The resistivity (ρ) is calculated by $\rho = R_s Area$ and the wall–plug efficiency at the maximum output optical power. The wall–plug efficiency involves the measurement of optical power, as described in section 2.5. There is a general trend for R_s to decrease with the increase of pixel size, and to understand this trend one needs to consider the following. The total active area is a collection of discrete points and at each point recombination occurs. The power supply sees each point as an electrical resistance, effectively being a resistor. As each point or resistor is adjacent to other, in other words in parallel, the collection of the points as whole presents less resistance than the individual points. Increasing the pixel size or active area means increasing the number of discrete points and therefore decreasing the overall resistance.

Table 2.1: Summary of the electrical characteristics of disc–shaped micro–LEDs of various sizes.

$\varnothing$ (μm)	A (μm^2)	R_s (Ω)	ρ (10^{-4} Ωcm^2)	V_{th} (V)	n_{ideal}	wall–plug (%)
20	314	10.1	0.32	5.72	22.10	1.76
40	1256	6.5	0.82	5.37	19.78	2.68
60	2827	6.0	1.70	5.15	18.97	3.35
80	5026	4.0	2.41	5.01	18.26	3.36
100	7854	3.4	2.71	4.71	16.58	3.79

2.4.2 Capacitance

The equivalent electrical model for an LED is presented in figure 2.12, and is a diode in parallel with R_p, in series with R_s in parallel with a capacitor. Capacitance can be a serious limitation for the modulation bandwidth of LEDs due to the RC limit as we will see below. The capacitance of an LED is given by the depletion capacitance at zero bias and above V_{th} by the diffusion capacitance.

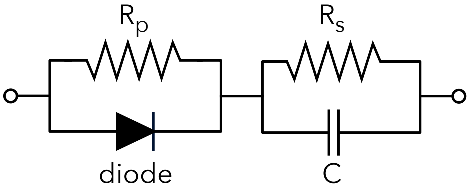

Figure 2.12: Equivalent circuit model of an LED.

Depletion

The depletion or junction capacitance is a space–charge capacitance and can be calculated by:

$$C_{sc} = \frac{\epsilon_0 \epsilon_r}{W} A \tag{2.15}$$

where ϵ_0 and ϵ_r are the vacuum and material permittivities, A is the active or junction area and W the separation width. The space charge capacitance for a micro–LED can be calculated assuming an overall permittivity for a typical junction of $InGaN$ with uniform composition of 30% InN and 70% GaN by

$$\epsilon = \epsilon_0 + \epsilon_r, \quad \epsilon_0 = 8.85 \times 10^{-12}\, Fm^{-1}$$

$$\epsilon_r|_{GaN} = 8.9, \quad \epsilon_r|_{InN} = 15.30$$

$$\epsilon_r|_{InGaN} = 0.3 \times 15.30 + 0.7 \times 8.9 = 10.82$$

thus, using equation 2.15, the space–charge capacitance becomes:

$$
\begin{aligned}
W &= 179nm, \quad \text{from figure 2.2} \\
A &= 7854\mu m^2, \quad \varnothing 100\,\mu m \text{ pixel from figure 2.11 (a)} \\
C_{sc} &= \frac{10.82 \times 8.85 \times 10^{-12}}{179 \times 10^{-9}} 7854 \times 10^{-12} = 4.2 \times 10^{-12} = 4.2\,pF
\end{aligned}
$$

assuming an resistance equal to R_s, the cut–off frequency is

$$f_c = \frac{1}{2\pi RC} = \frac{1}{2\pi \times 3.4 \times 4.2 \times 10^{-12}} = 1.114 \times 10^{10}\,Hz \approx 11\,GHz$$

when the LED is at zero bias or open circuit.

Similarly, a broad area LED fabricated on the same epitaxy with $\varnothing 1mm$, $A = 785398\mu m^2$, and assuming the same R_s yields:

$$
\begin{aligned}
C_{sc} &= \frac{10.82 \times 8.85 \times 10^{-12}}{179 \times 10^{-9}} 785398 \times 10^{-12} = \; 420pF \\
f_c &= \frac{1}{2\pi \times 3.4 \times 420 \times 10^{-12}} \approx 111\,MHz
\end{aligned}
$$

which means a significant reduction in the cut-off frequency due to the space-charge capacitance.

There are two more sources of space–charge capacitance, namely mesa size and track overlaying. The mesa acts as one plate as the n–GaN is good conductor, and thus capacitance can be decreased by decreasing the mesa size. Mask designs typically have part of the p–tracks overlaying the n–tracks insulated by SiO_2, creating an additional space–charge capacitance, see figure 2.3. Although this happens, SiO_2 is a low dielectric material ($\epsilon_r = 3.9$) with a large separation width ($\sim 1\mu m$) creating a capacitance of 3.4 pF for an overlaying area of 0.1 mm^2, $\sim 13\times$ larger than for a $\varnothing 100\mu$m pixel, corresponding to $f_c \approx 13\,\text{GHz}$ ($R = 3.4\,\Omega$). Therefore, this capacitance contribution can be ignored for large area pixels, although it might pose limitations for small area pixels.

Diffusion

The diffusion capacitance is due to the transport of charge carriers. When the junction is sufficiently biased above V_{th}, the electric field density forces the charges carriers to diffuse in the semiconductor.

$$C_{diff} = \frac{dQ}{dV} = \frac{dI(V)}{dV}\,\tau_t = g_d\,\tau_t \tag{2.16}$$

where g_d is the diffusion conductance and τ_t is the transit time of the charge carriers, a measure of how quickly a carrier responds to a change in voltage. Thus, the diffusion capacitance is linked to intrinsic properties of the semiconductor material and there is no viable way to reduce the diffusion capacitance of the device after the epitaxial growth.

2.5 Optical properties

As in section 2.4, the micro-LEDs used to take results reported in this section are part of a chip presented in more detail in section 4.4. The results here complement the characterisation presented in section 2.4.

Efficiency

An ideal LED emits one photon per injected electron. Non–radiative mechanisms in real LEDs mean that some electrons do not generate photons, and thus the internal quantum efficiency (IQE) is defined as:

$$IQE = \eta_{int} = \frac{\text{photons generated}}{\text{electrons injected}} \approx \frac{P_{int}}{I} \tag{2.17}$$

where P_{int} is the optical power generated at the active region.

Ideally, all the generated photons escape from the LED die into free–space. However, phenomena such as reabsorption and total internal reflections reduce the number of photons exiting the die. The extraction efficiency is thus defined as:

$$\eta_{extraction} = \frac{\text{photons at free–space}}{\text{photons generated}} \approx \frac{P}{P_{int}} \tag{2.18}$$

where P is the optical power in free–space.

Combining equations 2.17 and 2.18, the EQE is defined as

$$EQE = \eta_{ext} = \eta_{int}\,\eta_{extraction} = \frac{\text{photons at free–space}}{\text{electrons injected}} \approx \frac{P}{I} \tag{2.19}$$

it provides the ration between useful optical power and injected current. Maximising EQE is, therefore, of the ultimacy importance.

Finally, the power efficiency or wall–plug efficiency, provides the ratio between the useful optical power and the electrical power supplied to the LED, defined as

$$\eta_{extraction} = \frac{P}{VI} \tag{2.20}$$

2.5.1 Luminescence–current characteristics (L–I)

The L–I characteristic is a measure of the output optical power produced for a given injection current. The ideal L–I curve is a linear relationship, where a step increase of 1 mW in the injection current leads to a step increase of 1 mW in optical power, in other words, efficiency of 100% in any driving regime. Figure 2.13 (a) shows the L–I curve for the same micro–LEDs in section 2.4. The optical power has a parabolic increase with the injection current, reaching a maximum above which the optical power decreases. The maximum point is known as the *roll–over* and scales linearly with increase of pixel area, as shown by the dashed line in figure 2.13 (a). In this measurement the pixels were not driven hard enough to see the full roll–over effect as this can easily do irreversible damage. As expected, the optical power increases with pixel size, with the smallest pixel ($\varnothing 20\mu m$) producing ~ 1 mW and the largest ($\varnothing 100\mu m$) over 12 mW, an increase of ×12. The largest pixel has ×25 more area than the smallest one, thus the decrease in pixel size leads to higher optical power densities.

Figure 2.13 (b) show the EQE curves versus current density for the same pixels. The EQE peaks at very low currents and shows exponential decrease afterwards, an effect known as efficiency droop. The EQE values obtained from bare chip are typically low as extraction and collection efficiencies are estimated to be 10% and 66%, respectively. The peak values are higher for larger area pixels, but the droop is similar for all pixels. Smaller individual

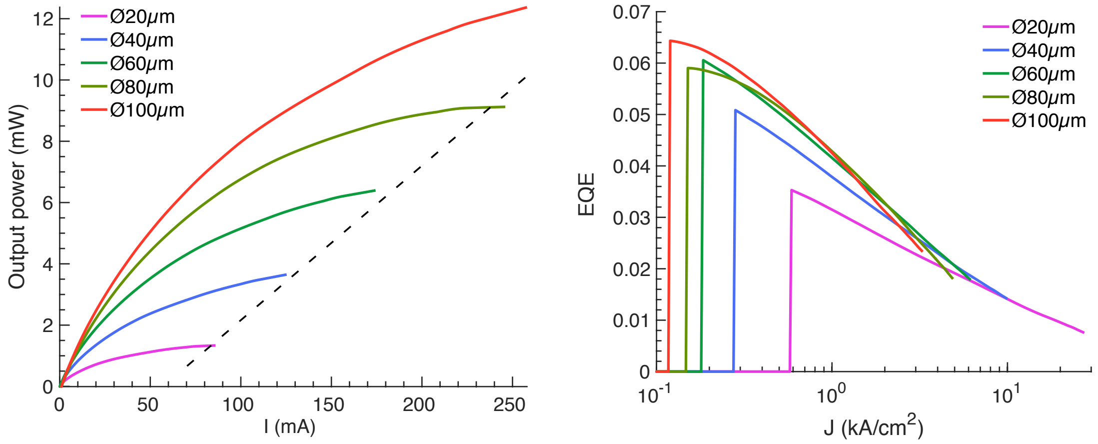

(a) (b)

Figure 2.13: In (a) the L–I curve and (b) the EQE for 450 nm emitting disc–shaped micro–LEDs at various sizes. Note that (a) is plotted vs. current an (b) vs. current density.

pixels are known to have higher R_s than large individual pixels (section 2.4), requiring higher voltage to achieve the same current, and thus more power, which leads to a decrease in the EQE. Higher EQE with micro–LEDs is possible via clusters of a larger number of small pixels, increasing the total active area significantly. Thermal aspects of this approach will be discussed in chapter 4.

The wall–plug efficiency for these devices is included in table 2.1 for the highest optical power achievable, with values calculated at the lowest values of EQE. The droop in EQE is a challenging problem. On the one hand to maintain high efficiencies devices must run at low currents, in the other hand to achieve high power devices they must run at high currents. The direct causes of the droop phenomenon is not fully understood and remain an area of active research.

2.6 Spectral properties

The photon energy emitted by spontaneous recombination in an LED is not simply equal to E_g. Electrons in the conduction band and the holes in valence band have a parabolic dispersion relation in k–space, see figure 2.5 (b) and also have thermal energy. Emission can occur at various wave vectors and hence carriers can recombine at higher energies than E_g.

The allowed energeis are governed by the density of states (DoS) and the probability of an energy state being occupied is given by the Fermi–Dirac function. Figure 2.14 presents the expected theoretical emission characteristics where the Boltzmann approximation is used for simplicity.

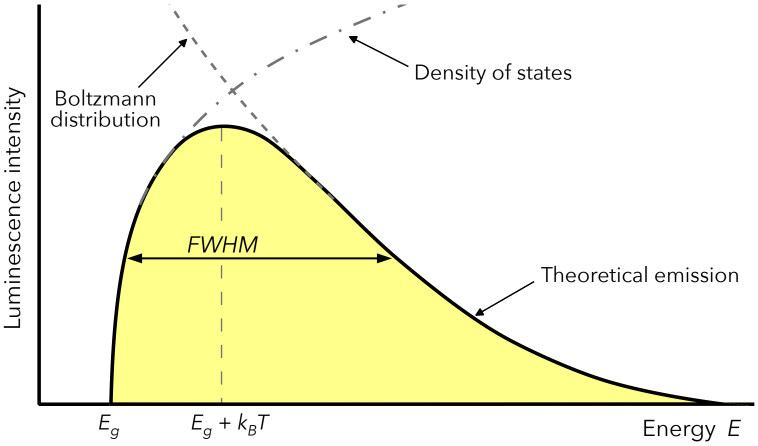

Figure 2.14: Theoretical luminescence emission spectrum of an LED. Adapted from [6].

Here, the maximum concentration of electrons occurs at $\frac{1}{2}k_BT$ above the bottom of the conduction band, and the maximum concentration of holes occurs at $\frac{1}{2}k_BT$ below the top of the valence band. The emission peak (E_{peak}) is then expected be maximum at the energy:

$$E_{peak} = \frac{E_g + k_BT}{q} \quad (eV) \qquad \text{or} \qquad \lambda_{peak} = \frac{hc}{E_g + k_BT} \quad (nm) \tag{2.21}$$

where q is the electron charge. Since there are many possible levels, there is a spread in energy induced by temperature which translates to a spread in emitted wavelengths characterised by the full width at half maximum (FWHM) or spectral linewidth $\Delta\lambda$ as:

$$\Delta E_{peak} = \frac{1.8k_BT}{q} \quad (eV) \qquad \text{or} \qquad \Delta\lambda = \frac{1.8k_BT\lambda_{peak}^2}{hc} \quad (nm) \tag{2.22}$$

where 1.8 is an empirical factor. The expected central wavelength and FWHM for a wafer designed to emit at 450 nm (2.76 eV) at 300 K are 445.8 nm (2.78 eV) and 7.45 nm (46 meV), respectively.

For a real device, we obtained spectra by collecting front-emitted photons with a fibre coupled spectrometer with 800 μm aperture aligned with the positional centre of the emission.

The spectra where then process via a Matlab^{TM} software (see appendix) where the curves were fitted with the equation that maximises the correlation coefficient, although no physical meaning is attached with this fitting process.

Figure 2.15 (a) presents the real emission spectra of a square-shaped $40 \times 40 \mu m^2$ LED with increasing injection current measured by a fibre spectrometer with effective spectral resolution of 1 nm. As the injection current increases three main phenomena occur: first, the emission has an asymmetrical bell–shape or Gaussian curve and the intensity increases with current corresponding to higher optical power; second, the FWHM broadens with injection current; third, the peak emission wavelength (λ_{peak}) moves slightly to lower and then to higher λs with injection current, corresponding to higher and lower energies, respectively.

In figure 2.15 (b) are shown the λ_{peak} and FWHM with increasing current. These are extracted from the spectra in figure 2.15 (a) via fitting with a double Gaussian function, but we note that no physical meaning is considered for these fits. The behaviour of λ_{peak} shows an initial strong blue-shift followed by a slower rising red-shift, this being typical behaviour of micro-LEDs. Piezo-electric fields due to crystal strain, misalignments (in k–space) of the energy bands and band-filling of the quantum wells are all associated with the blue-shift at low injection currents. The slow rising red-shift occurs from 40 mA onwards and is only due to increase in temperature reducing the bandgap. The self heat is generated by non-radiative recombination at the junction leads to bandgap reduction and thus longer λ_{peak}. It appears that the temperature induced red-shift is balanced by the initial blue-shift creating a smooth transition. Equation 2.22 predicts a linear relationship between FWHM and temperature. What is seen in figure 2.15 (b) is a non-linear increase of FWHM with current, which is mediates for temperature. The relation between temperature and current is also non-linear and does not compensate for the non-linearity seen here, as described in detail in the section 2.7.

Comparing the emission spectra between figures 2.14 and 2.15, it is evident that theoretical predictions do not match with the real device. Even at a low injection current ($T \approx 300\ K$), the real spectrum does not present an abrupt cutoff at lower energies (long λ) or the long tail at higher energies (short λ). This relates to the fact that the model does not account for the

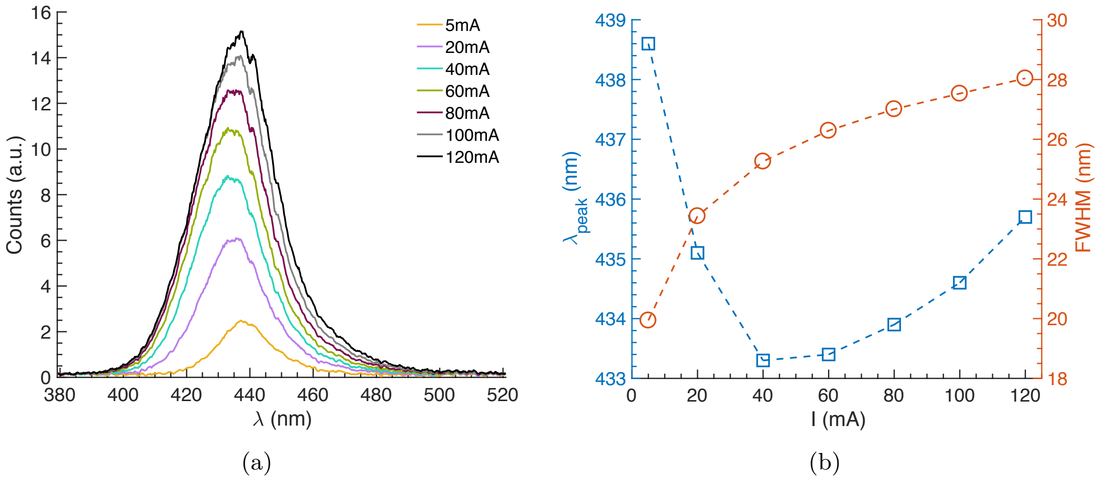

(a) (b)

Figure 2.15: Spectral properties of $40 \times 40 \mu m^2$ LED, (a) the emission spectra and (b) central peak and FWHM.

reabsorption of high energy photons, or for defects and impurities that create energy levels within the forbidden bandgap, emitting at lower energies.

2.7 Thermal properties

Temperature effect provide the ultimate limitation to LEDs, negatively affecting the output optical power, efficiency, device lifetime, reliability and colour rendering capabilities [107, 108]. A reduction in temperature of an LED under fixed driving conditions allows improvements in these aspects mentioned and increased performance. Temperature management is, therefore, crucial to achieve high–power LEDs for illumination applications. There are two main ways to reduce the temperature of an LED: minimise the heat generation sources on the chip and increase heat extraction (heatsink) from the chip. The former is given a great focus in this thesis and introduced in the next paragraphs. The latter is one of the main areas of focus of the LED industry.

The temperature at which LEDs degrade towards failure is experimentally determined to be typically $\sim 150°C$. This is, however, somewhat counterintuitive as during the fabrication process, the wafers are exposed to temperatures up to 300°C when is uniformly distributed and with tightly controlled temperature ramps. The reason why LEDs cannot achieve such high temperature under electroluminescence is due to the temperature difference between the operating pixel and the rest of the die. In the fabricated LED, the thermal coefficient of linear expansion is 6.66×10^{-6} for sapphire and 3.17×10^{-6} for GaN. This aspect combines with the rapid temperature rise of the LED in electroluminescence to generate a steep thermal gradient or shock between the operating pixel and its surroundings (including air), leading to strain, stress and ultimately cracks.

2.7.1 Junction temperature

Heat can be generated in the active region, cladding layers and contacts of an LED. Commonly known as T_j, the heat generated by the active region is predominant over other heat sources. Heat generated at the junction tends to accumulate and leads to an increase in T_j, an effect known as self-heating. This is severe for broad–area LEDs (see figure 2.1) due to the large area of the junction and it follows a similar principle to that described in section 2.4 for R_s, see figure 2.11 (b). The idea is based on the mutual heating of discrete points, leading to significant increase in temperature under DC conditions. This is illustrated in figure 2.16 by temperature curves from a single point source (situation I) to a number of point sources (situation IV). At a fixed heat generation rate (constant current), each point has an associated temperature curve (typically Gaussian) as shown in situation I. When two points are close together these curves overlay summing to larger temperature as shown in situation II and III. The peak overall temperature comes at the point of maximum overlay. The profile width is dependent on the heat dissipation capabilities of the substrate and thus strongly affects the peak temperature as shown in situation II and III. An LED junction can thus be seen as a large collection of point heat sources with temperature overlays, resulting in a significantly higher peak temperature. From the temperature profile one can extract T_j by calculating the mean temperature at the junction boundaries, denoted x_1 and x_2 in figure 2.16.

Micro–LEDs are at least one order of magnitude smaller in active area than broad–area LEDs, significantly reducing the temperature overlay effect and as consequence, decreasing T_j at the same current density (current per unit area).

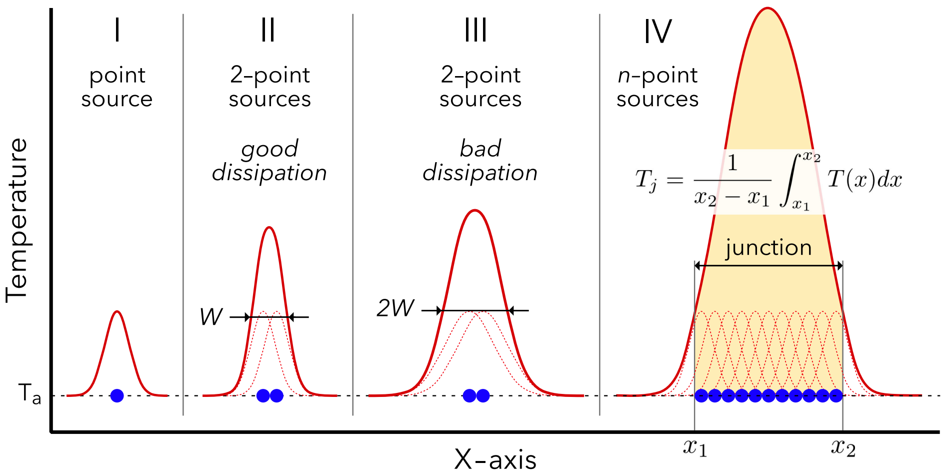

Figure 2.16: Illustration of the self heating effect of a point heat source and temperature overlay for multiple point sources.

2.7.2 Traditional methods to estimate junction temperature

There are three main approaches to estimate T_j of LEDs, namely the peak shift, forward voltage and high–energy slope methods. The principles behind each method are summarised below.

(i) The Peak shift method is based on the bandgap shrinkage with self–heating. It consists of a calibration measurement of emission spectra with increasing temperature at various pulsed currents with low duty cycle (no significant heat generated) creating a relationship between the peak–shift and temperature. A measurement of emission spectra under DC current is compared with the calibration to estimate T_j.

(ii) The Forward voltage method is based on an empirical relation of the I–V characteristic with temperature. It consists of calibration measurement of forward voltage in pulsed current and DC current. The calibration is done by heating the device in an oven and measuring an I–V characteristic with pulsed current at various temperatures. A DC current measurement is compared with the calibration to estimate T_j.

(iii) The High–energy slope method is based on the Boltzmann distribution of carriers which depends on the high–energy (short λ) part of the emission spectrum. The slope is proportional to $-1/(k_bT_j)$ and is determined by a fit of the linear region of the high–

energy side of the spectrum to extract T_j.

These three methods are generally accepted to provide good estimates of T_j for LEDs [6]. However, the choice of method for accurate results is considered case–by–case [107] and comparisons between devices are, therefore, very challenging.

Figure 2.17 presents the estimated T_j from the three methods for a 3×3 cluster of 40×40 μm^2 LED pixels with a total active area of 14400 μm^2, equivalent to a single pixel of ⌀135 μm. The high–energy slope gives an overestimation of T_j as it is a measure of the carrier temperature. The forward voltage is inconsistent as it is very sensitive to wire bond parasitics and Joule heating in the contacts and tracks. The peak–shift shows a slowly rising quadratic trend, which is in line with the expectation from the decrease in EQE.

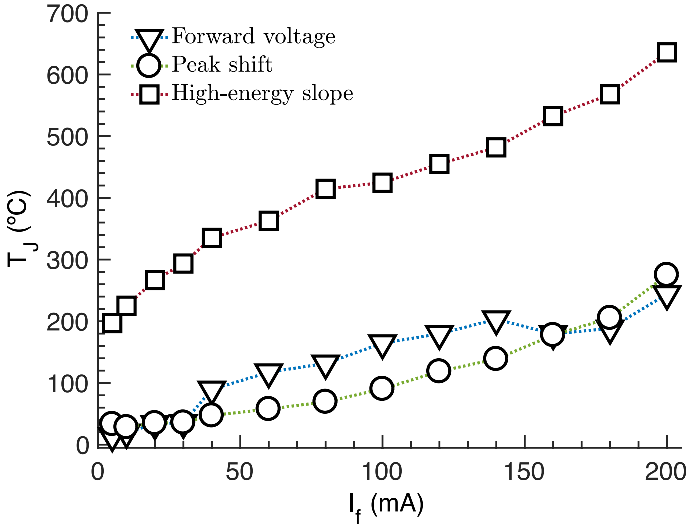

Figure 2.17: Estimation of junction temperature with peak–shift, forward voltage and high–energy slope for a 3×3 cluster of 40×40 μm^2 450 nm emitting pixels, total active area of 14400 μm^2.

The peak–shift method is the most common one used in the literature for LEDs. Gong *et al.* [86] tested the peak–shift method for micro-LEDs. At the maximum injection current for each pixel, as the pixel size decreased from ⌀300 μm to ⌀40 μm the inferred T_j decreased from $\sim 150°C$ to $\sim 65°C$, which was attributed to the strong band–filling effect observed in smaller pixels. In comparison, in broad–area LEDs this blue-shift is very small, easily accounted in the calibration, and thus the emission is strongly dominated by the red-shift at the operating region of interest [6].

In summary, the traditional methods to estimate junction temperature are limited, for the most part, by the calibration. The calibration is a time consuming step that is specific for each pixel and requires precision to deliver accurate and comparable results. These methods are based on indirect assumptions that are not valid for all LEDs, e.g. the alloy-broadening in ternary compounds such a InGaN, meaning the statistical fluctuation of active region composition, can influence the carrier temperature as used in the high–energy slope method [107]; the parasitics in series resistance compromise the forward voltage method; the strong blue–shift affects the principle of the peak–shift method.

2.7.3 Thermal imaging method to estimate junction temperature

This section presents a thermal imaging method to determine T_j that is quick, practical and reliable. An additional benefit of thermal imaging is the ability to *see* the pixel and its surrounding, allowing one to diagnose faults such as hot–spots within the pixel due to such factors as oxide layer breakdown, high–resistance tracks, short circuits, leakage current and metal adhesion. An example of such a measurement is show in figure 2.18 (a), taken using the setup in figure 2.18 (b).

Thermal camera

Thermal radiation is emitted by all materials above absolute zero temperature. Imaging an LED pixel at infra-red (IR) wavelengths is, therefore, a direct link to temperature. A thermal imaging technique was developed using a FLIR SC7600BB infra-red camera. The camera features a Indium Antimonide (InSb) sensor with resolution of 640 × 512 pixels, sensitivity of 20 mK, effective spectral band of $2.5 - 5.0$ μm and is equipped with a close-up lens ($f/2$) allowing a minimum feature size of 7.2 μm to be resolved. The typical measurement setup for a probed micro–LED is shown in figure 2.18. The thermal camera comes with control software (Altair^{TM}) that allows one to correct for emissivity ε (see below), absorption and other parameters not relevant for this study. The temperature correction for a chosen ε depends on the absolute temperature of the object, background IR of the scene and internal calibration curves of the InSb sensor, which also varies with the temperature range selected.

For example, it is very hard to obtain an accurate measurement close to room temperature due to the excessive IR photons emitted by all the materials in the scene. Images are acquired on a proprietary file format and data can be exported as a matrix of temperature values.

Emissivity calibration

Any given material has an associated ε. This is a dimensionless ratio of the quantity of IR photons emitted by the surfaces of the material to the black–body radiator (perfect emitter), and it also depends on wavelength, temperature and surface roughness. A blackbody has an ε of 1.0 at all temperatures, whereas non–metals have typical ε of $0.4 - 0.97$ and metals can go below 0.1.

In micro–LEDs the main heat source is the AlInGaN junction on top of a sapphire substrate. The junction is imaged through the 430 μm thickness of sapphire which absorbs 6% of the emitted IR. As the material and structure are very complex, the effective ε is the result of emission and reflection at various layers. To compensate for this, a 300×300 μm^2 flip–chip LED was bonded on a hotplate with a high thermal conductivity film (kapton) and images were recorded at a series of stable temperatures using the Altair^{TM} software with the LED switched off at all times. During acquisition the software was set to default settings using a 6% absorption and $\varepsilon = 1.0$. Data is processed offline by adjusting ε in steps of 0.01 at the junction area in order to reach the temperature set at the hotplate.

The data is empirically fitted with equation 2.23. This provides the ε values for a given temperature of the LED sample as shown in figure 2.19 (a). To obtain corrected temperature values T', one requires knowledge of how does a change in $\Delta\varepsilon$ affects the raw temperature. As a commercial product from FLIR, the camera and respective Altair^{TM} software do not disclose how this is achieved. As such, the curve was reverse–engineered by using the calibration images at various hotplate temperatures. For each image, starting at $\varepsilon = 1.0$, the corrected temperature T' calculated by the software is registered in steps of $\Delta\varepsilon = 0.1$. The data was empirically fitted with equation 2.24. Figure 2.19 (b) presents one the obtained curves for an initial temperature of $22°C$, where the minimum ε value accepted by the software is 0.1.

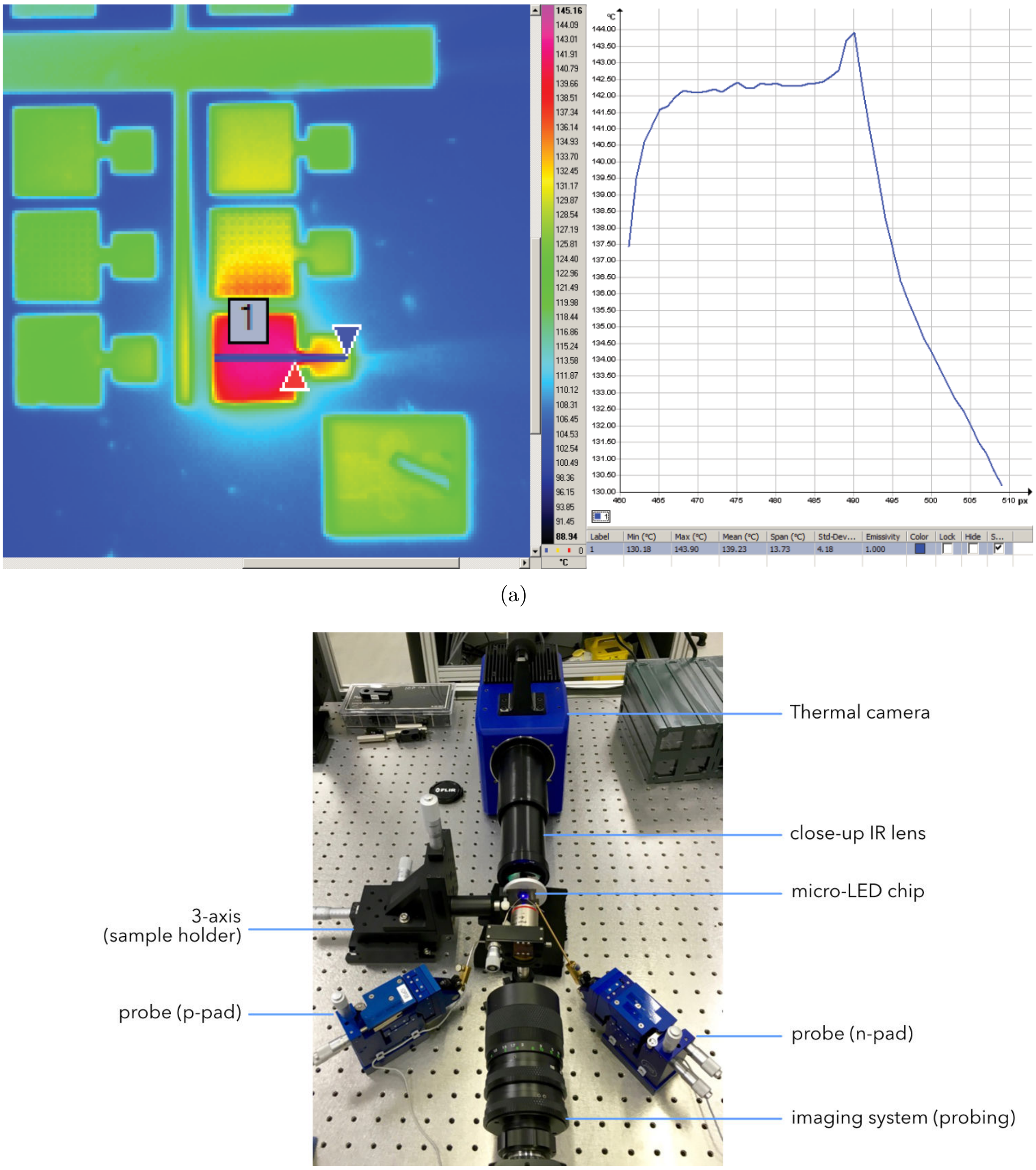

Label	Min (°C)	Max (°C)	Mean (°C)	Span (°C)	Std-Dev...	Emissivity	Color	Lock	Hide	S...
1	130.18	143.90	139.23	13.73	4.18	1.000	■	☐	☐	☑

(a)

(b)

Figure 2.18: In (a) a screenshot of the Altair^{TM} software during measurements of a 300×300 μm^2 LED pixel. The line drawn on the pixel allows one to analyse temperature across the pixel with the arrows showing the hottest and coldest points. The corresponding temperature profile appears on the right in (a) showing with a temperature peak that is due to the IR reflection at the pixel edge. In (b) a photograph of the thermal camera setup during measurements is shown.

$$\varepsilon\,(T) = a_1\, e^{\,b_1\, T_i} + a_2\, e^{\,b_2\, T} \tag{2.23}$$

$$T'\,(\varepsilon, T) = T\;\left(e^{\,\alpha_1\, \varepsilon} + e^{\,\alpha_2\, \varepsilon}\right) \tag{2.24}$$

Table 2.2: Fitting coefficients from figure 2.19 according to equations 2.23 and 2.24.

$\varepsilon(T)$		$T'(\varepsilon)$	
a_1	0.9848	α_1	-9.442
a_2	-6.045	α_2	-0.145
b_1	9.294×10^{-5}		
b_2	-0.071		

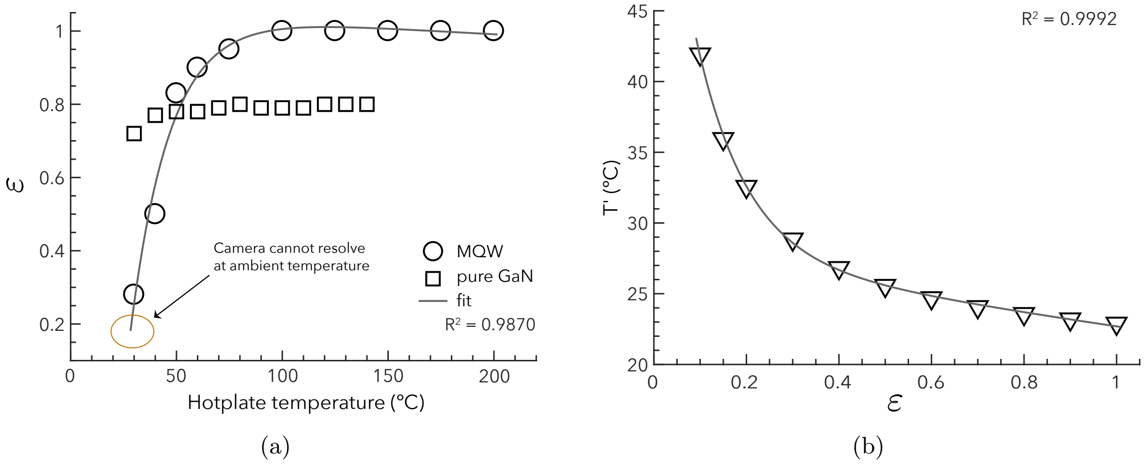

Figure 2.19: In (a) the fit for the emissivity ε as a function of the LED temperature. Data for a pure GaN sample is also included for reference. In (b) the fit for the corrected temperature T' as function of the emissivity ε as determined in (a) for a given T_i.

Correction method

Using an electrically driven micro–LED, at each injection current an image was taken assuming absorption of 6% (transmission of 94%) at $\varepsilon = 1.0$. Images where then exported in a text file as a matrix $T_{[640,512]}$ corresponding to the 640×512 pixels measured, and imported into Matlab^{TM} for batch processing.

Each pixel on every image was individually and independently analysed and corrected.

The algorithm is as follows. A pixel with coordinates $[i, j]$ with raw temperature $T_{i,j}$ was fed in equation 2.23 to obtain the corresponding value $\varepsilon_{i,j}$. Then each value $[T_{i,j}, \varepsilon_{i,j}]$ is fed in equation 2.24 to obtain the corrected temperature values $T'_{i,j}$. As the fitting equations are simple mathematical models, some hard conditions were introduced in the process as follows. The first condition is a lower limit for ε, where any determined value below 0.5 is set to 0.5. This is due to the low signal to noise ratio (SNR) due to high background IR at ambient temperature which gives very low ε values, which is a limitation from the calibration measurement. If not corrected, this results in temperatures up to 10°C higher than ambient temperature at zero current. At raw temperatures above 30°C this problem does not exist. The second condition is for values of ε above 1.0 are set to 1.0, which does not have any physical meaning. As shown in figure 2.19 (a), ε of the characterised sample saturates at about 100°C, which is a common behaviour for most materials.

Errors were calculated from an estimation based on the confidence bounds of the fit parameters and measurement conditions for ε and T' with the values of $\Delta\varepsilon = 0.05$ and $\Delta T = 0.5$, respectively. The superior limit of the error was calculated from equation 2.24 as:

$$\begin{aligned}\Delta T'(\varepsilon, T) &= \frac{\partial T'(\varepsilon, T)}{\partial \varepsilon}\,\Delta\varepsilon + \frac{\partial T'(\varepsilon, T)}{\partial T}\,\Delta T \\ &= \frac{\partial}{\partial \varepsilon}\Big(T\big(e^{\alpha_1\varepsilon} + e^{\alpha_2\varepsilon}\big)\Big)\,\Delta\varepsilon + \frac{\partial}{\partial T}\Big(T\big(e^{\alpha_1\varepsilon} + e^{\alpha_2\varepsilon}\big)\Big)\,\Delta T \\ &= T\,\left(\alpha_1\varepsilon\, e^{\alpha_1\varepsilon} + \alpha_2\varepsilon\, e^{\alpha_2\varepsilon}\right)\Delta\varepsilon + \left(e^{\alpha_1\varepsilon} + e^{\alpha_2\varepsilon}\right)\Delta T\end{aligned} \tag{2.25}$$

A Matlab^{TM} application was developed to apply the method described above in a batch process to obtain a full data set. See the Appendix for details.

Example with a calibration sample

In figure 2.20 (a) is presented the T_j of the LED used for calibration in electroluminescence. Increasing injection current leads to an increase in temperature, as expected, but also in the measurement error as this depends on the absolute value of temperature at each point. During the measurements, the SNR increases with temperature. These values, however, are accessible to the user and as a consequence are not considered in the error calculation.

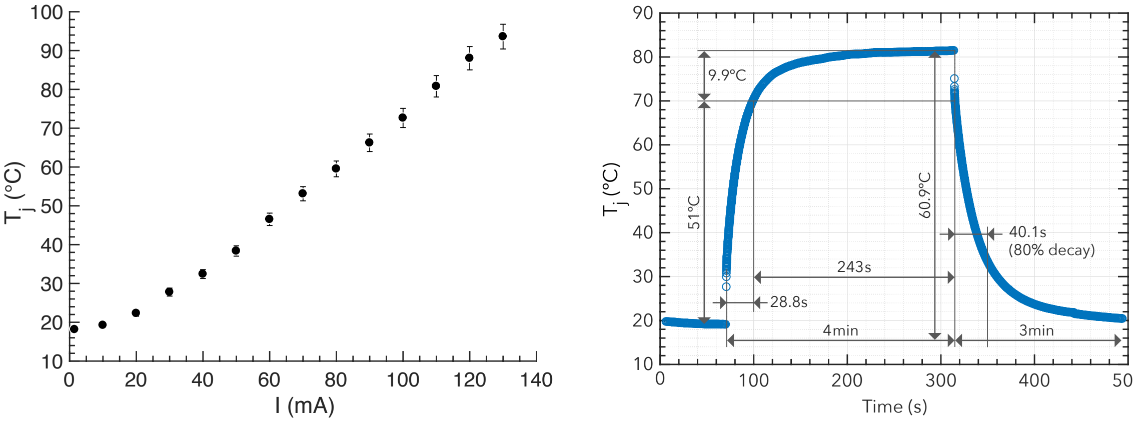

(a) (b)

Figure 2.20: Thermal characteristics for the reference LED ($300 \times 300\,\mu m^2$) used for calibration. In (a) is shown T_j as function of injection current; in (b) presented the time profile of T_j for a long current pulse at $120\,mA$ taken from a video at 25 Hz.

The thermal response to pulsed current is also analysed as shown in figure 2.20 (b). Rise time to 80% of maximum T_j is 30% shorter than the decay time from maximum to 20%. As only the active area is considered for these measurements, this indicates a limitation on the thermal conductivity (K) of the LED structure plus substrate. Given that the rise and decay times are in the order of seconds, it is feasible to apply large current or voltage swings at high frequency without a significant penalty in T_j. Nonetheless important that the time the LED takes to reach a stable temperature is in minutes, another indication of low thermal conductivity. This points towards a heat accumulation that needs to be taken into account for optical communications with such devices over long periods of time (>minutes) at high-power.

Measurements with a thermal camera for micro–LEDs are limited by the temperature range of the calibration, and requires careful control of errors and optical magnification for observing small small features.

Example with CMOS-bonded micro-LED array

A displays based on CMOS-bonded GaN micro-LEDs presents extraordinary brightness with a single pixel can providing an optical power density $> 150W/cm^2$. A range of factors influences the brightness achievable with micro-LED displays, including the quality of the epitaxial material, the layout of LEDs and CMOS, as well as thermal management. The layout of the n-contact in these devices is important to achieve the best device performance. Figure 2.21 presents a schematic view of two layouts for such a device: layout A with the shared n-metal surrounding the whole micro-LED array and layout B with the n-metal surrounding the individual pixels.

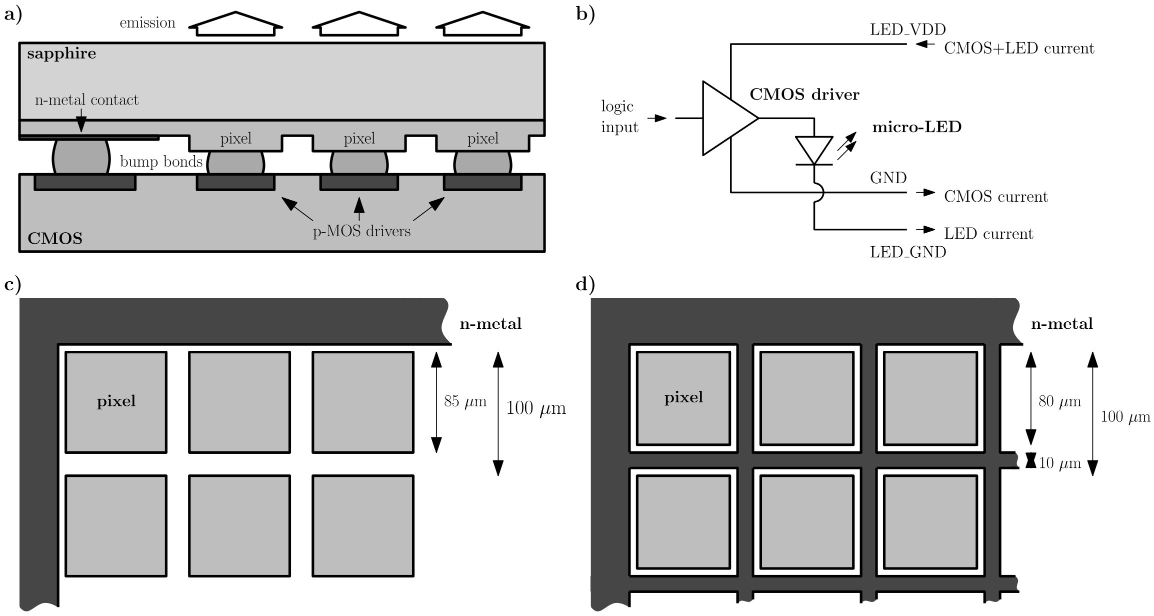

Figure 2.21: Schematic of the devices for experimental investigation. (a) Cross section showing the integration of the LED arrays with the CMOS-chip. (b) Electric circuit. (c) Layout A. (d) Layout B. From [7].

Figure 2.22 presents the thermal analysis via infrared imaging of the two layouts, A and B. One can see that the layout B, which uses surrounding n-metal for each pixel, presents lower pixel temperatures for the same driving conditions, see figure 2.21 (a). Infrared imaging can resolve temperature in the plane, see figure 2.21 (b). This capability further allows to validate the mutual heating effects of micro-LEDs, in this case by studying the profile for two pixel spaced apart, see figure 2.21 (c) and (d) for the layout A and B, respectively.

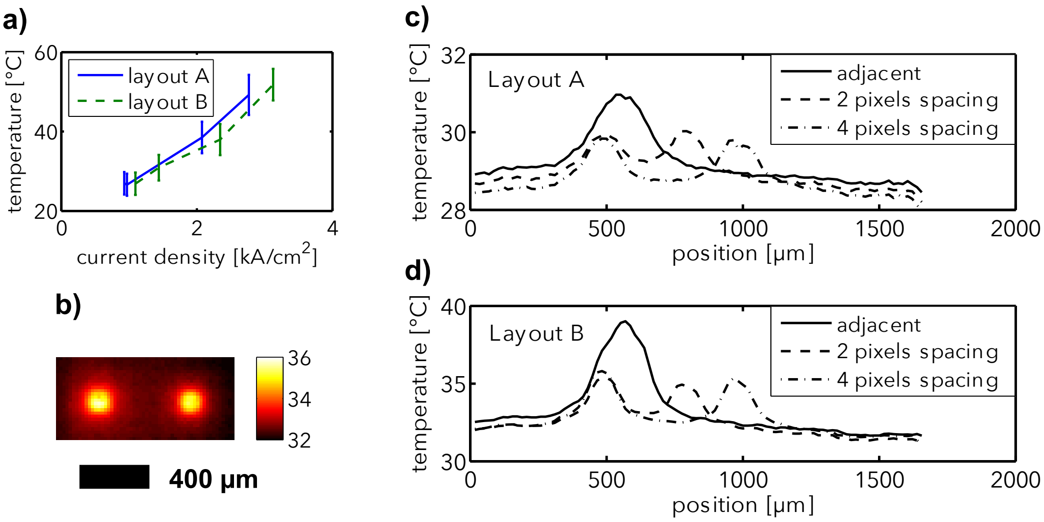

Figure 2.22: Thermal performance analysed by infrared imaging: a) junction temperature for a single pixel. b) image of two pixels switched on simultaneously (layout B, 4 pixels spacing). c) and d) temperature profiles of two pixels with different spacing operated at 4.8 V for c) layout A at 0.78 kA/cm2 and d) layout B at 1.28 kA/cm2. From [7].

2.8 Summary

In this second chapter was presented an historical view of the LED and micro-LED development. An overview of the basic steps for micro-fabrication and the operating principles for LEDs is also included. The characterisation and measurement methods are also included. Basic properties regarding electrical, optical, spectral and thermal characteristics of micro-LEDs are discussed. A new method for the thermal analysis is presented and compared with legacy methods.

Chapter 3

High-speed response of LEDs

This chapter introduces the concept of modulation bandwidth and recombination mechanisms and outlines their overall implications in optical communications. The fundamentals of modulation bandwidth given here are based on work from the 1970s for GaAs-based LEDs. That work also explored recombination mechanisms and the application to optical communication.

3.1 Modulation bandwidth

Modulation bandwidth is a measure of how fast a device responds to an input signal that varies in time. An accurate description for LEDs was given by Lee and Dentai in 1978 [109], as follows: "Intensity modulation of the output light can be accomplished by direct modulation of the injection current provided a rate of variation is slower than the rate of recombination of the injected electrons and holes. Parasitic elements such as the space-charge capacitance causes a delay of the carrier injection into the junction, and consequently a delay in the light output. This delay becomes negligible iff a constant forward bias is maintained so that the modulation bandwidth of the LED is limited only by the carrier recombination time." As defined by Liu and Smith in 1975 [110], the total light intensity output $|I(\omega)|$ from a small-current modulated LED at an angular frequency ω is as follows:

$$|I(\omega)| = \frac{I(0)}{\sqrt{1 + (\omega\, \tau_{eff})^2}} \tag{3.1}$$

where $I(0)$ is the intensity of light at zero modulation frequency and τ_{eff} is the effective carrier lifetime. The equation is valid when the diode is sufficiently forward biased for the parasitic capacitance to become negligible. Under the above conditions, one precise definition for modulation was given by Lee and Dentai [109], as follows: "The modulation bandwidth is defined as the frequency at which the detected electrical power ($\sim I^2(\omega)$) is half of that at zero modulation frequency, that is to say $I^2(\omega) = \frac{1}{2}I^2(0)$." Thus the bandwidth Δf is defined as:

$$\Delta f = \frac{\Delta\omega}{2\pi} = \frac{1}{2\pi\tau_{eff}}. \tag{3.2}$$

Th effective carrier lifetime is also known as the differential carrier lifetime as it corresponds to the derivative of the total recombination rate from equation 2.10.

3.1.1 Electro-Optical bandwidth

The intensity of a modulated optical device is typically measured by a semiconductor photodiode. These devices are designed to operate in reverse bias, thus when exposed to light they generate a photocurrent proportional to the intensity of light detected. This current is then measured as a voltage drop across a resistor ($50\,\Omega$) in a transimpedance amplifier (TIA). The TIA is a current-to-voltage converter plus pre-amplifier to enhance sensitivity, and for this reason photodiodes are also AC coupled and thus not sensitive to time-invariant intensity.

The electrical power dissipated in a resistor is $P = VI = RI^2$ and hence the electrical power for a current signal follows a quadratic dependence with photocurrent. From the description above, the bandwidth point (Δf) is defined as the frequency at which optical power is halved. Following the electrical definition this leads to $P(\omega)' = \frac{1}{2}P_0 = \frac{1}{2}RI^2$, which corresponds to the so called *electrical bandwidth* ($-3\,dB$) or *electrical-to-electrical* (E-E) *bandwidth.* However, this definition does not hold true for optical devices as the power is directly proportional to the photocurrent generated in the junction of the photodiode. At the bandwidth point the photocurrent is $I(\omega) = \frac{1}{2}I(0)$, thus the corresponding power is $P(\omega)' = R(\frac{1}{2}I)^2 = \frac{1}{4}RI$ or $-6\,dB$. This is also known as the *optical bandwidth* ($-6\,dBo$)

or *electrical-to-optical* (E-O) *bandwidth.* The definition for optical bandwidth is commonly known in electronics as the decibel definition for voltage:

$$G/L_{\ dB} = 20\, log_{10} \frac{V}{V_0}\ dB \tag{3.3}$$

where G/L is gain or loss, V is the measured voltage and V_0 is the reference voltage (1 mV). This definition already accounts for the difference seen in the power depending on the square of measured current.

The rest of this thesis refers to bandwidth as the small-signal electrical-to-optical (E-O) bandwidth.

3.1.2 Frequency response

Measurement of the frequency response of an LED is done in similar fashion to that of Namizaki *et al.* [111]. Figure 3.1 presented the setup used, where the LEDs are usually tested on chip with a high-speed probe with a bandwidth of 40 GHz (Cascade Microtech, ACP40-A-GSG-125). A closer view of high speed probe probing the micro–LEDs chip is shown in figure 3.2 (a). Packaged micro–LED chip onto a PCBs also need to be tested to assure no major differences are seen from the bare PCB, an example of this test is shown in figure 3.2 (b). Appropriated optics are used to collect and collimate the light output, and the final focus is onto the photodiode (Femto HSA-X-S-1G4-SI, bandwidth of 1.4 GHz) is done with a microscope objective. The devices are supplied with a signal containing a DC and AC component superimposed via a bias-tee. The DC component serves as a bias and is supplied as a constant current. The small signal AC component is generated by a network analyser. The modulated output light from the LED is collected by the photodiode, which filters the DC component and pre-amplifies the AC component. The received signal is then fed back to the network analyser.

The network analyser compares the output signal with the input signal by sweeping a range of frequencies. The standard output signal has a power of 0 dBm, corresponding to 10s of mV of modulation depth when applied on a load of 3 to 10 Ω, the typical values for R_s of

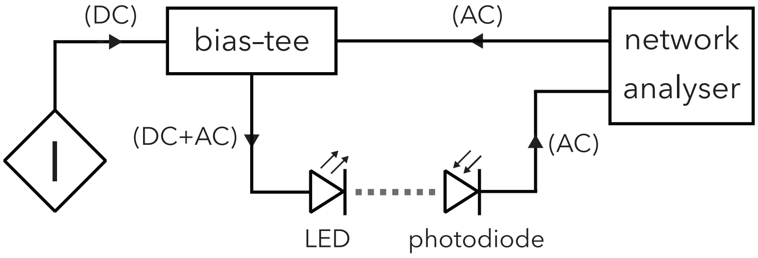

Figure 3.1: Setup to measure the frequency response of LEDs

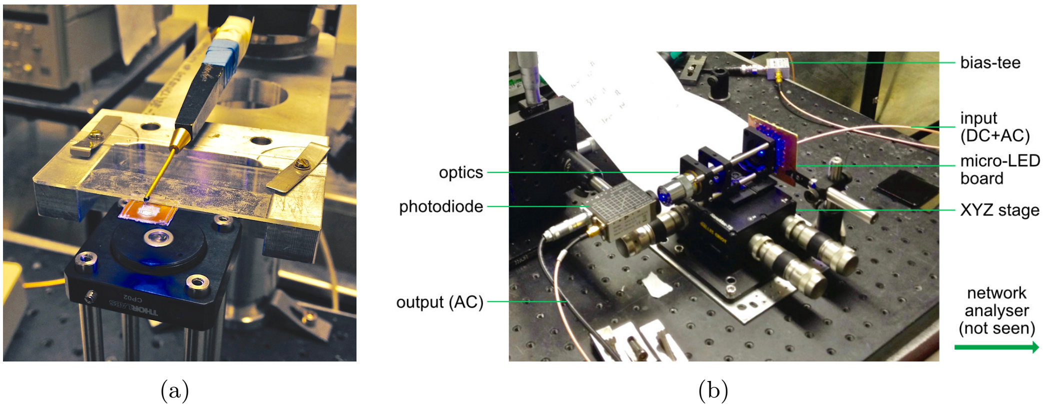

(a) (b)

Figure 3.2: Photographs of the setup for frequency response measurement, in (a) with a micro–LED packaged onto a PCB, and in (b) the close up of the direct probing.

micro–LEDs. Throughout this thesis the input AC power is always 0 dBm unless otherwise indicated. The response is expected to roll off with high frequency as the time constant of the signal becomes shorter than the total recombination lifetime of the LED. The typical frequency range is chosen to be 100 kHz to 1 GHz, allowing the sweep to span up to frequencies above the response of the LEDs where there is no optical output, thus showing the noise floor of the system, namely the receiver noise. In cases where the micro–LEDs have bandwidths over 600 MHz, the sweep is done up to 1.5 GHz to reach the noise floor. Note, however, that near 1.5 GHz the response decays significantly as it is over the bandwidth of the photodiode (1.4 GHz).

Figure 3.3 (a) presents typical frequency response curves of disk shaped LEDs with respective diameters of 40 μm, 150 μm and 500 μm at maximum current, where the bandwidth point is taken at the frequency where the response is reduced by $-6\,dB$ from the response at low frequency.

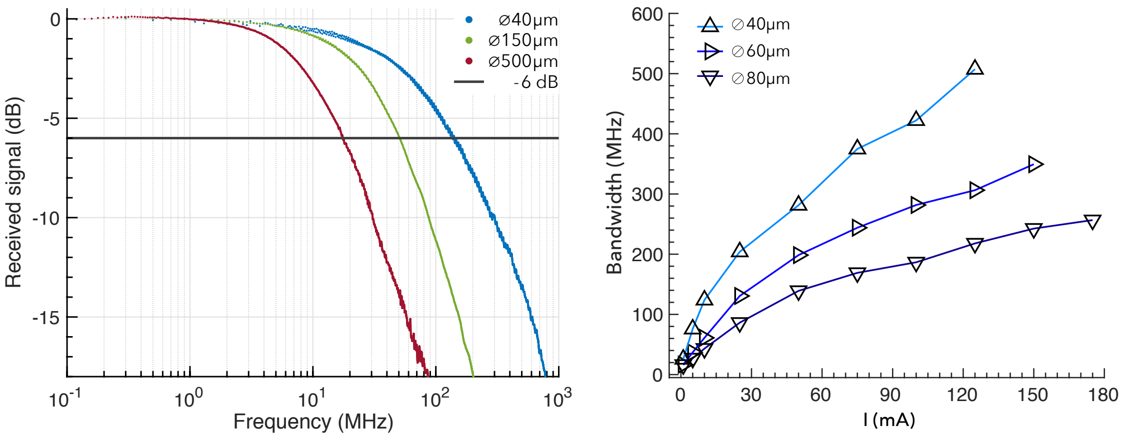

(a) (b)

Figure 3.3: In (a) the frequency response of typical disk shaped 450 nm LEDs of various diameters. The point at which the line marking the -6 dB intersects the data points defines the bandwidth of the device at a certain bias current previously chosen. In (b) the bandwidth values taken from the frequency response are plotted against current, for devices of diameter between 40 and 80μm.

The frequency response seen above is flat at low frequencies, followed by a soft decay as the frequency increases, which is opposite of the sharp cut-off seen in electrical devices. This characteristics allow the device to be driven two to three times above the bandwidth frequency, only limited by the SNR of the system. This means that a pixel with 200 MHz bandwidth in a system can be driven to 600 MHz, and we will see this in practice in chapter 5.

As the pixel size decreases, the current per unit area (current density) increases and as a result the bandwidth increases as result of the reduced differential carrier lifetime [46]. Figure 3.3 (b) presents the bandwidth with the injection current, in this case plotted for micro–LEDs over a small range of diameters (40–80μm) for easy comparison. Each pixel shows increasing bandwidth with the increase of current. The main difference is the slope, which is higher for smaller pixels. This slope is corrected by normalising the injection current to the respective active area (current density), as discussed in detail in chapter 4. The general rule of thumb is: smaller pixels present higher bandwidths but at the expense of optical power, as shown in figures 3.3 (b) and 2.13. This phenomenon observed for GaN micro–LEDs — the current density dependent bandwidth — was initially studied in our group by McKendry *et al.* using pixels that with diameters 14–84 μm at wavelengths of 370 nm, 405 nm, 450 nm and 530 nm [46]. The maximum bandwidth observed was ≈450 MHz for a pixel with diameter of

44 μm with ≈3 mW of output optical power. In terms of data rate, these devices achieved up to 512 Mbps with on–off keying (OOK) modulation, limited by the controlling electronics. Details about data rates and modulation techniques presented in section 3.3.

3.2 Implications for communications

In a telecommunications system the two most important factors for a good link are SNR and available bandwidth. The SNR is either limited by power or by noise. The available bandwidth can be limited by any component in the system. The requirement is to have the lowest noise floor possible at the maximum possible bandwidth. Typically, the bandwidth is limited by emitters or receivers; SNR is a balanced between the optical power received for a given bandwidth and the noise generated by the use electronic equipment. There are, however, other characteristics of emitters and receivers that determine the practical limits of a communication system. The optical communication links used in this thesis are the of type intensity-modulation direct-detection (IMDD), meaning that the output optical power is varied according to a modulated signal and that the photocurrent generated by the photo–receiver varies according to the intensity modulated light.

3.2.1 Luminescence–voltage characteristics (L–V)

The standard modulation adopted in telecommunications is a voltage signal. As such, in order to determine the useful dynamic range of an LED, the electroluminescence (power)–voltage (L–V) characteristic is used instead of the I–V and L–I curves. The linearity of the L–V curve of an LED is analogous to the transfer curve of an amplifier and, if not perfectly linear, it creates distortions to an input waveform. Figure 3.4 presents the measured L–V curves for the micro–LEDs introduced in figure 3.3 (b), and a schematic of the distortions created by these is also shown. The larger device has a symmetrical *S*–shape due to optical power roll-over at the top, and this leads to soft clipping of the signal and reduced dynamic range. The smaller device shows a bowing across the range, in other words an asymmetrical response that leads to compression at the top and stretching at the bottom. In the frequency domain these distortions generate even and odd harmonics which increase the noise level at higher frequencies.

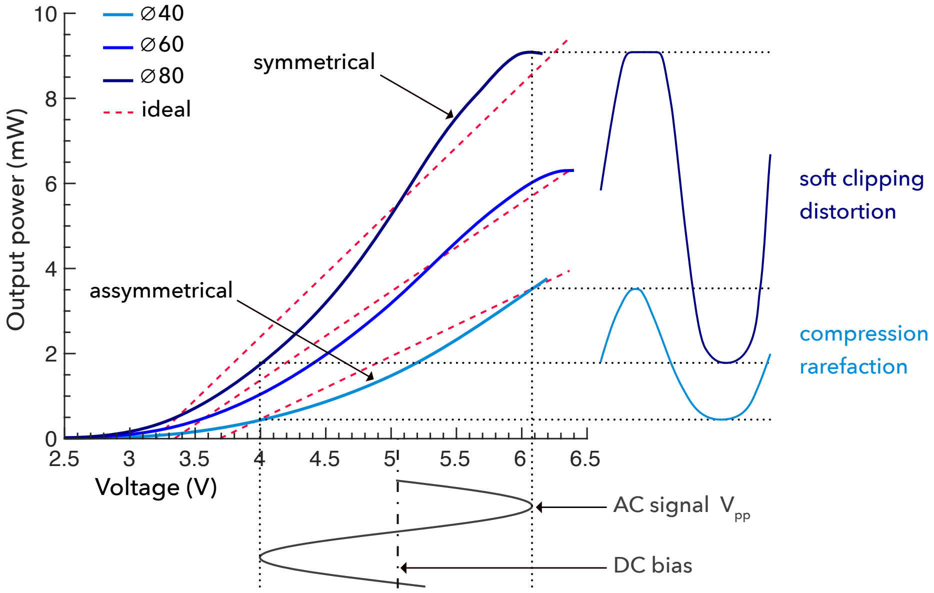

Figure 3.4: Luminescence–voltage (L–V) characteristics of disc–shaped micro–LEDs of different diameters with a schematic of the effects of non-linearities for an input sinusoidal signal.

As shown, the linearity of the L–V curve is an important metric for distortion of the waveform. This is, though, highly dependent on the modulation scheme, as some schemes rely on the actual shape of the waveform as a means of encoding data and others do not. These effects are common for optoelectronic devices and one way to compensate for it is to pre-distort the waveform such that the the optical output of the device is linear. Techniques for pre–distortion can be adopted to mitigate the L–V non-linearity by pre–allocating discrete levels of energy as function of the driving voltage to guarantee a linear output [112]. More details on the practical aspects of the L–V curve are presented in chapter 4 and 5.

3.2.2 Photo–receivers

In a VLC system, photon detection is as important as photon emission. Photoreceivers are responsible to convert light into an electrical current, e.g. optical signal to an electrical signal. These devices provide a direct detection for intensity modulated micro–LED. The principle photon detection technologies used in VLC are photodiode (PD), avalanche photodiode (APD), single photon avalanche photodiode (SPAD) and Silicon photon multiplier (SiPM), figure 3.5 shows example of these devices. The following paragraphs summarise the operation mechanisms of the photo detection technologies mentioned above.

A photodiode is composed of a PIN junction where a reverse bias — below the breakdown voltage — is applied to increase the depletion layer width, decreasing the junction capacitance and increasing the response time. When a photon of high enough energy reaches the diode it creates an electron–hole pair generating a photo current via the photoelectric effect corresponding to the unit gain (G=1). Typical values for blue-enhanced photodiodes are: photosensitivity of 025 A/W with a reverse voltage of 30 V.

An APD device is similar to a photodiode. The mechanism by which a photocurrent is generated inside an APD is the same as in a photodiode, but the APD is different from a photodiode in that it has a function to multiply the generated carriers. An APD is composed by a PN junction with an additional avalanche layer operating in reverse voltage below the breakdown voltage. When electron-hole pairs are generated in the depletion layer of an APD with a reverse voltage applied to the PN junction, the high electric field increases the kinetic energy of the carriers to collide with the crystal lattice generating new electron-hole pairs via ionisation. These electron-hole pairs then create additional electron-hole pairs in a chain reaction of ionisation. This allows the device to multiply the photocurrent generated at the junction by a large factor known as gain, which is proportional to electric field applied. Increasing the gain decreases the capacitance and increases the dark current e.g. noise. These devices are highly non-linear and require precise driving circuitry to compensate the gain factor for changes in temperature and light exposure. Typical values for blue-enhanced APDs are: responsivity for a gain of 100 of 28 A/W, reverse voltage of 170 V.

SPAD and SiPM are devices of the same class, meaning that both operate operate with the same fundamental mechanism, the Geiger mode. This is that the reverse voltage applied to the diode is above the breakdown voltage. When a sufficiently high electric field ($> 5 \times 10^5$ V/cm) is generated within the depletion region of the silicon, the ionisation process occurs. A single absorbed photon can trigger a self-perpetuating ionisation cascade. The silicon will break down and become conductive, effectively amplifying the original electron-hole pair into a macroscopic current flow. This process is called Geiger discharge, in analogy to the ionisation discharge observed in a Geiger–Müller tube. The application of a reverse bias beyond its nominal breakdown voltage creates the necessary high-field gradients across the junction. Once a current is flowing it should then be stopped or 'quenched'. Passive quenching (i.e. no active circuitry), is achieved through the use of a series resistors which limits the current drawn by the diode during breakdown. This lowers the reverse voltage seen by the diode to a value below its breakdown voltage, thus halting the avalanche process. The diode then recharges back to the bias voltage, and is available to detect subsequent photons. In terms of response, avalanche process produces peaks with rise times in the order of picosecond. The quenching and recovering process are referred as the 'dead' or recovery time and is typically 50–500 ns for commercial devices, depending on the cell size and quenching technology used. A modern SPAD device is composed of an array of SPAD cells with active quenching circuitry. SiPM technology represents an unprecedented attempt to create an ideal solid-state photon detector solving a double trade-off of avalanche processes: the higher multiplication gain inevitably results in higher multiplication noise, as well as, in longer multiplication time (the lower bandwidth). SiPM is similar to a SPAD array with passive quenching, but with a faster pixel recovery and higher fill factor. Typical values for blue-enhanced SiPMs are: responsivity for a gain of 5^6 of 1.1×10^6 A/W, reverse voltage <30 V, bandwidth ≈ 10 MHz.

Commercial photoreceivers are a relatively mature technology and so, in this thesis, commercial PDs and APDs are used for as receivers in the VLC systems. The decision factor for this choice is mainly the bandwidth capability. The main properties of interest are qualitatively summarised in table 3.1.

Table 3.1: Qualitative characteristics of photodiodes (PD), avalanche photodiodes (APD), single photon avalanche photodiodes (SPAD) and Silicon photomultipliers (SiPM) for visible wavelengths.

	PD	APD	SPAD	SiPM
bandwidth	high	high	low	low
sensitivity	low	high	very high	very high
noise factor	low	high	very high	very high
saturation	hard	mid	very easy	very easy
dynamic range	very high	high	mid	mid

The general parameters of photoreceivers are: bandwidth, capacitance, sensitivity, satur-

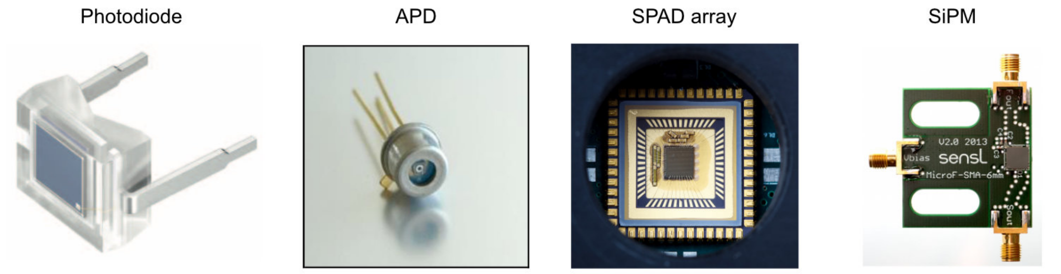

OSRAM BPW 34 B Laser Components AD800-11 Micro Photon Devices SPC^2 SensL MicroFC-SMA-60035

Figure 3.5: Example of commercial devices for the receiver technologies (from left to right): photodiode (PD), avalanche photodiode (APD), an array of single photon avalanche photodiode (SPAD) and silicon photomultipliers (SiPM).

ation, dark current, shot noise, reverse voltage and pre–amplification required for operation. A high sensitivity photodiode requires a large sensor area and thus it presents restricted bandwidth, and vice–versa. Typically, a fast response APD presents a gain dependent dark current — a source of noise that negatively affects SNR — and can easily saturate for optical powers above 100 μW. In practice, a good rule of thumb is: PDs perform better for optical powers above 100 μW, APDs perform better below 100 μW; SPAD arrays and SiPMs perform better below 20 μW. The ideal device for that gap is dependent on factors as rejection of the DC component, dark noise, and the trade-off between SNR and bandwidth for particular application. The application defines the the bandwidth, the collection aperture for a target received optical power and the maximum acceptable noise to achieve the minimum SNR target. In addition, certain VLC applications require the sensor to be exposed to ambient light which may significantly decrease the dynamic range available for the signal due to increase in the noise factors and saturate the receiver. These issue may, up to certain degree, be solved using bandpass filtering to restrict the collected photon to wavelengths of interest.

3.2.3 Shannon–Hartley theorem

In information theory, the Shannon–Hartley theorem, formulated by Claude Shannon and Ralph Hartley, provides the maximum rate at which information can be transmitted over a communications channel with a limited bandwidth and in the presence of noise [113]. The equation expression for theorem is based on two important concepts: first, in principle, a trade–off between SNR and bandwidth is possible; second, the data capacity depends on both SNR and bandwidth.

The Shannon–Hartley theorem is defined as:

$$C = B\, log_2 \left(1 + \frac{S}{N}\right) \qquad \text{(bit/second)} \tag{3.4}$$

where C is the channel capacity, B is the channel bandwidth in Hz, S/N is ratio between the average received signal power and the received noise over the bandwidth B.

For $S/N >> 1$, equation 3.4 can be linearly approximated by:

$$C \approx 0.332 \cdot B \cdot SNR \qquad \text{(bit/second)} \tag{3.5}$$

where $SNR = 10\, log_{10}(S/N)$ (dB). Assuming that the noise N is generally constant for a given system, the Shannon–Hartley theorem for data capacity can be approximated by a direct product between optical power and bandwidth [109]. It is important to note the theorem above is based on the Nyquist rate: on a communication channel the maximum number of pulses per second that can be sent is twice the bandwidth ($f_p = 2B$). This means that a bandwidth of 500 MHz allows a maximum pulse rate of 1 GHz. For a one bit system such as on-off keying, this means roughly 2 bit per Hz of bandwidth. Therefore, the Shannon limit is modulation scheme dependent [114].

For the purpose of device characterisation, the equation 3.5 is used directly and serves as a baseline for comparison. Let us consider the $\varnothing 40\mu m$ pixel in figure 3.3 with a maximum bandwidth of 500 MHz and assume an average SNR for that bandwidth of 12.5 dB, with a typical maximum of 25 dB (measured). Applying equation 3.5 one obtains a theoretical channel capacity of $C = 0.332 \times 500 \times 10^6 \times 12.5 = 2.075 \times 10^9$ (bit/s) = 2.075 (Gbps) for a pulse encoded data stream, also known as pulse width modulation (PWM). As this type of modulation only assigns one bit per pulse in a unipolar waveform, it is analogous with OOK using a bipolar waveform. Experimental results for real time OOK on a device with $\sim$ 800 MHz of bandwidth and an estimated 7 dB of SNR (limited by the 1.5 V modulation depth of the system) obtained an error-free data rate of 1.7 Gbps [115], given a theoretical channel capacity of ~ 1.8 Gbps. As the experimental results are in line with predictions by the Shannon–Hartley theorem, this metric can be adopted for a direct comparison of the communication capability of micro–LEDs. A slight modification must be introduced to the SNR. As the noise level of the system is unknown and system dependent (i.e. depends on quality of components), for the purpose of developing micro–LEDs, the absolute optical power is considered instead to provide an accurate relative comparison between well known devices and new designs.

3.3 Modulation schemes

Here, is presented a short introduction to the general principles behind modulation schemes and data transmission for guided-wave and free-space applications.

Digital data is, at its most basic level, a series ones and zeros, known as bits. Bits represent the information contained in electronic devices such as documents, photographs, music and video. Sending information from one place to another requires a transmission channel or link and a data encoding technique, known as a modulation scheme. Copper wire and optical fibre are examples of wired communication links, whereas RF and VLC are examples of wireless links. The medium that transports the information is known as the channel. Each channel has its own set of characteristics that affect the transmission of the information, e.g. RF can travel through walls but is highly attenuated by water; visible light cannot travel through walls but can fairly easily go through water. The channel influences how information is transmitted and received. As such, many modulation schemes have been developed throughout the years to tackle the the different channel characteristics. In this thesis the channels of focus are POF and free-space, corresponding to a media of PMMA and air. These are two independent classes of application that work better with modulation schemes of different types, as explained in the next sections.

All modulations schemes are ways of encoding the digital data in a waveform that drives a time varying voltage applied to the emitter device (here, the micro–LED) to send the waveform through light intensity variations through the medium onto the receiver device.

The recovered waveform is demodulated or decoded into digital data and compared with the data sent. For each received bit that does not match the sent data an error is generated, and this is known as the bit error ration (BER). The BER is the ratio between bit errors and the total number of transferred bits during the time interval. The IEEE sets firm rules for the acceptable BER in a communication link. A BER of $3.8 \times 10^{-}3\ s^{-1}$ is the ceiling for forward error correction (FEC). This is a technique that uses a 7 % data rate overhead to include redundant information that allows, at the receiver end, error–correcting code (ECC) or channel coding algorithms to partially or totally recover the lost bits. The limits set for FEC for a good quality communication link effectively determine the maximum data rate achievable by the link.

DC–biased modulation

LEDs require a threshold voltage to start normal operation in the milli–Ampere regime and emit photons of average power above the μWatt. Their bandwidth is also dependent on the injection current or, more precisely, the current density. Modulation schemes exist to cope with these needs by using bipolar signals. That is, a signal that, in the time domain, exists above and below a threshold. DC–biased modulation corresponds to a situation where the transmitter is biased with an optimal voltage and a bipolar signal is applied to use, as much as possible, the dynamic range of the LED. In most situations this corresponds to signal that is 50% above the DC–biased point and 50% below, settings that can be adjusted to fit a specific requirement. This type of modulation means that the average bandwidth or *speed* of the device is set by the current consumed at the DC–bias point.

Single–carrier modulation for optical links were first implemented for IrDA [116]. Single–carrier means that all the bandwidth is used to transmit one carrier of information through the link. As optical links are dispersive, single–carrier modulation requires complex equalisers at the receiver. Single–carrier modulation schemes used in this thesis are OOK and pulse amplitude modulation (PAM).

Multi–carrier modulation is the basis of modern wireless communications including WiFi and 4G LTE. It consists of a method of transmitting data by dividing it into several components and sending each of component over a separate carrier signal. The individual carriers only use a narrow bandwidth, and the sum of all carrier completes the broad bandwidth of the link. The only multi–carrier modulation scheme used in this thesis is DC–biased (or offset) OFDM (DCO-OFDM).

3.3.1 On-off keying (OOK)

The simplest modulation scheme is OOK. OOK is a single carrier modulation scheme and widely used as a baseline from which a system can be scaled up to high–level modulation schemes. The main advantages of OOK are its simplicity of implementation and the ability to visually represent the system performance in what is known as an eye diagram (see below).

In OOK, data is encoded in digital pulses representing a one for a pulse (“on” state) and a zero for the absence of a pulse (“off” state). Data is transmitted in a series of light pulses, representing the ones and zeros of the digital stream. The system implementation can add variants such as a DC–bias, where the OOK signal is bipolar meaning positive pulses above the DC–bias and negative pulses below the DC–bias.

The basic system setup for OOK is presented in figure 3.6. This is very similar to the setup for frequency response measurements (figure 3.1). Here the DC–bias is chosen at a mid current level and an AC–signal is superimposed. The signal consists of a pseudo-random bit sequence pattern ($2^7 - 1$ bits long) from a pattern generator. The received signal is fed into the error detector which compares it with the pre–programmed pattern. The system clock is fed to both the pattern generator and error detector externally using a network analyser. As the system runs in real time, synchronisation is very important and using the rule of thumb that one foot of cable equals one nanosecond of delay, cabling needs to be manually adjusted to guarantee a correct synchronisation between the instruments. Finer picosecond adjustments are available using the instruments themselves.

A typical OOK signal is presented in figure 3.7 (a) at 500 Mbps using a pixel of the segmented micro–LED A, more details this particular micro-LED are shown in section 4.3. In the input is used $V_{pp} \approx 2V$ resulting in a received signal with $V_{pp} \approx 0.6V$. As the received signal is a pattern and it repeats itself, a time superposition of the pattern frame allows display

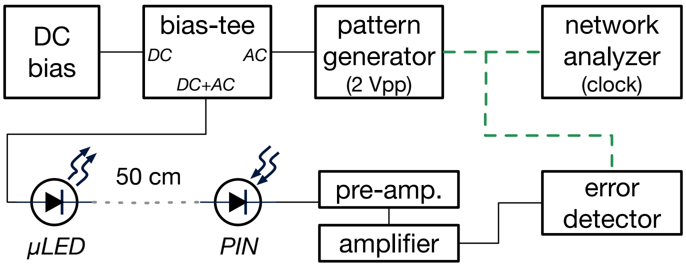

Figure 3.6: Setup for data transmission in real time using a BERT with OOK modulation.

in the form of an eye diagram. Figure 3.7 (b) shows the eye diagram at three bit rates. The open space between the bottom and top levels is known as the eye, where a larger eye ideally it should looking squared or rectangular means higher link quality, allowing lower BER. Note that in OOK the device runs at full speed set by the clock frequency, and increasing data rate requires a higher clock frequency. When an increase in the bit rate leads the eye to close, one approaches the bandwidth limit of the micro–LED source, assuming no other limitation in the system. As the speed increases the response decreases; i.e. the probability for a carrier to recombine in phase with the signal decreases. As such, the optical power carrying the intended signal decreases and the SNR decreases leading to higher noise at higher bit rates. Figure 3.7 (c) presents the data rates as a function of optical power up to 1.7 Gbps. Note that at these high data rates the clock frequencies are already above the bandwidth of the photodiode (Femto HSA-X-S-1G4-SI, 1.4 GHz), although with an extended bandwidth (no sharp cutoff), it attenuates the received V_{pp} signal with no influence on the DC optical power.

This micro–LED device has a bandwidth over 800 MHz, presented in more detail in section 4.3. The result shown here indicates that the micro–LEDs can easily run at significantly higher speeds than their bandwidth point. At 1.7 Gbps with OOK, meaning a clock of 1.7 GHz, it just over twice the bandwidth of the device and the measured BER in real time sits at 10^{-9} or six orders of magnitude lower than the 10^{-3} limit for FEC or channel coding. This level of performance is very high for LEDs and demonstrates the capability for higher level modulation schemes.

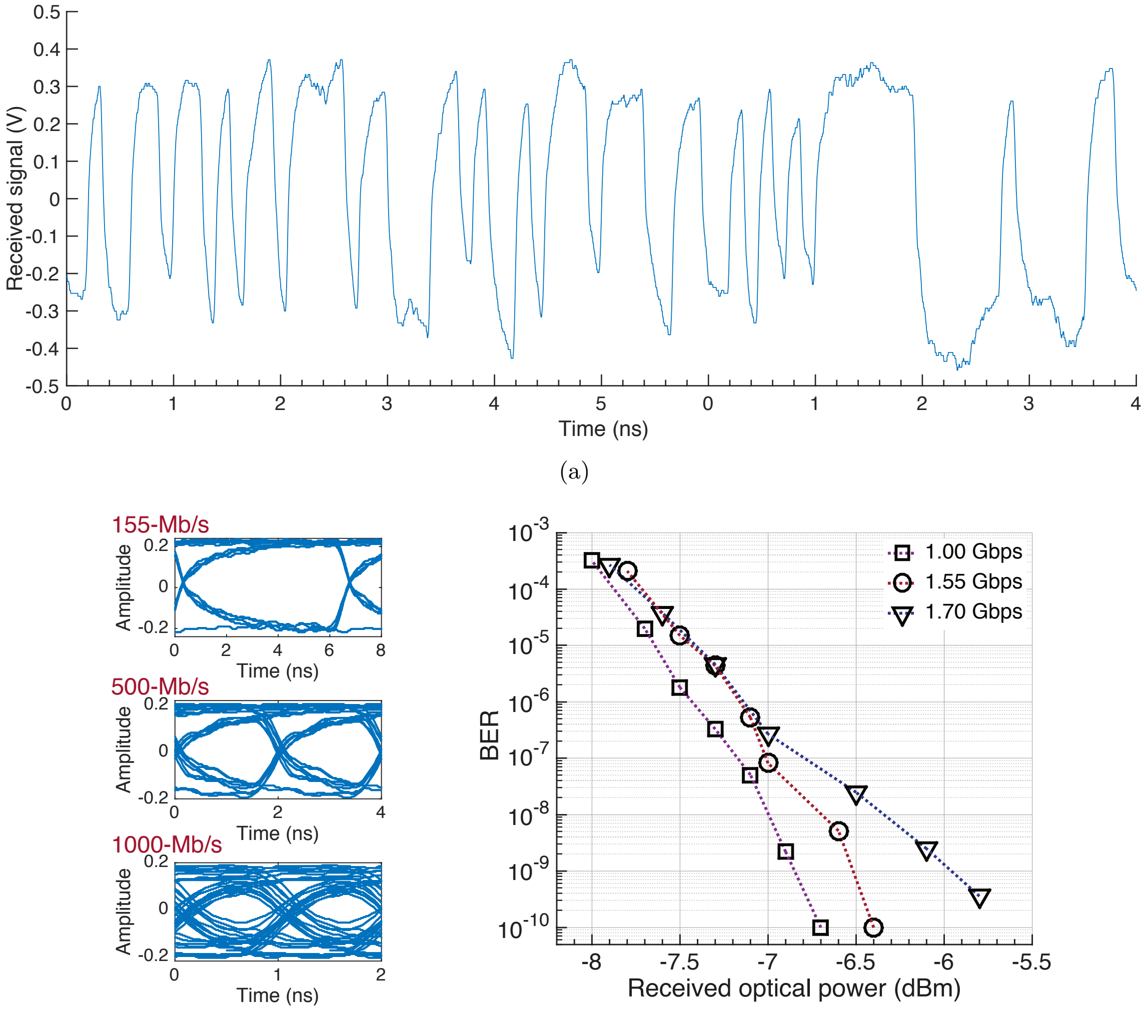

(a)

(b)

(c)

Figure 3.7: Received OOK signal at 500 Mbps in (a) where the zero level marks the decision boundary; eye diagrams at 155 Mbps, 500 Mbps and 700 Mbps for a segmented micro–LED in (b), amplitude is in Volts; BER as function of optical power at 1 Gbps, 1.55 Gbps and 1.7 Gbps.

3.3.2 Pulse amplitude modulation (PAM)

PAM is a single carrier modulation scheme that follows the same working principle as OOK as a time domain data encoding scheme but it uses amplitude as an extra degree of freedom. PAM encodes data in the amplitude of the signal by dividing it in multiple levels, each level carries a symbol that represents a binary word. Thus OOK can be considered to be a 2-level PAM or 2–PAM. The word length depends on the number of levels which is adjusted to the available SNR and required bit rate. Increasing the number of levels assigned increases the number of bits sent per unit of time at the same clock frequency. PAM is strong against abnormalities in frequency response such as dips and resonances created by signal reflection between connections. It can deal with low optical power at the μW level, scales linearly with the available bandwidth. In the other hand, PAM is sensitive to non–linear optical response and distortion which affect the differences between the amplitude levels, and thus requires complex equalisers at the receiver for best performance.

3.3.3 Orthogonal frequency division multiplexing (OFDM)

Orthogonal frequency division multiplexing is a modulation scheme widely used in both wired and wireless communications systems [8]. Instead of transmitting the bit stream with a single carrier using all the available bandwidth, as OOK and PAM seen above, OFDM makes use of a large number of closely spaced orthogonal subcarrier frequencies within the available bandwidth that are transmitted in parallel. Data is digitally encoded in the frequency domain rather than the time domain. Modulation is achieved digitally with an inverse fast Fourier transform (iFFT), allowing precise generation of orthogonal signals that is computationally efficient. In OFDM the spectra of individual subcarriers overlap in the frequency domain as illustrated in figure 3.8 (a). OFDM subcarriers typically use quadrature amplitude modulation (QAM). QAM is a signal in which the modulated carriers are shifted in phase by 90 degrees and assigned different amplitudes, and the output consists of variations both in amplitude and phase. This can be scaled in an *M–array* and visualised in a constellation, and figure 3.8 (b) illustrates a 16–QAM example. Each point in the constellation carries a 4 bit word resulting in a total of 4 bits per symbol for 16–QAM. The channel is estimated for a SNR spectrum of the whole system, and based on the minimum SNR within the bandwidth set, an M–QAM level is decided. The implementation by the research groups of the Universities of Edinburgh and Oxford uses an advanced version of OFDM. Here, instead of loading the channel with a constant M–QAM level (or bit loading) through the whole bandwidth, the QAM levels are decided based on the available SNR for each carrier. This technique is referred to as adaptive bit and power loading, and it results in higher M–QAM level for higher SNR carriers and lower M–QAM level for low SNR carriers, thus significantly increasing spectrum efficiency (bit/s/Hz). In practice, this provides two advantages versus fixed bit loading: first, for the same bandwidth higher bit rates can be achieved; second, as the lower SNR level does not decided the bit loading of the whole band, bandwidth can be extended with the use of lower M–QAM levels, increasing the bit rate of the system. In a communications system, micro–LEDs can achieve up to 256–QAM for a SNR ≈30 dB. In this thesis, OFDM measurements correspond to DC–biased OFDM with QAM modulation with adaptive bit and power loading, referred to as DCO–OFDM.

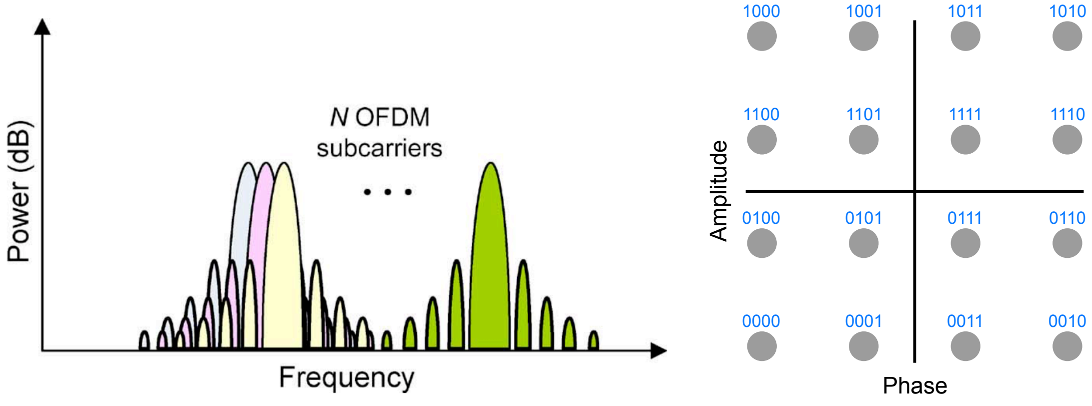

(a) (b)

Figure 3.8: In (a) we show schematically the frequency spectrum of the OFDM subcarrier frequencies, from [8]. In (b) a 16–QAM constellation is displayed.

3.4 Summary

In this chapter we presented the fundamentals regarding the frequency response characteristics of micro–LED and the electro-optic modulation bandwidth. Aspects related with the modulation technique and the linearity of the electrical to optical signal transfer were discussed. An overview of the photo–receiver technologies for VLC was also presented. This chapter finishes with a short introduction to the modulation schemes used with our partners with key differences are highlighted. Results using PAM and OFDM are presented in chapter 5 for the devices introduced in chapter 4.

Chapter 4

New designs of micro–LED

This chapter introduces the main innovation regarding fast response micro–LEDs, and describes the respective devices and their characterisation. Here, the main driver for innovation is the understanding of the thermal performance, followed by a micro–LED design targeting specific applications. This chapter starts with thermal management to address a few important aspects such as: the thermal dissipation dependancy with pixel design, the thermal uniformity within the active area. It progresses to understanding of how temperature influences other properties of the device and how to mitigate these effects. The relationship between these properties is found to be complex and interdependent. The knowledge gained forms the basis for the second part of this chapter. There, the focus shifts to pixel design resulting in shapes that improve device performance forward, tailored for visible light communications. The application of these devices is presented subsequently in chapter 5.

4.1 Thermal management

The major limitation for performance of an LED is it operating temperature. Temperature limits efficiency and thus, optical power and maximum injection current density. Any reduction in operating temperature provides direct benefits. The most obvious step to increase the bandwidth of LEDs is to increase their capability to sustain high current densities [46]. Current densities of 20 kA/cm^2 in micro–LEDs are not unprecedented [45]. As seen in chapter 3, small LED pixels can provide higher bandwidth at the expense of optical power, and, conversely, large pixels can provide high optical power at the expense of bandwidth.

A key challenge is therefore, within standard fabrication processes and with commercial epitaxial material, increase the output optical power while maintaining high bandwidth, thus maximising the channel capacity. As was seen in section 2.7, small pixels provide better thermal management than large pixels, allowing higher current densities and, thus bandwidth. The first question we address is if there is a viable format to multiplex a number of small pixels in a single chip to increase the overall optical power, ideally without a bandwidth penalty. In order to answer this question, an understanding of actual heat dissipation of a single pixel and multiple pixel is required.

4.1.1 Modelling

COMSOL^{TM} is a software package that allows one to model heat dissipation and temperature buildup in a given structure with particular material properties [117]. This software uses finite element analysis to solve the steady-state heat equation, which in the 3D case is:

$$\begin{gathered} \frac{\partial^2 \Delta T}{\partial x^2} + \frac{\partial^2 \Delta T}{\partial y^2} + \frac{\partial^2 \Delta T}{\partial z^2} = 0 \\ T(x,y,z) - T_a = \Delta T \end{gathered} \tag{4.1}$$

where T is the temperature in a given point in space, ΔT is the increase of temperature over the ambient temperature and T_a is the ambient temperature.

This permits a comparison of the thermal performance of several pixel configurations. For the purpose of modelling the wafer structure presented in figure 2.2 is now simplified to three layers: 430 μm for the sapphire, 6 μm for the GaN buffer and 179 nm for the stack of MQWs. The power-to-heat conversion is assumed as 80 % and an ambient temperature of $T_a = 20°$C is set as a boundary condition at the bottom of the die. Note that no additional heatsink mechanism being considered. The parameters assumed in the modelling are presented in table 4.1, values which are dependent on temperature, crystal orientation, alloy content and layer thickness.

Figure 4.1 presents the temperature on the GaN layer of 3 pixels with a separation of

Table 4.1: Parameters used for thermal modelling with COMSOL, retrieved from [10, 11].

		Sapphire	GaN
Thermal conductivity K	$(W\,m^{-1}K^{-1})$	35	253
Specific heat capacity C_p	$(J\,kg^{-1}K^{-1})$	788	490
Density ρ	$(kg\,m^{-3})$	3980	6070

$20 - 150\,\mu m$. The pixels are identical in each die, with an active dimension of (a) 20 μm and (b) 40 μm in (b) in a 1 mm die. The heat generation is applied to the MQW layer as a power density of $1.115 \times 10^{15}\ W/m^3$, derived from the total electrical power at current density of $5\ kA/cm^2$ of a real device of similar size. In a real device, the typical junction temperature (Tj) for breakdown is $\sim 150°C$, thus the situation in (a) is within practical limits and (b) is not viable. Increasing the gap between adjacent pixels reduces the mutual heating at the cost of die area. The best choice is also dependent on factors such as required optical power, beam diameter and current density capability.

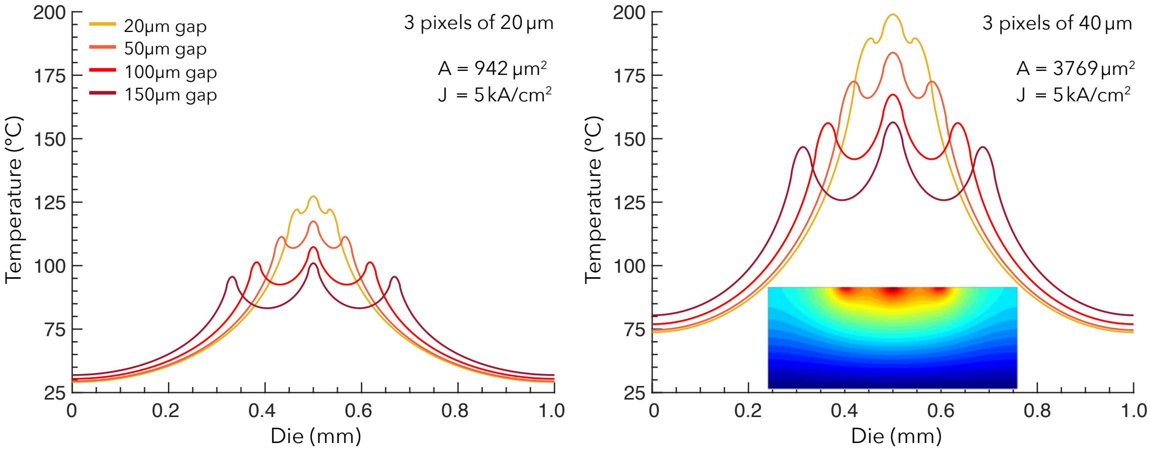

(a) (b)

Figure 4.1: COMSOL simulation of temperature at the top of the die for three pixels of (a) 20 μm and (b) 40 μm active length at a current density of $5\ kA/cm^2$. The inset show the cross section of isothermals inside the die of $\oslash$40 μm with 150 μm gap.

In the context of modelling, one can assume the LED efficiency as a constant for all the operating range and consequently achievable optical power becomes linear with the active area of the device. The next question is wether for a large active area required to achieve a certain level of optical power, a design where that area is divided to a higher number of small pixels presents better thermal performance than a design with lower number of larger pixels. Figure 4.2 (a) shows the resulting simulated temperature in the GaN layer of a fixed active dimension of 200 μm divided in to 5 and 15 pixels equally spaced with pixel dimension of 40 μm and 13.3 μm, respectively. The power density applied here is $2.23 \times 10^{14}\ W/m^3$, corresponding to a current density of $1\ kA/cm^2$.

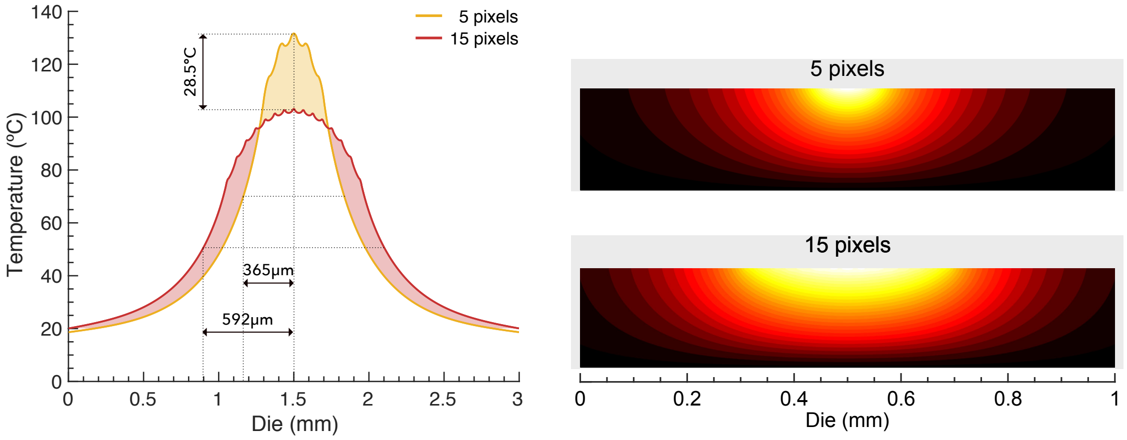

(a) (b)

Figure 4.2: Simulation of 200 μm active length divided into 5 pixels of $40\mu m$ each and 15 pixels of $13.3\mu m$ each, with $50\mu m$ pixel gap at $1\ kA/cm^2$. The temperature curves obtained are shown in (a) and the cross section with isothermal contours in (b). The colour bar for (b) is the range of displayed in (a), with white indicating the highest temperature.

Subdividing a wide active length in a large number of small segments allows the heat to be distributed instead of accumulated. This is seen by the width of the temperature curves in figure 4.2 (a) and the warm region in figure 4.2 (b). Note that the colour scales in (b) correspond to the dynamic range shown in (a). The second conclusion is related to the limited thermal conductivity of sapphire ($K = 35\ W/(mK)$) resulting in restricted heat extraction through the substrate. This leads to heat buildup and, consequently, a rapid rise in temperature. Figure 4.2 (b) clearly shows that by distributing the active area over a larger die area, one is effectively increasing the channel through which heat escapes the active region thus reducing the temperature at the active region.

4.2 High-power LEDs

This section presents a study of current crowding, i.e. spatial regions of high current density in the device. This study is performed with broad–area LEDs as the effects examined here are difficult to characterise with small pixels and the solutions found can, in principle, be directly adopted for micro–LEDs.

Current crowding [6, 118], is a factor limiting increase in the injected current density in LEDs. Current crowding occurs in mesa-structured LEDs grown on insulating substrates such as sapphire used in GaN-based LEDs [119]. In these LEDs, the p-electrode is usually located on the top of the mesa, while the n-electrode is located to the side of the pixel on the n-type GaN at the bottom of the mesa. As a result, carriers injection is lateral to the LED mesa and current tends to crowd on the edges of the mesa towards the n-electrode [120].

LEDs operating under non-uniform current densities create thermal hotspots due to non-radiative recombination [106]. These hotspots are responsible for device failure under steady-state high-power operation [121]. High current densities lead to localised peaks of carrier density and therefore, localised peaks of modulation bandwidth [109]. Furthermore, high-frequency operation creates stress in the intrinsic defects [122] leading to a quicker degradation in the regions of current crowding. For GaN LEDs grown on sapphire, differences in lattice constant, thermal expansion coefficients and thermal gradients can also lead to degradation. Current crowding of LEDs grown on insulating substrates has been investigated in a number of reports [119, 123, 106, 124]. Possible solutions to address this issue include shaping and patterning of p-electrodes for top-emitting devices [119, 106], and shaping of n-electrodes for devices in a flip-chip architecture [123, 124]. Spatially-resolved photocurrent has been used to relate spatial current distribution and light emission for AlInSb LEDs [125]. We have recently reported a theoretical demonstration of the impact of the n-electrode layout to current distribution and brightness of a GaN-based micro-display [7].

Here, we look at changes in the n-electrode layout and pixel shape as means to mitigate current crowding, increase optical power and reduce junction temperature. Spatially-resolved measurements of bandwidth linked to localised carrier density via the differential carrier lifetime, show localised current crowding regions. Thermal imaging and spatially-resolved peak emission wavelength monitoring are also considered and compared to the modulation bandwidth in the context of current crowding.

4.2.1 Device designs

To explore the effects of the n-electrode layout and pixel shaping, four broad-area LEDs were fabricated on a single chip with the same active area of $0.2\,mm^2$, equivalent to a pixel 500 μm in diameter. Figure 4.3 presents the four LEDs with the respective changes as seen from the top, where the overlay represents the p- and n-metal insulation. The pixels for LEDs A and B are disk shaped, and LEDs C and D are semi-ring shaped. LEDs A and C have localised n-electrodes, and LEDs B and D have n-electrodes surrounding the whole pixel.

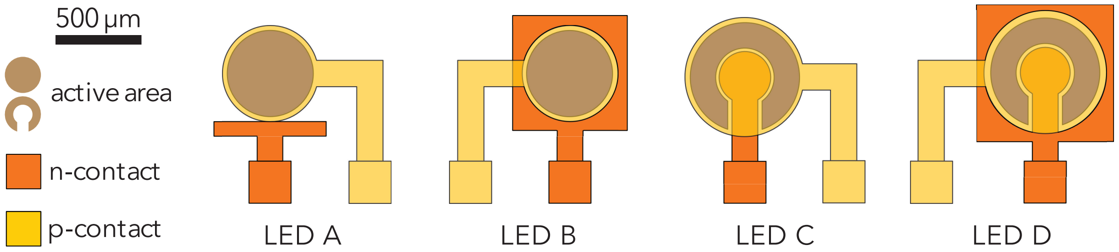

Figure 4.3: Diagram of the four LEDs in flip-chip architecture seen from the top, light emission exists through the bottom (substrate). LEDs A and B use different n-electrode layout, LED C and D differ from A and B in the shape of the pixellated area. LEDs B and D have the whole mesa surrounding the pixel covered with the n-electrode.

Design principles

The principle proposed to address current crowding is the following. At high current densities, the current flow between the n- and p-electrodes is such that, in order to minimise the electrical resistance, the current flow chooses a path through the structure that avoids passage through the highly resistive p-GaN layer. This effect is illustrated in figure 4.4 (a) where the n-electrode is positioned on one side of the pixel, on example corresponding to LED A. In these regions, light intensity is typically higher [119]. One solution to this is to minimise the path length for the current to flow through, meaning that the average resistance is minimal. This can be achieved by surrounding the whole pixel with the n-electrode metal, distributing the current flow around the edges of the pixel (inner and outer) as illustrated in figure 4.4 (b) for LED D. In this case an interior n-electrode is added to further increase the lateral injection perimeter and thus minimising the variation of resistance.

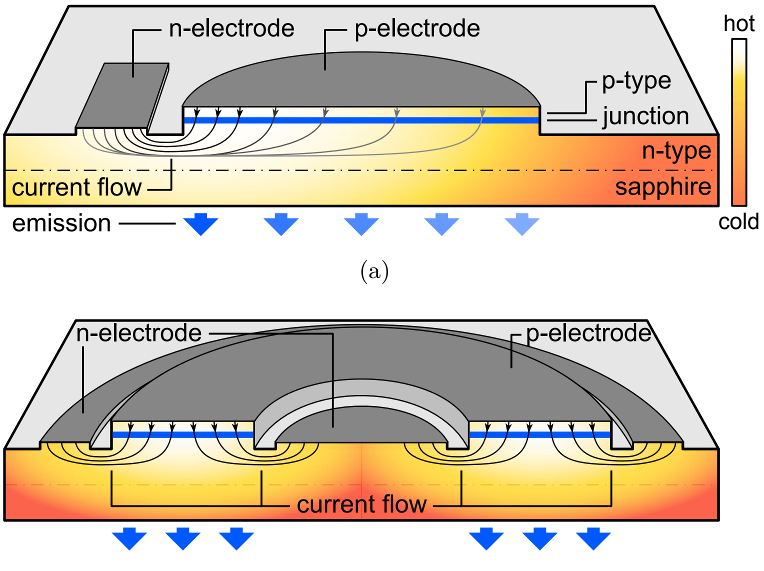

(b)

Figure 4.4: Cross-section diagrams of the predicted effect of n-electrode layout and pixel shaping on the current distribution through the junction, intensity of light emission and heat dissipation for high current regimes, (a) for LEDs A and (b) for LED D. Note that light intensity is typically higher at the regions of current crowding.

The next effect to consider is thermal management. The junction can be interpreted as a collection of discrete points in area at which current flows and recombination occurs. Each point acts as a heat source or hotspot generating heat that dissipates through the crystal lattice. As each point is adjacent to others, there is an overlap of the heat curves from the points that represent a pixel. Reducing the pixel size decreases this effect significantly [86]. The challenge is to keep the pixel size large for high optical output power while reducing the accumulated heat. One solution is to design the pixel such that the active area is distributed through a larger device area. Doing so decreases the length of the line connecting two opposite pixel edges, effectively reducing the number of points that contribute to a heat accumulation. Therefore, LEDs C and D were designed with these concepts in mind. Figure 4.4 (b) illustrates the current flow and thermal dissipation principles for LED D.

4.2.2 Performance of the LEDs

Optical power

LEDs were probed on chip and the emission collected by a power meter with a collection efficiency of $\sim$ 66% for all devices, A, B, C and D. Figure 4.5 presents the (a) I–V and (b) L–I curves for all four devices. The R_s is 10.4–11.2 Ω and V_{th} is 2.2–3.0 V for all, as expected for devices of this size [6]. The optical power of all four LEDs follows the same trend up to ≈250 mA, a current at which the curves diverge. This indicates that current crowding and thermal effects may dominate device performance. At low driving voltage, slightly lower differential resistances are seen in LED B and D versus LED A and C, indicating that the n-electrode layout provides a contribution to the decrease of resistance, potentially slightly lowering current densities.

LED A presents a roll-over of the optical power at ≈380 mA producing ≈40 mW of optical power. At the same injection current, LEDs B, C and D produce more power, showing evidence of increased efficiency at high current. LEDs B and C produce similar optical power and roll-over points at ≈430 mA. This indicates that for output power, changes in n-electrode layout and pixel shape give equivalent results. LED C is sightly above LED B, which might be due to a slightly higher extraction efficiency typical of ring shaped devices. The highest power achieved was 46 mW for LED D at ≈480 mA, representing an increase of 20 % in the injection current and 15 % in the optical power versus LED A, the 5 % difference coming from the reduced efficiency at high currents.

Thermal effects

The differences seen in the optical power and injection current at roll-over (figure 4.5 (b)) indicates a thermal dependence. Figure 4.6 (a) presents the thermals images for all the LEDs at an injection current of 350 mA, near the roll-over point of LED A (figure 4.5). Note that the calibration of the emissivity is applied to the whole image meaning that temperature values are accurate only for the active area. High contrast seen for the mesas of LEDs A and C is due to the transparent sapphire substrate and the near perfect reflectivity of Pd at the

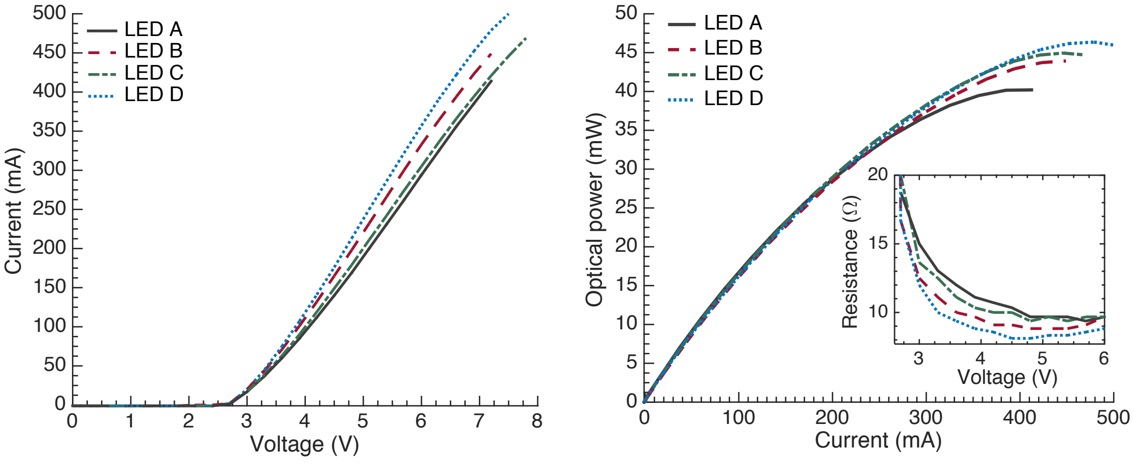

(a) (b)

Figure 4.5: I–V (a) and L–I (b) curves for all four LEDs. The inset shows the differential resistance as a function of the driving voltage.

IR wavelengths [126]. Note that for LEDs B and D the mesa is fully covered with TiAu metal from both n- and p-electrodes, leading to blurred images.

LED A shows a clear hotspot near the n-electrode, marking the minimum resistive path connecting the p- and n-electrodes. A higher temperature indicates a region with more non-radiative recombination. This evidence points towards a link between current crowding and observed temperature. As such, a higher carrier density is expected in this region, of which details to follow in section IV. Let us consider LED A as the baseline for comparison. LED B introduces a change of n-electrode layout, and the temperature is decreased due to the spreading of heat across the pixel, being slightly more concentrated in between the p- and n-tracks. The uniformity seen indicates an even carrier density and thus current crowding might be reduced. LED C introduces a change in pixel shape. Thermal imaging shows a significant decrease in temperature across the pixel. A hot region is seen on the path connecting the p- and n-tracks, indicating that current crowding was not reduced compared to LED A. Note that with the change of pixel shape to a semi-ring, an inner n-electrode was also introduced. This change is able to dissipate heat over a larger area, effectively reducing the observed temperature. LED D is the combination of both changes introduced with LED B and C. Heat distribution is significantly more uniform, leading to the lowest temperature of the set.

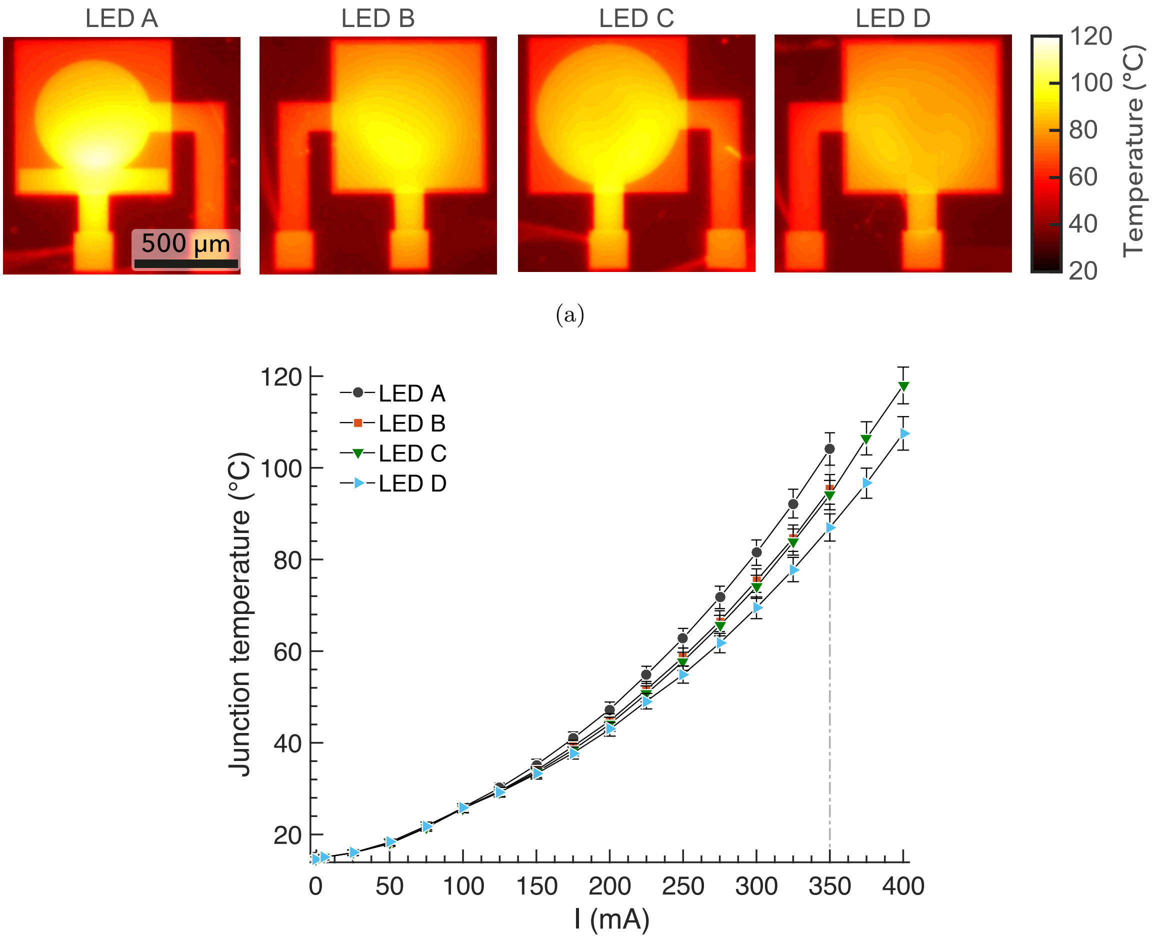

(a)

(b)

Figure 4.6: In (a) the temperature distribution across the pixel via infra-red imaging is shown at 350mA for all four LEDs. Note that the blur seen in LED B and D is due to the reflective *Pd* metal covering the whole mesa. Images are presented in the same orientation as figure 4.3. In (b) the mean junction temperature of whole pixel with increasing injection current is shown, the dashed line marks the injection current of 350 mA at which the images in (a) were taken.

A detailed look at LEDs C and D shows a slightly colder region at the centre of the pixel, attributed to a smaller thermal overlap from the junction profiles of the semi-ring.

A direct comparison of the T_j is presented in figure 4.6 (b). The T_j is calculated from the thermal images as the mean temperature within the pixel area for each current. Thus the whole active area responsible heat generation contributes to the final value of junction temperature. The junction temperature increases quadratically with the increase in injection current. Up to 150 mA the temperature differences are negligible. This is due to two factors. Firstly, when the device operates near room temperature, the ratio between the emitted IR photons and the background photons limits the technique ability to discern small differences. Secondly, the current crowding effect is more pronounced at high injection currents [6]. Thus, at lower injection currents, differences in junction temperature are expected to be small. For this reason, measurements presented later in section III were done at 150 mA.

In the high injection current regime, differences in junction temperature appear, with LED A being the hottest and LED D the coldest of the set. At an injection current of 350 mA, the current at which figure 4.6 (b) is presented, the respective differences in T_j are $\Delta T_{A-A} = 0°C$, $\Delta T_{A-B} = 8.82°C$, $\Delta T_{A-C} = 10.06°C$, $\Delta T_{A-D} = 17.13°C$. This means that at the same driving conditions LED D runs at 16% lower T_j than LED A, leading to benefits in efficiency as seen in increased optical power (figure 4.5) and reliability for continuous operation over long periods. Note that at 350 mA the optical power for LEDs C and D does not roll-over. Furthermore, the pixels with lower T_j have an extra margin to increase the injection currents up to 400 mA before reaching a similar temperature to LED A.

As shown in figure 4.6, thermal imaging as a non-evasive method also offers the advantage to see thermal effects of the whole structure under normal operating conditions in. This method is also widely used for power electronics, an area where, like in LEDs, thermal performance is major limiting factor for performance [127].

4.2.3 Spatially-resolved measurements

In this section we look at spatially-resolved measurements of modulation bandwidth and peak emission wavelength (λ_{peak}). Higher carrier density can be achieved by increasing the injection current or by confining the current flow to certain zone creating current crowding. Therefore, carrier density serves as a direct link to the current crowding. The λ_{peak} is a function of the injected current. Typically, λ_{peak} depends on the screening of the piezo-electric fields and band-filling at low currents (blue-shift), and on thermally-induced bandgap reduction at high currents (red-shift).

The setup for the spatially-resolved measurements is presented in figure 4.7. LEDs are probed on chip, light is collimated and magnified to 13 mm diameter and projected onto a screen. A detector is placed in the screen position and measurements are obtained by rastering the detector on a 13 × 13 grid with steps of 1 mm, with one acquisition per step. Measurements of frequency response are made with a photodiode and the emission spectra were recorded with a fibre coupled spectrometer, both having a collection diameter of 800 μm. The data was processed in Matlab^{TM} to determine bandwidth and the λ_{peak}. The images were constructed in the same orientation as in the diagram presented in figure 4.3.

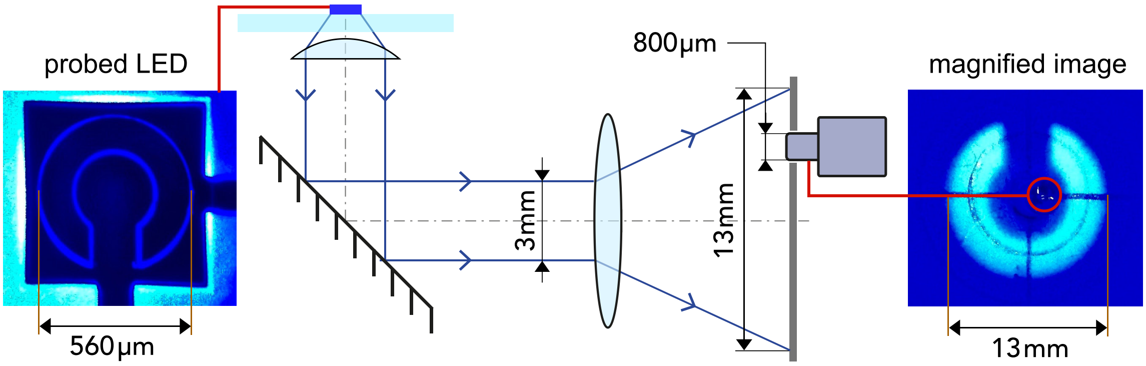

Figure 4.7: Setup schematic for spatially-resolved measurements of bandwidth and λ_{peak}. The image projected on a screen in (a) corresponds to LED C, vertically and horizontally flipped with respect to representation used in this text.

Figure 4.8 (a) presents the spatially-resolved bandwidth, measured as above, for all four LEDs at a chosen DC bias current of 150 mA. There are no thermal differences at this current (figure 4.6) and this guarantees that the overall thermal effects do not play a large role on the observed trend of the measurements. The constant current ensures that regardless of crowding, the mean carrier density is equal for all devices. The input power for the AC signal was chosen to be 10 dBm, above the usual 0 dBm value as these devices consume more power than micro–LEDs, corresponding to a modulation depth of $\approx$ 67 mV applied to the LED. LED A shows a higher bandwidth in the bottom half towards the n-electrode and a lower bandwidth at the top half, thus having a bandwidth that varies spatially from 10 MHz to 18 MHz, the smallest and largest values of the set. The device is strongly affected by current crowding and this agrees with the high temperature zone presented in figure 4.6 (b). In the case of LED B the current crowding is highly reduced versus LED A. The change in the n-electrode layout is able to effectively reduce the current crowding as the carrier density is now distributed more evenly around the edges. The left side of the pixel shows a medium bandwidth, just slightly higher than the mean value of 13 MHz. This is attributed to the contribution of the p-electrode to the crowding phenomenon, which remains unchanged for all four devices. LED C introduces a new pixel shape which is able to reduce the effective junction temperature as was seen in figure 4.6 (a). However, this change does not reduce current crowding according to figure 4.8 (a). The change in pixel shape also benefits from an inner n-electrode, which seems to distribute the carrier density on both sides of the pixel profile. This agrees with the hot region seen in Fig 4.6 (b). LED D is the combination of the change in n-layout and pixel shape. As with LED B, the n-electrode layout distributes carriers across inner and outer the edges, reducing current crowding.

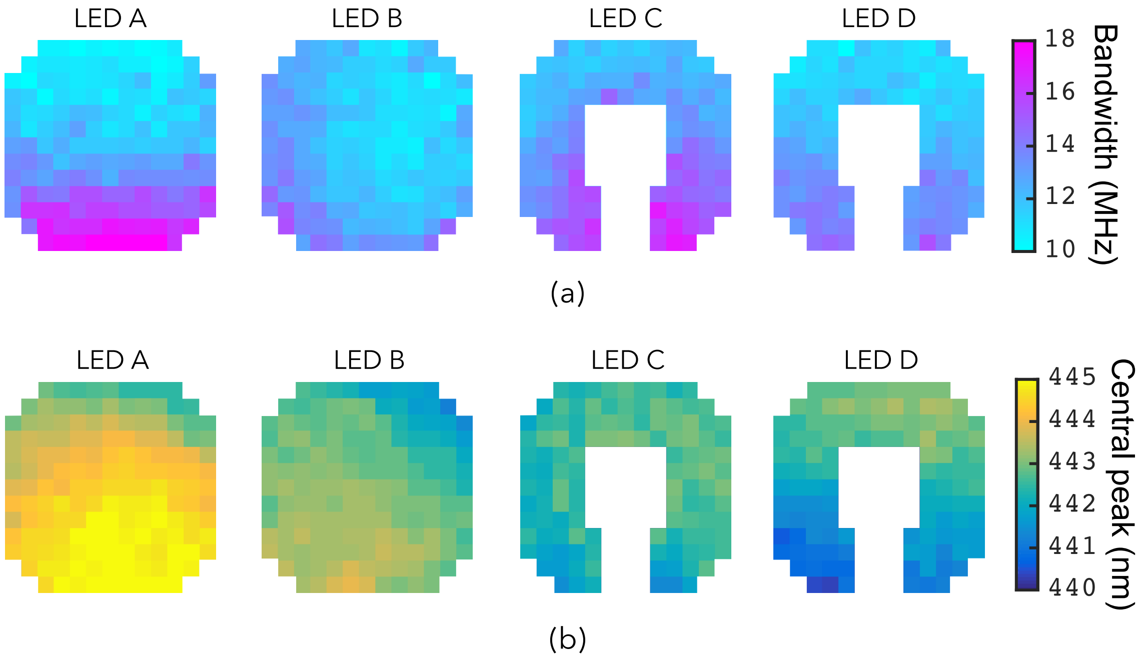

Figure 4.8: Spatially-resolved measurements at a constant injection current of 150 mA for bandwidth in (a) and λ_{peak} in (b) for all four LEDs. The mean values are $[13.0, 12.2, 13.5, 12.3]$ MHz for bandwidth, and $[444.1, 442.9, 442.5, 442.1]$ nm for the λ_{peak} corresponding to LED A, B, C and D, respectively. Images are presented with orientation as in figure 4.3.

Fig 4.8 (b) presents the spatially-resolved λ_{peak} for all four LEDs. The devices in question present both blue- and red-shifts under CW conditions, where in general the red-shift dominates for injection currents above 150 mA. LED A shows a strong red-shift in the bottom half pixel, towards the n-electrode, which has a strong correlation with temperature as seen in figure 4.6 (b). This indicates that the thermally–induced red–shift is correlated with the high bandwidth zone seen in figure 4.8 (b). However, this red-shift covers the majority of the pixel area unlike the current crowding, indicating an indirect dependence between λ_{peak} and current crowding. LED B shows a reduced red-shift and increased uniformity, in-line with the previous observation for the temperature. LED C features a change in the pixel shape and presents a uniform distribution of λ_{peak} across the pixel area. From temperature and bandwidth measurements one would expect to see a distinct zone as seen for LED A. This points towards a balance between the higher temperature (red-shift) and current crowding (blue-shift), leading to a neutral λ_{peak} across the pixel area. LED D includes both changes mentioned above. It exhibits a small red-shift on the top half of the pixel, attributed to a slightly lower carrier density. On the bottom half a small blue-shift is observed in the same region of higher carrier density and temperature. This is attributed to a lower overall temperature that allows extending of the injection current at which the band-filling effect dominates over the thermal induced bandgap reduction. Overall, we see that the λ_{peak} alone can provide qualitative information regarding temperature and current crowding when comparing various LEDs with a reference under equal driving conditions.

4.2.4 Summary

A method to measure spatially-resolved bandwidth and λ_{peak} has been introduced. Bandwidth is directly linked to current crowding via carrier density, allowing one to discern crowding regions. The results show that at medium injection currents, the influence of current crowding on the λ_{peak} is also dependent on factors such as band-filling and thermal management of the LED. The strong crowding towards the n-electrodes for flip-chip LEDs on insulating substrates such as sapphire was assessed with minimum disruption to the fabrication process. A set of four LEDs was fabricated with simple changes in the n-electrode layout and pixel shape. Reductions in crowding were observed with the change in n-electrode layout from LED A to B. The introduction of a new semi-ring shape in LED C increased the heat dissipation leading to an increase in optical power and a decrease in junction temperature. The combination of both changes, embodied in LED D, led to the highest performance of the set, with a 15% increase in optical power and 16% decrease in the T_j under equivalent driving conditions.

These improvements were attained on commercial epitaxial material by simple changes in the mask design and no extra fabrication steps.

4.3 Segmented micro–LEDs

One way to take VLC a step further is to increase bandwidth of the emitters. This plays an important role at two levels: first, larger available bandwidth in principle allows higher data rates; second, more bandwidth allows a flatter channel (maximises SNR over a larger frequency band) which leads to a more resilient communication link and maximises performance at lower SNR. Micro–LEDs for fibre communications in the visible range with the cost effective POF can achieve Gbps [50, 53]. One limitation for data transmission with a single emitter pixel at long lengths is the low power margin or budget of the link (analogous to SNR), where values in the order of 3–10 dB are typical [50, 49]. Furthermore, step–index fibres are based on PMMA with a bandwidth limitation proportional to the length, due to temporal dispersion [128]. At 50 m, for example, length the bandwidth is estimated to be ≈250 MHz. As such, the metric for a fibre system is the data length product [19], which accounts for the photonic device characteristics, the transmission line and the coupling losses. The largest loss is the optical coupling loss in and out of the POF, which is typically 3–6 dB per interface. An idea to mitigate this problem is to operate multiple pixels in full dynamic range to generate the discrete optical levels that represent the data symbol to be sent through the fibre. This can be achieved with an array of closely packed individually addressable micro–LEDs, a concept that is introduced in this work.

A significant increase in the modulation bandwidth exceeding 800 MHz for a single LED was also obtained.

4.3.1 Segmented micro–LEDs devices

Two segmented geometries of micro-LEDs were developed with designations A and B, having active areas of 435 and 1369 μm^2, respectively. These areas are equivalent to those of disk–shaped micro-LEDs with diameters of 24 μm for LED A and 42 μm for LED B. Figure 4.9 (see also Appendix 6.2) shows large concentric arrays of these LEDs designed primarily for use with POF without lenses. Within these constraints, the pixels were chosen with dimensions that maximise the perimeter for required active area to maximise the heat dissipation through the substrate, following the principles shown in figure 4.1. LED A is composed of 15 segmented pixels displaced in two concentric circular arrays, and LED B is a single circular array with 8 segmented pixels. The design is optimised to be aligned concentrically with the POF core to guarantee an equal optical coupling for every pixel. For the specific case of LED A, with both inner and outer arrays, the pixels in the outer array are ≈7% larger in active area to compensate for the increased out-coupling given the distance to the centre axis. This difference, however, is only seen by the peak optical power of an outer pixel being ≈4% higher, and is ignored in the characterisation.

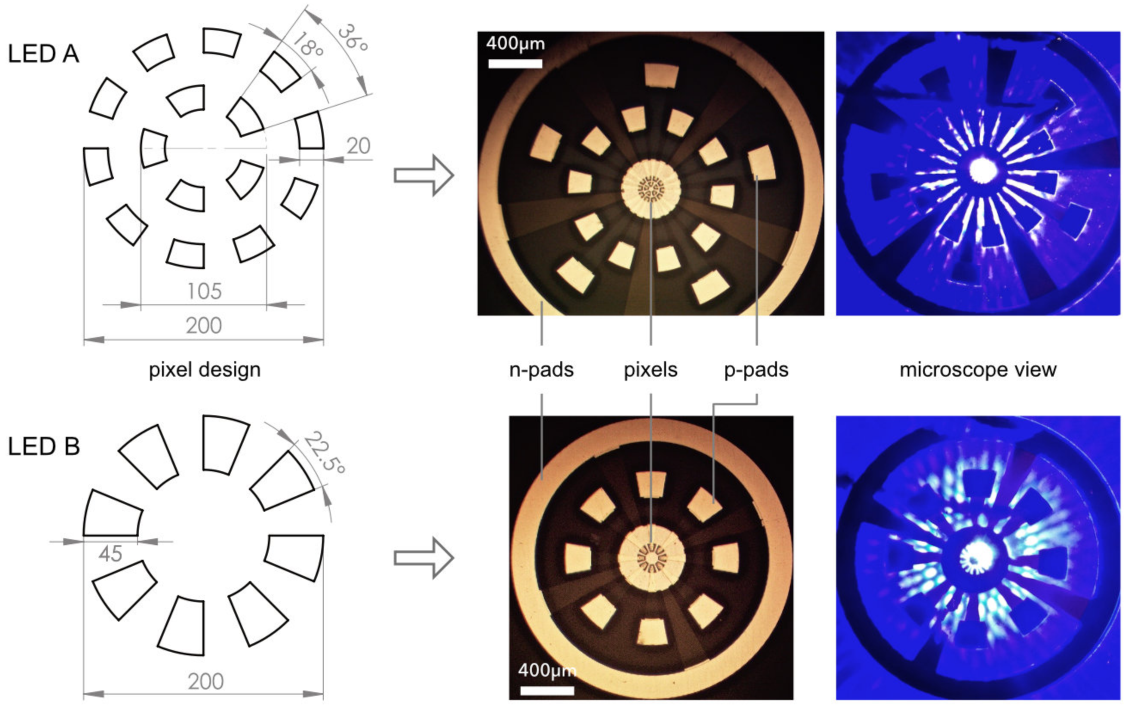

Figure 4.9: Micro-LED designs in concentric multiple element geometries. LED A is a single element of (a) and LED B is a single element of (b), where dimensions are given in micrometre. The upper diagrams correspond to the pixels which are located at centre of the photographs. The positions of the n and p bonding pads are noted.

The fabrication of the segmented micro-LEDs follows the process described in section 2.2. The mesa is deep etched down to the sapphire substrate, confining the n-GaN to match the

LED active area, thus reducing capacitance of each pixel. Changes in fabrication combined with a change of LED shape and electrode layout are the key factors to which the improvements in performance shown in the following sections are attributed.

4.3.2 Performance of the segmented devices

Characterisation was performed on single elements of the micro–LED segmented arrays. A direct comparison of relative size and shape of LED A and B can be found in the inset of figure 4.10 (a).

I–V, L–I & L–V characteristics of the segmented devices

Figure 4.10 (a) presents the current-voltage (I-V) and output power-current (L-I) characteristics of the segmented micro-LEDs. The DC current densities are up to a remarkable 19.5 kA/cm^2 for device A and 8.7 kA/cm^2 for device B. The optical power is 2.7 mW for LED A and 5.7 mW for LED B, corresponding to optical power densities (at the LED face) of 655 W/cm^2 and 415 W/cm^2 for LED A and B, respectively. This corresponds to an increase in optical power of three times compared with our previous reports for non-segmented devices of comparable size [46]. Figure 4.10 (b) presents the L–V curve for LED A and B, when the inset shows a single pixel of LED B in operation. The L–V characteristic is of great importance for data transmission as it sets the DC–bias and modulation depth in order to use the full dynamic range of the devices.

The high current density capability is characteristic of flip-chip micro-LEDs and is attributed to improved thermal management and reduced current crowding [129]. Higher series resistance is common for small active areas and increases with the decrease of area [83, 130]. In these devices the improved p-contact with Pd results in a lower contact resistance in comparison to previous reports using Ni/Au [46]. The lower resistance reduces the Joule heating, thus contributing to a lower junction temperature for similar active areas. In addition, the pixel shape is designed to increase the surface-to-active-area ratio, which enables a more efficient thermal dissipation. As such, in comparison with our previous report for devices of equivalent areas, these devices show an increase by a factor of 2 in the current densities at

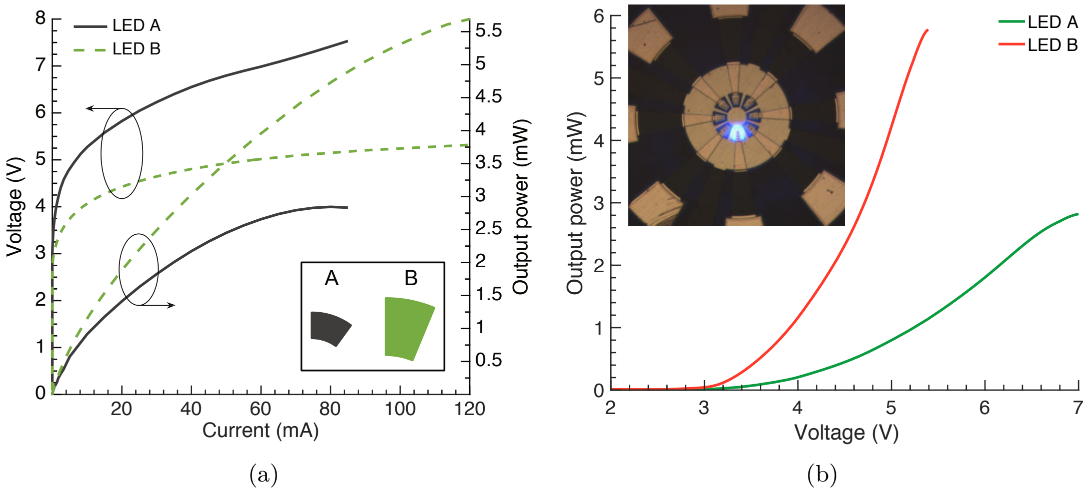

(a) (b)

Figure 4.10: In (a) the I–V and L–I characteristics of LED A and B with respective maximum optical power densities of 655 and 415 W/cm^2 at current densities of 19.5 and 8.7 kA/cm^2, respectively. Inset shows the relative size and shape of the micro-LEDs. In (b) the corresponding L–V curve for use in data transmission. The inset is a single pixel of LED B under operation.

which the roll-over point occurs [46].

Thermal characteristics of the segmented devices

Multi–pixel devices suffer from mutual heating, reducing efficiency and resulting in overall optical power being less than the sum of the power of the individual pixels. The geometric layout of this design combined with carefully chosen driving conditions can significantly mitigate this problem. Figure 4.11 presents thermal images the LED B with two pixels operating in DC conditions at 80 mA. The images shows the effect on device temperature of the increased separation around the circumference of the array. The first image is a single pixel with a T_j of 67 $°C$, serving as a baseline; the second image for two adjacent pixels with T_j of 89 $°C$; in the last image, showing pixels at opposite sides of the array, T_j is 77 $°C$, and is thus 12 $°C$ above of a single pixel. This physical separation represents a 50% reduction in T_j for two pixels in simultaneous operation under DC conditions.

In communication application using a bipolar modulation scheme, the input power of the DC + AC signal over one second averages at the DC point, note that to use the full dynamic range the DC bias must be ≈40 mA to be at half the optical power as shown in figure 4.10 (a). Using a table that maps the pixels that are further apart as possible for a given optical

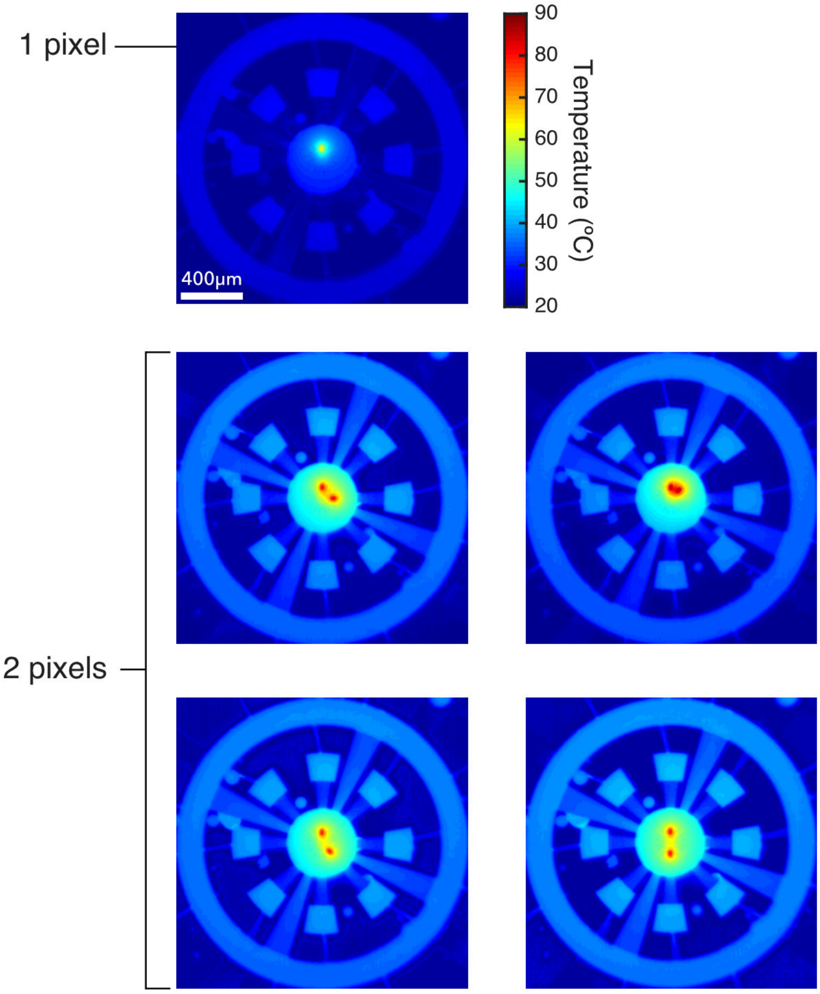

Figure 4.11: Thermal images of device B with one and two active pixels at 80 mA with increasing separation within the array.

power level, this can further reduce the mutual heating in the time domain.

Modulation bandwidth of the segmented devices

Figure 4.12 presents the (E-O) bandwidth as a function of the injected current density for LEDs A and B. These devices achieve high current densities enabling modulation bandwidths up to ≈830 MHz for LED A and 400 MHz for LED B. We have previously shown that increasing the current densities in the active region decreases the differential carrier lifetime [6, 46]. The differential carrier lifetimes are calculated from equation 3.2 to be 0.19 ns (at 19.5 kA/cm^2) for LED A and 0.40 ns (at 8.7 kA/cm^2) for B, which we attribute to the combined effect of high carrier densities. As a comparison, the micro-LEDs reported in [46] had differential carrier lifetimes down to 0.37 ns at $< 10\ kA/cm^2$, which suggests that the high current densities possible from LED A, in particular, are key in enabling the high modulation bandwidths shown here. Lower capacitance in these devices due to the etch process going down to the substrate may have also reduced parasitic capacitance that might otherwise have affected the modulation response of the LEDs.

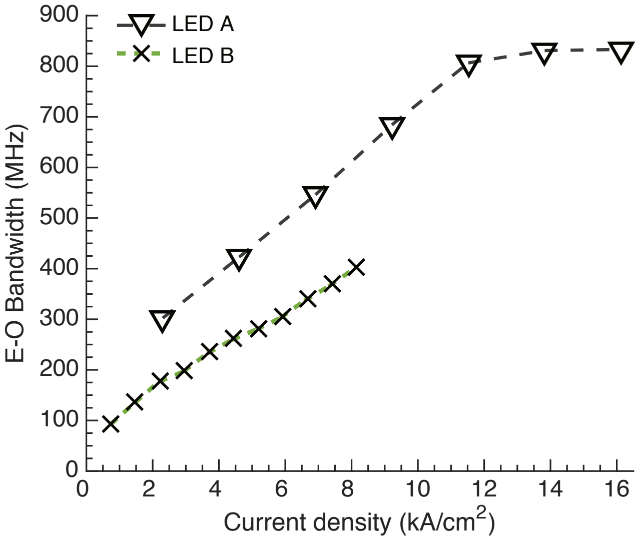

Figure 4.12: E-O bandwidth as function of the injected current density for micro-LEDs A and B. The maximum bandwidths are 833 MHz and 397 MHz, respectively. Note that these current densities correspond to a DC bias range of 10–70 mA for LED A and 10–110 mA for LED B.

In addition, at the same injected current densities the observed bandwidths are higher for device A than device B. This effect differs from previous reports with 450 nm devices [46]. This difference may be attributed to improved current spreading across the active area of the small pixel and an associated reduction in the junction temperature [86]. Furthermore, temperature differences at the same current densities may contribute to this effect.

4.3.3 Summary

Two new segmented micro-LED designs for VLC and polymer optical fibre systems were developed. These devices demonstrate that using simple changes in the pixel design it is possible to improve the balance between optical power and bandwidth. As such, the segmented micro-LEDs shown record modulation bandwidths while simultaneously producing a few mW of optical power, and consequently – as shown in chapter 5 – record throughputs in data transmission applications. The devices sustain very high current densities producing higher optical power densities than comparable commercial devices while retaining multi-mW optical power. The performance achieved by these micro-LEDs is attributed to three factors: deep etch of the mesa down to substrate; improved metallisation of the *Pd* p-contact and the shaping of the active area. The individual contributions of these factors is not yet clear, however, and requires further research.

4.4 Ring–shaped micro–LEDs

In section 3.2.3 we introduced the Shannon–Hartley theorem. This raises a paradigm of the optical power × bandwidth product: larger pixels have high power but slow response (section 4.2), whereas very small pixels have very fast response but lower optical power (section 4.3). In both cases there is a tradeoff between optical power and bandwidth. In data communications applications what is important is to maximise the data capacity capability [109]. The key challenge is to maintain high efficiency for optical power while increasing response speed [33]. Given the required use commercial epitaxial material to show mass market exploitation potential, the degrees of freedom we have are fabrication and LED design.

The devices developed here consist of ring–shaped pixels with areas smaller than a $100 \times 100 \mu m^2$. Previous publications on micro-rings in our group focused only on the increase of optical power via enhancement of the light extraction efficiency using a large array [84]. Here, a step forward is taken towards individually addressable single micro-ring elements for VLC.

4.4.1 Ring-shaped micro-LEDs, rings and half-rings

The thinking behind the design of the rings and half–ring micro-LEDs is to optimise the thermal management of a given active area. We choose active areas which, based on our previous knowledge, meet the performance requirements in optical power and bandwidth for the various application in data communications.

The ring LEDs are based on the same principles as described in section 4.2 for broad area devices. In a circular shaped pixel, the hottest spot is at the centre. Removing this centre spot by shaping the intended active area in a circular segment or ring simultaneously reduces T_j and current crowding, as was shown in section 4.2. This allows operation over an extended range of current density and, thus, higher bandwidth. In addition, this configuration increases the light extraction efficiency, giving benefits in optical power [84]. As such, there is a basic approach in place here to simultaneously increase optical power and bandwidth.

Figure 4.13 presents a schematic diagram of all the rings and half–ring micro-LED designs. Here, a ring is defined by the aperture diameter and the width of the solid material or wall. To explore a range of optical power and bandwidth, twenty pixels were designed with a range of 20–100 μm in aperture diameter and 10–20 μm in wall width.

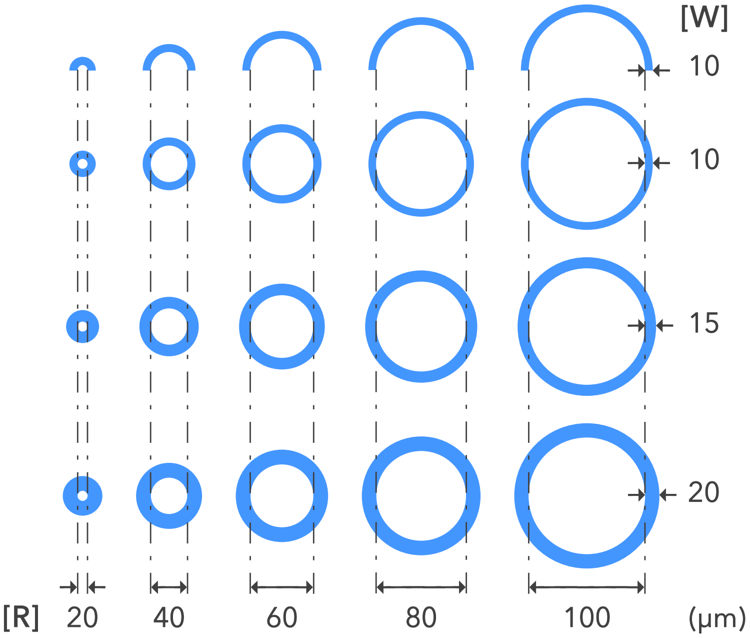

Figure 4.13: Schematic diagram of the set of ring-shaped micro-LEDs

The nomenclature is defined as: `R` for ring aperture diameter and `W` for wall width, e.g. `R40W15` is a ring with 40 μm aperture diameter and wall width of 15 μm, where the ring outer diameter is $40 + 15 \times 2 = 70$ μm. Of the twenty pixels, fifteen are ring shaped and five are half–ring shaped, the latter having the nomenclature `HR`. These are a copy up the upper row of rings corresponding to `W10`. Thus, all the half-rings have a wall width of 10 μm, the limiting feature size for good quality fabrication. The reason for introducing half–rings is to decrease the active area with minimum perturbation to the mask design and the fabrication process.

Figure 4.14 shows photographs of: (a) the chip; (b) a group of rings for `W10` and `W15`; (c) a group with all the half–rings. The chip size is 1.5×1 *cm*, significantly larger than typical for a micro–LED chip. It hosts a total of 50 different LEDs, including rings, half–rings and clusters. In this chip the various pixels have a large clearance with short metal tracks to eliminate parasitics for high frequency modulation. In addition, a larger chip allows superior thermal performance as it allows heat to dissipate further away from the pixels, while at the same time providing a larger area of contact with the next thermal interface, in this case air.

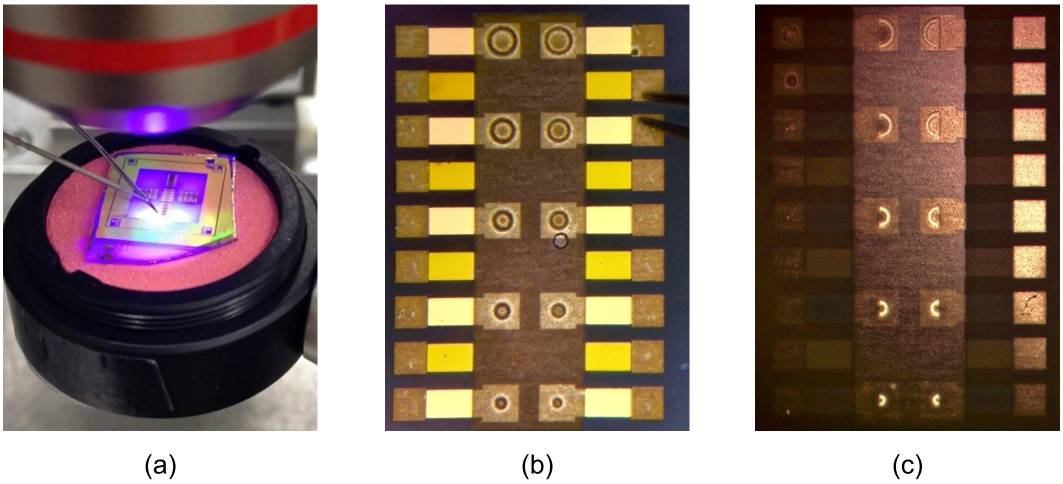

Figure 4.14: Photographs of the ring and half-ring devices. In (a) a photograph of the whole die sitting on a power meter under probing, in (b) the rings of wall width of 15 μm (left column) and 10 μm (right column), in (c) the half-rings of wall width of 10 μm with right column being a mirrored copy of the left column.

In the mask, the pixels are organised in groups of ten, sharing the same mesa (n–contact). Included in this mask are disc–shaped pixels with sizes of, respectively 20, 40, 60, 80, 100] μm in diameter. Overall, there are three groups with ten pixels each, totalling thirty pixels. One group contains the half–rings only, where the pixels are duplicated to guarantee a working pixel of every size given the fabrication difficulties of smaller sized devices.

Thermal modelling of the devices

Attention was given to the thermal performance of the variously shaped pixels. The devices were studied at the design stage via thermal modelling with COMSOL^{TM}, following procedure is presented in section 4.1. The final pixel shapes, ring and half–ring, result from balancing considerations between three aspects: thermal management, feasibility for active area scale up and practicality for optical collimation.

Figure 4.15 presents a 3D simulation result for `HR80` and `R40W20` at 12 kA/cm^2 and 8 kA/cm^2, respectively. The block considered is 3 × 3 mm, corresponding to typical chip size. From the bottom up, the structure consists of sapphire (430 μm), GaN (6 μm) and MQW (179 nm). The heat power is assigned to the MQW using values from the I–V curve of a similar size device, as described in section 4.1 and the results presented correspond to a steady state. These shapes radiate heat through the first interface, in this case GaN, on both the inside and outside of the active area, as seen in the top view simulation. At high current densities, such as the ones used here, the maximum temperature spot seen in `R40W20` is not located at active area, but instead, it is located in the centre opening. This is the first indication of the design being able to effectively take the highest mutual heating region outside the active area, thus, reducing the chance of junction breakdown. For a baseline comparison please see LED B in figure 4.6 (a), showing a measured hotspot directly on the active area at high current in a traditional disc-shaped pixel. The half–ring `HR80` presents a similar thermal response to high current densities. Here the mutual heating is almost non-existent, and instead the heat is evenly radiated outside the active area without a the generation of an hotspot. In practice these advantages allow one to operate the pixels at higher current densities than previously possible with pixels of similar active area. In addition, an even temperature distribution decreases the chance for steep temperature gradients, thus, increasing reliability. These simulated temperatures — based on typical maximum current densities achieved with micro–LEDs of similar size — are similar to the ones measured for broad–area LEDs at high current density, see figure 4.6, an indication of the accuracy of the model used. Please note that thermal conductivity and thermal resistivity are fixed by the wafer epitaxial structure. Our own simulations and test devices have shown that heat conduction via additional top layers during the fabrication does not provide significant benefit at the operation range of interest.

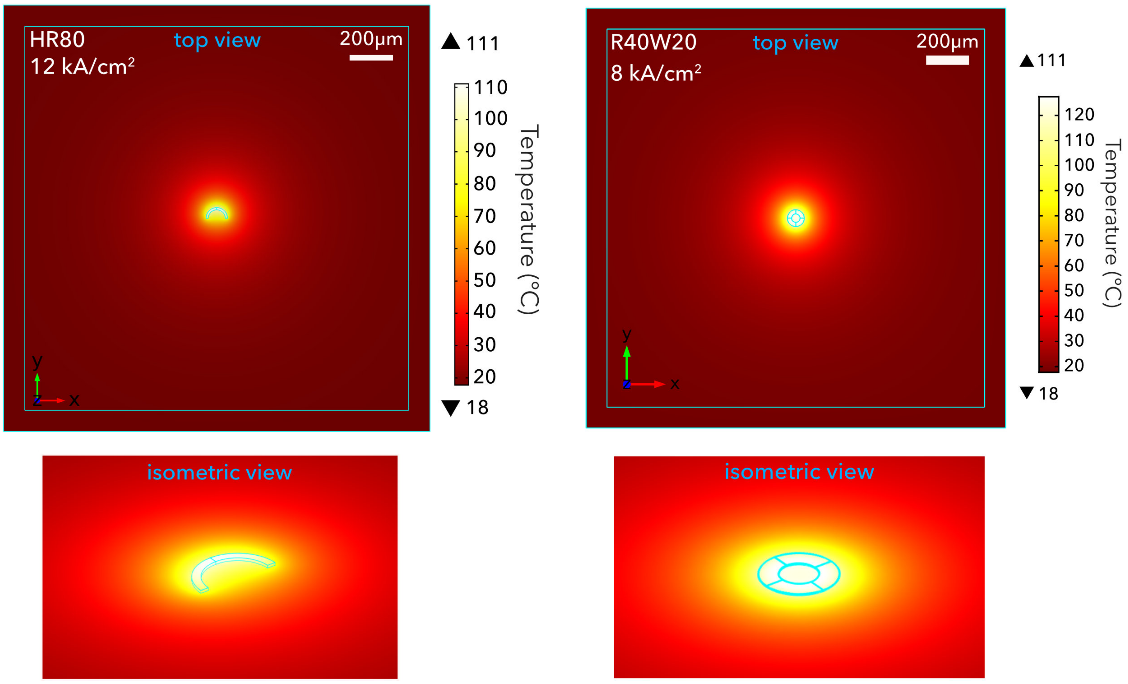

(a) (b)

Figure 4.15: 3D simulation thermal modelling for (a) HR80 ad (b) R40W20 devices, respectively. The images below show oblique views of the simulations, in close up.

4.4.2 Performance of ring-shaped micro-LEDs

As, in this study, the number of pixels is twenty, the following analysis is mostly focused on the `R60` rings and half–rings. The `R60` rings have fixed diameter and three variation of wall width, whereas the half-rings have fixed wall width and five respective diameters.

I–V, L–I, & L–V characteristics

Figure 4.16 presents (a) the I–V and (b) the L–I characteristics for the `R60` rings and the various half–rings, (c) are the L–V curves for the half–rings only. The devices on the graphs are listed by increasing active area. As the area increases the series resistance decreases, see table 4.2 for numerical values. Similarly, the optical power increases with the increase of active area. The trend saturates for larger areas of each device type, meaning that the step increase in active area does not lead to a step increase in optical power. The L–I curves normalised to the active area are plotted in the inset of figure 4.16 (b). Current density is a determinant for the optical power density performance in the optimum working range, up to 80% of the roll–over point. This is independent of the pixel size or active area. This particular aspect is a direct indication of thermally limited performance as previously introduced in section 2.7. The rest of the rings present similar I–V and L–I trends, the ones with larger wall width (larger active area) showing lower resistance and higher optical power.

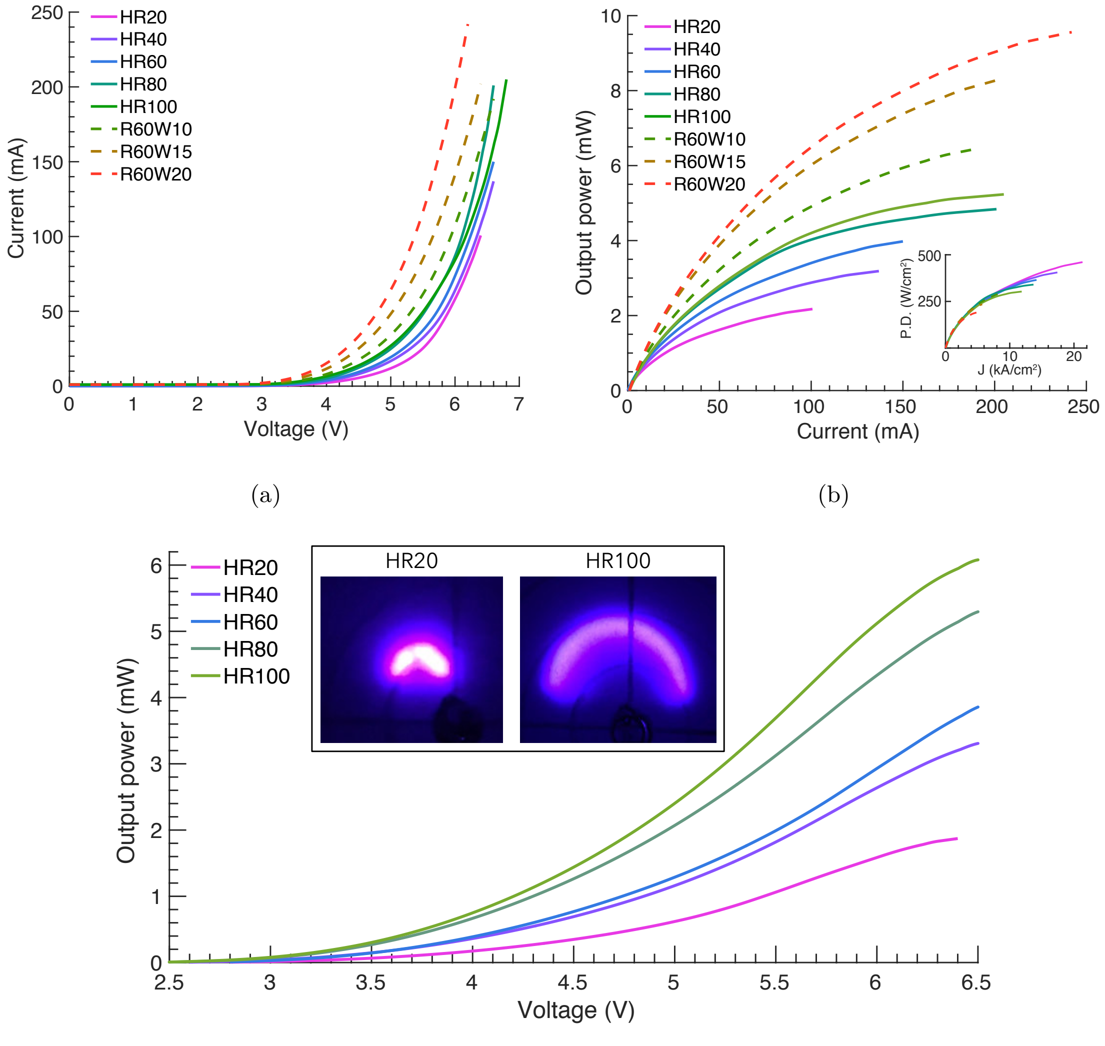

(a) (b)

(c)

Figure 4.16: In (a) the I–V and (b) the L–I curves of the `R60` rings and half–rings micro–LEDs measured up to the roll–over points. In (c) is presented the L–V curve for half–rings only. The inset in (b) corresponds to optical power density P.D. (W/cm^2) as a function of current density J (kA/cm^2). The inset in (c) is a projection of the emission for `HR20` and `HR100` at 26 mA and 50 mA, respectively.

The L–V curves are shown in figure 4.16 (c) for the half–rings only. Note that L–V curves for these devices present higher linearity than for the segmented devices, which were shown in figure 4.10 (b). In a communications context this allows to reduce distortions of the transfer function and potentially increase the SNR thus, increasing in data rate or reducing errors. More details will be provided in chapter 5. The insets in (c) show two photographs of the frontal projection on white paper for `HR20` and `HR100` measured at 26 mA and 50 mA, respectively. These currents are chosen to match a T_j of $50°C$ via figure 4.18, assuring thermal effects are negligible. In both devices there are no obvious brightness differences within the pixel area, indicating a low degree of current crowding. Differences between the photographs are due to acquisition conditions such as the focus points and shutter time.

Figure 4.17 (a) presents the optical power performance as function of the active area for all the rings and half–rings, showing maximum values only. This follows an inverse quadratic increase as expected from the decrease in efficiency as the total active area increases. Some rings at similar active area show up to 40% more optical power than others. This is attributed to the ratio between absolute size and wall width proving beneficial when it minimises the heat accumulation. One important metric to understand this phenomena is the ratio between the active area and total perimeter (A/P) [45, 131], shown in figure 4.17 (b). Increasing the total perimeter for the same active area (reducing A/P) increases the edge that dissipates heat through the material resulting in benefits in optical power. The curved trend seen for the half–rings pixels is due to a 20 μm section of perimeter at the bottom of the pixel that is constant with the increase in size.

Table 4.2 summarises the basic parameters of the ring and half–ring micro-LEDs. Current density and optical power density are included for the maximum measured values. These are at very high values given the active areas $> 400\ \mu m^2$. In this single pixel measurement, HR20 achieved $\sim 21kA/cm^2$ producing >2 mW of optical power compared to previous art of $\sim 20kA/cm^2$ producing 0.25 mW with $\varnothing 14\,\mu m$ (154 μm^2) pixel [45].

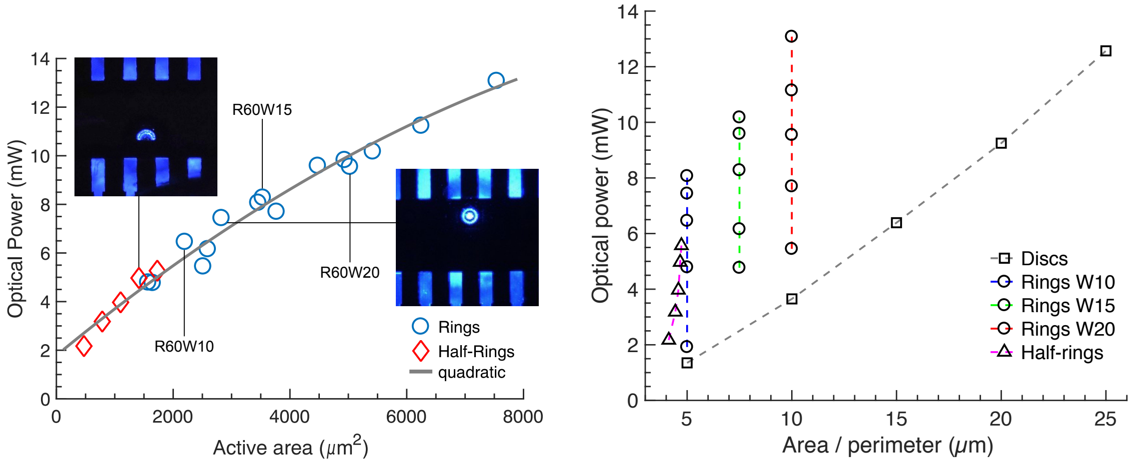

(a) (b)

Figure 4.17: In (a) the optical power for all the rings and half–rings is shown with increasing active area. The photographs are `HR80` and `R80W10` as seen from the top of the chip. In (b) the area to the sidewall perimeter ratio is shown. Please note that the optical power presented corresponds to the maximum measured, and in most cases is not at the roll–over point.

Table 4.2: List of electrical and optical properties of the `R60` rings and half–rings, showing maximum measured values. The nomenclature P.D. corresponds to optical power density, J to current density and A/P to the active area/perimeter ratio.

Pixel	Active area (μm^2)	Rs (Ω)	J (kA/cm^2)	P.D. (W/cm^2)	A/P (μm)
HR20	472	9.93	21.33	460	4.12
HR40	786	7.95	17.42	405	4.43
HR60	1100	7.01	14.21	361	4.58
HR80	1414	7.56	13.64	342	4.67
HR100	1728	6.84	11.86	302	4.72
R60W10	2199	6.15	8.73	294	5.00
R60W15	3534	6.06	5.71	234	7.49
R60W20	5027	4.54	8.81	190	9.99

These pixels present a R_s slightly higher than typical disc-shaped pixels present on the same chip, see figure 2.11 and table 2.1. This is attributed to the increase in the edge perimeter for the same active area. This region is slightly degraded due to the pillar etching generating a highly resistive region. Pixel-to-pixel variation due to fabrication also influences R_s, as seen in the case of HR80.

Thermal imaging

The ring and half–ring devices were characterised in terms of their thermal performance via infra–red imaging, following the procedure presented in section 2.7.3. Figure 4.18 (a) presents the T_j with increasing current for the rings `R60` and half–rings. These devices show a quadratic increase in T_j with the increasing current, a typical effect due to efficiency droop at higher currents [88]. As the pixels increase in active area, the T_j decreases for the same injection current, providing additional capability to handle higher currents. The rings show a clear decrease in T_j with the increase in wall width from `R60W10` to `R60W15`, a 60 % increase in active area. The gap in T_j between these increases linearly for higher currents, an indication of a combined reduced mutual heating provided by the shape with the higher current capability of a larger active area pixel. From `R60W15` to `R60W20`, although the active area increases by 70 %, the reduction in T_j is not as significant. This means that for same heat power generated, this geometry does not provide significant benefits above `W15`, the difference seen being due to a larger active area. These differences are also reflected in optical power due to efficiency; in figure 4.17 (a), `R60W10` and `R60W15` are above the curve, whereas `R60W20` is below the curve. The half-rings scale up in active area with the diameter, with a thin wall width of 10 μm. These present a consistent decrease in T_j at the same injection current. In addition, the gap between adjacent curves increases with the increase in injection current, an indication of a reduced mutual heating for increases in heat generation. This is mainly due the geometry providing simultaneously an increase in active area and spacing for heat dissipation. The T_j curve for `HR100` sits very close to `HR80`, which is unexpected. As a result the optical power does not scale up with its active area as seen in figure 4.17 (a). This is believed to be due to a fabrication issue, possibly a high resistance p–contact generating extra heat at the interface.

In order to validate the initial thermal model predictions, a comparison between the predicted and measure T_j is presented in figure 4.18 (b). The data used is from figure 4.15 and thermal imaging for the pixels `HR80` and `R40W20`. The curves show a good agreement confirming two aspects: good fabrication quality and that the assumptions and simplifications used for the thermal model are correct.

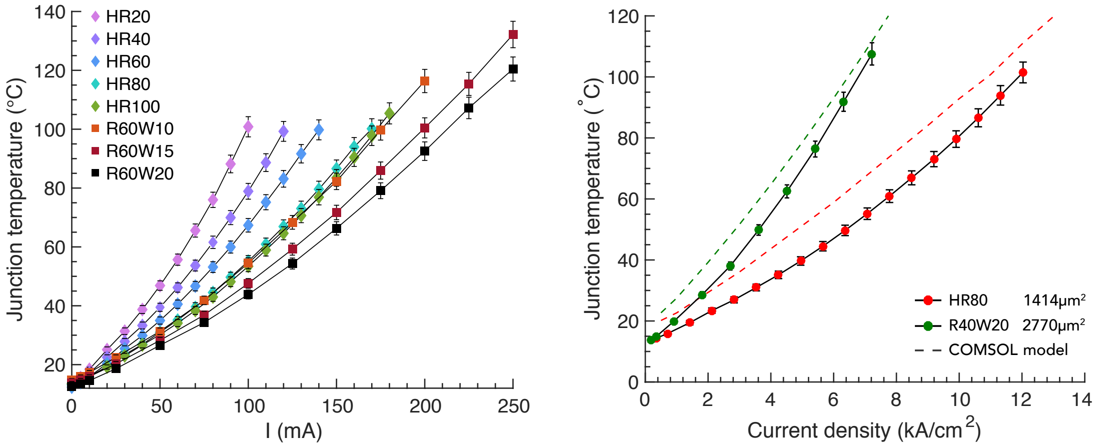

(a) (b)

Figure 4.18: Thermal performance of R60 rings and half–rings. In (a) we show T_j with injection current and in (b) the comparison between the thermal model and final device measurement of T_j.

The T_j assumed in the thermal model is the highest temperature of a pixel at the GaN interface. In addition, the model assumes a linear scale of heat power with reference to the heat power from a previous device at mid injection current. As such, T_j on the model scales linearly as it is not corrected for changes of efficiency due to the efficiency droop. Moreover, the reference heat power is for a traditional disc–shaped pixel which does not benefit from improved heat dissipation, thus the model slightly overestimates T_j. Figure 4.19 presents the thermal images of the pixels in figure 4.18 (b) at the highest measured current density. Here, `R40W20` presents the highest temperature at the centre, confirming the prediction from the thermal model in figure 4.15. That is, the ring geometry is able to shift the mutual heating from being on the active area to being on an empty area, creating a temperature gradient that does not affect the pixel directly. In the case of `HR80` there is no clear hotspot, heat dissipation is even and temperature gradients are lower that in the case of `R40W20`.

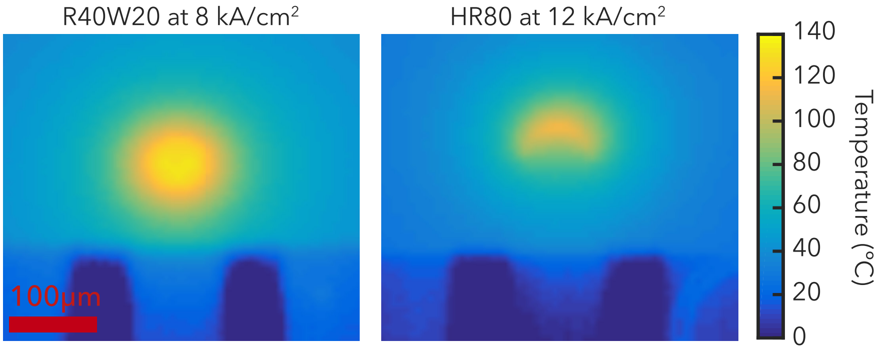

Figure 4.19: Thermal imaging comparing the dissipation capability between a ring (R40W20) and a half–ring (HR80) at high current density. Please note that the temperature is only corrected for the reference emissivity at the pixel area.

Emission spectra

The spectral response of these devices is presented in figure 4.20 in terms of λ_{peak} and FWHM under DC conditions. The peak emission in (a) shows with increasing current a blue–shift followed by a red–shift typical of micro–LEDs, as was shown in section 2.6. The increase in active area reduces the range of these shifts, allowing a more controlled colour rendering capability. The inflection point from blue–shift to red–shift increases with the active area from 30 mA to 100 mA for the half–rings and 70 mA to 110 mA for the rings presented on the graph. These inflection points match a similar T_j, indicating a thermal dependence. The increase in active area leads to decrease in the thermal shift which, given the geometry of the pixels, is an indication of a more efficient heat dissipation as the active area is spread over a larger die area. This aspect is observed by a narrower emission from the larger pixels in figure 4.20 (b). Taking into account the ramp up of T_j and spectral shift, the thermal broadening is assumed dominant at high currents, i.e. the linear region of the FWHM graph. As such, the slope of a linear fit on this region is empirically associated with the thermal broadening. The inset in figure 4.20 (b) presents the slope extracted from the fit with the active area of each pixel. In the case of the half–rings, the increase in active area is due to a larger diameter, thus allowing spacing of hot zones further apart which results in a sharp decrease in the thermal broadening effect. In the case of the `R60` rings, the diameter is fixed and the increase in active area is due to the wall width. The thermal broadening effect is surprisingly reduced. This is an indication of very low current crowding of these devices, capable of a even current density distribution across the pixel.

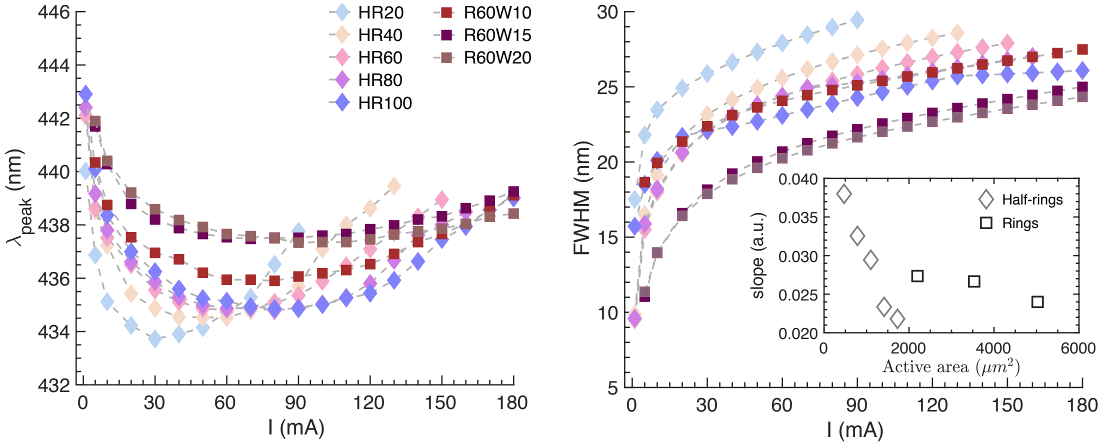

(a) (b)

Figure 4.20: Spectral characteristics of under DC conditions for `R60` rings and half–rings, (a) peak emission and (b) FWHM, where the legend is shared for both graphs. The inset in (b) presents the FWHM slope variation with increasing active area taken by fitting the linear region of the FWHM at high currents.

Modulation bandwidth

Studying of the frequency response of the ring devices is performed as was described in section 3.1. The modulation bandwidth is inversely dependent on the differential carrier recombination time, meaning, it increases as the differential carrier recombination time decreases. The differential carrier recombination time is dependent on the current density and therefore decreases as the average current density through the junction increases [109, 46]. This occurs only when the recombination time constant due to parasitic capacitance is smaller than the carrier recombination time [109]. The intrinsic electrical capacitance using a parallel plate approximation is estimated to be 4.42 pF for `R100W20`, the largest pixel of the whole set, with a cutoff frequency of $f_c \approx 8$ GHz, implying significantly higher modulation speeds than the achievable with earlier micro-LEDs geometries.

Micro–LEDs typically show a trend for bandwidth to decrease (increase) with the increase (decrease) in size or active area [131]. Up to this point this the case for all micro–LEDs presented in this thesis. Figure 4.21 (a) presents the highest measured bandwidth as function of the active area for all the ring and half–ring devices. The ring pixels show a typical bandwidth decrease with the increase in active area. This is relatively linear, in line with a previous report by Green et al. [131]. The small differences in bandwidth are attributed to thermal performance of each pixel configuration enabling higher or lower current density, and measurement conditions also contribute. The half–ring pixels show the opposite effect with the maximum bandwidth increasing with the increase in active area. This effect is very linear up to `HR80`, saturating for `HR100`, active area $> 1500\,\mu m^2$. In order to explore this new aspect, a detailed view of the bandwidth as a function of current density for `R60` and half–rings is presented in figure 4.21 (b).

The bandwidth curves for `R60` line up for the three pixels, meaning that at the same current density each pixel presents identical bandwidth, which is seen for all the ring pixels. This consistent behaviour of the bandwidth scaling with current density is believed to be the main driver for the recombination time and is a sign of good fabrication quality, as reported in previous work [46]. However, in the case of the half-rings at the same current density, larger pixels present higher bandwidth. This is an intriguing phenomenon which led to multiple repeated measurements on the bare die, the bare die with a substrate thermal tape acting as a heatsink and measurements with the die wire–bonded to a PCB. Although the measurements conditions were changed, the trend was always consistent even with device ageing, and only small differences in absolute measured values were observed.

At a respective current density of $6.4kA/cm^2$, the half–rings show bandwidths with differences that are consistent and higher than the typical pixel–to–pixel variation. This is evident in the frequency response at 6.4 kA/cm^2 as presented in figure 4.22. The frequency at the bandwidth point is higher for larger devices with a slow decay for frequencies above the bandwidth point. A clear response is seen up to 1.5 GHz, just above the 1.4 GHz bandwidth of the detector. The curves are roughly parallel to each other showing a consistent behaviour at high modulation frequencies. In addition, the network analyser used for the measurement in figure 4.22 has a very low noise floor, typically at -80 dB. As such, it provides an insight into the maximum dynamic range these devices can provide, both in terms of optical signal and system bandwidth.

These results indicate that current density might not be the only factor determining bandwidth. The difference is attributed to the uniformity of heat distribution across the active area and a lower junction temperature. Other factors such as very thin pixels, and smaller ratio between the active area and sidewall perimeter may also contribute.

On this basis two intriguing questions emerge: how does bandwidth vary with T_j at a fixed current density, and how does bandwidth depend on current density for a fixed T_j? These issues can be addressed by interpolating thermal and frequency response data found in figures 4.18 and 4.21, selecting the points for each pixel that match a condition in junction temperature or current density and plotting against the respective degrees of freedom. The result is presented in figure 4.23 (a) for the first question and figure 4.23 (b) for the second question. At a current density of 6.4 kA/cm^2 the bandwidth increases from `HR20` to `HR100` as expected from figure 4.21 (b), an increase that systematically occurs at a higher T_j. This is not surprising as smaller pixels can sustain higher current densities than larger pixels. However, the difference between `HR20` and `HR100` for T_j is $\sim 27°C$ leading to an increase in bandwidth of 280 MHz (131 %). This trend is in line with the expected behaviour of semiconductors [132], but it is usually masked by other effects or limitations of the device. The implications of bandwidth increasing with temperature at the same current density are seen in the answer to the second question for bandwidth against current density at a fixed T_j presented in figure 4.23 (b).

Here `HR100` does not follow the trend of the remaining pixels as previously seen in figure 4.21. This is attributed to limitation of the design intended to keep low current crowding at large diameters, where the device might be larger than the current spreading length [133]. Considering the difference between the pixels `HR80` to `HR20`, an increase in current density of 7.46 kA/cm^2 leads to a decrease in bandwidth of 104 MHz at $Tj = 76°C$. In other words, at the same T_j the smaller pixel of set needs significantly higher current density to achieve a similar level of bandwidth, and thus short carrier lifetime. It represents a strong indication of more than one determining factor for bandwidth. Using a pixel design that reduces mutual heating, an electrode layout that significantly mitigates current crowding and pixel sizes below the current spreading length, these micro-LEDs are able to show high bandwidths at lower current densities than traditional pixel's shapes.

4.4.3 Summary

Micro-LEDs in ring and half–ring or semi–ring shapes have been designed to tackle issues with mutual heating, current crowding and current spreading length. Devices show optical power higher than equivalent area disc–shapped micro–LEDs. The junction temperature is also lower enabling stable operation at very high current densities. The electro–optical modulation bandwidths are very high for LEDs that produce optical powers at multi–milliwatt level. From the range of devices investigated, the half–rings stand out with bandwidths increasing with the active area. This observation puts in question the role of current density as the main driver to achieve higher bandwidth. The developed micro-LEDs prove that under certain conditions, bandwidth and current density can be decoupled. As the bandwidth is higher for larger pixels, it is effectively scaling up with optical power. This is very interesting property for VLC as it maximises the channel capacity by simultaneously increasing bandwidth and SNR, as introduced in section 3.2.3. Results applying these designs to VLC are presented in chapter 5.

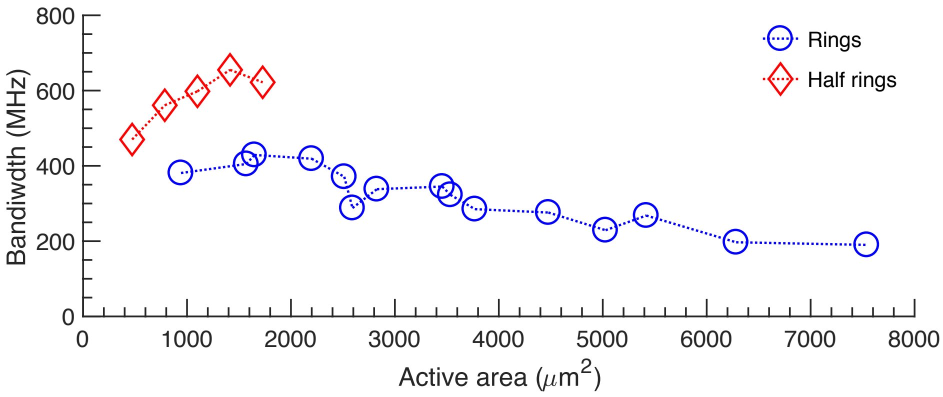

(a)

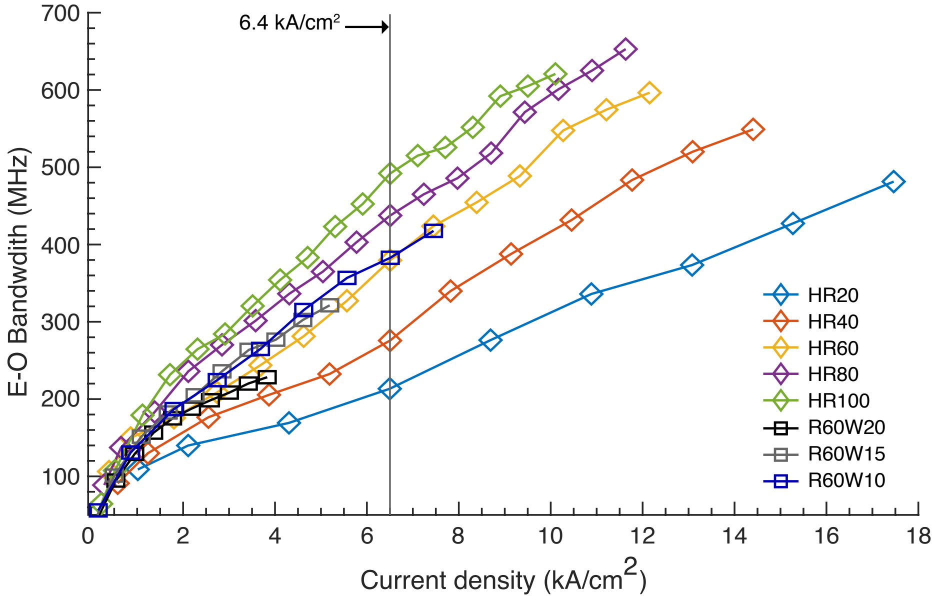

(b)

Figure 4.21: Modulation bandwidth for ring and half–ring devices. In (a) we show the maximum measured bandwidth for each pixel against the respective active area. In (b) the bandwidth as function of bias current for the half–ring and `R60` pixels is displayed.

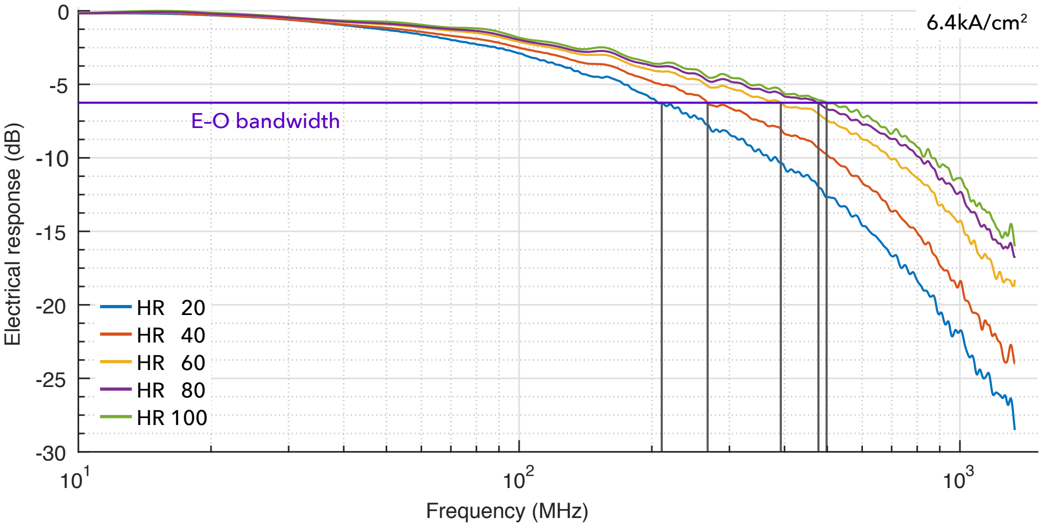

Figure 4.22: Small signal frequency response from 10–1500 MHz for the half–ring pixels at a DC bias of 6.4 kA/cm^2, corresponding to the marked line in figure 4.21 (b). The response is normalised to 0 dB for easy comparison.

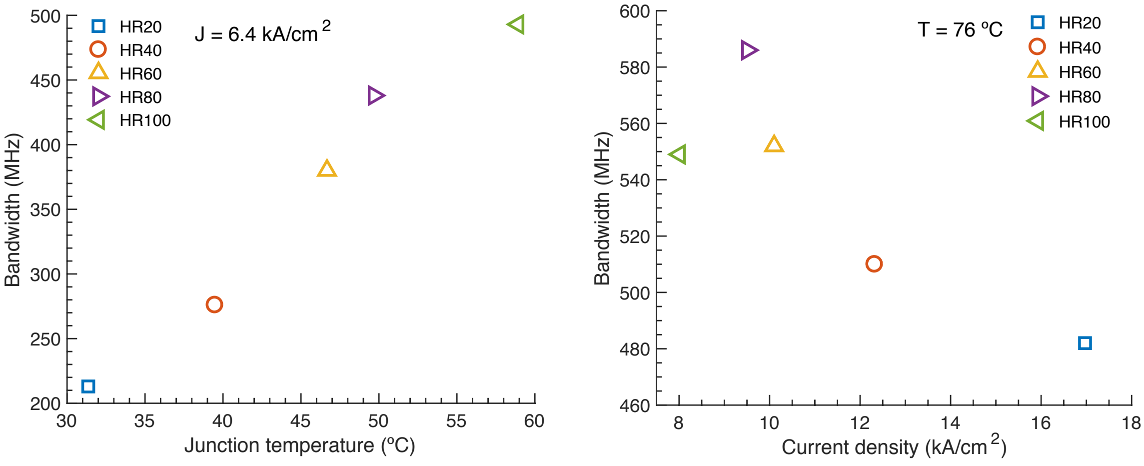

(a) (b)

Figure 4.23: Bandwidth dependence with T_j and current density for the half–rings using information from thermal imaging. In (a) we show the bandwidth as a function of T_j at a fixed current density of 6.4 kA/cm^2. In (b) the bandwidth as a function of current density at a fixed $Tj = 76°C$ is shown.

Chapter 5

Application in data transmission

This chapter presents experimental results from close collaboration with communications systems engineering research groups from the Universities of Cambridge, Edinburgh, Glasgow, Oxford and Strathclyde. Data transmission was in every case performed with the presence of the author to guarantee the most efficient use of transmitters, receivers and optics to achieve the highest possible data rates deliverable by the system. Here, we focus on results for the micro–LEDs with segmented and ring type design as presented in chapter 4, work which well represents the systems used for all other types of micro-LEDs devices as well. These results are obtained by probing the pixels straight on chip for the highest performance and with no heat–sink applied. In addition, the data and graphs shown are only for the best results obtained, results which, at the time of writing, represent the highest data rates known for LED–based VLC under their specific application. In order to present a clear view and distinguish the main differences between the two different applications and their inherent modulation schemes, this chapter merges work that has been done in various locations and with different groups. The names of the people involved in the various aspects of this work are acknowledged at the start of this thesis.

5.1 Guided–wave operation of micro–LEDs

The guided-wave investigations used polymer optical fibre (POF) and micro-LEDs modulated by pulsed amplitude modulation (PAM). The objective was to maximise the data rates for long lengths of fibre. Chromatic dispersion in the PMMA material of the fibre limits the system bandwidth at long distance, to about 250 MHz in 50 m long POF for 450 nm wavelength emitters. As such, the relevant figure of merit is the bandwidth–distance product for the system and bit rate–length product for the data transmission [134].

5.1.1 System setup

Figure 5.1 (a) presents the setup as used at the University of Cambridge for data transmission with POF using PAM modulation schemes. The system consists mainly of an emitter, the micro–LED, from which light is coupled in and out of a roll of POF (ESKA Mega step index) using off the shelf lenses, and an APD photo receiver (First Sensor AD500-11) to detect the output. An arbitrary waveform generator (AWG), Tektronix AWG70001A, generates the PAM signal which is amplified by an SHF 100AP amplifier to $2.5 - 3.5\,V_{pp}$ to feed the DC–biased micro–LED. The transmission medium is PMMA which has an absorption of ≈0.1 to 0.2 dB·m^{-1} [128] in the visible region. The facets where chosen to be cleaved but not polished, and this adds a measured coupling loss of ≈9 dB. At the working lengths presented here $1 - 25\,m$, the total optical power loss adds to $9.1 - 11.5$ dB. The long reach of POF and the low power nature of micro–LEDs require high sensitivity at the receiver side. As such, APD detectors were chosen and tested to provide higher system margin over the bandwidth of interest. The received signals captured on the oscilloscope and the digital signal processing (DSP) was done offline in Matlab^{TM}. This last step includes post-equalisation and decoding of the 16–PAM signal into a bit stream, and more details of this process are available in Li et al. [56].

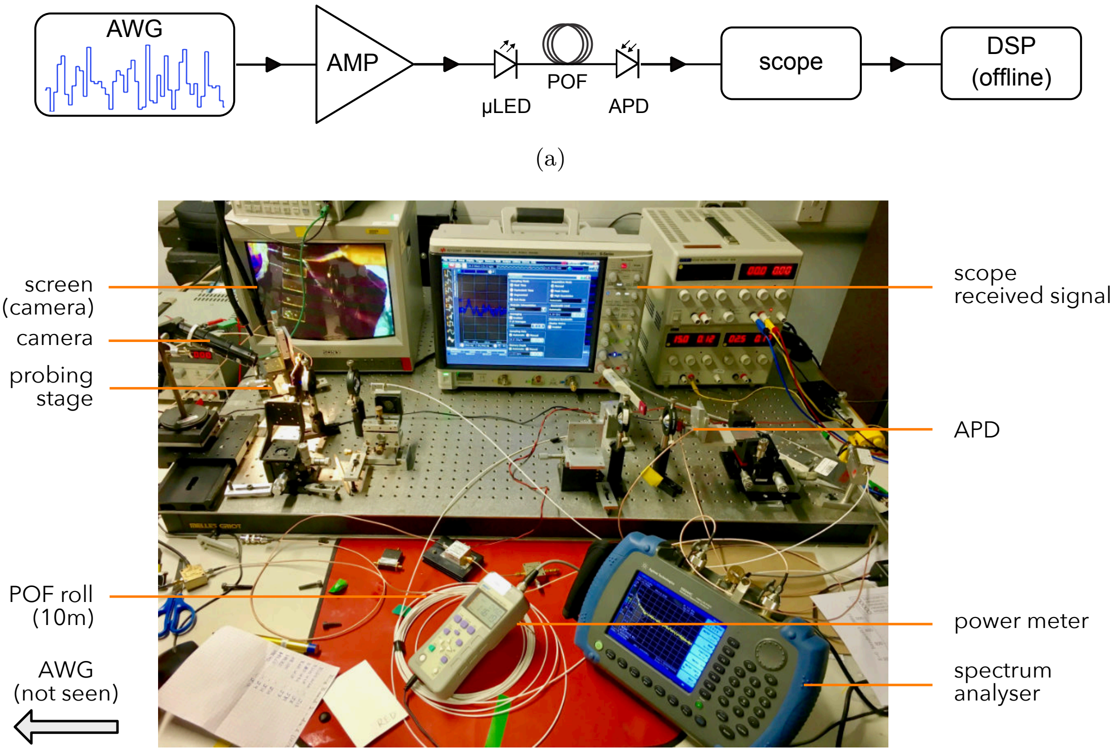

(a)

(b)

Figure 5.1: In (a) we show the setup for data transmission in POF using PAM modulation, where the micro–LED is DC-biased separately; in (b) a photograph of one experimental session at the University of Cambridge is shown.

5.1.2 Data transmission

Data transmission capability was tested with 4 to 32 levels (PAM–4 and PAM–32), in this thesis only the PAM–16 results are presented as these provide the best overall performance. Many configurations for POF reach, micro-LED DC–bias and modulation depth, APD gain voltage were tested. In the next two section are presented the best results only for the segmented LED A and half–ring HR100.

Segmented micro–LEDs

Segmented micro–LEDs present, to our best knowledge, the highest reported bandwidth of any LED fabricated with commercial epitaxial material [115]. LED A presents a bandwidth over 800 MHz and optical power up to 2.1 mW in a design that matches the geometry of POF for multi–pixel use and has achieved a coupling loss of 6 dB.

In figure 5.2 are presented the BER performance as a function of POF length for a PAM–16 signal running at data rates of 6 Gbps in (a) and 8 Gbps in (b). For short reach, i.e. 1–10 m, the BER is very low; in the case of 6 Gbps data rate at 1 m the BER goes below 10^{-14} (calculated offline) when the received optical power is maximised (not shown in the figure to keep the graph readable). This represents a probability to get one error every three thousand years! As the FEC limit for the BER is 3.8×10^{-3} as set by the IEEE standard, is was possible to increase the POF reach up to 25 m while maintaining the BER bellow the limit. Note that increasing the reach is not the same as decreasing the received the optical power. The POF material attenuates the signal and is intrinsically dispersive, distorting the waveform and thus limiting the maximum useful bandwidth. The results show very little difference in the maximum optical power received at any length. The reason for this is the maximum gain of the APD. Although there is significantly more optical power available, the saturation current for the APD does not allow one to use it. As such, the main differences in the BER obtained are due to the dispersive nature of the POF, with the exception of the case at 25 m where attenuation was significant. Note that the optical power shown here is a calibrated conversion for the measured gain current at the APD. This means it includes AC signal effects on top of the DC emission, which due to the non-linearity characteristic of the micro-LED, the real power may be slightly higher.

At 6 Gbps the link was limited in reach due to the lower power of the micro–LED. A test at 8 Gbps was executed under the same conditions by increasing the symbol rate to from 1.5 to 2.0 GBaud for a data rate of 8 Gbps, see figure 5.2 (b). At this rate, the BER for short reach went up about two orders of magnitude, clearly showing a bandwidth limitation. However, the received optical is similar to the previous case. Still, the BER does not have enough margin to increase the reach any further than 10 m.

In order to better understand the effect of length and bit rate, the received waveforms for a full frame are presented in figure 5.3 (a) and (b) at 6 Gbps and 8 Gbps, respectively. The decrease in peak response for longer reaches is very small. Instead, the smaller variations between close PAM levels become more indistinguishable. Note that these waveforms are a product of the whole system response. The case of 6 Gbps at 25 m is clearly a limitation

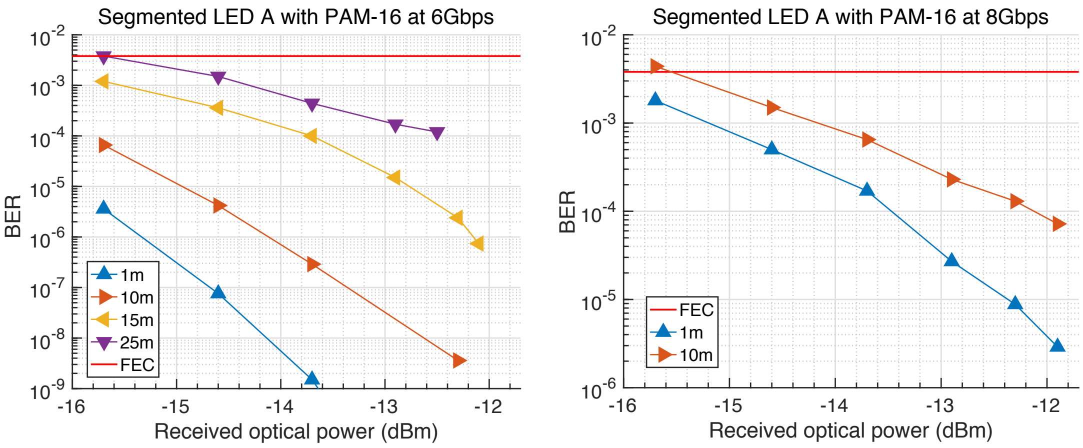

(a) (b)

Figure 5.2: BER performance with PAM-16 at various POF lengths at (a) 6 Gbps and (b) 8 Gbps. The received waveforms are shown in figure 5.3 (a) and (b) for 6 Gbps and 8 Gbps, respectively.

of POF bandwidth. When the PAM frame has a series of levels going up, the response seen is significantly higher than for isolated high levels. This is due to the micro–LED rise time being longer than the pulse duration. There are similar effects for series of low PAM levels due to the decay time of the micro–LED. DSP can corrects these effects, to certain degree, via equalisation [135]. At 8 Gbps the symbol rate is 33% higher and the waveforms show a weaker and rounded response to peak changes indicating a bandwidth limitation of the system. This is due to two separate factors: first, the APD E–E bandwidth is 650 MHz, whereas the micro–LED E–E bandwidth is 300 MHz at the bias point; secondly, at a symbol rate of 2 GBaud the system is running far above the bandwidth of both devices. A test of frequency response of the whole system showed it can be pushed to nearly 2 GHz under a penalty of dynamic range. This means that improvements in bandwidth of either the micro–LED or the APD would provide higher data rates at short reach. Such high data rates are not possible for long reach as the POF limits the bandwidth (250 MHz at 50 m).

Ring micro–LEDs

The ring and half–ring micro–LEDs have also been tested for data transmission in POF. `HR100` provides about 200 MHz less bandwidth than the segmented LED A but with 240 % higher optical power. `HR100` was chosen for these tests as PAM schemes rely heavily on large

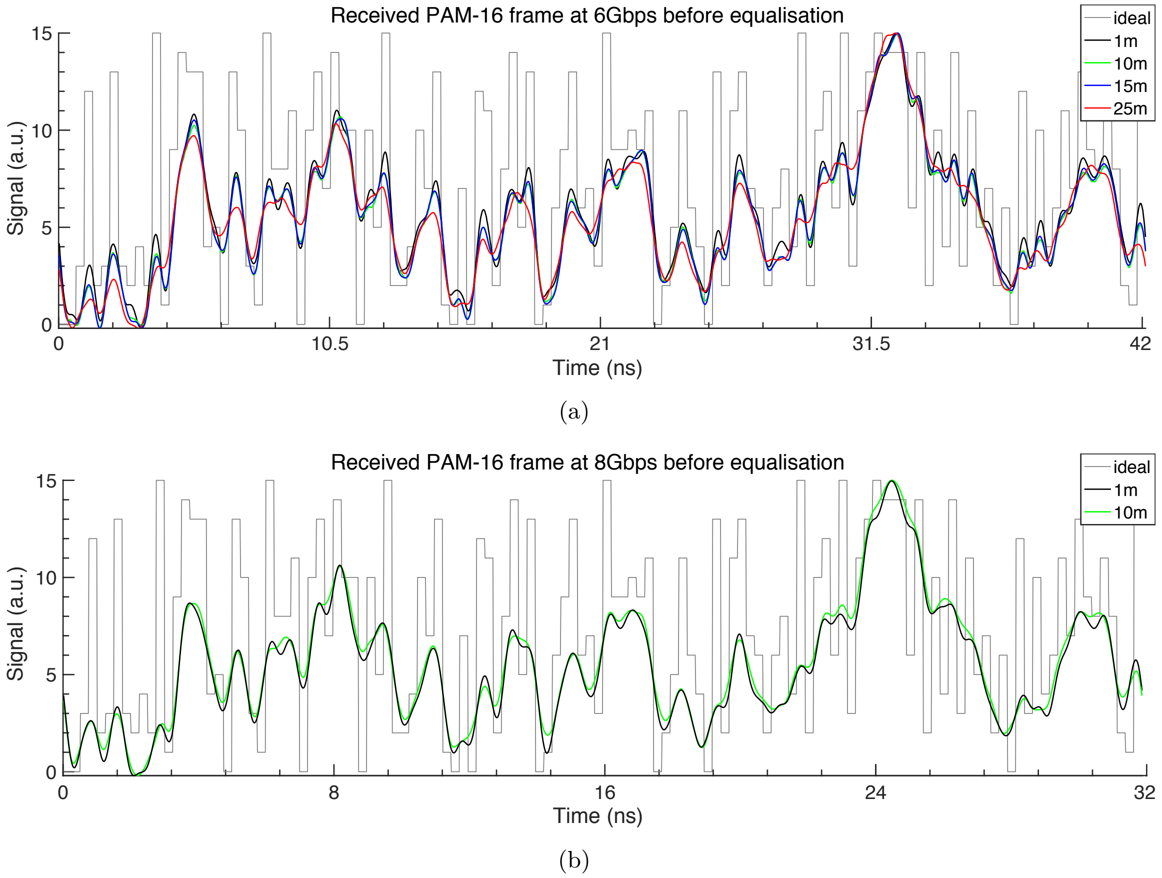

(a)

(b)

Figure 5.3: Received waveforms for PAM-16 at various POF lengths at (a) 6 Gbps and (b) 8 Gbps.

bandwidth to achieve high data rates. In addition, the geometry of this pixel is not optimised for optical coupling with POF and a coupling loss of 10 dB was observed.

Figure 5.4 (a) presents the bit rate test at short reach (without major penalties from the POF), showing that 6 Gbps is the highest achievable rate while maintaining a good quality link. Figure 5.4 (b) shows `HR100` at 6 Gbps maintaining good a quality link up to 10 m. These results are in line with those of the segmented LED A, with a 25 % decrease in bandwidth leading to a 25 % decrease in bit rate under the same conditions. The additional optical power of `HR100` versus the segmented LED A only provided marginal advantage in the link quality for POF lengths up to 25 m. In this is due to a lower optical coupling loss for the segmented micro-LEDs, the low POF attenuation at 450 nm of 0.18 dB·m^{-1} and to the high POF bandwidth at short reach, bandwidth-length product of 10 GHz·m, where the LED bandwidth is the dominating factor for performance [135, 136]. However, a test performed at 50 m reach (taking advantage of the high optical power) have shown a similar capability as a commercial 650 nm RC–LED (at 1.5 Gbps) in a previous report [50], although the APD sensitivity is lower at 450 nm is than at 650 nm. Although from the point of the device capability such a result is significant, from the perspective of fibre communications it does not add link capabilities.

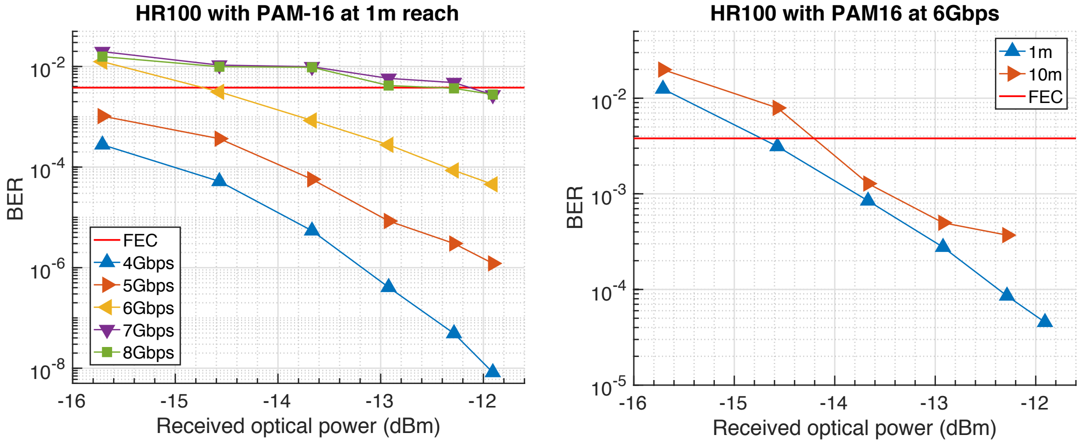

(a) (b)

Figure 5.4: BER performance for HR100 with PAM-16 at (a) 6 Gbps at various POF lengths and (b) at 1 m at various bit rates.

5.2 Free–space operation of micro–LEDs

The work presented in this section was executed in different locations, in laboratories at the Universities of Edinburgh, Glasgow and Oxford. Between the different laboratories there are slight setup differences regarding the optical assembly and electrical components that accomplish the same function without having any substantial influence on the results. In cases where the components do have an effect, it will be stated below.

The VLC applications over free–space are explored in this thesis at short distances up to 1 m with OFDM modulation schemes, with only one exception using PAM for result comparison. The objective is to maximise the data rates for variations in optical power, DC–bias and modulation depths V_{pp}. The characteristics of OFDM are such that bit rate scales up with both optical power and bandwidth available. This allows one to explore a range of micro–LEDs with a different balance of these characteristics. The figure of merit for OFDM schemes is the number of bits sent given the available bandwidth per unit of time (bit/Hz/s). We propose that, in an optical system, the figure of merit should also include a relationship with the optical power received, which is directly correlated to the SNR necessary to achieve high QAM levels.

5.2.1 System setup

Figure 5.5 (a) presents a schematic of the setup as used at the Universities of Edinburgh and Oxford for free-space data transmission using DCO–OFDM. The differences to the setup used for PAM (figure 5.1 (a)) are that the receiver is now a PD and the physical medium is now air. This has two significant implications. First, the PDs used have from 1 GHz to 1.4 GHz bandwidth with about two orders of magnitude less sensitivity and noise floor. Secondly, the free–space link does not suffer from the 6–9 dB of coupling loss, allowing significantly significantly larger AC–signals to pass through the system. In a free–space system transmitting in air, the absorption at visible wavelengths is negligible at close range (<5 m) as is required for systems being part, in principle, of the illumination infrastructure [137]. Each micro–LEDs was biased at a current that provides half of the optical power and then a $Vpp = 3.0 - 3.5\,V$ was applied to explore the full dynamic range of the L–V curve, see figure 4.16 (c) for an example.

Although many configurations for system components were tested, here we only present results where the system has a minimised or known influence on the obtained data rates. In other words, we wish to measure the capability of micro–LEDs, as opposed to a limitation in the system. During the course of many experiments, various limitations have been found that degrade OFDM performance such as the linearity of amplifiers, the bandwidth and sensitivity of the photo receivers, wire bounds from chip to PCB, and RF interference on the electronics.

5.2.2 Data transmission

Segmented micro–LEDs were tested at the University of Oxford for data transmission in free–space with DCO–OFDM. Ring micro–LEDs were initially tested at the University of

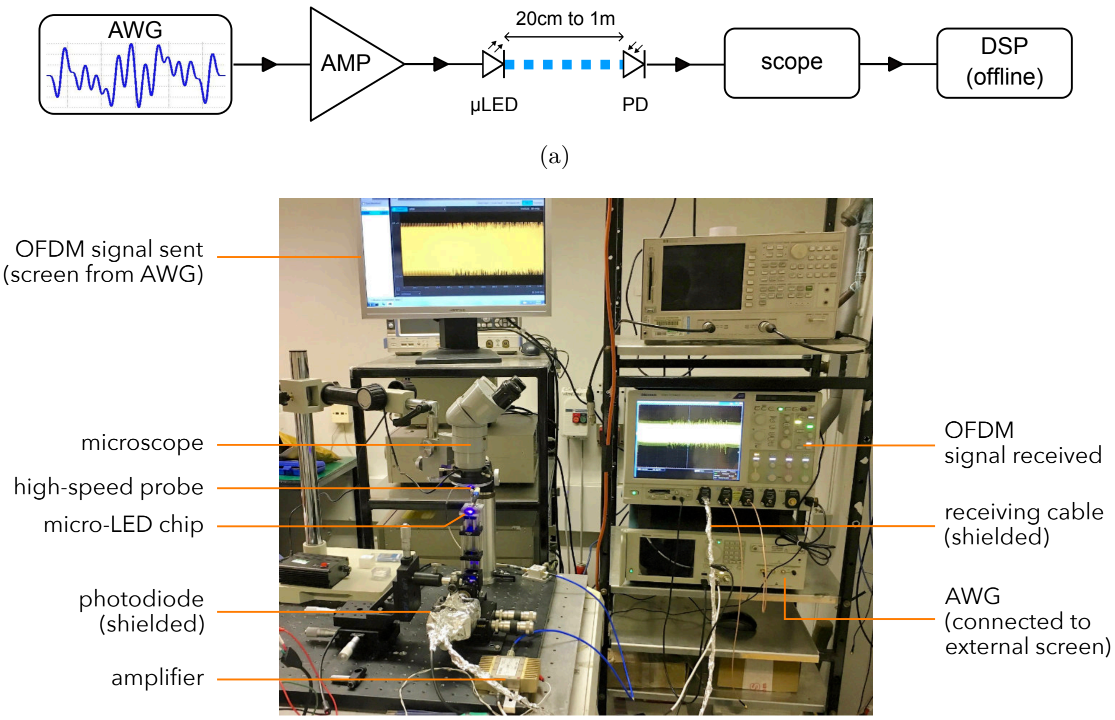

(a)

(b)

Figure 5.5: In (a) the setup for data transmission in free–space using OFDM modulation is shown, the micro–LED is DC-biased separately; in (b) is shown a photograph of one experimental session at the University of Glasgow, undertaken with colleagues from the University of Edinburgh.

Edinburgh. From this work problems were identified and solutions arranged for a second test at the University of Oxford. At a later stage a final test was made targeting the highest possible bit rates. This was done at University of Glasgow, involving colleagues from the University of Edinburgh.

Segmented micro–LEDs

Segmented micro–LEDs present what we believed to be the highest reported bandwidth of any GaN LED fabricated with commercial epitaxy material [115]. The high bandwidth comes at a cost of optical power, however. Although not an issue for PAM–based systems, in practice OFDM–based systems require a minimum SNR threshold to provide significant improvements over other PAM schemes. This threshold was barely achievable with the highest bandwidth LED A. In addition, at the time of testing at the University of Oxford, the chips were wire bonded onto a PCB which was later found to have significant parasitics in its frequency response (signal resonances). These issues were found to come from the length of metal between conductor interfaces, wire bounds and PCB tracks. The chip for LED B did not suffer from such parasitics, in part due to a more restricted bandwidth and in part due to smaller dimensions of the packaging to accommodate 8 pixels instead of 15 as in the case of LED A.

A PAM-L signal was generated using a pseudo-random bit sequence (PRBS) of $2^{14}-1$ and transmitted via the micro-LED. Due to the limited bandwidth of the micro-LED, an adaptive decision feedback equaliser (DFE) was adopted at the receiver. The data rate versus BER for a PAM-4 scheme is shown in Fig. 5.6 (a). The achievable data rate below the forward error correction (FEC) floor of 3.8×10^{-3} is ~3.8 Gbps, which corresponds to a net data rate of 3.5 Gbps, after applying a 7 % FEC overhead reduction. Higher order PAM schemes were also tested, however the data rates achieved were below this value.

The spectrally efficient DCO-OFDM scheme was also tested for the same link setup. DCO-OFDM signal generation and decoding is described in detail in [47], and we have adopted a similar approach. Fig. 5.6 (a) presents the data rate versus BER for DCO-OFDM and PAM-4 schemes, respectively.

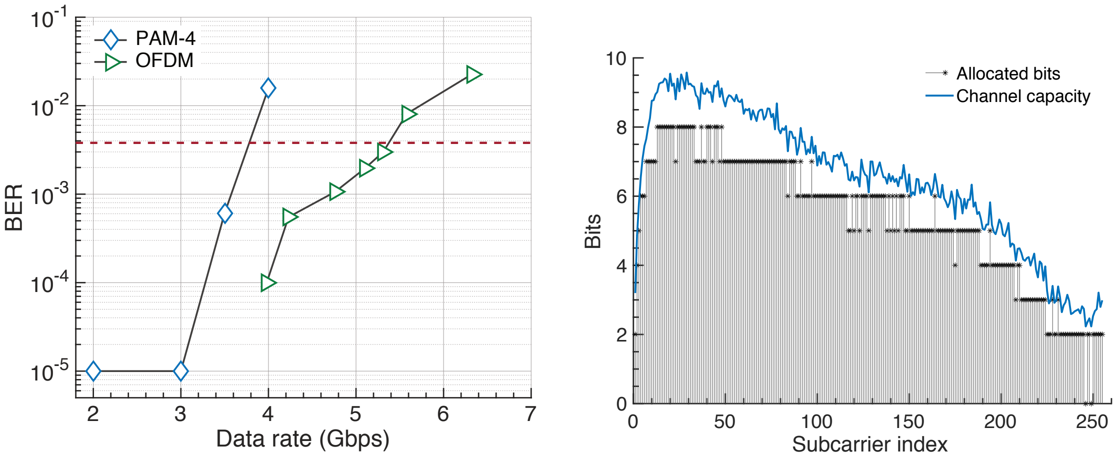

(a) (b)

Figure 5.6: In (a) we show the BER as function of the data rate for the segmented LED B in free-space with PAM-4 and DCO-OFDM. In (b) is the bit loading per subcarrier index for the OFDM signal at 5.5 Gbps.

Fig. 5.6 (b) presents the adaptive bit loading for the DCO-OFDM. A maximum data rate of 5.37 Gbps was achieved at a FEC limit of 3.8×10^{-3}. Also shown in the figure are the allocated bits for different subcarriers and the channel capacity. Taking into account the 7 % FEC overhead, the net bit rate is 5 Gbps. This compares to 3 Gbps over 5 cm reported in [47], and represents what we believe to be the fastest LED–based wireless link at blue wavelengths ($\sim$450 nm) [115]. As the system bandwidth is limited to 1 GHz, the micro–LED still has unexplored capacity above 1 GHz which in principle can increase the bit rates by an estimated maximum of 600 Mbps for an extra 300 MHz at 2 bit/Hz/s.

Half–ring micro–LEDs

In chapter 4, ring and half-ring micro–LEDs were presented as devices that achieve an improved balance between bandwidth and optical power. A linear approximation of the Shannon–Hartley capacity, as introduced in section 3.2.3, is presented in figure 5.7. In this metric, the ring-shaped pixels span a large range of active areas, showing a slight roll–over for active areas above 3000 μm^2. Nonetheless, their capability remains very high in comparison with half–rings and segmented pixels. This was confirmed with early OFDM tests where data rates were maintained at high levels. The pixel of `R60W15` achieved 3.40 Gbps in a system limited to 500 MHz and 5.37 Gbps in system with 1 GHz of bandwidth, see section 4.4 for details of this device. This case alone confirms that a better balance between bandwidth and optical power provides higher performance. The more interesting case is that of half–ring pixels. As presented in figures 4.17 and 4.21, the half–ring pixels achieved a bandwidth that increases with optical power. This characteristic places them at the top of the graph of bandwidth power product, the metric of interest for high bit rates. Segmented pixels A and B are included as a reference for the data rates presented below.

All the five half–ring devices were tested at Oxford University with the intent to confirm if the simultaneous increase of bandwidth and optical power results in higher bit rates. The results are presented in figure 5.8. The step increase in data rates shown by the blue bars in (a) is a very clear evidence that larger half–rings perform better with data rates easily crossing the 5.5 Gbps mark previous set by the segmented LEDs under the same test. In addition, the larger the pixel the more linear the L–V response, as shown in figure 4.16 (c), a

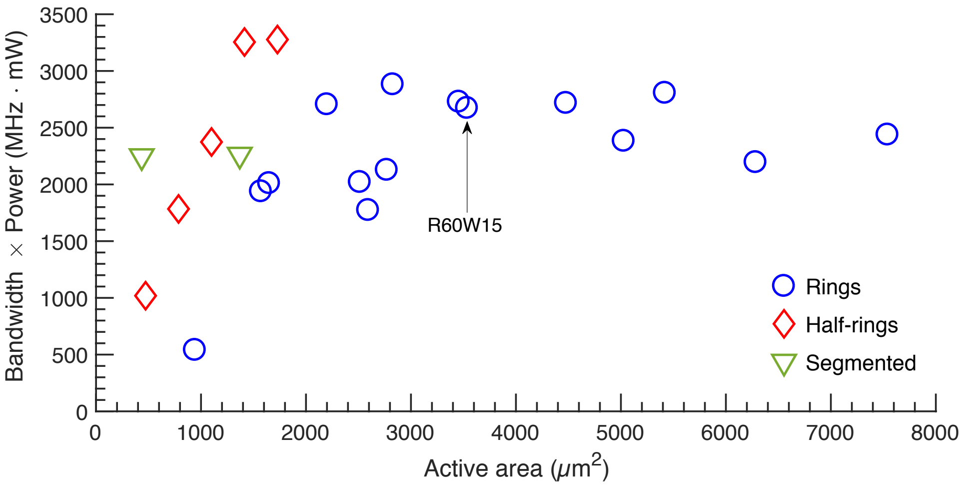

Figure 5.7: Data capacity for the ring and half–rings based on a linear approximation of the Shannon–Hartley theorem. Segmented devices are included for comparison.

property which benefits OFDM bit rates. These measurements were limited to 1 GHz system bandwidth by the amplifier and photodiode. During the tests it was clear by the high SNR at full bandwidth that we were not at the limit of the devices. This leads us to study the system decay above 1 GHz and a test at 1.33 GHz with `HR100` increased the data rate to 6.99 Gbps. Although, at this high frequency there is an SNR penalty, the test successfully proved that the half–ring devices keep very good performance levels at frequencies over two times their maximum bandwidth. Figure 5.8 (b) summarises the bit rates against the predictions from bandwidth power product, showing a linear correlation between the the two. The inset shows the bit loading and QAM–256 constellation for `HR100` at 1 GHz system bandwidth. The test at 1.33 GHz bandwidth is also shown in an attempt to use the 15 dB unused SNR from `HR100` at 1 GHz. Note that the data rate in this case does not align well with the other results, an indication that the true bit rate limit for the half–rings may be a parallel line in the graph at higher bit rates.

As the previous test did not fully explore the device capability, a new set of measurements were performed with the group of the University of Edinburgh using a 1.4 GHz (40% larger) bandwidth system in the laboratories of the University of Glasgow. The limit is now imposed by the photodiode (Femto HSA-X-S-1G4-SI), and a very linear 25 GHz bandwidth amplifier (SHF 100AP) was also used. A higher bandwidth receiver has a smaller active area, and thus,

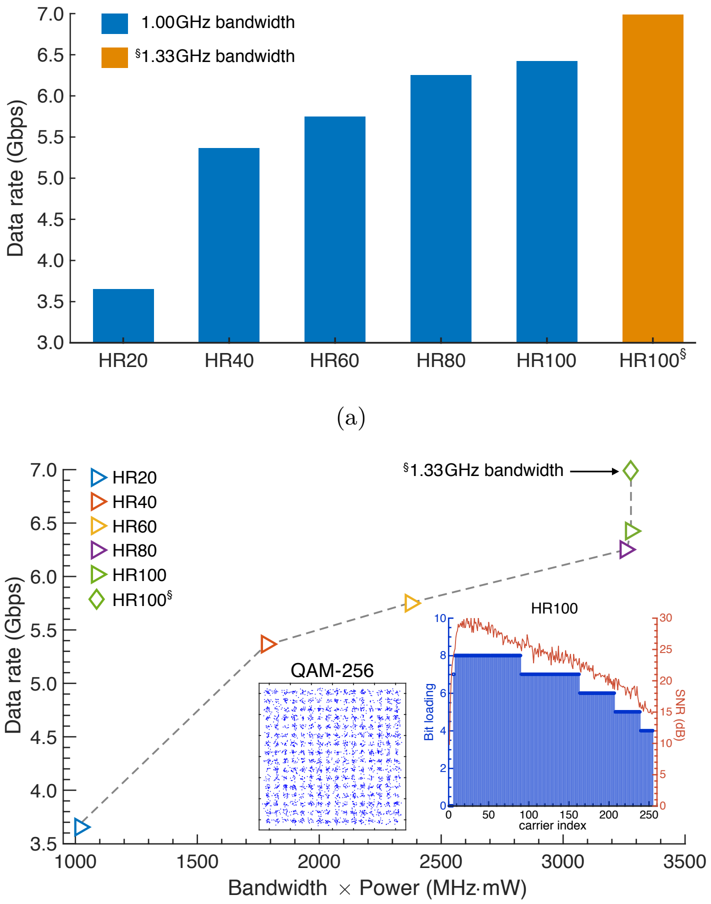

(a)

(b)

Figure 5.8: In (a) is the BER as function of the data rate for the segmented LED B in free-space with PAM-4 and DCO-OFDM. In (b) is the bit loading per subcarrier index for the OFDM signal at 5.5 Gbps. All the results are for BER below the FEC limit of 3.8×10^{-3}, the highest BER was 3.8×10^{-3} at 6.99 GHz for `HR100` at 1.33 GHz system bandwidth.

lower collection area resulting in a measured SNR penalty of 2–4 dB. Device degradation due to heavy use with large AC signals may also contribute. A photograph of this system is shown in figure 5.5 (b), where the photodetector and receiving cable were shielded with kitchen aluminium foil in an attempt to reduce RF interference from mobile networks.

The focus was then is now to use `HR100`, as it is the pixel with the highest capability, to set a bit rate benchmark for LED–based communication systems in free–space. In this test we have experienced high noise from the detector, the cause of which is not yet known. In addition, RF interference was significant – it was easy to spot signals from the 800 MHz and 900 MHz 4G LTE bands on the oscilloscope. For this reason we measured the bit rate performance using 64 waveform averages in addition to the typical case. Averaging allows to significantly reduce the random noise from the instruments and increasing the SNR. A reduction in RF interference (the RF signal were not random) permitted a reduction in the non-linearity of the our signal. Figure 5.9 (a) presents the BER agains data rate. The bit rates obtained below within the FEC limit are up to 6.5 Gbps without averaging and up to 9 Gbps with averaging. The result with averaging is still not completely inference free, but it is closer to the true maximum performance of the micro–LED. The result without averaging is about the same bit rate as achieved in Oxford, although through a different route, i.e. less SNR but larger bandwidth.

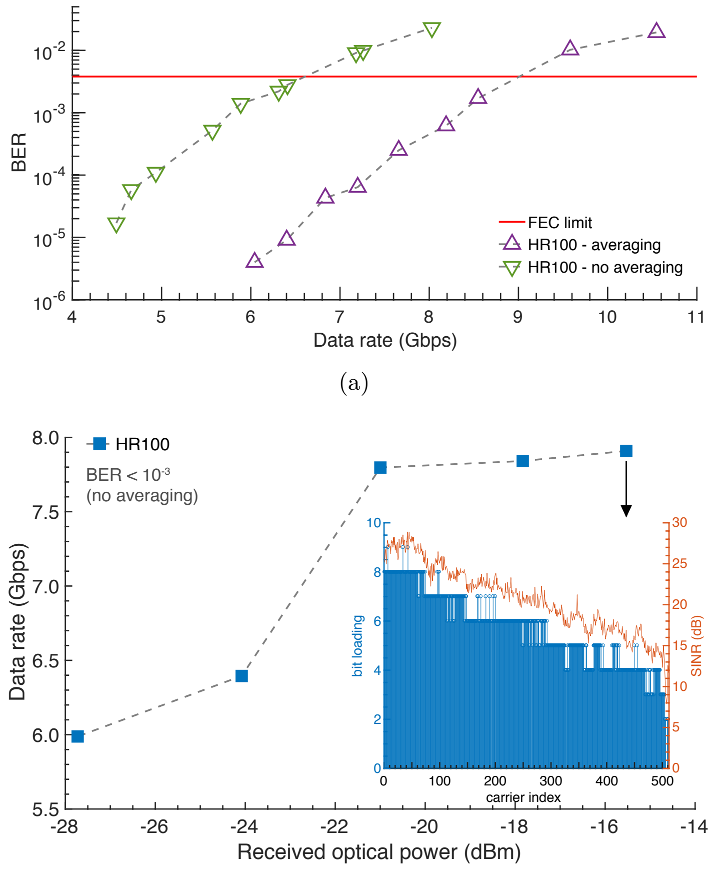

(a)

(b)

Figure 5.9: In (a) is the BER as function of the data rate for `HR100` in free-space with DCO-OFDM at a system bandwidth of 1.4 GHz. Measurements were executed with and without averaging to observe the noise and interference impact on the results. In (b) is a separate measurement of the data rate against received optical power using neutral density attenuation. The inset shows the bit loading and SINR at 7.9 Gbps.

A separate measurement of bit rate performance with decreasing optical power at the receiver is presented in figure 5.9 (b) without averaging. The highest measured bit rate was 7.9 Gbps, and the bit loading and SINR (accounting for interference) is shown in the inset. The SINR curve achieves a maximum of 27 dB, 2 dB lower than the test at Oxford, and presents a sharp cutoff at 1.4GHz due to the detector bandwidth.

From figure 5.9 (b) on can see that the bit rate degradation is marginal up to a 7 dBm reduction in optical power. Below this point the maximum modulation order (at low frequency) drops from QAM–256 to QAM–128. At 13 dBm reduction, optical power of -18 dBm or 16 μW, the bit rate decreases to 5.98 Gbps. This demonstrates that at low optical power, a very high performance capability is possible for a system with large bandwidth. In a realistic free-space scenario, the received optical power is below $\sim$ 100 μW, the result above proves that large bandwidth photonic devices provide high speed communication links even at very low received optical power.

These results are an improvement over the tests done at Oxford, being about 1 Gbps or 15 % higher, although this is below our initial expectations. The reason is a combination of three factors: excessive noise from the detector; unexpected RF interference in the system; and micro–LED degradation leading to slightly lower optical power and weaker frequency response.

5.3 Summary

In this chapter we presented typical communication systems and setups for VLC targeting high performance. The devices studied were the segmented and half–ring micro–LEDs, achieving a record 8 Gbps with PAM–16 in guided-wave and 7.9 Gbps with OFDM in free-space, respectively. To our knowledge, at the time of writing, these represent the highest data rates known in the VLC field using GaN LEDs. The highest bandwidth micro–LED used is the segmented LED A, although in a different system and modulation scheme, `HR100`, even with less bandwidth, is able to match the same level of performance by proving significantly higher optical power. The particular case of the half–ring micro–LEDs present a new effect of bandwidth increasing with optical power. The benefits for data transmission with OFDM were confirmed with bit rates that increase linearly with the bandwidth power product. This simple metric for data capacity based on raw device performance demonstrated a close relationship with measured bit rates. The performance of these pixels was demonstrated for low power as well, providing an overall advantage versus traditional square or circular shaped micro–LEDs.

At the time of writing, we have published: for POF systems 8 Gbps using segmented micro–LEDs at 450 nm with PAM-16 [135]; for free-space systems with OFDM, 5 Gbps using 450 nm segmented micro–LEDs [115] and 7.9 Gbps at 400 nm using segmented micro–LEDs [138].

Chapter 6

Conclusion

We conclude this thesis with an overview of the key findings followed by suggestions for future directions of research building on this work.

6.1 Summary of key findings

The approach taken to extend micro–LED performance to a higher level was to look first at the specifics of the VLC applications and then to understand the main device drivers which influence them. The two key limitations from micro–LEDs we identified relevant to VLC applications are current crowding and junction temperature. Our investigations of these problems opened up routes to higher optical power and higher bandwidth.

We presented two novel techniques: spatial–resolved bandwidth to tackle current crowding, and thermal imaging to tackle junction temperature. The solution to key problems lies on a good understanding of LEDs properties and dynamics at high temperature. One such problem is the dependancy of electrical resistance with DC–bias plus AC–signal to find the ideal driving conditions for data communications. As the DC–bias creates an increase in junction temperature, the electrical resistance decreases. An AC–signal is voltage driven and strongly depends on resistance of the device, non-linearities, clipping and degradation might quickly occur that were not accounted for. Another unexpected problem is the metal thickness for the back reflector and p–track in the flip-chip format. A thicker metal layer reduces electrical resistance and the change for device failure at the pillar sidewall. At the same time it decreases the chance for proper thermal annealing, consequently, electrical properties are voltage dependent. Higher temperature and prolonged annealing can solve the electrical problem at the expense of pixel performance. Such problems were carefully studied during the corse of fabrication and characterisation of many micro–LEDs. The solution I have found was to completely redesign the pixels in such a way that would mitigate the current crowding and reduce mutual heating. This lead me to study specific designs that would at the same time route the electrical current evenly across the pixel by minimising lower resistance points, and allow lower overlap of heat dissipation paths. This was studied in detail using broad area LEDs as they are easier to measure with the referred techniques. This was also based on the assuming that major benefits seen in these would also be true for micro–LEDs. It was found a complex relationship between current crowding and junction temperature, both affecting properties such as the emission spectrum in ways that not yet clearly understood.

New micro–LED designs were developed to implement and improve the learnings at small scale, targeting high performance VLC. Segmented pixels were specifically designed to mach the fibre geometry and generate discrete PAM signals. Such application was never implemented by systems engineers, instead effort was devoted into single pixel links. These pixels demonstrated the highest bandwidth for LEDs the excess of 800 MHz. In addition, segmented pixel also demonstrated the highest reported LED–based POF links at visible wavelengths with bitrates up to 8 Gbps. At free-space, segmented pixels easily crossed the 5 Gbps mark with OFDM being the highest reported link in the field.

A second generation of micro–LED designs target a better balance between optical power and modulation bandwidth. Old ideas of micro–rings were further developed into a coherent set of 20 ring–shaped pixels for mid power and mid bandwidth. This allowed to explore thermal management advantages of certain ratios of sizes and active areas, as well as their impacts on device performance. In addition, a small version of ring pixels was developed as half–ring pixels. This was to achieve smaller active areas with the minimum disruption to the fabrication process. Such pixels have demonstrated, to the best of my knowledge, modulation bandwidths increasing with the increase in active area, and as a consequence optical power.

Thermal properties were carefully studied and linked with modulation bandwidth. The dynamics of these devices are not well understood and the answers may lie a few layers down in the impacts of current crowding and junction temperature in MQWs at high temperature (>300K). Still, such unusual properties enable greater data capacities for VLC. Bitrates were obtained with a consistency that proves the design as a better tradeoff for optical communications. Results were in line predictions drawn the bandwidth power product, derived from a simplification of the Shannon–Hartley theorem. This metric is introduced as the simplest figure of merit for LED targeting VLC applications. A record high 6.9 Gbps and 7.9 Gbps free–space OFDM was obtained in separate occasions with a single half–ring micro–LED. The capability of these devices to withstand various measurements at peak (and over the peak) performance for long sessions is abnormal for micro–LEDs without heat–sink.

6.2 Future research

Here, we present some directions one could to improve on the work presented in this thesis. This is divided in two parts: the device level improvements and the application in optical communications. A view for the industry integration of VLC and LiFi products is also presented.

The study of device physics for micro–LEDs fabricated on commercial epitaxy is very challenging as the detailed structure is unknown. During the course of the PhD various attempts were made to study the device physics and other effects underpinning the new performance levels observed. These efforts depend on assumptions and informed guesses based on publication from other groups. As such, there is opportunity to understand the impacts that a micro-LED designed for high performance have on characteristics such as internal quantum efficiency and reliability. This could be achieved collaboration with research groups growing III–V materials, which could help to do a consistent study on the devices physics using well known epitaxial structures. In addition, this may open the possibility to investigate the benefits of semi-polar and non-polar substrates for the purposes of fast response, and possibly to further develop a better understanding of the recombination mechanisms, e.g. the ABC model and efficiency droop. Micro-LEDs designed for high speed modulation have shown fast degradation with just a few operating hours. The reason for this is not completely clear. In our own tests, we see that at constant DC current, the device degrades as expected, showing less than 10% decrease in optical in the first 50 hours of use [139], for the chip without heat sink. As the active area reduces, for the same current density and period of time, the lower the degradation is. This makes sense as the smaller pixels are capable of handling very high current densities. However, in the case of investigations we did targeting high speed optical communications, we explored the devices at their limits and high degradation is to be expect. It remains for one to find what is the real cause of degradation, is it the high DC current density, the fast AC modulation or the non-optimised thermal dissipation? The device fabrication by our group, although already optimised, has limitations due to the available equipment. Processes that allows smaller feature size may improve on two aspects: first, a more accurate mask alignment for etching and deposition steps will increase yield and quality, allowing more consistent testing for the various fabrication runs; secondly, feature size below 10 μm could further reduce current crowding and increase the thermal dissipation capability, allowing for extended operating range, higher current densities and, in principle, faster response (higher bandwidth). Currently, our micro–LED chips are fabricated on GaN LED wafers grown on sapphire substrates. A combination of technologies such as laser liftoff, which allows to remove the sapphire substrate, flip-bonding, a mature technique to bond chips, or transfer printing, a pick and place technique for quantum well platelets, may allows to construct transceivers on chip. An schematic example of what may be possible is illustrated in figure 6.1 for the case of flip-chip bonding in (a) and the case of transfer print in (b), respectively. The case for flip-chip bonding may permit to stack chips on their native substrates, if transparent, creating a multi-wavelength emitter that with correct control may render high quality white light. Variations with colour converting materials are also possible. This is illustrated in figure 6.2. Packaged devices could also integrate custom optics such micro-lenses and concentrators to control the field of view of the emitting and receiving pixels, and to potentially improve thermal dissipation characteristics.

The applications of micro–LEDs in optical communications can be further divided in two

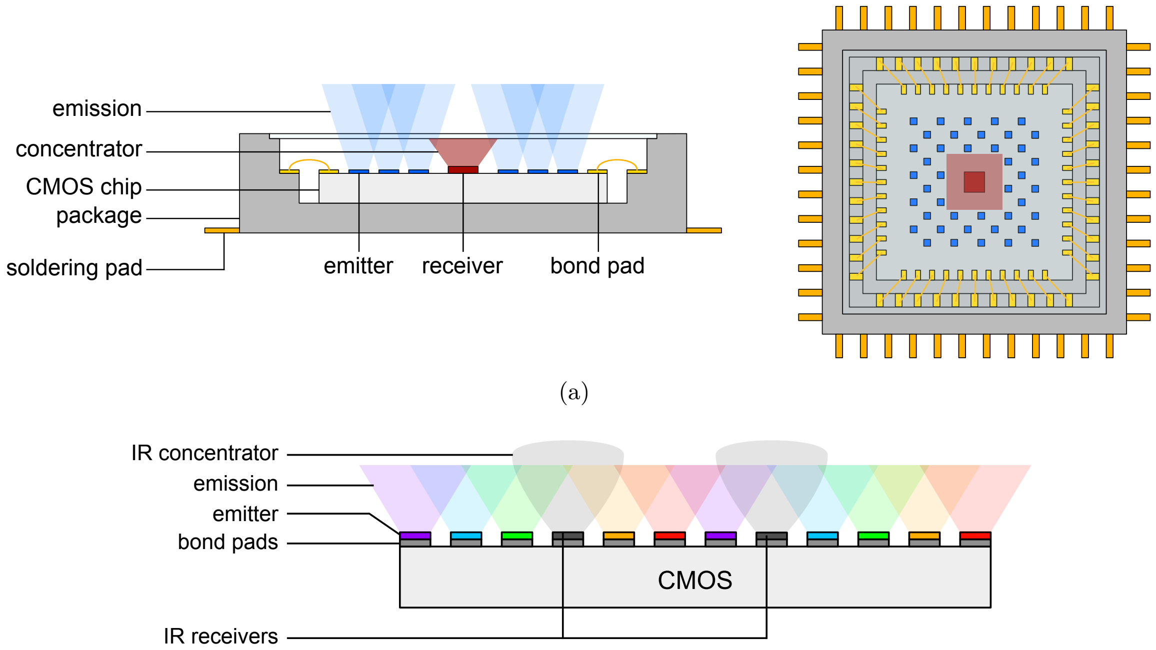

(a)

(b)

Figure 6.1: Schematics of CMOS chip integration of micro-LEDs. In the case of (a) a transceiver implemented with current flip-chip bonding technology, the case of (b) a multi-wavelength transceiver chip that could be achieved with the new transfer-print technology.

parts: driving techniques and photo receivers. In this thesis, the driving technique used was a bipolar modulated voltage superimposed on a DC bias set in current. This mixed format allows to have some control over the average power consumed by the LED, the DC bias power, and still be compatible with voltage signals as commonly used in test equipment. This, however, is not the ideal format and in practice it incurs in some issues: firstly, the real average power of the DC bias and the bipolar signal can be significantly higher than the DC bias power due to the exponential response of the I–V curve, leading to distortion of the light signal and increased degradation of the device; secondly, the bandwidth of micro–LEDs depends linearly with the current density, as such a voltage modulation means that the bandwidth of the device becomes non-linear and as such difficult to model. As such, these two issues can addressed by switching the driving technique to current mode for both the DC bias and the AC signal. This requires test equipment with a current digital-to-analogue converter (DAC) capable outputting a current signal large enough to drive the micro–LEDs at high sampling frequencies. Such equipments are very specialised and not common for

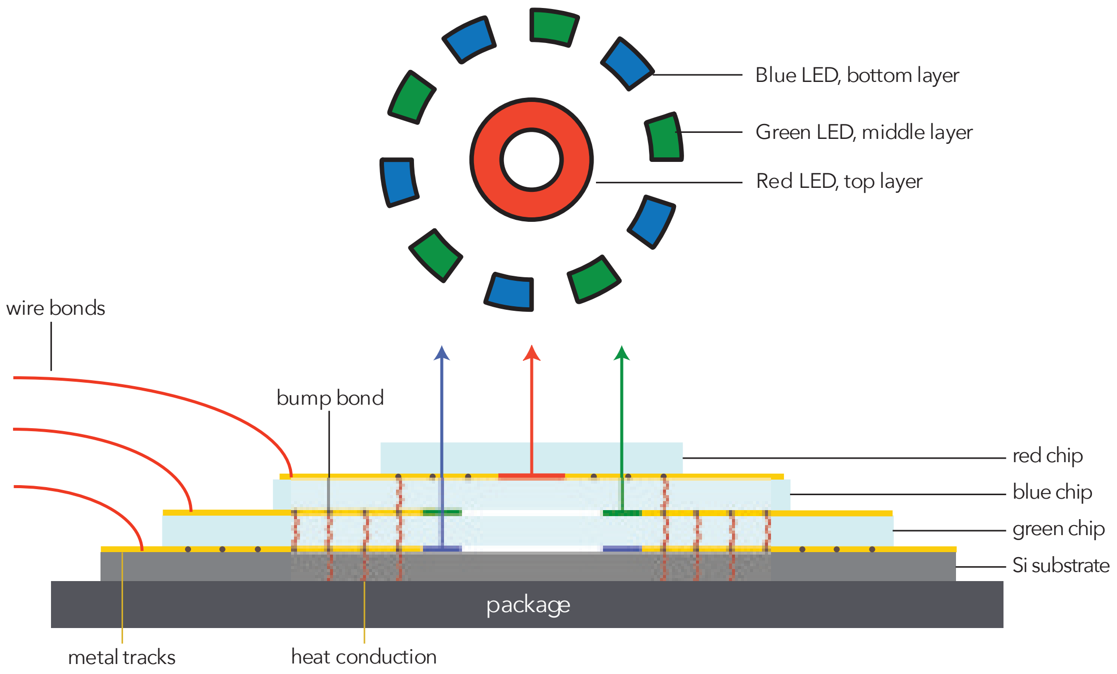

Figure 6.2: Schematic illustration of the a stacked multi chip device with three wavelengths via flip-chip bonding.

telecommunication testing. One alternatives be a custom designed electronics capable of converting the voltage signal to a current signal, and to amplify the small current signal to the power level required to drive the micro–LEDs. Using current signals can create issues with the frequency response due to inductance on long cables. This best practice is to keep the cable length as short as possible and the shortest possible for the purpose of research is to integrate the driving circuitry and the micro–LED in a single PCB. Note that the exact specifications are dependent on the specific of the micro–LED device in use and the targeting performance. The appropriate photo receiver technologies for VLC are PD, APD, SPAD and SiPM. In the cases presented in this thesis only PDs and APDs were used due to their high bandwidth capability. In the case of real operating conditions, two factors must be considered: first, the emitted power density levels need to comply with eye safety requirements for a modulated radiation source, the IEC 60825 [16]; second, the emitted beam may be divergent and the collecting apertures may be limited, significantly reducing the total optical power reaching the receiver, opposite to the case of our own laboratory demonstrations. This issues indicate that in real conditions the receiver technology may play a large role, and it might be the limiting factor for the overall system performance. The other two technologies, SPAD and SiPM, may be a solution for the issues above stated. These can offer significantly higher responsivity due to the higher gain factors. These devices operate in a fire mode fashion, where the signal response peaks sharply, within a few picoseconds, on the arrival of a photon into a cell but requires long recovery times, few nanoseconds or higher. As such, the higher responsivity comes tradeoff of bandwidth and potentially SNR as well. Although, this is not ideal for benchmarking systems, in practice can be the best solution for VLC in scenarios where is the received power is very low. This is, in principle, the case of real conditions which a VLC product may need to operate. Using SPADs and SiPMs require careful biasing circuitry and transimpedance amplification. These circuits are high sensitive to noise in the DC supply rail and RF interference, e.g. WiFi and mobile networks signals. To take full advantage of SPADs and SiPMs, custom designed analogue electronics and RF shielding are required. These circuitry can, in principle, be integrated in the CMOS controlling chip as shown in figure 6.1.

In this thesis, progress was shown to further increase the speed of cost effect POF links for the last kilometre. Further improvements in length are dependent on the optical power of the emitter and possibly POF technologies such as microstructured fibres or thin core fibres ($\approx$10 μm) coupled to large core fibres via a tapper to. Ultimately, the upper limit in term of bit rate for a single pixel LED-based optical communication links, both in free-space and guided-wave, is dictated by bandwidth. Bit rated of 10 Gbps and slightly above are attainable in for current micro-LEDs using a system bandwidths under 2 GHz, as shown in this thesis in chapter 5. When attached to low noise electronics such as integrated chips, the noise is significantly reduced and the SNR is increased. Bit rates up to 15 Gbps using current micro–LEDs may be achievable for high bandwidth and high SNR systems (>35 dB) where higher OFDM modulation orders such as QAM–512 or QAM–1024. Bit rates beyond for 20 Gbps require micro–LED devices with bandwidths above 1 GHz. Such devices may require significant improvements in the GaN epitaxial material. Higher bit rates are possible via multiplexing techniques such as MIMO and WDM described above. In addition to the guided–wave route explored in this thesis — the last kilometre with POF — the interconnects is also an interesting application with mature technology already developed in the infrared using laser technology. The possibility to maintain a full LED-based optical link from board to board via waveguides to rack to rack via POF is exiting. Here, data rates are critical and micro–LEDs may be competitive with existing technologies on the cost and on par with bit rates via multiplexing a number of channels with waveguide arrays and multicore fibres. The question is now more dependent fabrication techniques for the waveguides and on material properties of the polymers used for VLC wavelengths. Moreover, a full optical link in a local network may be possible from the rack directly to a AP to dispersive the signal into free–space and received by a user device. Such a configuration would centralise all the active components in a single place, with the rooms to serve only requiring to install an optical fibre in the ceiling that can serve illuminations and communication to the whole via passive front-end optics. This poses significant changes in the modulation schemes, calling for a new standard to serve channels of free–space and POF equally, and reduce the overall complexity.

The prospects the realisation of VLC / LiFi products and the market success are as follows. Currently, investment is in VLC and LiFi technologies is growing every year, as well as the number of publish patents. The public is becoming more aware of the technology since the term LiFi was found in the source code of Apple's iOS operation system. Since then, the quantity of news articles has significantly increase in the last two years with titles such as: *“LiFi is 100 times fast than WiFi”* and *“A New Type of Li-Fi Has Reportedly Cracked 40 Gbps, 100 Times Faster Than The Best Wi-Fi”*. These articles describe the technology as: *“Li-Fi uses common household LED (light emitting diodes) lightbulbs to enable data transfer, boasting speeds of up to 224 gigabits per second”* and *“At more than 40 Gbit/s per ray, the Li-Fi system's data capacity is greater than that of a Wi-Fi system”*. The confusion increases with the field of free-space optics (FSO), a laser-based mature technology for long range high speed optical links primarily used between buildings and satellites. These reveals a large misconception of the VLC and LiFi technology by non-technical newspapers, creating a very high level of expectation for consumers and increasing the pressure in the industry. For comparison, current product from the UK company pureLiFi, the LiFi–X, based on commercial white LEDs is rated for 40 Mbps PHY link rate. This means that investment by new companies are of high risk as the products may not meet the market expectation, and consequently it might not be successful. The grounds behind the needs for high-speed optical wireless communication is based on the exponential growth in data consumption and spectrum crunch, as shown in figures 1.4 and 1.5. Today's reality in the RF communications for the final delivery to the consumer is as follows. Current WiFi systems based on 802.11ac standard is rated for theoretical PHY link rate up to 6.77 Gbps operating at the 5 GHz band, future systems based on the 802.11ay standard for 2019 are targeting a PHY link rate up to 176 Gbps using 2.6GHz of total bandwidth operating at the 60 GHz band. In the case of the mobile networks, in the mobile world congress 2017, Qualcomm announced a baseband chip with bit rate up to 1 Gbps for current 4G LTE infrastructure; the next generation of mobile networks (5G) is expected to be released around 2020 operating at the 28, 38, 60 and 72–73 GHz bands, the target bit rates are not yet defined although, links up to 70 Gbps have been demonstrated. In summary of the above, as the pressure for data consumption increases, the RF-based industry is responding with increasingly higher speed systems based on millimetre wave frequency bands. There are three questions regarding that may dictate the success this approach: safety due to radiation exposure at millimetre wave frequency band; economical viability due to high deployment costs; and the implications for the fibre optic infrastructure that sits behind the wireless technologies. This last point is today's limitation in the delivered bit rate to consumers is not the wireless technology. For example, South Korea has the highest average connection speed for homes at 29 Mbps in 2016. This is about 0.04 % of the capacity of current technology (802.11ac) and about 10 % of the capacity of typical 300 Mbps WiFi AP installed in our homes. This limitation comes from two parts, the capacity of land and seabed fibre optics, and the capacity of the last kilometre delivery from the street exchange to homes in copper cables. As such, in terms of link speed the immediate benefit of VLC comes from the implementation of POF in the last kilometre. The benefit of VLC for optical wireless communications is questionable as the mature RF-based industry is increasing the link speed by order of magnitude. This means that the success of optical wireless communication technology may lie on the combination of characteristics such as: increased security, higher data density, interference-free links, number of wavelengths available, low power consumption and long range. Examples of applications where these advantages may be advantageous are as follows. The IoT applications envisions connecting all sorts objects together. These connections may be direct (object to object) or through the network (object to network to object) or simply to the internet or local network. In a aircraft manufacturing scenario, one prefers the connections between equipments to be totally isolated from the network, and that the connection to the network to not interfere with the equipment links. This situation the advantages in channels via wavelength, long range via control of the field of view and the directionality of point to point links may be the decision factor. In defence applications, secure communications free from external disruption may be one the highest priorities and VLC or LiFi can guarantee very high levels of security by physically containing the information in covered area and wavelength, in addition to the standard encryption as used in WiFi. In addition, optical wireless communications may provide alternatives to the use of separate dedicated cabling in ships, submarines and aircrafts. Although, light only travels in straight lines, one can envision the combined use passive mirrors and lens, and active relay devices to transmit signals through corridors, intersections, and staircases operating both in the visible and infrared. Increase capacity or redundancy may be as simple as replicating the system using different corners. Moreover, an optical wireless communications system operating with redundancy and extra wavelengths available may significantly increase security by spreading the transmission of data packets on the various available channels or wavelengths following an algorithm inscribed in the PHY, e.g. the baseband chip. Consumer applications for indoor geolocation already exist and are increasing, especially for retail services. This is associated with the smart lighting and consumer implementation of IoT. These operate in broadcast only from the infrastructure to the user mobile device using the front camera. Although this proves the basic functionality, the next stage may be integrating an high speed optical receiver with existing optoelectronic devices for proximity sensing and ambient light detection, present in all modern smartphones.

Bibliography

[1] `http://www.cisco.com/c/en/us/solutions/collateral/service-provider/visual-networking-index-vni/mobile-white-paper-c11-520862.pdf`, January 2015.

[2] `https://www.ntia.doc.gov`, April 2016.

[3] Dipl.-Ing. Peter E. Zamzow Professor Dr.-Ing. Werner Daum (auth.) Professor Dr.-Ing. Olaf Ziemann, Professor Dr. Jürgen Krauser. POF Handbook: Optical Short Range Transmission Systems. Springer-Verlag Berlin Heidelberg, 2 edition, 2008.

[4] `http://purelifi.com`, March 2016.

[5] `https://www.ted.com/talks/harald_haas_a_breakthrough_new_kind_of_wireless_internet`, September 2015.

[6] E. F. Schubert. Light-Emitting Diodes. Cambridge University Press, 2006.

[7] J. Herrnsdorf, J.J.D. McKendry, S. Zhang, E. Xie, R. Ferreira, D. Massoubre, A.M. Zuhdi, R.K. Henderson, I. Underwood, S. Watson, A.E. Kelly, E. Gu, and M.D. Dawson. Active-matrix GaN micro light-emitting diode display with unprecedented brightness. Electron Devices, IEEE Transactions on, 62(6):1918 – 1925, June 2015.

[8] J. Armstrong. OFDM for optical communications. Journal of Lightwave Technology, 27(3):189–204, Feb 2009.

[9] IEEE standard for local and metropolitan area networks–part 15.7: Short-range wireless optical communication using visible light. IEEE Std 802.15.7-2011, pages 1–309, Sept 2011.

[10] Hiroyuki Shibata, Yoshio Waseda, Hiromichi Ohta, Kazumasa Kiyomi, Kenji Shimoyama, Kenji Fujito, Hirobumi Nagaoka, Yuji Kagamitani, Rayko Simura, and Tsuguo Fukuda. High thermal conductivity of gallium nitride (GaN) crystals grown by HVPE process. Materials Transactions, 48(10):2782–2786, 2007.

[11] C. Mion, J.F. Muth, Edward A. Preble, and Drew Hanser. Thermal conductivity, dislocation density and GaN device design. Superlattices and Microstructures, 40(4–6):338 – 342, 2006. E-MRS 2006 Symposium S: Material Science and Technology of Wide Bandgap Semiconductors 2006 Spring Meeting of the European Materials Research Society.

[12] `https://www.itu.int`, April 2016.

[13] G.P. Agrawal. Fiber-Optic Communication Systems. Wiley Series in Microwave and Optical Engineering. Wiley, 2012.

[14] R.P. Feynman, R.B. Leighton, and M.L. Sands. The Feynman Lectures on Physics. Number v. 1 in The Feynman Lectures on Physics. Addison-Wesley, 1963.

[15] S. Rajagopal, R.D. Roberts, and Sang-Kyu Lim. Ieee 802.15.7 visible light communication: modulation schemes and dimming support. Communications Magazine, IEEE, 50(3):72–82, March 2012.

[16] `https://webstore.iec.ch/publication/21820`, 2014.

[17] `http://www.3gpp.org`, April 2017.

[18] IEEE standard for information technology–telecommunications and information exchange between systems - local and metropolitan area networks–specific requirements part 11: Wireless LAN medium access control (MAC) and physical layer (PHY) specifications amendment 1: Fast initial link setup. Technical report, IEEE, Dec 2016.

[19] Olaf Ziemann, P. E. Zamzow, J. Krauser, W. Daum, W. Daumeister, and Et Al. Polymer Optical Fibers for Data Communication. Springer-Verlag New York, Inc., Secaucus, NJ, USA, 2002.

[20] A. M. J. Koonen, H. P. A. van den Boom, E. Ortego Martinez, A. Pizzinat, Ph. Guignard, B. Lannoo, C. M. Okonkwo, and E. Tangdiongga. Cost optimization of optical in-building networks. Opt. Express, 19(26):B399–B405, Dec 2011.

[21] Xue Bai, Gianvito Caputo, Zhendong Hao, Vânia T. Freitas, Jiahua Zhang, Ricardo L. Longo, Oscar L. Malta, Rute A. S. Ferreira, and Nicola Pinna. Efficient and tuneable photoluminescent boehmite hybrid nanoplates lacking metal activator centres for single-phase white LEDs. Nat Commun, 5, 12 2014.

[22] `http://www.ted.com/talks/harald_haas_wireless_data_from_every_light_bulb`, July 2011.

[23] `http://www.ledsmagazine.com/articles/2017/02/philips-acquires-french-li-fi-company.html`, 2016.

[24] H. Haas, L. Yin, Y. Wang, and C. Chen. What is LiFi? Journal of Lightwave Technology, 34(6):1533–1544, March 2016.

[25] L. R. Varshney. Transporting information and energy simultaneously. In 2008 IEEE International Symposium on Information Theory, pages 1612–1616, July 2008.

[26] Z. Wang, D. Tsonev, S. Videv, and H. Haas. On the design of a solar-panel receiver for optical wireless communications with simultaneous energy harvesting. IEEE Journal on Selected Areas in Communications, 33(8):1612–1623, Aug 2015.

[27] Shuji Nakamura Isamu Akasaki, Hiroshi Amano. Efficient blue light-emitting diodes leading to bright and energy-saving white light sources, 2014.

[28] T Matsuoka, T Ito, and T Kaino. First plastic optical fibre transmission experiment using 520nm LEDs with intensity modulation/direct detection. Electronics Letters, 36(22):1836–1837, 2000.

[29] `http://www.ieee802.org/15/pub/TG7.html`, January 2009.

[30] M. R. Krames, O. B. Shchekin, Regina Mueller-Mach, Gerd O. Mueller, Ling Zhou, G. Harbers, and M. G. Craford. Status and future of high-power light-emitting diodes for solid-state lighting. Display Technology, Journal of, 3(2):160–175, June 2007.

[31] K. Hohn, A. Debray, P. Schlotter, R. Schmidt, and J. Schneider. Wavelength-converting casting composition and light-emitting semiconductor component, October 11 2001. US Patent App. 09/843,080.

[32] `http://www.cree.com/News-and-Events/Cree-News/Press-Releases/2014/March/300LPW-LED-barrier`, March 2014.

[33] M. H. Crawford, J. J. Wierer, A. J. Fischer, G. T. Wang, D. D. Koleske, G. S. Subramania, M. E. Coltrin, R. F. Karlicek, and J. Y. Tsao. Solid-State Lighting: Toward Smart and Ultraefficient Materials, Devices, Lamps, and Systems, pages 1–56. John Wiley & Sons, Inc., 2015.

[34] T. Komine and M. Nakagawa. Fundamental analysis for visible-light communication system using LED lights. Consumer Electronics, IEEE Transactions on, 50(1):100–107, Feb 2004.

[35] Fang-Ming Wu, Chun-Ting Lin, Chia-Chien Wei, Cheng-Wei Chen, Hou-Tzu Huang, and Chun-Hung Ho. 1.1-Gb/s white-LED-based visible light communication employing carrier-less amplitude and phase modulation. Photonics Technology Letters, IEEE, 24(19):1730–1732, Oct 2012.

[36] A. M. Khalid, G. Cossu, R. Corsini, P. Choudhury, and E. Ciaramella. 1-Gb/s transmission over a phosphorescent white LED by using rate-adaptive discrete multitone modulation. Photonics Journal, IEEE, 4(5):1465–1473, Oct 2012.

[37] A.G. Dentai, T.P. Lee, C.A. Burrus, and E. Buehler. Small-area, high-radiance c.w. InGaAsP l.e.d.s emitting at 1.2 to 1.3 μm. Electronics Letters, 13(16):484–485, August 1977.

[38] W. Harth, W. Huber, and J. Heinen. Frequency response of GaAlAs light-emitting diodes. Electron Devices, IEEE Transactions on, 23(4):478–480, Apr 1976.

[39] S. X. Jin, J. Li, J. Z. Li, J. Y. Lin, and H. X. Jiang. GaN microdisk light emitting diodes. Applied Physics Letters, 76(5), January 2000.

[40] Y.-K. Song, M. Diagne, H. Zhou, A. V. Nurmikko, R. P. Schneider, and T. Takeuchi. Resonant-cavity InGaN quantum-well blue light-emitting diodes. Applied Physics Letters, 77(12):1744–1746, 2000.

[41] I. Ozden, M. Diagne, A.V. Nurmikko, J. Han, and T. Takeuchi. A matrix addressable 1024 element blue light emitting ingan qw diode array. physica status solidi (a), 188(1):139–142, 2001.

[42] S. X. Jin, J. Shakya, J. Y. Lin, and H. X. Jiang. Size dependence of III-nitride microdisk light-emitting diode characteristics. Applied Physics Letters, 78(22):3532–3534, 2001.

[43] C. W. Jeon, K. S. Kim, and M. D. Dawson. Fabrication of two-dimensional InGaN-based micro-LED arrays. Physica Status Solidi A, 192(2):325–328, 2002.

[44] J. J. D. McKendry, R. P. Green, A. E. Kelly, Zheng Gong, B. Guilhabert, D. Massoubre, E. Gu, and M. D. Dawson. High-speed visible light communications using individual pixels in a micro light-emitting diode array. Photonics Technology Letters, IEEE, 22(18):1346–1348, Sept 2010.

[45] Pleun P. Maaskant, Haymen Shams, Mahbub Akhter, William Henry, Menno J. Kappers, Dandan Zhu, Colin J. Humphreys, and Brian Corbett. High-speed substrate-emitting micro-light-emitting diodes for applications requiring high radiance. Applied Physics Express, 6(2):022102, 2013.

[46] J. J. D. McKendry, D. Massoubre, S. Zhang, B. R. Rae, R.P. Green, E. Gu, R. K. Henderson, A. E. Kelly, and M. D. Dawson. Visible-light communications using a CMOS-controlled micro-light- emitting-diode array. Journal of Lightwave Technology, 30(1):61–67, Jan 2012.

[47] D. Tsonev, H. Chun, S. Rajbhandari, J. J. D. McKendry, S. Videv, E. Gu, M. Haji, S. Watson, A.E. Kelly, G. Faulkner, M. D. Dawson, H. Haas, and D. O'Brien. A 3-Gb/s single-LED OFDM-based wireless VLC link using a gallium nitride μLED. Photonics Technology Letters, IEEE, 26(7):637–640, April 2014.

[48] Liang Geng, Jinlong Wei, Richard V. Penty, Ian White, and David G. Cunningham. 3 Gbit/s LED-Based step index plastic optical fiber link using multilevel pulse amplitude modulation. In Optical Fiber Communication Conference/National Fiber Optic Engineers Conference 2013, page OTh4A.1. Optical Society of America, 2013.

[49] X. Li, J. L. Wei, N. Bamiedakis, R. V. Penty, and I. H. White. Avalanche photodiode enhanced PAM-32 5 Gb/s LED-POF link. In 2014 The European Conference on Optical Communication (ECOC), pages 1–3, Sept 2014.

[50] Liang Geng, Richard V. Penty, Ian H. White, and David G. Cunningham. FEC-free 50 m 1.5 Gb/s plastic optical fibre link using CAP modulation for home networks. In European Conference and Exhibition on Optical Communication, page Th.1.B.4. Optical Society of America, 2012.

[51] L. Peng, M. Hélard, S. Haese, M. Liu, and J. F. Hélard. Hybrid PN-ZP-DMT scheme for spectrum-efficient optical communications and its application to SI-POF. Journal of Lightwave Technology, 32(18):3149–3160, Sept 2014.

[52] J. Vinogradov, R. Kruglov, K. Chi, J. Shi, M. Bloos, S. Loquai, and O. Ziemann. GaN light–emitting diodes for up to 5.5 Gb/s short–reach data transmission over SI-POF. Photonics Technology Letters, IEEE, PP(99):1–1, 2014.

[53] Y. Wang, J. Müller, and J. Speidel. 3 Gbit/s transmission over plastic optical fiber with adaptive Tomlinson–Harashima precoded systems. In 2013 IEEE International Conference on Consumer Electronics (ICCE), pages 629–632, Jan 2013.

[54] S. C. J. Lee, F. Breyer, S. Randel, O. Ziemann, H. P. A. van den Boom, and A. M. J. Koonen. Low-cost and robust 1–Gbit/s plastic optical fiber link based on light-emitting

diode technology. In Optical Fiber communication/National Fiber Optic Engineers Conference, 2008. OFC/NFOEC 2008. Conference on, pages 1–3, Feb 2008.

[55] J. W. Shi, C. W. Lin, W. Chen, J. E. Bowers, J. K. Sheu, C. L. Lin, Y. L. Li, J. Vinogradov, and O. Ziemann. Very high-speed GaN-based cyan light emitting diode on patterned sapphire substrate for 1 Gbps plastic optical fiber communication. In Optical Fiber Communication Conference and Exposition (OFC/NFOEC), 2012 and the National Fiber Optic Engineers Conference, pages 1–3, March 2012.

[56] X. Li, N. Bamiedakis, J.L. Wei, J.J.D. McKendry, E. Xie, R. Ferreira, E. Gu, M.D. Dawson, R.V. Penty, and I.H. White. μLED-based single-wavelength bi-directional POF link with 10 Gb/s aggregate data rate. Lightwave Technology, Journal of, 33(17):3571–3576, 2015.

[57] J.-M. Wun, C.-W. Lin, W. Chen, J.-K. Sheu, C.-L. Lin, Y.-L. Li, J.E. Bowers, J.-W. Shi, J. Vinogradov, R. Kruglov, and O. Ziemann. GaN-based miniaturized cyan light-emitting diodes on a patterned sapphire substrate with improved fiber coupling for very high-speed plastic optical fiber communication. Photonics Journal, IEEE, 4(5):1520–1529, Oct 2012.

[58] P.J. Pinzon, I. Perez Garcilopez, and C. Vazquez. Efficient multiplexer/demultiplexer for visible WDM transmission over SI–POF technology. Lightwave Technology, Journal of, 33(17):3711–3718, Sept 2015.

[59] Xin Li, Nikolaos Bamiedakis, Jonathan Mckendry, Enyuan Xie, Ricardo Ferreira, Erdan Gu, Martin Dawson, Richard Penty, and Ian H. White. 11 Gb/s WDM transmission over SI-POF using violet, blue and green μLEDs. In Optical Fiber Communication Conference, page Tu2C.5. Optical Society of America, 2016.

[60] Xin Li, Nikos Bamiedakis, Jinlong Wei, Jonathan Mckendry, Enyuan Xie, Ricardo Ferreira, Erdan Gu, Martin Dawson, Richard V. Penty, and Ian H. White. 6.25 Gb/s POF link using GaN μLED arrays and optically generated pulse amplitude modulation. In CLEO: 2015, page STu4F.7. Optical Society of America, 2015.

[61] `http://standards.ieee.org/about/get/802/802.15.html`, 2016.

[62] S. Hranilovic, L. Lampe, and S. Hosur. Visible light communications: The road to standardization and commercialization (part 1). IEEE Communications Magazine, 51(12):25–68, December 2013.

[63] S. Hranilovic, L. Lampe, S. Hosur, and Richard D. Roberts. Visible light communications: The road to standardization and commercialization (part 2). IEEE Communications Magazine, 52(7):62–98, July 2014.

[64] Henry Joseph Round. A note on carborundum. Electrical World, 49(19):309–310, 1907.

[65] Oleg Vladimirovich Lossev. Luminous carborundum detector and detection effect and oscillations with crystals. The London, Edinburgh, and Dublin Philosophical Magazine and Journal of Science, 6(39):1024–1044, 1928.

[66] Oleg Vladimirovich Lossev. Light relay. Patent No. 12191, 1929.

[67] Pasynkov V. V. Tairov Y. M. Violin E. E., Kalnin A. A. and Yaskov D. A. Silicon Carbide – 1968. In 2nd International Conference on Silicon Carbide, published as a special issue of the Materials Research Bulletin, page 231, 1969.

[68] J. I. Pankove, E. A. Miller, D. Richman, and J. E. Berkeyheiser. Electroluminescence in GaN. J. Luminescence, 4(63), 1971.

[69] H.P. Maruska, D.A. Stevenson, and J.I. Pankove. Violet luminescence of Mg–doped GaN. Applied Physics Letters, 22(6):303–305, 1973.

[70] J.I. Pankove. Frequency response of GaN light-emitting diodes. Proceedings of the IEEE, 60(11):1456–1457, Nov 1972.

[71] Hiroshi Amano, Masahiro Kito, Kazumasa Hiramatsu, and Isamu Akasaki. P–type conduction in Mg–Doped GaN treated with low–energy electron beam irradiation (LEEBI). Japanese Journal of Applied Physics, 28(12A):L2112, 1989.

[72] Shuji Nakamura, Masayuki Senoh, and Takashi Mukai. Highly p-typed Mg-Doped GaN films grown with GaN buffer layers. Japanese Journal of Applied Physics, 30(10A):L1708, 1991.

[73] Itoh K. Koide N. Akasaki I., Amano H. and Manabe K. GaN based UV/blue light–emitting devices. In GaAs and Related Compounds conference, volume 129 of Inst. Phys. Conf. Ser., 1992.

[74] Shuji Nakamura, Masayuki Senoh, and Takashi Mukai. P-GaN/N-InGaN/N-GaN double-heterostructure blue-light-emitting diodes. Japanese Journal of Applied Physics, 32(1A):L8, 1993.

[75] Shuji Nakamura, Takashi Mukai, and Masayuki Senoh. Candela–class high–brightness InGaN/AlGaN double–heterostructure blue light–emitting diodes. Applied Physics Letters, 64(13):1687–1689, Mar 1994.

[76] S. Nakamura and G. Fasol. The Blue Laser Diode. Springer, Berlin, 1997.

[77] K. Bando, Y. Noguchi, K. Sakano, and Y. Shimizu. (in japanese) tech. digest. In Phosphor Res. Soc., 264th Meeting, November 1996.

[78] `http://www.osram.co.uk/osram_uk/news-and-knowledge/led-home/professional-knowledge/led-basics/led-history/index.jsp`, May 2013.

[79] `www.philips.com/consumerfiles/newscenter/main/design/resources/pdf/Inside-Innovation-Backgrounder-Lumens-per-Watt.pdf`, May 2013.

[80] J. Heinen. 1.3μm InGaAsP/InP light emitting diodes with internally defined emission area prepared by single-step LPE technique. Electronics Letters, 18(1):23–24, January 1982.

[81] `http://www.samsung.com/global/business/led/lighting/component/csp`, February 11 2016.

[82] J. Y. Lin S. X. Jin, J. Li and H. X. Jiang. InGaN/GaN quantum well interconnected microdisk light emitting diodes. Applied Physics Letters, 77(20), September 2000.

[83] H. W. Choi, C. W. Jeon, M. D. Dawson, P. R. Edwards, and R. W. Martin. Fabrication and performance of parallel-addressed InGaN micro-LED arrays. Photonics Technology Letters, IEEE, 15(4):510–512, April 2003.

[84] H. W. Choi, M. D. Dawson, P. R. Edwards, and R. W. Martin. High extraction efficiency InGaN micro-ring light-emitting diodes. Applied Physics Letters, 83(22):4483–4485, 2003.

[85] A. Chitnis, J. Sun, V. Mandavilli, R. Pachipulusu, S. Wu, M. Gaevski, V. Adivarahan, J. P. Zhang, M. Asif Khan, and A. Sarua. Self-heating effects at high pump currents in deep ultraviolet light-emitting diodes at 324 nm. Applied Physics Letters, 81(18):3491–3493, 2002.

[86] Zheng Gong, Shirong Jin, Yujie Chen, Jonathan McKendry, David Massoubre, Ian. M. Watson, Erdan Gu, and Martin D. Dawson. Size-dependent light output, spectral shift, and self-heating of 400 nm InGaN light-emitting diodes. Journal of Applied Physics, 107(1):013103, 2010.

[87] Pengfei Tian, Jonathan J. D. McKendry, Zheng Gong, Benoit Guilhabert, Ian M. Watson, Erdan Gu, Zhizhong Chen, Guoyi Zhang, and Martin D. Dawson. Size–dependent efficiency and efficiency droop of blue InGaN micro-light emitting diodes. Applied Physics Letters, 101(23):231110, 2012.

[88] Pengfei Tian, Jonathan J. D. McKendry, Johannes Herrnsdorf, Scott Watson, Ricardo Ferreira, Ian M. Watson, Erdan Gu, Anthony E. Kelly, and Martin D. Dawson. Temperature-dependent efficiency droop of blue InGaN micro-light emitting diodes. Applied Physics Letters, 105(17), 2014.

[89] Z. Gong, E. Gu, S. R. Jin, D. Massoubre, B. Guilhabert, H. X. Zhang, M. D. Dawson, V. Poher, G. T. Kennedy, P. M. W. French, and M. A. A. Neil. Efficient flip-chip InGaN micro-pixellated light-emitting diode arrays: promising candidates for micro-displays and colour conversion. Journal of Physics D: Applied Physics, 41(9):094002, 2008.

[90] S. Zhang, Z. Gong, J. J. D. McKendry, S. Watson, A. Cogman, E. Xie, P. Tian, E. Gu, Z. Chen, G. Zhang, A. E. Kelly, R. K. Henderson, and M. D. Dawson. CMOS–controlled color-tunable smart display. Photonics Journal, IEEE, 4(5):1639–1646, Oct 2012.

[91] N. Laurand, B. Guilhabert, J. McKendry, A. E. Kelly, B. Rae, D. Massoubre, Z. Gong, E. Gu, R. Henderson, and M. D. Dawson. Colloidal quantum dot nanocomposites for visible wavelength conversion of modulated optical signals. Opt. Mater. Express, 2(3):250–260, Mar 2012.

[92] H. X. Zhang, D. Massoubre, J. McKendry, Z. Gong, B. Guilhabert, C. Griffin, E. Gu, P. E. Jessop, J. M. Girkin, and M. D. Dawson. Individually-addressable flip-chip AlInGaN micropixelated light emitting diode arrays with high continuous and nanosecond output power. Opt. Express, 16(13):9918–9926, Jun 2008.

[93] A.E. Kelly, J.J.D. McKendry, S. Zhang, D. Massoubre, B.R. Rae, R.P. Green, R.K. Henderson, and M.D. Dawson. High-speed GaN micro–LED arrays for data communications. In 2012 14th International Conference on Transparent Optical Networks (ICTON), pages 1–5, 2012. ISBN: 9781467322287.

[94] H. Jiang, J. Lin, S. Jin, and J. Li. Micro–size LED and detector arrays for minidisplay, hyper-bright light emitting diodes, lighting, and UV detector and imaging sensor applications, June 25 2002. US Patent 6,410,940.

[95] B. Thibeault and S. DenBaars. Enhanced light extraction through the use of micro-LED arrays, June 25 2002. US Patent 6,410,942.

[96] M.D. Dawson, H.W. Choi, and C.W. Jeon. Micro-LEDs, October 6 2009. US Patent 7,598,149.

[97] P. Maaskant, B. Corbett, and B. Henry. Micro–LED array with filters, August 22 2013. WO Patent App. PCT/EP2013/053,215.

[98] Christopher Percival. Methods and apparatus for improving micro–LED devices, May 2015. US201514705607 20150506, GB20140008084 20140507.

[99] `http://www.faqs.org/patents/assignee/luxvue-technology-corporation/`, July 2015.

[100] `https://www.crunchbase.com/organization/luxvue-technology#/entity`, 2014.

[101] E. Y. Xie, Z. Z. Chen, P. R. Edwards, Z. Gong, N. Y. Liu, Y. B. Tao, Y. F. Zhang, Y. J. Chen, I. M. Watson, E. Gu, R. W. Martin, G. Y. Zhang, and M. D. Dawson. Strain relaxation in InGaN/GaN micro-pillars evidenced by high resolution cathodoluminescence hyperspectral imaging. Journal of Applied Physics, 112(1), 2012.

[102] Matthias Auf der Maur, Alessandro Pecchia, Gabriele Penazzi, Walter Rodrigues, and Aldo Di Carlo. Efficiency drop in green InGaN/GaN light emitting diodes: The role of random alloy fluctuations. Phys. Rev. Lett., 116:027401, Jan 2016.

[103] Emmanouil Kioupakis, Qimin Yan, Daniel Steiauf, and Chris G Van de Walle. Temperature and carrier-density dependence of auger and radiative recombination in nitride optoelectronic devices. New Journal of Physics, 15(12):125006, 2013.

[104] David S. Meyaard, Qifeng Shan, Jaehee Cho, E. Fred Schubert, Sang-Heon Han, Min-Ho Kim, Cheolsoo Sone, Seung Jae Oh, and Jong Kyu Kim. Temperature dependent efficiency droop in GaInN light-emitting diodes with different current densities. Applied Physics Letters, 100(8), 2012.

[105] Tae-Yeon Seong, Jung Han, and Hiroshi Amano. III–Nitride Based Light Emitting Diodes and Applications. Topics in Applied Physics 126. Springer, 2013.

[106] V. K. Malyutenko, S. S. Bolgov, and A. D. Podoltsev. Current crowding effect on the ideality factor and efficiency droop in blue lateral InGaN/GaN light emitting diodes. Applied Physics Letters, 97(25):251110, 2010.

[107] S. Chhajed, Y. Xi, Y. L. Li, Th. Gessmann, and E. F. Schubert. Influence of junction temperature on chromaticity and color-rendering properties of trichromatic white-light sources based on light-emitting diodes. Journal of Applied Physics, 97(5):–, 2005.

[108] J. Senawiratne, A. Chatterjee, T. Detchprohm, W. Zhao, Y. Li, M. Zhu, Y. Xia, X. Li, J. Plawsky, and C. Wetzel. Junction temperature, spectral shift, and efficiency in GaInN-based blue and green light emitting diodes. Thin Solid Films, 518(6):1732 – 1736, 2010.

[109] T.P. Lee and A.G. Dentai. Power and modulation bandwidth of GaAs-AlGaAs high-radiance LED's for optical communication systems. Quantum Electronics, IEEE Journal of, 14(3):150–159, Mar 1978.

[110] Y.S. Liu and D.A. Smith. The frequency response of an amplitude-modulated GaAs luminescence diode. Proceedings of the IEEE, 63(3):542–544, March 1975.

[111] Hirofumi Namizaki, M. Nagano, and S. Nakahara. Frequency response of $Ga_{1-x}Al_xAs$ light-emitting diodes. Electron Devices, IEEE Transactions on, 21(11):688–691, Nov 1974.

[112] S. Dimitrov and H. Haas. Information rate of OFDM-based optical wireless communication systems with nonlinear distortion. Journal of Lightwave Technology, 31(6):918–929, March 2013.

[113] Anu A. Gokhale. Introduction to telecommunications. Thomson/Delmar Learning,, Clifton Park, NY :, 2nd ed. edition, 2005. Includes index.

[114] Zabih Ghassemlooy Anthony Boucouvalas Eszter Udvary Murat Uysal, Carlo Capsoni, editor. Optical Wireless Communications - An Emerging Technology. Signals and Communication Technology. Springer International Publishing, 2016.

[115] R. Ferreira, E. Xie, J. McKendry, S. Rajbhandari, H. Chun, G. Faulkner, S. Watson, A. Kelly, E. Gu, R. Penty, I. White, D. C. O'Brien, and M. Dawson. High bandwidth GaN-based micro-LEDs for multi-Gbps visible light communications. IEEE Photonics Technology Letters, 28(19):2023–2026, October 2016.

[116] J. M. Kahn and J. R. Barry. Wireless infrared communications. Proceedings of the IEEE, 85(2):265–298, Feb 1997.

[117] J. Senawiratne, Y. Li, M. Zhu, Y. Xia, W. Zhao, T. Detchprohm, A. Chatterjee, J.L. Plawsky, and C. Wetzel. Junction temperature measurements and thermal modeling of GaInN/GaN quantum well light-emitting diodes. Journal of Electronic Materials, 37(5):607–610, 2008.

[118] Johannes Herrnsdorf, Yue Wang, Jonathan McKendry, Zheng Gong, David Massoubre, Benoit Jack Eloi Guilhabert, Georgios Tsiminis, Graham A Turnbull, Ifor D. W. Samuel, Nicolas Laurand, Erdan Gu, and Martin Dawson. Micro-LED pumped polymer laser: a discussion of future pump sources for organic lasers. Laser and Photonics Reviews, 7(6):1065–1078, 11 2013.

[119] X. Guo and E. F. Schubert. Current crowding and optical saturation effects in GaInN/GaN light-emitting diodes grown on insulating substrates. Applied Physics Letters, 78(21):3337–3339, 2001.

[120] Asif Khan, Krishnan Balakrishnan, and Tom Katona. Ultraviolet light-emitting diodes based on group three nitrides. Nat Photon, 2(2):77–84, 02 2008.

[121] K. C. Yung, H. Liem, H. S. Choy, and W. K. Lun. Degradation mechanism beyond device self-heating in high power light-emitting diodes. Journal of Applied Physics, 109(9), 2011.

[122] Marek Osiński, Joachim Zeller, Pei-Chih Chiu, B. Scott Phillips, and Daniel L. Barton. AlGaN/InGaN/GaN blue light emitting diode degradation under pulsed current stress. Applied Physics Letters, 69(7):898–900, 1996.

[123] I. Yu. Evstratov, V. F. Mymrin, S. Yu. Karpov, and Yu. N. Makarov. Current crowding effects on blue LED operation. physica status solidi (c), 3(6):1645–1648, 2006.

[124] M. V. Bogdanov, K. A. Bulashevich, O. V. Khokhlev, I. Yu. Evstratov, M. S. Ramm, and S. Yu. Karpov. Current crowding effect on light extraction efficiency of thin-film LEDs. physica status solidi (c), 7(7-8):2124–2126, 2010.

[125] Laura Meriggi, Matthew J. Steer, Ying Ding, Iain G. Thayne, Calum MacGregor, Charles N. Ironside, and Marc Sorel. Enhanced emission from mid-infrared alinsb light-emitting diodes with p-type contact grid geometry. Journal of Applied Physics, 117(6), 2015.

[126] Jonas Beermann, René L. Eriksen, Tobias Holmgaard, Kjeld Pedersen, and Sergey I. Bozhevolnyi. Plasmonic black metals via radiation absorption by two-dimensional arrays of ultra-sharp convex grooves. Scientific Reports, 4:6904 EP, November 2014.

[127] Thomas E. Salem, D. Ibitayo, and B.R. Geil. Calibration of an infrared camera for thermal characterization of high voltage power electronic components. In Instrumentation and Measurement Technology Conference, 2005. IMTC 2005. Proceedings of the IEEE, volume 2, pages 829–833, May 2005.

[128] Joseba Zubia and Jon Arrue. Plastic optical fibers: An introduction to their technological processes and applications. Optical Fiber Technology, 7(2):101 – 140, 2001.

[129] Tae-il Kim, Yei Hwan Jung, Jizhou Song, Daegon Kim, Yuhang Li, Hoon-sik Kim, Il-Sun Song, Jonathan J. Wierer, Hsuan An Pao, Yonggang Huang, and John A. Rogers. High-efficiency, microscale GaN light-emitting diodes and their thermal properties on unusual substrates. Small, 8(11):1643–1649, 2012.

[130] H. Xu, J. Zhang, K. M. Davitt, Y. K. Song, and A. V. Nurmikko. Application of blue–green and ultraviolet micro-LEDs to biological imaging and detection. Journal of Physics D: Applied Physics, 41(9):094013, 2008.

[131] Richard P. Green, Jonathan J. D. McKendry, David Massoubre, Erdan Gu, Martin D. Dawson, and A. E. Kelly. Modulation bandwidth studies of recombination processes in blue and green InGaN quantum well micro-light-emitting diodes. Applied Physics Letters, 102(9):091103, 2013.

[132] Donald Neamen. Semiconductor Physics And Devices. McGraw-Hill, Inc., New York, NY, USA, 3 edition, 2003.

[133] Han-Youl Ryu and Jong-In Shim. Effect of current spreading on the efficiency droop of ingan light-emitting diodes. Opt. Express, 19(4):2886–2894, Feb 2011.

[134] Govind P. Agrawal. Fiber-Optic Communication Systems. Optical Communications. Wiley, 4th edition edition, 2010.

[135] Xin Li, Nikos Bamiedakis, Jonathan D. McKendry Jinlong Wei, Enyuan Xie, Ricardo Ferreira, Erdan Gu, Martin D. Dawson, Richard V. Penty, and Ian H. White. 8 Gb/s single-wavelength bi-directional PAM-16 SI-POF link using blue μLEDs and avalanche photodiodes. In Optical Interconnects XV, Photonics West Opto. SPIE, 2015.

[136] Nikos Bamiedakis, Xin Li, Ricardo X G Ferreira, Xiadao Meng, Jonathan McKendry, Enyuan Xie, Erdan Gu, Martin Dawson, Richard Penty, and Ian White. 8 Gb/s PAM-16 data transmission over 10 m of SI POF using novel 450 nm micro-pixelated LEDs. In European Conference on Optical Communication (ECOC 2016) (ECOC 2016), SC 4 - Subsystems for Optical Networking and Datacoms, Düsseldorf, Germany, September 2016.

[137] M. Uysal and H. Nouri. Optical wireless communications - an emerging technology. In 2014 16th International Conference on Transparent Optical Networks (ICTON), pages 1–7, July 2014.

[138] Mohamed Sufyan Islim, Ricardo X. Ferreira, Xiangyu He, Enyuan Xie, Stefan Videv, Shaun Viola, Scott Watson, Nikolaos Bamiedakis, Richard V. Penty, Ian H. White, Anthony E. Kelly, Erdan Gu, Harald Haas, and Martin D. Dawson. Towards 10 Gb/s orthogonal frequency division multiplexing-based visible light communication using a GaN violet micro-LED. Photonics Research, 5(2):A35–A43, Apr 2017.

[139] Pengfei Tian, Ahmad Althumali, Erdan Gu, Ian M Watson, Martin D Dawson, and Ran Liu. Aging characteristics of blue InGaN micro-light emitting diodes at an extremely high current density of 3.5 $kA \cdot cm^2$. Semiconductor Science and Technology, 31(4):045005, 2016.

Publications

The following is a chronological list of peer reviewed journal publications, conference presentations and proceedings papers that resulted and/or are related with the work presented in this thesis. Article publications in peer reviewed journals are included here in full length.

Journals

[1] Sujan Rajbhandari, Aravind V. N. Jalajakumari, Hyunchae Chun, Grahame Faulkner, Katherine Cameron, Robert Henderson, Dobroslav Tsonev, Harald Haas, Enyuan Xie, Jonathan J. D. McKendry, Johannes Herrnsdorf, Ricardo Ferreira, Erdan Gu, Martin D. Dawson, Dominic O'Brien, "A Multi-Gigabit/sec Integrated Multiple Input Multiple Output VLC Demonstrator", Journal of Lightwave Technology, 2017.

[2] Mohamed Sufyan Islim, Ricardo X. Ferreira, Xiangyu He, Enyuan Xie, Stefan Videv, Shaun Viola, Scott Watson, Nikolaos Bamiedakis, Richard V. Penty, Ian H. White, Anthony E. Kelly, Erdan Gu, Harald Haas and Martin D. Dawson, "Towards 10 Gb/s orthogonal frequency division multiplexing-based visible light communication using a GaN violet micro-LED", Photonics Research, 5(2), 2017.

[3] Ricardo X. G. Ferreira, Enyuan Xie, Jonathan J. D. McKendry, Sujan Rajbhandari, Hyunchae Chun, Grahame Faulkner, Scott Watson, Anthony E. Kelly, Erdan Gu, Richard V. Penty, Ian H. White, Dominic C. O'Brien and Martin D. Dawson, "High bandwidth GaN-based micro-LEDs for multi-Gbps visible light communications", IEEE Photonic Technology Letters, vol.28, no.19, pp.2023-2026, Oct. 1 2016.

[4] X. Li, N. Bamiedakis, X. Guo, J. McKendry, E. Xie, R. Ferreira, E. Gu, M. Dawson, R. Penty, and I. White, “Wireless visible light communications employing feed-forward pre-equalization and PAM-4 modulation”, Lightwave Technology, Journal of, vol.34, no.8, pp.2049-2055, 2016.

[5] J. Herrnsdorf, J. McKendry, S. Zhang, E. Xie, R. Ferreira, D. Massoubre, A. Zuhdi, R. Henderson, I. Underwood, S. Watson, A. Kelly, E. Gu, and M. Dawson, “Active-matrix GaN micro light-emitting diode display with unprecedented brightness”, Electron Devices, IEEE Transactions on, vol.62, no.6, pp.1918-1925, June 2015.

[6] X. Li, N. Bamiedakis, J. Wei, J. McKendry, E. Xie, R. Ferreira, E. Gu, M. Dawson, R. Penty, and I. White, “μLED-based single-wavelength bi-directional POF link with 10 Gb/s aggregate data rate”, Lightwave Technology, Journal of, vol.33, no.17, pp.3571-3576, Sept. 2015.

[7] A. J. Trindade, B. Guilhabert, E. Y. Xie, R. Ferreira, J. J. D. McKendry, D. Zhu, N. Laurand, E. Gu, D. J. Wallis, I. M. Watson, C. J. Humphreys, and M. D. Dawson, “Heterogeneous integration of gallium nitride light-emitting diodes on diamond and silica by transfer printing”, Opt. Express, vol.23, no.7, pp.9329-9338, Apr 2015.

[8] P. Tian, J. J. D. McKendry, J. Herrnsdorf, S. Watson, R. Ferreira, I. M. Watson, E. Gu, A. E. Kelly, and M. D. Dawson, “Temperature-dependent efficiency droop of blue InGaN micro-light emitting diodes”, Applied Physics Letters, vol. 105, no.17, 2014.

Conferences

[1] X. Li, N. Bamiedakis, J. Mckendry, E. Xie, R. Ferreira, E. Gu, M. Dawson, R. Penty, and I. H. White,“11 Gb/s WDM Transmission Over SI-POF Using Violet, Blue and Green μLEDs”, in Optical Fiber Communication Conference, OSA Technical Digest (online) (Optical Society of America, 2016), paper Tu2C.5.

[2] K Rae, EY Xie, AJ Trindade, B Guilhabert, R Ferreira, JJD McKendry, D Zhu, N Laurand, E Gu, IM Watson, CJ Humphreys, DJ Wallis, MD Dawson, “Integrated dual-color InGaN light-emitting diode array through transfer printing”, IEEE Photonics Conference (IPC), 390-391, 2015.

[3] X. Li, N. Bamiedakis, X. Guo, J. J. D. McKendry, E. Xie, R. Ferreira, E. Gu, M. D. Dawson, R. V. Penty, I. H. White, “2 Gb/s μLED-APD based visible light communications using feed-forward pre-equalization and PAM-4 modulation”, European Conference on Optical Communication (ECOC), 2015.

[4] Xin Li, Nikos Bamiedakis, Jinlong Wei, Jonathan Mckendry, Enyuan Xie, Ricardo Ferreira, Erdan Gu, Martin Dawson, Richard V Penty, Ian H White, “6.25 Gb/s POF link using GaN μLED arrays and optically generated pulse amplitude modulation”, OSA CLEO: Science and Innovations 2015, paper STu4F.7.

[5] Xin Li, Nikos Bamiedakis, Jinlong Wei, Jonathan D. McKendry, Enyuan Xie, Ricardo Ferreira, Erdan Gu, Martin D. Dawson, Richard V. Penty, Ian H. White, “8 Gb/s single-wavelength bi-directional PAM-16 SI-POF link using blue μLEDs and avalanche photodiodes”, SPIE Photonics West Opto: Optical Interconnects XV, 2015.

[6] N Bamiedakis, X Li, JJD McKendry, E Xie, R Ferreira, E Gu, MD Dawson, RV Penty, IH White. “Micro-LED-based guided-wave optical links for visible light communications”, IEEE 17th International Conference on Transparent Optical Networks (ICTON), 2015.

[7] Enyuan Xie, Jonathan D. McKendry, Ricardo Ferreira, Johannes Herrnsdorf, Sujan Rajbhandari, Hyunchae Chun, Grahame E. Faulkner, Erdan Gu, Dominic C. O’Brien, Martin D. Dawson, “Individually-n-addressable GaN-based micro-LED arrays for high-speed visible light communications at over 1 m”, SPIE Photonics West Opto, 2015.

[8] Jinlong Wei, Xin Li, Liang Geng, Jonathan J. D. McKendry, Enyuan Xie, Ricardo Ferreira, Erdan Gu, Martin D. Dawson, Richard V. Penty, Ian H. White, “High Speed Plastic Op-

tical Fiber Data Links Using LEDs", International Conference On Communication Problem-Solving (ICCP), 2014.

This article has been accepted for publication in a future issue of this journal, but has not been fully edited. Content may change prior to final publication. Citation information: DOI 10.1109/JLT.2017.2694486, Journal of Lightwave Technology

A Multi-Gigabit/sec Integrated Multiple-Input Multiple-Output VLC Demonstrator

Sujan Rajbhandari, *Member IEEE,* Aravind V. N. Jalajakumari, Hyunchae Chun, Grahame Faulkner, Katherine Cameron, Robert Henderson, Dobroslav Tsonev, *Member IEEE,* Harald Haas, *Member IEEE,* Enyuan Xie, Jonathan J. D. McKendry, *Member IEEE,* Johannes Herrnsdorf, Ricardo Ferreira, Erdan Gu, Martin D. Dawson, *Fellow IEEE,* Dominic O'Brien, *Member IEEE*

Abstract— In this paper, we report the performance of an imaging multiple input multiple output (MIMO) visible light communication (VLC) system. The VLC transmitter consists of a two-dimensional, individually addressable Gallium Nitride micro light emitting diode (µLED) array. The receiver uses a two-dimensional avalanche photodiode (APD) array fabricated using complementary metal oxide semiconductor (CMOS). Using integrated CMOS-based LED drivers, a data rate greater than 1 Gbps was obtained at a link distance of 1 m with the system field of view (FOV) of 3.45 degree using four channels. At a reduced link distance of 0.5 m, a data rate of 7.48 Gbps was obtained using a nine channel MIMO system. This demonstrates the feasibility of compact MIMO systems which offer substantial data rates.

***Index Terms*—Visible light communications, multiple input multiple output, VLC demonstrator, integrated VLC**

I. INTRODUCTION

Visible light communications (VLC) systems, realized using solid-state lighting (SSL) devices, can offer high-speed data communication in addition to their primary purpose of illumination. With the white light emitting diodes (LEDs) expected to be the dominant illumination device in the home and office environment in the near future, the use of VLC systems will grow exponentially over the coming decades [1]. As a result, there has been significant research and commercial interest in VLC systems over the last ten years (see [2] for the detailed review). This is largely due to several key advantages that VLC offers in comparison to the existing radio frequency (RF) technology, including license-free operation, high available bandwidth, high spatial diversity, innate security, and controlled beam shaping.

Phosphor based white LEDs have a low communication bandwidth (a few MHz) due to the long photoluminescence lifetimes of the phosphor [3]. The bandwidth of the blue LED itself is limited to 20-30 MHz. Using pre and post- equalisation for on-off keying (OOK) modulation, a data rate of 550 Mbps was demonstrated using a phosphorescent white LED [4]. Further enhancement in data rate was achieved by adopting advanced modulation schemes including carrierless phase and amplitude modulation (CAP) and orthogonal frequency division multiplexing (OFDM) [5], [6].

To increase the data rates further, VLC systems must use wavelength division multiplexing (WDM) and/or spatial multiplexing (also known as multiple input multiple output (MIMO)) [2]. Using WDM, VLC systems with data rates up to 10 Gbps were demonstrated [7], [8]. However, there are limited practical work using spatial MIMO and most of these are low data rate proof-of-the-concept demonstrations [9]–[11]

Research progress has been substantial in the past few years [2], and whilst a 'killer app' may provide a kick-start for VLC system [12], it is also essential to explore technologies that can make a high-speed bi-directional VLC system compatible for energy-efficient integration with existing CMOS-based consumer electronics (e.g. mobile devices). Except for the use of CMOS-based image sensors [13], [14] and other low-speed demonstrations [15], most of the practical VLC demonstrations used off-the-shelf components that are not suitable for mass production and difficult to integrate into mobile devices. In a real-time application, device and system constraints that are not encountered in the laboratory environment, including limited memory, real-time processing power, and clock rates, also need to be addressed.

In this paper, we report high-speed imaging MIMO systems which address the issues of integrating transmitter and receiver components. We have demonstrated four and nine channel MIMO systems with maximum data rate of ~890 Mbps per channel with an aggregate data rate of 7 Gbps for nine channels. Higher data rates have been demonstrated using similar transmitter devices using significantly larger area photodiodes (PDs) and bigger optical aperture at the receiver. However, these demonstrations have a very limited field of view (FOV) as collimating and focusing is used to concentrate most of the

---

Manuscript received Jan 2016;

S. Rajbhandari is with the Centre for Mobility and Transport, School of Computing, Electronics and Mathematics, Coventry University, Coventry, UK. E-mail: sujan.rajbhandari@coventry.ac.uk

H. Chun, G. E. Faulkner, and D. C. O'Brien are with the Department of Engineering Science, University of Oxford, Oxford, UK. e-mail: {hyunchae.chun, grahame.faulkner, dominic.obrien}@eng.ox.ac.uk.

K. Cameron, A. V. N. Jalajakumari, and R. Henderson are with CMOS Sensors & Systems Group, the University of Edinburgh, Edinburgh, EH9 3JL, U.K. e-mail: {K.Cameron, A.Venugopalan, Robert.Henderson}@ed.ac.uk.

D. Tsonev and H. Haas are with pureLiFi Ltd. and the Institute for Digital Communications, Li-Fi R&D Centre, The University of Edinburgh, Edinburgh, EH9 3JL, U.K. e-mail: dobroslav.tsonev@purelifi.com; h.haas@ed.ac.uk."

E. Xie, J. J. D. McKendry, J. Herrnsdorf, Ricardo Ferreira, E. Gu, and M. D. Dawson are with the Institute of Photonics, Department of Physics, University of Strathclyde, Glassgow, U.K. e-mail: {enyuan.xie, jonathan.mckendry, johannes.herrnsdorf, ricardo.ferreira, erdan.gu, m.dawson}@strath.ac.uk.

Color versions of one or more of the figures in this paper are available online at http://ieeexplore.ieee.org.

This article has been accepted for publication in a future issue of this journal, but has not been fully edited. Content may change prior to final publication. Citation information: DOI 10.1109/JLT.2017.2694486, Journal of Lightwave Technology

emitted power onto the detector [28]. Hence, the contribution of the paper is as follows:

a) Demonstration of fully integrated MIMO-VLC

CMOS technology is widely used to realize integrated circuits, especially for mass production due to low power and high-speed performance. Previously reported CMOS based LED drivers have low driving currents (less than 70mA) and limited data rate support (up to 155 Mb/s) (see [17], Table x). The CMOS-based LED driver circuit reported here can deliver up to 500 MS/s at a maximum full-scale current of 255 mA and has a power efficiency of 67%. The driver supports different modulation schemes (pulse amplitude modulation (PAM), CAP, OFDM) with the capability to drive multiple LEDs in MIMO or single-input-single-output (SISO) modes. A detailed description of the driver is reported in [18].

The fully integrated system uses an array of blue µLEDs driven by a CMOS driver and an array of avalanche photodiodes (APDs) and processing circuitry manufactured using CMOS technology. Preliminary results using 1st generation APDs receiver with a bandwidth of ~ 22 MHz (without the CMOS driver) was reported in [19], [20]. Further, results with the second generation of APDs were reported in [21]. To the best of authors' knowledge, this is the first fully integrated MIMO demonstration.

b) Demonstration of spatially dense high-speed MIMO-VLC

MIMO-VLC has so far been demonstrated only for limited data rates (often far below the maximum rate demonstrated using a single channel) [9]–[11]. In this paper, we have demonstrated data rates up to 7 Gbps using nine channels with transmitter separation of 750 µm and receiver separation of 250 µm. This demonstration improves upon /surpass the existing systems in terms of i) **higher data rate:** the previously reported maximum data rates for MIMO system (in an ideal condition i.e. without optical cross-talk) was 1.3 Gbps [10], [22]. In this paper, we have improved the data rate to 7 Gbps. This data rate was achieved using significantly smaller size photodiode (200 × 200 µm^2) instead of using large area PDs such as 7.1 mm^2 in [11], [22], 10.24 mm^2 in [10] and 15 mm^2 in [9] ii) **spatial data density:** in comparison to above-mentioned work, we demonstrated system with a high spatial density. The previous MIMO work was demonstrated with transmitter spacing in cm range (e.g. 5 cm in [11], 15 cm in [10] and 25 cm in [9]).]). In comparison, the current system has transmitter spacing of 750 µm increasing the spatial density by >4000channel/cm^2. Though this increase in the spatial density may not directly translate into the similar increment in the data rate, this demonstration provides a platform to use the multiple LEDs chips within each luminaire of the commercial chip-on-board (COB) LED architecture of illumination devices for parallel data transmission iii) **higher MIMO order:** the previously reported high-speed MIMO-VLC system are limited to 4-parallel channels. In the work, we have improved the number of channel to nine, limited by available transceivers and iv) **scalability:** since the transceiver is manufactured in CMOS technology, the system is readily scalable. We have demonstrated that the same system can be scaled from 4-channel to 9-channel. Higher order MIMO system is feasible with a larger array of the transceiver.

To the best of authors' knowledge, this is the first large-scale MIMO-VLC demonstration as we practically demonstrated a 9×9 MIMO system. We have reported a complete system with full devices and communication link characterization including error probability within the coverage distance. With the demonstration of high-speed, high-density, a large-scale MIMO-VLC system using CMOS-based LED driver and APD receiver, we have not only made system compact but also more practical for large scale integration with the existing system.

The rest of the paper is organized as follows: section II gives an overview of the MIMO VLC system. The sub-systems of the demonstrator are described in detail in this section. Section III details the experimental set-up. The experimental results are presented in Section IV. Finally, conclusions are given in Section V.

II. INTEGRATED SYSTEM DESCRIPTION

The device parameters for optimum performance of a VLC system depend on the device constraints of both the transmitter and the receiver. At the transmitter, there is an inter-relationship between the µLED area, optical power, and bandwidth. Similarly, the photodiode bandwidth depends on its active area. By incorporating the power penalty for multilevel PAM with µLED constraints (area-bandwidth-output power relationship) and APD constraints (area-bandwidth relationship) in link budget analysis, a realistic target of 1 Gbps at 1m distance was established for this integrated MIMO-VLC system. A conservative goal of 1 Gb/s over 1 m was chosen based on the preliminary modelling of likely available µLED devices and CMOS-based receiver sensitivities. Though the link distance is lower than average distance ceiling/user, the system is scalable to a longer distance. Refer to [19] for detailed derivations of these parameters and numerical values.

A. Transmitter Subsystem

The transmitter subsystem consists of the µLED driver chips, the µLED array and associated printed circuit boards (PCB). The µLED driver chip is designed and implemented in an Austria Micro Systems 0.18 µm CMOS process. Each chip consists of four independent current steering digital to analogue converter (DAC) based driver channels each with 8-bit resolution. The chip can drive four individual LEDs in a ganged mode (i.e. all channels driving the same data stream) or MIMO mode (each channel driving an independent data stream). In MIMO mode, each driver operates with four times lower clock rate. Each driver channel can deliver full-scale current up to 255 mA (i.e. ~1A per chip), and power efficiency is 67 % [18]. The DC bias current of each DAC can be varied independently from 16 mA to 255 mA with a 4-bit resolution. The DAC is designed to operate at a maximum sampling frequency of 500 MS/s. A custom PCB platform provides an interface between the driver chip and a field programmable gate array (FPGA) card (Opal Kelly XEM6310) (see Fig. 1). The FPGA provides the data, sampling clock, and other control signals to the driver chip. The full electrical characteristic of driver chip was reported in [18].

This article has been accepted for publication in a future issue of this journal, but has not been fully edited. Content may change prior to final publication. Citation information: DOI 10.1109/JLT.2017.2694486, Journal of Lightwave Technology

B. µLEDs

The MIMO device consists of a 6×6 array of individually-addressable µLEDs with 39 µm diameter and was fabricated from commercially available GaN LED wafer material, grown on a 2” c-plane sapphire substrate. Each individual µLED has a common p-contact and an individually addressable n-contact to make them compatible for driving with an NMOS-based CMOS driver. The MIMO µLED array is arranged in nine 2×2 clusters with a pitch of 69 µm between two adjacent µLED elements (**Error! Reference source not found.**(a)). The separation between adjacent clusters is 750 µm making an end-to-end separation of 1500 µm. The nominal peak emission wavelength for each µLED is 450 nm with 20 nm full width at half maximum line width.

The µLED array is wire bonded to a 132-pin ceramic package which is attached to a daughter card (see **Error! Reference source not found.**(b)). The daughter card is connected to a motherboard through four high-speed connectors, and the motherboard is connected to the LED driving subsystem. This hierarchical approach allows the LED array to be easily exchanged with another array.

C. Receiver

A 3×3 APD array of detectors, each 200 µm×200 µm on 240 µm pitch was designed and fabricated in 0.18µm CMOS process as shown inside the rectangular box in Fig. 3. The outer APDs are tested structures not relevant to this work. The APDs have a responsivity of 2.61 A/W at 450 nm with a reverse bias voltage of 9.1 V. Each APD has an associated transimpedance amplifier in a shunt-shunt feedback topology. The shunt-shunt feedback topology was selected as it offers better noise performance than alternatives. The outputs of all nine APDs can be accessed simultaneously via SMA connectors.

D. Optical Design

An imaging MIMO system is preferred over a non-imaging MIMO system, as the channel **H**-matrix of an imaging system can be well-conditioned [14]. To achieve a full rank matrix in the imaging MIMO system, the image of more than one source should not fall entirely into the same receiver i.e.

$$\frac{p}{f} \le \frac{s}{d}\ ; \qquad (1)$$

where s is the source spacing, p is the PD width, f is the focal length of the receiver optics system and d is the link length. The ratio (p/f) governs the receiver FOV of the imaging system.

The transmitter and the receiver optical systems are designed using a combination of commercially available aspheric singlet lenses (see **Error! Reference source not found.**). The transmitter and receiver optics have apertures of 45 mm and 23 mm, respectively and the distances of 37 mm and 21.5 mm to the lenses front edge from µLED and PD, respectively. The optics system was optimized for a 4×4 imaging MIMO system using ray tracing software. However, there is a flexibility to adjust the optics for other MIMO configurations. The transmitter optics is designed to offer a full divergence angle of 7.5 degrees. The divergence angle and FOV are calculated based on a link budget analysis to offer at least 1 Gbps data rate at a 1m link distance. The receiver optics does not only create an image of the LED array but also provides an optical gain. The receiver has full FOV of 3.5 degrees. The FOV of the receiver is limited by the number of available APDs in the array. In order to increase the FOV, a significantly larger array of APDs is required [23].

III. EXPERIMENTAL SET-UP

In this paper, we report a practical demonstration of the integrated four-channel MIMO-VLC system using state-of-the-art CMOS technology. We have also demonstrated four and nine-channel MIMO-VLC system driven using arbitrary waveform generator (AWG) that show the high-speed capacity of the system. A simplified block diagram of the MIMO-VLC experimental set-up using CMOS driver is shown in

(a) and picture of the setup is given in

(b). To achieve an aggregate data rate of 1 Gbps or higher, two DAC driver chips were required as the maximum sampling rate the Opal Kelly FPGA supports was limited to 375 MS/s. Each DAC chip drives two µLEDs in MIMO mode. The synchronization of the two driver chips was achieved by configuring them in a master-slave configuration where a 10 MHz clock from a master DAC chip was used as the reference clock for the slave chip.

In the AWG-based system, DAC drivers are replaced with AWGs (Agilent 81150A). One µLED in each cluster of four were used for nine-channel system whereas only µLEDs from corner clusters were used for the four-channel system (see Fig. 2(a)). The electrical outputs from the APDs were acquired using oscilloscopes for further offline processing which includes low pass filtering, equalisation and signal decoding. The four-channel MIMO systems were evaluated at a link distance of 1m and the nine-channel system was evaluated at 0.5 m

In a bandlimited MIMO system, both spatial (among MIMO channels) and temporal (intersymbol) interferences occur. To mitigate these interferences, a joint spatial and temporal decision feedback equalization (DFE) as outlined in [24] are adopted in this work.

IV. SYSTEM PERFORMANCE

The system under test is fully characterized and optimum operating conditions for both transmitter and receiver are determined. For data rate evaluation, a bit error threshold of 3.8×10^{-3} is adopted as recommended by ITU [25].

A. System characterization

The measured intrinsic bandwidth and optical power of µLED device are shown in Fig. 6(a). The electrical-to-electrical (E-E) bandwidth and optical power of µLED increase with the driving current. The measured optical power at 100mA current is ~3.3 mW. The measured frequency response of the APD arrays is given in Fig. 6(b). Except for two APDs which show a resonant dip at 63 MHz, the remaining APDs have a bandwidth >90 MHz which is limited by parasitic capacitance. The resonant dips in these two APDs are possibly caused by them being close to the pads. Further investigation on the issue is being carried out and will be rectified in future iterations.

In order to determine if the DAC driver has any adverse effect on the system performance, the bandwidth of the system was evaluated by driving µLEDs with a DAC and with an AWG under similar bias current using sinusoidal signals of different frequencies. The sampling rate of the DAC is fixed to 250 MS/s whereas the AWG has a sampling rate of 2 GS/s. Fig. 7 shows the measured bandwidth of the complete system (µLED + APD). As expected, the bandwidth of the µLEDs increases with an increase in the average current (see Fig. 6(a)). It can be observed that the DAC driver has a lower bandwidth than the AWG. The DAC output waveforms exhibit longer fall times than rise times as the CMOS driver has an active rise and passive fall due to the current-steering approach, which reduces the bandwidth. Nonetheless, the DAC does not significantly degrade the frequency response. For example, a -4 dB level is obtained at 52 MHz and 50 MHz for AWG and DAC, respectively (~ 4% difference). Note that frequency response beyond 50 MHz is not reliable for the DAC due to a low sampling rate. Based on this result, the average current per LEDs was set to ~ 45mA for the results presented in the following sections.

B. *System FOV*

The overall FOV of the system (transmitter with the transmitter optics and receiver with the receiver optics) was evaluated by driving a single µLED and measuring the output signals from all APDs. The transmitter position was fixed while the receiver was displaced horizontally (perpendicular to the direction of propagation of light) in steps of 5 mm. The total received power was calculated by summing the APDs' output. The normalized total received power (i.e. DC channel gain) versus the horizontal displacement is shown in **Error! Reference source not found.**. The coverage diameter at 1 m distance is ~60 mm, which corresponds to an overall system FOV of 3.45 degrees, limited by the number of available APDs. With a larger APD array, the FOV can be increased e.g. with an array of 5×5 APDs, the FOV is estimated to be ~7 degrees. The maximum achievable data rate using maximal-ratio combining (MRC) and equal gain combining (EGC) methods are also shown in the figure for a 4-PAM scheme with DFE. As expected, MRC offers higher data rate than EGC. The maximum data rate achieved using EGC and MRC are of 440 Mbps and ~500Mbps, respectively.

C. *4-channel MIMO performance*

1) *DAC drivers*

To evaluate the performance of the full integrated MIMO system, four µLEDs were driven by two DAC drivers in the MIMO mode with independent data streams. The signals from all the APDs were captured and further processing (filtering, downsampling and equalization) was done offline. The aggregate data rates against the displacement of the MIMO system with 4-PAM modulation scheme is shown in **Error! Reference source not found.**. As it was not feasible to obtain an aggregate data rate beyond 750 Mbps for 2-PAM due to FPGA limitations, 2-PAM results are not presented here. The minimum and maximum data rates achieved were ~1.23 and ~1.3 Gbps, which correspond to a net rate of ~1.14 and ~1.21 Gbps respectively after 7 % forward error correction (FEC) overhead reduction. The data rates with the DAC drivers were limited by the available sampling rate and lower bandwidth.

2) *Waveform generators*

As outlined in [26], the optimum PAM level with a DFE depends on the ratio of the bandwidth and data rate, available signal-to-noise (SNR) and dynamic range. Hence, it is necessary to establish the optimum PAM level case-by-case basis as a generalized conclusion is difficult to draw. In order to determine the optimum PAM level, the BER performance of different PAM level under the identical operating condition is evaluated. Fig. 10 illustrates the data rate against BER of 2, 4 and 8-PAM with DFE, evaluated for a single channel (without any cross-talk) at 1 m link distance. This clearly demonstrates that 4-PAM offers the optimum performance closely followed by 2-PAM. 8-PAM offered a significantly lower BER performance.

Fig. 1. The data rate vs BER for 2, 4 and 8-PAM with DFE, evaluated for a single channel at 1m link distance.

The aggregate data rates against the displacement of the four-channel MIMO-VLC system with 2-PAM and 4-PAM modulation schemes for the experiments with AWGs is shown in Fig. 11(a). The minimum and maximum data rates achieved within the coverage area using 4-PAM are 1.35 and 1.96 Gbps (i.e. 1.25 and 1.8 Gbps, respectively after the 7 % overhead FEC reduction). This corresponds to a maximum data rate of ~ 500 Mbps per channel. Note that higher data rates (2 Gbps using pre-equalised 4-PAM [27] and 3 Gbps using OFDM [28]) were achieved using µLEDs. However, those demonstrations used significantly larger area PDs and bigger optical aperture; and hence had significantly higher SNR with limited FOV.

Fig. 2. a) the aggregate data rates versus the displacement of the integrated MIMO system with the AWGs b) eye-diagrams of the received 4-PAM signal at 200 Mbps (left) and after applying ZF (right) for channel 2 at a displacement of 5 mm and c) eye-diagrams of the received 4-PAM signal at 200 Mbps (left) and after applying ZF (right) for channel 2 at a displacement of 20 mm.

As shown in Fig. 11, there is a variation in the aggregate data rates within the FOV. The variation in data rates is due to: a) variation in inter-channel interference (ICI) and b) fill factor of APD array. It is feasible to design MIMO optical system with negligible cross-talk for a point-to-point link with the fixed transceiver position. However, when the transceiver positions are not fixed, the ICI (i.e. the condition number of the **H**-matrix and system capacity) depends on the relative position and orientation the transceiver. Secondly, the APD array has a fill factor of ~80 %. As the orientation of the transceiver changes, a significant proportion of the optical intensity may not be detected, this reduces the overall received power. For example, the overall channel gain (i.e. the sum of all the elements in **H**-matrix) at a displacement of 15 mm is 0.16 which is ~11% less than at 5mm where the channel gain is ~0.18. However, the **H**-matrix condition numbers are 2.7 and 2.2 (~ 18% variation) which significantly reduced the achievable data rate at 15 mm. On the other hand, the channel gain at 35mm is 0.12 and a significantly lower data rate is expected. The optical cross-talk at different displacements is demonstrated by Fig. 11(b) and (c). Fig. 11(b) shows eye-diagrams of the received signal and the signal after applying zero-forcing (ZF) equalizer at 5 mm where the cross-talk is negligible. Hence, a clear eye-opening can be observed. On the other hand, Fig. 11(c) demonstrates that the signal recovery is not possible without an equalizer as the eye is completely closed due to ICI.

D. Nine Channel MIMO with AWGs

In order to demonstrate the feasibility of higher order, high-speed, dense spatial density MIMO system, a nine channel MIMO-VLC was studied. Nine is the maximum channel that the current set-up accommodates due to the limited number of available APDs. However, it is feasible to scale the system when the receiver with a higher number of APDs became available. To evaluate the performance of the 9×9 MIMO system, one µLED from each cluster of nine (see Fig. 2(a)) was driven by AWGs. The link distance was reduced to 0.5 m so that the imaging MIMO condition given by (1) was satisfied.

As in the case of 4-channel system, 2,4 and 8- PAM with DFE were evaluated to determine the best performance. The 8-PAM offered the best performance, followed by 4-PAM as reducing link distance to half (0.5 m) increases the SNR by at least 6 dB (see [26] for a theoretical comparison PAM under different ISI and SNR).

The BER against the date rate for nine channel MIMO system for 8-PAM is given in Fig. 12. The BER for a channel was measured when all µLEDs corresponding to its neighboring channels were active so that the channel experiences the maximum possible inter-channel interference. For example, to estimate data rate for µLEDs in the top-left corner (Fig. 2(a)), all µLEDs except the one in the bottom-right corner were active. The signal from APDs was then captured and joint MIMO decoding algorithm was applied. Each channel can support data rates up to 890 Mbps. The aggregate data rate for the nine channels is 7.48 Gbps, which is ~ 6.95 Gbps after removing 7% FEC overhead. Note that the FOV of the 9 channel MIMO system is significantly smaller (theoretically less than 8 mrad) due to a limited number of available APD.

V. CONCLUSIONS AND FUTURE WORK

In this work, we have developed and demonstrated a complete integrated MIMO-VLC system that can support complex modulation schemes such as PAM and. Using two-dimensional arrays of µLEDs and APDs, and imaging optical system specifically designed for this purpose, combined with an imaging optical system, an integrated 4-channel MIMO system was demonstrated with aggregate data rates beyond 1 Gbps. Furthermore, we also we demonstrate a four-channel system with a minimum aggregate date rate of 1.35 Gbps and an FOV of 3.45 degrees at 1m. This paper also shows the feasibility of a high-speed spatially dense nine-channel MIMO system that achieved data rates beyond 7 Gbps at a link distance of 0.5 m.

The FOV and range of the current system is limited due to the number of available APDs, as well as the source array size. Work to use WDM, improved receiver optics, more efficient sources, and novel receiver designs is underway. This will focus on achieving practical fields of view and coverage areas, whilst maintaining high data rates.

ACKNOWLEDGMENT

The authors gratefully acknowledge support by the UK Engineering and Physical Sciences Research Council (EPSRC) under grant EP/K00042X/1.

Associated data for the figures can be found at http://dx.doi.org/10.15129/bac75eed-3f9e-4a14-81f6-56f25d11138a

REFERENCES

[1] A. Jovicic, L. Junyi, and T. Richardson, “Visible light communication: opportunities, challenges and the path to market,” *Commun. Mag. IEEE*, vol. 51, no. 12, pp. 26–32, 2013.

[2] S. Rajbhandari, J. J. D. Mckendry, J. Herrnsdorf, H. Chun, G. Faulkner, H. Haas, I. M. Watson, D. O. Brien, and M. D. Dawson, “A review of Gallium Nitride LEDs for multi-gigabit-per-second visible light data communications,” *Semicond. Sci. Technol.*, vol. 32, no. 2, p. 23001, 2017.

[3] H. Le Minh, D. O’Brien, G. Faulkner, Z. Lubin, L. Kyungwoo, J. Daekwang, O. Yunje, and W. Eun Tae, “100-Mb/s NRZ visible light communications using a postequalized white LED,” *IEEE Photonics Technol. Lett.*, vol. 21, no. 15, pp. 1063–1065, 2009.

[4] H. Li, X. Chen, J. Guo, and H. Chen, “A 550 Mbit/s real-time visible light communication system based on phosphorescent white light LED for practical high-speed low-complexity application,” *Opt. Express*, vol. 22, no. 22, pp. 27203–27213, 2014.

[5] F. Wu, C. Lin, C. Wei, and C. Chen, “1.1-Gb/s white-LED-based visible light communication employing carrier-less amplitude and phase modulation,” *IEEE Photonics Technol. Lett.*, vol. 24, no. 19, pp. 1730–1732, 2012.

[6] A. M. Khalid, G. Cossu, R. Corsini, P. Choudhury, and E. Ciaramella, “1-Gb/s transmission over a phosphorescent white LED by using rate-adaptive discrete multitone modulation,” *IEEE Photonics J.*, vol. 4, no. 5, pp. 1465–1473, 2012.

[7] H. Chun, S. Rajbhandari, G. Faulkner, D. Tsonev, E. Xie, J. J. D. McKendry, E. Gu, M. D. Dawson, D. O’Brien, and H. Haas, “LED based wavelength division multiplexed 10 Gb/s visible light communications,” *J. Light. Technol.*, vol. 34, no. 13, pp. 3047–3052, 2016.

[8] Y. Wang, L. Tao, X. Huang, J. Shi, and N. Chi, “8-Gb/s RGBY LED-Based WDM VLC System Employing High-Order CAP Modulation and Hybrid Post Equalizer,” *IEEE Photonics J.*, vol. 7, no. 6, pp. 1–7, 2015.

[9] A. Burton, H. Minh, Z. Ghassemlooy, E. Bentley, and C. Botella, “Experimental demonstration of 50-Mbps visible light communications using 4 × 4 MIMO,” *IEEE Photonics Technol. Lett.*, vol. 26, 2014.

[10] A. H. Azhar, T. Tran, and D. C. O’Brien, “A gigabit/s indoor wireless transmission using MIMO-OFDM visible-light communications,” *IEEE Photonics Technol. Lett.*, vol. 25, no. 2, pp. 171–174, 2013.

[11] W. Yuanquan, C. Nan, Y. Wang, and N. Chi, “Demonstration of high-speed 2x2 non-imaging MIMO Nyquist single carrier visible light communication with frequency domain equalization,” *Light. Technol. J.*, vol. 32, no. 11, pp. 2087–2093, 2014.

[12] S. Hranilovic, L. Lampe, S. Hosur, and R. D. Roberts, “Visible light communications: The road to standardization and commercialization (Part 2),” *IEEE Commun. Mag.*, vol. 52, no. 7, pp. 62–63, 2014.

[13] S. D. Perli, N. Ahmed, and D. Katabi, “PixNet: interference-free wireless links using LCD-camera pairs,” *Proceedings of the sixteenth annual international conference on Mobile computing and networking*. ACM, Chicago, Illinois, USA, pp. 137–148, 2010.

[14] I. Takai, S. Ito, K. Yasutomi, K. Kagawa, M. Andoh, and S. Kawahito, “LED and CMOS image sensor based optical wireless communication system for automotive applications,” *IEEE Photonics J.*, vol. 5, no. 5, p. 6801418, 2013.

[15] A. Mirvakili and V. Koomson, “A flicker-free CMOS LED driver control circuit for visible light communication enabling concurrent data transmission and dimming control,” *Analog Integr. Circuits Signal Process.*, vol. 80, no. 2, pp. 283–292, 2014.

[16] R. X. G. Ferreira, E. Xie, J. J. D. McKendry, S. Rajbhandari, H. Chun, G. Faulkner, S. Watson, A. E. Kelly, E. Gu, R. V Penty, I. H. White, D. C. O’Brien, and M. D. Dawson, “High bandwidth GaN-based micro-LEDs for multi-Gbps visible light communications,” *IEEE Photonics Technol. Lett.*, vol. 28, no. 19, pp. 2023–2026, 2016.

[17] T. Kishi, H. Tanaka, Y. Umeda, and O. Takyu, “A high-speed LED driver that sweeps out the remaining carriers for visible light communications,” *J. Light. Technol.*, vol. 32, no. 2, pp. 239–249, 2014.

[18] A. V. N. Jalajakumari, D. Tsonev, K. Cameron, H. Haas, and R.

This article has been accepted for publication in a future issue of this journal, but has not been fully edited. Content may change prior to final publication. Citation information: DOI 10.1109/JLT.2017.2694486, Journal of Lightwave Technology

Henderson, “An energy efficient high-speed digital LED driver for visible light communications,” in *2015 IEEE International Conference on Communications (ICC)*, 2015, pp. 5054–5059.

[19] S. Rajbhandari, H. Chun, G. Faulkner, K. Cameron, A. V. N. Jalajakumari, R. Henderson, D. Tsonev, M. Ijaz, Z. Chen, H. Haas, E. Xie, J. J. D. McKendry, J. Herrnsdorf, E. Gu, M. D. Dawson, and D. O Brien, “High-speed integrated visible light communication system: Device constraints and design considerations,” *IEEE J. Sel. areas Commun.*, vol. 33, no. 9, pp. 1750–1757, 2015.

[20] S. Rajbhandari, H. Chun, G. Faulkner, K. Cameron, A. V. N. Jalajakumari, R. Henderson, D. Tsonev, M. Ijaz, Z. Chen, H. Haas, E. Xie, J. J. D. McKendry, J. Herrnsdorf, E. Gu, and M. D. Dawson, “Imaging-MIMO Visible Light Communication System using µLEDs and Integrated Receiver,” in *Globecom Workshops (GC Wkshps), 2014 IEEE*, 2014, pp. 621–625.

[21] S. Rajbhandari, C. Hyunchae, G. Faulkner, D. O’Brien, A. V. N. Jalajakumari, K. Cameron, R. Henderson, X. Enyuan, J. J. D. McKendry, J. Herrnsdorf, E. Gu, M. D. Dawson, D. Tsonev, M. Ijaz, and H. Haas, “Multi-Gigabit integrated MIMO visible light communication system: Progress and updates,” in *Summer Topicals Meeting Series (SUM), 2015*, 2015, pp. 230–231.

[22] T. Chen, L. Liu, Z. Zheng, J. Song, K. Wu, and W. Hu, “Fisheye-lens-based space division multiplexing system for visible light communications,” *EURASIP J. Wirel. Commun. Netw.*, vol. 2015, no. 1, pp. 1–7, 2015.

[23] P. Djahani and J. M. Kahn, “Analysis of infrared wireless links employing multibeam transmitters and imaging diversity receivers,” *IEEE Trans. Commun.*, vol. 48, no. 12, pp. 2077–2088, 2000.

[24] R. Fischer, J. Huber, and C. Windpassinger, “Signal processing in decision-feedback equalization of intersymbol-interference and multiple-input/multiple-output channels: a unified view,” *Signal Processing*, vol. 83, no. 8, pp. 1633–1642, 2003.

[25] ITU, “Forward error correction for high bit-rate DWDM submarine systems ,” *ITU G.975.1*. ITU, 2004.

[26] S. Randel, F. Breyer, S. C. J. Lee, and J. W. Walewski, “Advanced modulation schemes for short-range optical communications,” *IEEE J. Sel. Top. Quantum Electron.*, vol. 16, no. 5, pp. 1280–1289, 2010.

[27] X. Li, N. Bamiedakis, X. Guo, J. McKendry, E. Xie, R. Ferreira, E. Gu, M. Dawson, R. Penty, and I. White, “Wireless visible light communications employing feed-forward pre-equalization and PAM-4 modulation,” *J. Light. Technol.*, vol. 34, no. 8, pp. 2049–2055, 2016.

[28] D. Tsonev, H. Chun, S. Rajbhandari, J. McKendry, S. Videv, E. Gu, M. Haji, S. Watson, A. Kelly, G. Faulkner, M. Dawson, H. Haas, and D. O’Brien, “A 3-Gb/s single-LED OFDM-based wireless VLC link using a Gallium Nitride µLED,” *IEEE Photonics Technol. Lett.*, vol. 26, no. 7, pp. 637–640, 2014.

Research Article Vol. 5, No. 2 / April 2017 / *Photonics Research* A35

PHOTONICS Research

Towards 10 Gb/s orthogonal frequency division multiplexing-based visible light communication using a GaN violet micro-LED

Mohamed Sufyan Islim,[1,*,†] Ricardo X. Ferreira,[2,†] Xiangyu He,[2,†] Enyuan Xie,[2] Stefan Videv,[3] Shaun Viola,[4] Scott Watson,[4] Nikolaos Bamiedakis,[5] Richard V. Penty,[5] Ian H. White,[5] Anthony E. Kelly,[4] Erdan Gu,[2] Harald Haas,[3] and Martin D. Dawson[2]

[1]*Li–Fi R&D Centre, the University of Edinburgh, Institute for Digital Communications, King's Buildings, Mayfield Road, Edinburgh EH9 3JL, UK*
[2]*Institute of Photonics, Department of Physics, University of Strathclyde, Glasgow G1 1RD, UK*
[3]*Institute for Digital Communications, Li–Fi R&D Centre, the University of Edinburgh, King's Buildings, Mayfield Road, Edinburgh EH9 3JL, UK*
[4]*School of Engineering, University of Glasgow, Glasgow G12 8LT, UK*
[5]*Centre for Advanced Photonics and Electronics, Electrical Engineering Division, Department of Engineering, University of Cambridge, Cambridge CB3 0FA, UK*
**Corresponding author: m.islim@ed.ac.uk*

Received 28 November 2016; revised 9 February 2017; accepted 9 February 2017; posted 10 February 2017 (Doc. ID 280671); published 28 March 2017

Visible light communication (VLC) is a promising solution to the increasing demands for wireless connectivity. Gallium nitride micro-sized light emitting diodes (micro-LEDs) are strong candidates for VLC due to their high bandwidths. Segmented violet micro-LEDs are reported in this work with electrical-to-optical bandwidths up to 655 MHz. An orthogonal frequency division multiplexing-based VLC system with adaptive bit and energy loading is demonstrated, and a data transmission rate of 11.95 Gb/s is achieved with a violet micro-LED, when the nonlinear distortion of the micro-LED is the dominant noise source of the VLC system. A record 7.91 Gb/s data transmission rate is reported below the forward error correction threshold using a single pixel of the segmented array when all the noise sources of the VLC system are present.

OCIS codes: (060.4510) Optical communications; (060.2605) Free-space optical communication; (230.3670) Light-emitting diodes; (230.3990) Micro-optical devices.

https://doi.org/10.1364/PRJ.5.000A35

1. INTRODUCTION

The increasing demands of communication services are challenging radio frequency (RF) wireless communications technologies. The overall number of networked devices is expected to reach 26.3 billion in 2020 [1]. Visible light communication (VLC) is a promising solution to the limited availability of the RF spectrum as the visible light spectrum offers abundant bandwidth that is unlicensed and free to use. VLC improves the spectral efficiency per unit area, which enhances the quality of service in crowded environments and allows for secure and localized services to be provided.

General lighting is under a rapid transformation to become semiconductor based due to huge energy savings. This transformation has already enabled applications such as active energy consumption control and color tuning. Solid state lighting devices such as gallium nitride (GaN)-based inorganic light emitting diodes (LEDs) are ubiquitous power-efficient devices to enable illumination and communications. Commercially available LEDs have a limited frequency response due to the yellow phosphor coating on top of the blue LED chips. However, the slow response of the yellow phosphor can be filtered out using a blue filter in front of the receiver. Recent results for VLC using a phosphorescent white LED with adaptive bit and energy loading were reported at 2.32 Gb/s aided by a two-staged linear software equalizer [2].

Micro-LEDs are promising candidates in enabling lighting as a service (LaaS) and Internet of things (IoT). The introduction of micro-LEDs has enabled high-performance value-added lighting functions such as VLC and indoor positioning and tracking [3]. Micro-LEDs are known for their small active areas enabling high current density injection, which drives the modulation bandwidth to hundreds of megahertz [4,5]. At 450 nm, micro-LEDs have set the standard for high-speed VLC. A 60 μm diameter pixel has achieved 3 Gb/s [6], and more recently a single pixel of a new segmented array has demonstrated 5 Gb/s [7]. The novel micro-LEDs emitting at

2327-9125/17/020A35-09 Journal © 2017 Chinese Laser Press

400 nm featured in the current work offer a number of advantages over the 450 nm devices previously reported [7]. From typical trends concerning the internal quantum efficiency (IQE) of indium GaN-based active regions, comparable IQEs are expected at 400 and 450 nm, whereas the IQE decreases steeply at shorter emission wavelengths [8]. For generation of white light for illumination, the use of violet-emitting LEDs exciting tricolor (red, green, and blue) phosphors also offers advantages over the widely used method of combining blue direct LED emission with a yellow-emitting phosphor. These include much superior color rendering indices [9,10] and the absence of a direct blue component, which has proven to be disruptive to the human circadian rhythm [11]. The micro-LED die shapes employed in this work are also expected to be advantageous for efficient light extraction, by analogy with previous designs employing non-circular emitting areas [12].

VLC is enabled by incoherent illumination from the light sources. Therefore, only real and positive modulating waveforms can be realized. Single carrier modulation schemes such as on–off keying (OOK), pulse amplitude modulation (PAM), and pulse width modulation (PWM) are straightforward to implement. However, the performance of these modulation schemes degrades as the transmission speed increases due to the increased inter-symbol interference (ISI). Equalization techniques can be used to improve the system performance at significant computation cost [13]. Multi-carrier modulation techniques such as orthogonal frequency division multiplexing (OFDM) are promising candidates for VLC. Computationally efficient single-tap equalizers are straightforward to realize in OFDM. Adaptive bit and energy loading in OFDM allows the channel utilization to approach the information capacity limit. In addition, multiple access can be easily supported in OFDM by assigning groups of subcarriers to multiple users, which is known as orthogonal frequency division multiple access (OFDMA).

Previously, a 40 μm diameter micro-LED at 405 nm achieved a data rate of 3.32 Gb/s at an optical power of 2.5 mW with electrical–optical bandwidth up to 307 MHz [14]. In this paper, we present a high bandwidth VLC link at 400 nm. The emitter consists of a single pixel of the segmented micro-LED array design introduced in Ref. [7]. This device achieves 2.3 mW of optical output power while maintaining an electrical-to-optical (E-O) bandwidth of 655 MHz. A VLC system is realized with a modulation bandwidth of 1.81 GHz, evaluated beyond the 3 dB bandwidth of the system. A transmission rate of 11.95 Gb/s is presented, when the nonlinear distortion noise of the micro-LED is the major source of noise in the system. A record transmission rate at 7.91 Gb/s is presented when all the noise sources of the VLC system are considered.

2. VIOLET MICRO-LED

A. Design and Fabrication

The design of standard GaN LEDs is based on a large-area chip assembled on a package that maximizes heat extraction through an n-pad at the bottom for a flip-chip configuration. This creates two limitations: a large capacitance due to the package contact area and an upper limit on the current density due to the rapid self-heating of a large-area chip. The design and fabrication process of the micro-LED array used in this work is as reported in our previous work [7]. It consists of two circular micro-LED arrays, an inner and an outer, containing 5 and 10 pixels, respectively. Originally designed to match the geometry of plastic optical fiber, the inner and outer pixels have active areas of 435 and 465 μm^2, respectively. This compares with the 1256 μm^2 active area for the 405 nm device in Ref. [14]. Figure 1 shows optical images of this micro-LED array, together with a schematic of the pixel layout.

The wafer used in this work is for a commercially available GaN-based LED emitting at 400 nm. In order to fabricate these arrays, micro-LEDs emitters are etched by inductively coupled plasma to expose n-type GaN. An annealed Pd layer is used as a metal contact to p-type GaN. Each emitter is isolated by a layer of SiO_2. The metallization on the n-type GaN is formed by depositing a Ti/Au metal bilayer, which fills the area between each micro-LED and enables an improved current spreading. This bilayer connects each micro-LED emitter in order to individually address them. The micro-LED array allows increasing the total output power with minimal reduction in performance due to mutual heating between pixels. The low optical power per pixel in micro-LEDs is a challenge when combined illumination and communication is considered. This problem can be addressed by using large arrays of pixels, where a system capable of handing the communication link over multiple pixels can be designed to reduce the duty cycle, reduce the junction temperature on individual pixels, and maintain high efficiency. These investigations are subject to future work.

B. Performance Measurements

The electrical performance of the micro-LED arrays was measured by a semiconductor analyzer (HP 4155). The optical power of the arrays under direct current (DC) conditions was measured using a Si detector placed in close proximity to the polished sapphire substrate. A spectrometer and a charge coupled device detection system were used for the collection

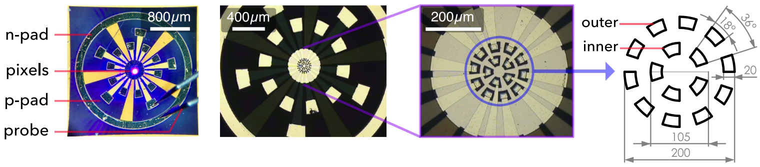

Fig. 1. Plan view micrographs of the segmented micro-LED arrays. The magnified micrographs on the right show the array configuration and individual pixel design. A diagram is also included noting the inner and outer pixels (dimensions in micrometers).

of electroluminescence spectra. The small signal frequency response was measured by a network analyzer with a 20 mV alternating current (AC) frequency sweep signal combined in a bias-tee with a DC-bias current ranging from 5 to 50 mA. The optical response was collected by a lens system and focused onto a fast photodiode (PD) and fed to the network analyzer. All the measurements were performed at room temperature with the device directly probed on chip with a high-speed probe to guarantee minimal parasitic effects.

1. *I–V and L–I Characteristics*

Devices with linear luminescence–voltage (L–V) characteristics and high optical power allow for a large dynamic range that can accommodate large swings of modulating signals, and this subsequently improves the signal-to-noise ratio (SNR) of the VLC system. The current–voltage (I–V) and luminescence–current (L–I) characteristics for the micro-LED are presented in Fig. 2. The pixels present a shunt resistance responsible for a subthreshold turn-on; this is attributed to damaged regions in the junction and by surface imperfections. Differences between the inner and the outer pixels are minimal in I–V with a series resistance of 27 and 26 Ω and threshold turn-on voltage of 4.60 and 4.64 V for the inner and outer pixels, respectively. In terms of optical power, at the roll-over point, the outer pixels achieve a maximum of 2.79 mW, 17% higher than the inner pixel, which is expected given the larger active area. This compares to 2.5 mW from a pixel at 405 nm with a 2.88 times larger active area [14]. The improvement in the optical power is due to the improved *Pd p*-type contact, resulting in 50% higher optical power compared to Ref. [14]. In addition, the commercially supplied wafer for this micro-LED gives better IQE.

2. *Frequency Response*

The frequency response from 100 kHz to 1.5 GHz for the lowest and highest bias currents of the testing set are presented in Fig. 3. At 1.5 GHz modulation, the pixels do not reach the noise floor of the system, thus providing a large useful bandwidth for data transmission. The calculated E-O bandwidth against current density is shown in the inset of Fig. 3 for the set of bias currents covering the full operating range. The current densities for these pixels are in line with what was previously seen at 450 nm [7], meaning that the pixels achieve similar bandwidth at the same current density. This is also compared with 307 MHz bandwidth for the 405 nm device in Ref. [14]. The improvement in bandwidth over [14] is due to the smaller active area of the device that allowed higher current density and shorter carrier lifetime. With a bandwidth of 655 MHz for the inner pixel, to the authors' best knowledge, this micro-LED has the highest bandwidth yet shown in the violet wavelength band.

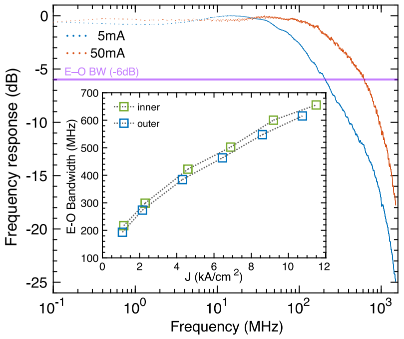

Fig. 3. Small signal frequency response for the inner pixel at 5 and 50 mA. The inset shows 6 dB E-O bandwidth at different values for the current density *J*, corresponding to DC-bias values of 5–50 mA.

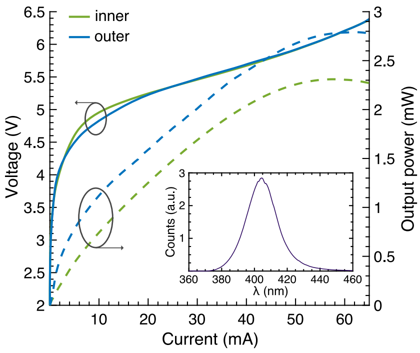

Fig. 2. Combined current–voltage (I–V), left, and luminescence–current (L–I), right, characteristics of both inner and outer pixels. The inset shows the emission spectrum of an inner pixel at 50 mA.

3. VLC SYSTEM

A. Optical OFDM

Multiple variants of OFDM have been proposed for VLC [15]. Conventional OFDM waveforms are both complex and bipolar; however, Hermitian symmetry can be imposed on the OFDM subcarrier frame to realize real-valued OFDM waveforms, $X[k] = X^*[N_{\mathrm{FFT}} - k]$, where N_{FFT} is the OFDM frame size, and k is the subcarrier index. In addition, subcarriers at $X[0]$ and $X[N_{\mathrm{FFT}}/2]$ are set to zero. DC-biased optical OFDM (DCO-OFDM) uses a DC bias to shift most of the negative real-valued OFDM samples into positive. The block diagram for OFDM is shown in Fig. 4. The generation of DCO-OFDM in this VLC experiment starts with generating a real-valued OFDM waveform in MATLAB. A pseudo-random bit sequence (PRBS) is generated and then modulated using quadrature amplitude modulation (QAM). Given the *a priori* estimated SNR, the M_k-QAM constellation size at subcarrier k and its corresponding relative energy, ν_k^2, are adaptively allocated based on the probability of error target, P_e^T.

The QAM symbols are loaded into orthogonal subcarriers with subcarrier spacing equal to the symbol duration. The OFDM frame size is set to $N_{\mathrm{FFT}} = 1024$ subcarriers. Smaller sizes for the OFDM frame result in less statistical significance; larger sizes result in an increased peak-to-average power ratio (PAPR). The symbols can then be multiplexed into a serial time

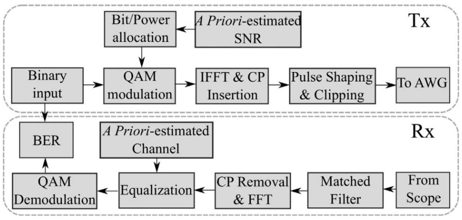

Fig. 4. Block diagram for OFDM transmitter and receiver.

domain output using an inverse fast Fourier transform (IFFT). Cyclic prefixes (CPs) are inserted at the start of each OFDM frame. Adequate length of the CPs, N_{CP}, allows for ISI to be eliminated by the computationally efficient single-tap equalizer. A value of $N_{\mathrm{CP}} = 5$ is found to be sufficient for the ISI to be removed at less than 0.97% loss in the spectral efficiency. Root-raised cosine (RRC) pulse shaping filter is used to achieve band limited communication since it allows a trade-off control between pulse duration and bandwidth requirements [16]. OFDM time domain waveforms have high PAPR due to the coincidence of multiple in-phase QAM symbols in the same OFDM frame. Extreme values for the OFDM modulating signal are clipped to minimize the effect of nonlinearity at acceptable error margins. The upper and lower clipping values are set to $+3\sigma_x$ and $-3.5\sigma_x$, respectively, where σ_x is the standard deviation of the OFDM waveform. Asymmetric values for the clipping points are used since the upper clipping due to the saturation of the micro-LED is higher than the lower clipping. The received waveform is processed with matched filters, fast Fourier transform (FFT) with CPs removal, single-tap equalizer using the *a priori* estimated channel, and demodulator. Bit error rate (BER) is calculated based on the demodulated binary stream.

Before any data transmission, the channel is first estimated by pilots composed of multiple OFDM frames. A conventional mean estimator is used with random pilots that would take the nonlinearity effects into account. Details about the used estimation method can be found in [17]. An estimation of the SNR is also obtained using the same method. The received OFDM waveform, $y(t)$, can be expressed as follows:

$$y(t) = h(t) * z(x(t)) + n(t), \tag{1}$$

where $h(t)$ is the VLC system channel, $n(t)$ is the additive white Gaussian noise (AWGN) at the receiver with a variance σ_n^2, and $z(\cdot)$ is the nonlinear transformation of the micro-LED. For Gaussian inputs such as the real-valued OFDM waveform, the Bussgang theorem can be applied and the nonlinear transformation can be expressed as [18]

$$z(x(t)) = \alpha x(t) + d(t), \tag{2}$$

given that the processes $x(t)$ and $d(t)$ are uncorrelated $E[x(t)d(t)] = 0$, where $E[\cdot]$ is the statistical expectation and $d(t)$ is the distortion noise. The constant α can be calculated as [18]

$$\alpha = \frac{E[z(x(t)) \cdot x(t)]}{\sigma_x^2}. \tag{3}$$

The distortion noise $d(t)$ is a non-Gaussian noise. However, its representation in the frequency domain $D(f)$ follows a Gaussian distribution with a DC mean and a variance σ_d^2 [18]. Detailed analysis of the nonlinear distortion noise effect on DCO-OFDM can be found in Ref. [19]. The used arbitrary waveform generator (AWG) has 10 bits resolution for the digital-to-analog converter (DAC), and the oscilloscope used has an effective number of bits of 5.5 for the analog-to-digital converter (ADC). The nonlinearity effect from the amplifier is minimal at the operational frequencies and at the injected power levels. The harvested optical power at the photoreceiver is well below the saturation level. Therefore, the micro-LED is assumed to be the main source of nonlinearity in the overall system due to the relatively limited dynamic range, compared to other system components.

The estimated SNR is used to adaptively load the subcarriers with variable constellation sizes at different energy levels based on the Levin–Campello algorithm [20]. The algorithm allows more energy to be allocated to the subcarriers, which require minimal additional power to be elevated into larger constellation sizes, while preserving the probability of error target, P_e^T. Assuming that $N_{\mathrm{FFT}} > 64$, the adaptive bit and energy loading can be formulated in the following optimization problem:

$$\underset{\eta}{\text{maximize}}\ \eta = \frac{\sum_{\substack{k=1\\M_k>0}}^{\frac{N_{\mathrm{FFT}}}{2}-1} \log_2 M_k}{(N_{\mathrm{FFT}} + N_{\mathrm{CP}})(1+\beta)}, \tag{4a}$$

$$\text{subject to BER}\left(M_k, \frac{\nu_k^2 \alpha^2 E_{bk}}{N_o/|H(k)|^2 + \sigma_d^2}\right) \le P_e^T, \tag{4b}$$

$$\sum_{\substack{k=1\\M_k>0}}^{\frac{N_{\mathrm{FFT}}}{2}-1} \frac{\nu_k^2}{\frac{N_{\mathrm{FFT}}}{2} - 1} = 1, \tag{4c}$$

where β is the roll-off factor of the RRC filter, E_{bk} is the energy per bit at subcarrier k, N_o is the double-sided power spectral density (PSD) of the noise at the receiver, $|H(k)|^2$ is the channel gain at subcarrier k when a zero forcing (ZF) equalizer is used, η is the spectral efficiency given in bits/s/Hz, and BER (M_k, γ_k) is the theoretical BER equation of M_k-QAM at subcarrier k and SNR per bit γ_k, given in non-flat channels as [21]

$$\begin{aligned}\text{BER}(M_k, \gamma_k) \cong{}& \frac{4}{\log_2(M_k)}\left(1 - \frac{1}{\sqrt{M_k}}\right)\\ &\times \sum_{l=1}^{R} \sum_{k=1}^{N_{\mathrm{FFT}}} Q\left((2l-1)\sqrt{\frac{3\log_2(M_k)\gamma_k}{2(M_k-1)}}\right),\end{aligned} \tag{5}$$

where $Q(\cdot)$ is the complementary cumulative distribution function (CCDF) for the standard normal distribution, and $R = \min(2, \sqrt{M_d})$.

The adaptive bit and energy loading on each subcarrier is shown in Fig. 5 along with the channel capacity limit defined by Shannon as [22]

$$C = \log_2\left(1 + \frac{\alpha^2 E_{bk}}{N_0/|H(k)|^2 + \sigma_d^2}\right). \tag{6}$$

It is shown that the gap between the exact loading and the capacity limit is already small; however, it can be closed when

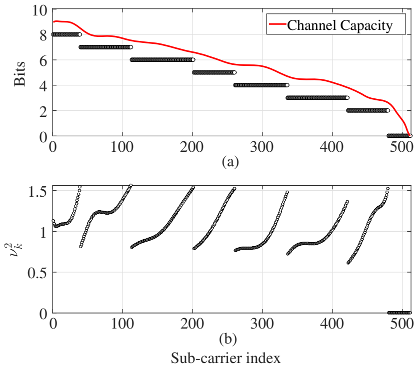

Fig. 5. (a) Bit loading and channel capacity per subcarrier, both given in bits per subcarrier. (b) Energy loading per subcarrier.

channel coding is employed. The cumulative distribution function (CDF) of the estimated SNR for multiple QAM constellation sizes is presented in Fig. 6. The results show the distribution of the SNR values required to achieve a BER below the forward error correction (FEC) target based on the bit and energy loading algorithm.

B. Experimental Setup

The experimental setup, shown in Fig. 7, starts with a laptop connected to a Tektronix AWG (AWG70001A) that has a maximum sampling frequency of 50 GS/s with an ADC resolution of 10 bits per sample. Bipolar OFDM waveforms are generated in MATLAB as detailed in Section 3.A and then transmitted to the AWG. The maximum peak-to-peak voltage (V_{PP}) of the AWG is 0.5 V_{PP}. The output of the AWG is amplified with a broadband amplifier (SHF 100AP) that has a maximum gain of 20 dB in the bandwidth range (100 kHz–20 GHz). A 3 dB attenuator is used at the output of the amplifier to allow flexible control of the signal modulation depth, V_{PP}. The power budget of the system is adjusted to allow complete utilization of the micro-LED dynamic range shown in Fig. 2.

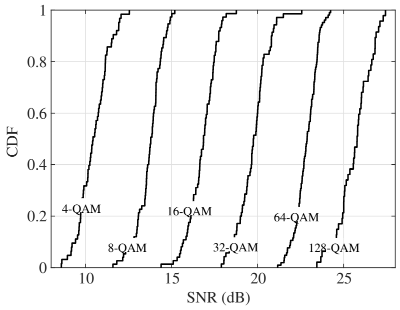

Fig. 6. Statistical CDF for different QAM constellation sizes realized at BER $= 2.3 \times 10^{-3}$, below the FEC target.

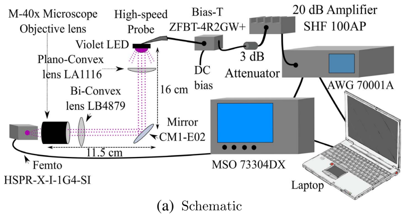

(a) Schematic

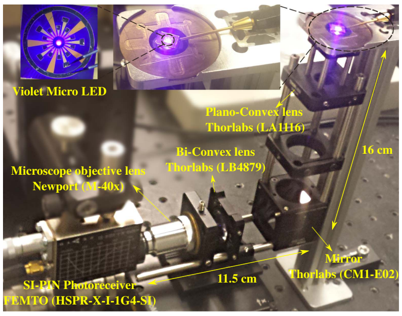

(b) Photograph

Fig. 7. Experimental setup. (a) Schematic setup of the experiment showing the optical system, AWG, oscilloscope, amplifier, attenuator, and Bias-tee. (b) Photograph of the optical system showing the micro-LED, the optical lens system, and the photoreceiver.

The amplified bipolar signal is DC-biased with a Bias-tee (Mini-Circuits ZFBT-4R2GW+). Low values for the DC bias result in high zero-level clipping of the OFDM waveform, which degrades the SNR. High values for the DC bias result in optical power saturation at the micro-LED, which also degrades the SNR. After extensive experiments, the DC bias is set to $I_{\mathrm{DC}} = 30$ mA corresponding to a measured DC voltage of $V_{\mathrm{DC}} = 5.23$ V. This value allows the OFDM bipolar signal to swing in the linear region of the L–V characteristic of the micro-LED. The biased signal is then fed to the micro-LED via a high-speed probe. An optical plano-convex lens (Thorlabs LA1116) is used to collimate most of the light into a dielectric mirror (Thorlabs CM1-E02) with higher than 97% reflectance in the desired wavelength region. The reflected light is then focused onto the photoreceiver by a bi-convex lens (Thorlabs LB4879) followed by a microscopic objective lens (NewPort M–40 ×) with a numerical aperture (NA) of 0.65. A silicon positive–intrinsic–negative (PIN) photoreceiver is used (Femto HSPR-X-I-1G4-SI) with a 3 dB bandwidth of 1.4 GHz and a responsivity of 0.135 A/W around 400 nm.

4. RESULTS AND DISCUSSION

The VLC data transmission experiment was only conducted on the inner pixels due to their higher E–O bandwidth compared to the outer pixels. The sampling frequency of the AWG is set to 29 GS/s with an oversampling factor of eight samples per symbol, which results in a single-sided modulation bandwidth of 1.81 GHz. The subcarriers are equally spaced within the Nyquist rate of the modulation signal with a subcarrier spacing of 3.54 MHz. The high-speed equipment used in the measurements allowed for the overall system bandwidth to be limited by the bandwidth of the micro-LED. Figure 8 shows the data rates, and the corresponding theoretical lower bounds and experimentally obtained values for the BERs at different dimming levels. The theoretical lower bounds for the BER estimations are calculated based on the experimentally estimated SNR as described in Eq. (5), and they are shown to be close to the experimental results. The data rates start with 3.46 Gb/s at a received optical power, $P^{\text{opt}} = -4.94$ dBm, which corresponds to a DC bias of $V_{\text{DC}} = 4.16$ V and a DC current of $I_{\text{DC}} = 10$ mA. The data rate increases, but starts to saturate as the DC bias increases until it reaches a maximum of 4.91 Gb/s at $P^{\text{opt}} = -2.29$ dBm corresponding to $V_{\text{DC}} = 5.21$ V and $I_{\text{DC}} = 35$ mA. The data rate starts to decrease as the DC bias increases beyond 35 mA. This result is expected due to the increased clipping distortion caused by the optical power saturation shown in Fig. 2. The achieved BER for all the studied cases in this test is well below the 3.8×10^{-3} FEC threshold. The optimized DC bias was selected for the rest of the measurements as $V_{\text{DC}} = 5.11$ V and $I_{\text{DC}} = 30$ mA, since the system performance for a larger swing of the peak-to-peak modulation signal starts to degrade at $I_{\text{DC}} = 35$ mA. The theoretical lower bounds of the BER versus data rates at different dimming levels are shown in Fig. 9 with a comparison to the experimental results. The deviation between theoretical and experimental validation points at $P^{\text{opt}} = -4.94$ dBm is due to the severe clipping distortion at DC current $I_{\text{DC}} = 10$ mA.

The system performance as a function of the modulation signal depth, V_{PP}, is investigated. A large modulation signal swing is expected to increase the SNR due to the increased signal power, σ_x^2. Nevertheless, it incurs additional nonlinear distortion, σ_d^2, due to the increased clipping. It is shown in Fig. 10 that the SNR improves as the modulation depth increases. The nonlinear distortion is present on the first 250 MHz; however, the improvement in the signal power σ_x^2 is more significant at higher frequencies. This result is justified by the fact that signals at higher frequencies are attenuated due to the lower channel gain at these high frequencies. Therefore, these values become less affected by the nonlinearity of the device. This result shows that tolerating additional nonlinearity by employing a larger signal swing can improve the communication system performance.

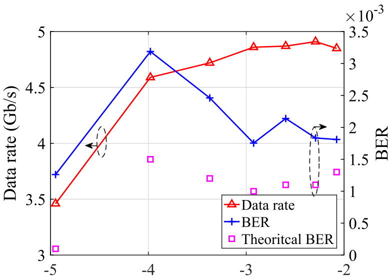

Fig. 8. Experimentally obtained results and theoretical bounds of data rate and BER versus different dimming levels at a modulation depth of $V_{\text{PP}} = 2.36$ V. The values for the received optical power correspond to DC-bias values ranging from 10 to 40 mA.

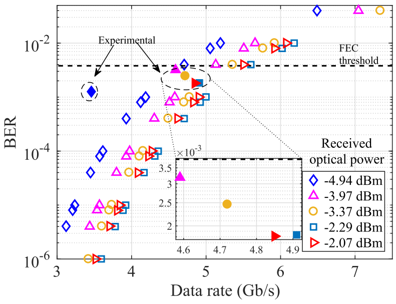

Fig. 9. Theoretical bounds on the data rate versus BER for different dimming levels at a modulation depth of $V_{\text{PP}} = 2.36$ V. The values for the received optical power correspond to DC-bias values ranging from 10 to 40 mA. Filled markers denote experimental results.

The experimentally optimized values for the DC bias at 30 mA and the modulation signal swing at 3.88 V_{PP} are used to investigate the system data rate performance against BER. The experimentally obtained data rates versus BERs are presented with the theoretical lower bounds for the BER performance in Fig. 11. The theoretical lower bounds are shown to be very close to the experimentally obtained results. As shown in Fig. 11, a transmission data rate of 7.91 Gb/s is experimentally achieved at a BER below the FEC threshold, 3.8×10^{-3}. To guarantee reliable communications, the data rate is reduced to 7.36 Gb/s to allow for a 7% FEC overhead to be employed. This compares to 5 Gb/s for a device with similar design emitting at 450 nm [7]. To the best of the authors' knowledge,

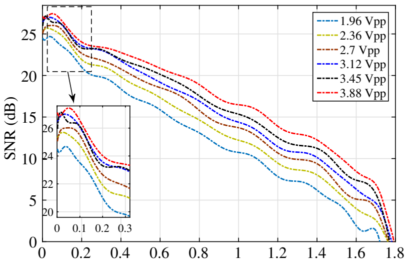

Fig. 10. SNR versus frequency for different modulation depths at DC-bias current $I_{\text{DC}} = 30$ mA. The values for the modulation signal swings correspond to feeding the micro-LED with varying power levels from 5.85 to 11.78 dBm.

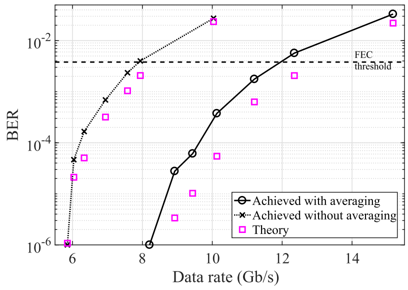

Fig. 11. Data rates versus BER for the experimentally obtained and the theoretical bounds at DC-bias current $I_{\text{DC}} = 30$ mA corresponding to $P^{\text{opt}} = -2.6$ dBm and modulation depth $V_{\text{PP}} = 3.88$ V.

this record is the highest for VLCs data transmission speeds using single micro-LED.

The system data rate performance is investigated when the waveform averaging acquisition mode of the oscilloscope is activated. Averaging acquisition was shown to be useful in drawing conclusions from experimental studies that could influence practical system design [23]. The averaging acquisition mode in this experiment allows for a better characterization of the micro-LED by reducing the AWGN of the photoreceiver, which limits the system performance to the nonlinear distortion noise of the micro-LED. It is shown in Fig. 11 that data rates up to 11.95 Gb/s can be achieved at a BER below the FEC threshold. This is reduced to 11.12 Gb/s when 7% FEC overhead is used. The results for the waveform acquisition mode of the oscilloscope are only presented to show the effect of the nonlinear distortion in the absence of the photoreceiver AWGN noise. All other reported results were conducted without waveform averaging acquisition.

5. RANGE AND ALIGNMENT CONSIDERATIONS

The VLC system was realized using an optical system to collect, collimate, and focus the light on the PD. The used optical system imposes restrictions on the link alignment and transmission range. Introducing optimized optics and deploying more micro-LED pixels from the array can improve both the coverage and the range of the system. The feasibility of demonstrating long transmission distances was demonstrated at a free-space distance of 10 m and a data rate of 1.1 Gb/s in Ref. [24]. This was achieved using an avalanche photodiode (APD) with an integrated concentrator, and a micro-LED with an optical power of 4.5 mW, which is 1.96 times higher than the optical power of the micro-LED pixel used in this work.

The obtained data rates and BERs for different received optical power presented in Fig. 8 enable us to investigate the system performance against the transmission range based on the widely accepted line-of-sight (LoS) optical wireless communication (OWC) propagation models [25]. The methodology is to compute the distances which result in the respective received optical power presented in Fig. 8 and the distances are then cross-mapped with the data rates achieved in Fig. 8. Note that the results shown in Fig. 8 are obtained at different dimming levels by varying the DC-bias point, which limits the operating bandwidth and the experimentally obtained data rates. An analysis of the system range is provided based on four studies: (I) with transmitter and receiver lenses, (II) with transmitter lens only, (III) with receiver lens only, and (IV) without any optics. In all cases we assume that all array pixels are used (15 micro-LEDs) in a ganging OFDM mode. This can increase the mutual heat between the pixels and consequently degrade the total aggregate data rates; therefore the results in this section can be considered as upper bounds on the system performance.

The LoS channel gain can be given as [25]

$$H(0) = \frac{(m+1)A}{2\pi d^2}\cos^m(\phi)T(\psi)g(\psi)\cos(\psi), \tag{7}$$

where $m = -1/\log_2(\cos(\Phi_{1/2}))$ is the Lambertian order of the optical source and $\Phi_{1/2}$ denotes its semi-angle; ϕ is the angle of irradiance; A is the detection area of the APD; d is the Euclidean distance between the optical source and the APD; ψ is the angle of incidence; $T(\psi)$ represents the gain of the optical filter used at the receiver; and $g(\psi)$ represents the gain of the optical concentrator, given as [25]

$$g(\psi) = \begin{cases} \frac{n^2}{\sin^2(\Psi_{\text{fov}})}, & 0 \le \psi \le \Psi_{\text{fov}} \\ 0, & \psi > \Psi_{\text{fov}} \end{cases}, \tag{8}$$

where n is the refractive index of the optical concentrator used at the APD. The optical power after the transmitter lens can be given as [26]

$$P_{\text{opt}}^{R,\text{lens}} = \frac{(m_{\text{LED}}+1)D_{\text{lens}}^2}{8d'^2}T_{\text{lens}}P_{\text{opt}}^{T,\text{LED}}, \tag{9}$$

where m_{LED} denotes the Lambertian order of the micro-LED, D_{lens} is the lens diameter, T_{lens} is the transmittance of the lens, and d' is the distance between the micro-LED and the transmitter lens. The existence of the transmitter lens affects the micro-LED beam divergence. The half power semi-angle $\Phi_{1/2}^{\text{lens}}$ can be given as [26]

$$\Phi_{1/2}^{\text{lens}} = \frac{D_s}{2d'}, \tag{10}$$

where D_s is the diameter of the micro-LED. The transmitter lens used in this investigation is an aspheric condenser lens (Thorlabs ACL7560U-A) with a diameter of $D_{\text{lens}} = 75$ mm, and a focal length of lens $f = 60$ mm.

A commercially available compound parabolic concentrator (CPC) is assumed to be in front of the APD. The field-of-view (FOV) of the concentrator is 25°, with a refractive index of $n = 1.5$. We assume the use of a high-speed commercially available APD at the receiver (Thorlabs APD210) instead of the used PIN receiver (Femto HSPR-X-I-1G4-SI). The APD diameter is 0.5 mm, and the modulation bandwidth is 1.6 GHz. The APD improves the sensitivity of the receiver; therefore an APD conversion gain factor is introduced to allow a fair comparison between the experimentally obatined results using the PIN and the numerical results using the APD photoreceivers:

$$\Lambda^{\text{APD}} = \frac{G^{\text{APD}}}{G^{\text{PIN}}}, \tag{11}$$

where G^{APD} and G^{PIN} are the conversion gains of the APD and PIN photoreceivers given in V/W, respectively. Using Eqs. (7)–(11), the received optical power at the APD can be given as

$$P_{\mathrm{opt}}^{Rx,\mathrm{APD}} = \frac{(m_{\mathrm{lens}}+1)A}{2\pi d^2}\cos^{m_{\mathrm{lens}}}(\phi) \times T(\psi)g(\psi)\cos(\psi)\Lambda^{\mathrm{APD}} P_{\mathrm{opt}}^{R,\mathrm{lens}}, \tag{12}$$

where m_{lens} is the Lambertian order of the lens based on Eq. (10).

The LoS propagation model is used to compute the transmission ranges that can achieve certain values for the received optical power between −5 and −2 dBm. These values for the received optical power were demonstrated experimentally to achieve data rates between 3.46 and 4.91 Gb/s using the experimentally realized VLC system. An upper bound on the data rates can be estimated by cross-mapping the computed received power at each distance, with the experimentally obtained data rates provided in Fig. 8. The distance versus received optical power and data rate for Studies I and II and Studies III and IV is shown in Fig. 12, respectively. The largest distances can be achieved using transmitter and receiver optics. Specifically, it was found that at 3.69 m distance a data rate of 4.91 Gb/s can be achieved, and at 5.25 m distance the data rate reduces to 3.46 Gb/s. As expected, the transmitter lens is shown to boost the range more than the receiver concentrator lens. At a data rate of 4.91 Gb/s, the maximum distance is 1.04 m and 4.7 cm for Studies II and III, respectively. At a data rate of 3.46 Gb/s, the maximum distance is 1.47 m and 6.6 cm for Studies II and III, respectively. The transmission ranges that can be supported at data rates above 3.46 Gb/s are less than 2 cm when optics are not used.

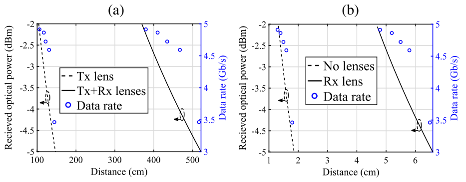

Fig. 12. Distance versus received optical power (left) and data rate (right). (a) Study I with transmitter and receiver lenses and Study II with transmitter lens only. (b) Study III with receiver lens only and Study IV without any optics.

The received optical power distribution is investigated as a function of the receiver's vertical–horizontal misalignments for the four considered studies, as shown in Fig. 13. The results are presented for the received optical power values that allow a maximum of −2 dBm and a minimum of −5 dBm, corresponding to data rates of 4.91 and 3.46 Gb/s, respectively. The transmission range and the system robustness against misalignments are both improved when optics are used for both front-end components in Study I, which makes this scenario suitable for high-speed point-to-point applications. The transmitter lens in Study II improves the transmission range but reduces the system robustness against misalignments. The receiver lens in Study III reduces the performance degradation caused by misalignment at the expense of reducing the system range. The transmission range and the system robustness against misalignments are both degraded in Study IV. However, Studies III and IV are suitable for board-to-board communication links, where wired links are not possible because of the rotational requirements between the boards for example.

6. CONCLUSION

A novel violet micro-LED array with two sets of inner and outer pixels is reported in this paper. The inner pixels allow very high current densities due to the small active area, enabling E–O bandwidth up to 655 MHz at an optical output power of 2.3 mW. An OFDM-based VLC system using a single pixel of

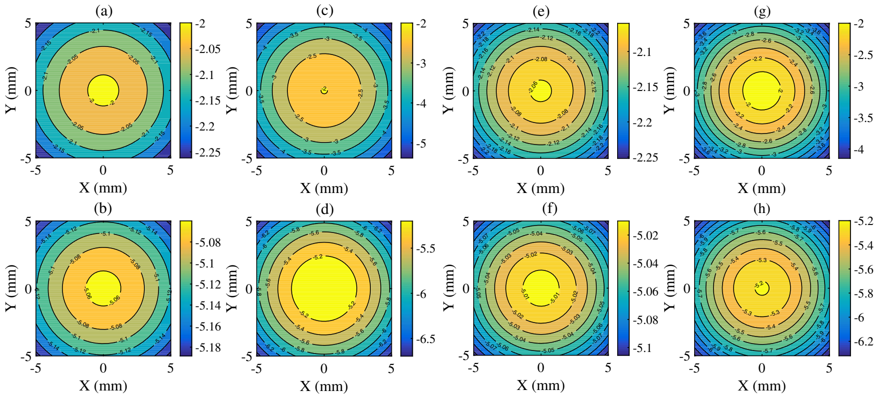

Fig. 13. Received optical power distribution in dBm as a function of vertical–horizontal displacements. (a) Study I at a distance of 369 cm; (b) Study I at a distance of 525 cm; (c) Study II at a distance of 104 cm; (d) Study II at a distance of 147 cm; (e) Study III at a distance of 4.7 cm; (f) Study III at a distance of 6.6 cm; (g) Study IV at a distance of 1.3 cm; (h) Study IV at a distance of 1.9 cm.

the proposed violet micro-LED is realized using adaptive bit and energy loading. The nonlinear distortion is found to affect the slow frequency region of the overall system bandwidth due to the limited dynamic range of the micro-LED. A transmission rate of 11.12 Gb/s, including the 7% FEC overhead, is achieved by averaging out thermal and shot noise of the photoreceiver and limiting the overall VLC system noise to the nonlinear distortion of the micro-LED. This result represents an upper bound on the proposed micro-LED performance that can be approached when higher quality system components with lower noise margins are used. A data transmission rate of 7.36 Gb/s, including the 7% FEC overhead, is also reported when all the noise sources of the VLC system are considered. The theoretical bounds are in good approximation with the experiment results.

The numerical investigation of the range and alignment highlights the role of optimized optics in increasing the transmission distance and improving system robustness.

Funding. Engineering and Physical Sciences Research Council (EPSRC) (EP/K00042X/1, EP/M506515/1).

[†] These authors contributed equally to this work.

REFERENCES

1. Cisco Visual Networking Index, "The zettabyte era: trends and analysis," Cisco White Paper, 2015, http://www.cisco.com/c/en/us/solutions/collateral/service-provider/visual-networking-index-vni/VNI_Hyperconnectivity_WP.pdf.
2. Y. Zhou, J. Zhao, M. Zhang, J. Shi, and N. Chi, "2.32 Gbit/s phosphorescent white LED visible light communication aided by two-staged linear software equalizer," in *10th International Symposium on Communication Systems, Networks and Digital Signal Processing (CSNDSP)* (IEEE, 2016), pp. 1–4.
3. J. Herrnsdorf, J. J. D. McKendry, E. Xie, M. J. Strain, E. Gu, I. M. Watson, and M. D. Dawson, "Gallium nitride structured illumination light sources," in *Light, Energy and the Environment Conference* (Optical Society of America, 2016), paper SSM2C.1.
4. J. J. D. McKendry, R. P. Green, A. E. Kelly, Z. Gong, B. Guilhabert, D. Massoubre, E. Gu, and M. D. Dawson, "High-speed visible light communications using individual pixels in a micro light-emitting diode array," IEEE Photon. Technol. Lett. **22**, 1346–1348 (2010).
5. P. P. Maaskant, H. Shams, M. Akhter, W. Henry, M. J. Kappers, D. Zhu, C. J. Humphreys, and B. Corbett, "High-speed substrate-emitting micro-light-emitting diodes for applications requiring high radiance," Appl. Phys. Express **6**, 022102 (2013).
6. D. Tsonev, H. Chun, S. Rajbhandari, J. J. D. McKendry, S. Videv, E. Gu, M. Haji, S. Watson, A. E. Kelly, G. Faulkner, M. D. Dawson, H. Haas, and D. O'Brien, "A 3-Gb/s single-LED OFDM-based wireless VLC link using a gallium nitride μLED," IEEE Photon. Technol. Lett. **26**, 637–640 (2014).
7. R. Ferreira, E. Xie, J. McKendry, S. Rajbhandari, H. Chun, G. Faulkner, S. Watson, A. E. Kelly, E. Gu, R. Penty, I. White, D. O'Brien, and M. D. Dawson, "High bandwidth GaN-based micro-LEDs for multi-Gbps visible light communications," IEEE Photon. Technol. Lett. **28**, 2023–2026 (2016).
8. C. J. Humphreys, "Solid-state lighting," MRS Bull. **33**(4), 459–470 (2008).
9. A. Zukauskas, R. Vaicekauskas, and M. S. Shur, "Colour-rendition properties of solid-state lamps," J. Appl. Phys. D **43**, 354006 (2010).
10. J. M. Phillips, M. E. Coltrin, M. H. Crawford, A. J. Fischer, M. R. Krames, R. Mueller-Mach, G. O. Mueller, Y. Ohno, L. E. S. Rohwer, J. A. Simmons, and J. Y. Tsao, "Research challenges to ultra-efficient inorganic solid-state lighting," Laser Photon. Rev. **1**, 307–333 (2007).
11. Q. Dai, Q. Shan, H. Lam, L. Hao, Y. Lin, and Z. Cui, "Circadian-effect engineering of solid-state lighting spectra for beneficial and tunable lighting," Opt. Express **24**, 20049–20058 (2016).
12. Z. Gong, Y. F. Zhang, P. Kelm, I. M. Watson, E. Gu, and M. D. Dawson, "InGaN micro-pixellated light-emitting diodes with nano-textured surfaces and modified emission profiles," Appl. Phys. A **103**, 389–393 (2011).
13. D. J. F. Barros, S. K. Wilson, and J. M. Kahn, "Comparison of orthogonal frequency-division multiplexing and pulse-amplitude modulation in indoor optical wireless links," IEEE Trans. Commun. **60**, 153–163 (2012).
14. J. McKendry, D. Tsonev, R. Ferreira, S. Videv, A. Griffiths, S. Watson, E. Gu, A. Kelly, H. Haas, and M. Dawson, "Gb/s single-LED OFDM-based VLC using violet and UV gallium nitride μLEDs," in *IEEE Summer Topicals Meeting Series (SUM)* (IEEE, 2015), paper TuD4.3.
15. M. S. Islim and H. Haas, "Modulation techniques for Li-Fi," ZTE Commun. **14**, 29–40 (2016).
16. D. Tsonev, S. Sinanovic, and H. Haas, "Complete modelling of nonlinear distortion in OFDM-based optical wireless communication," J. Lightwave Technol. **31**, 3064–3076 (2013).
17. D. Tsonev, S. Videv, and H. Haas, "Unlocking spectral efficiency in intensity modulation and direct detection systems," IEEE J. Sel. Areas Commun. **33**, 1758–1770 (2015).
18. P. Banelli and S. Cacopardi, "Theoretical analysis and performance of OFDM signals in nonlinear AWGN channels," IEEE Trans. Commun. **48**, 430–441 (2000).
19. S. Dimitrov and H. Haas, "Information rate of OFDM-based optical wireless communication systems with nonlinear distortion," J. Lightwave Technol. **31**, 918–929 (2013).
20. H. E. Levin, "A complete and optimal data allocation method for practical discrete multitone systems," in *Proceedings of IEEE Global Telecommunications Conference* (IEEE, 2001), pp. 369–374.
21. F. Xiong, *Digital Modulation Techniques*, 2nd ed. (Artech House, 2006).
22. C. E. Shannon, "A mathematical theory of communication," Bell Syst. Tech. J. **27**, 379–423 (1948).
23. L. Peng, S. Haese, and M. Hèlard, "Optimized discrete multitone communication over polymer optical fiber," J. Opt. Commun. Netw. **5**, 1313–1327 (2013).
24. J. Jiang, Y. Huo, F. Jin, P. Zhang, Z. Wang, Z. Xu, H. Haas, and L. Hanzo, "Video streaming in the multiuser indoor visible light downlink," IEEE Access **3**, 2959–2986 (2015).
25. J. M. Kahn and J. R. Barry, "Wireless infrared communications," Proc. IEEE **85**, 265–298 (1997).
26. J. Fakidis, M. Ijaz, S. Kucera, H. Claussen, and H. Haas, "On the design of an optical wireless link for small cell backhaul communication and energy harvesting," in *IEEE International Symposium on Personal, Indoor and Mobile Radio Communications (PIMRC)* (IEEE, 2014), pp. 58–62.

IEEE PHOTONICS TECHNOLOGY LETTERS, VOL. 28, NO. 19, OCTOBER 1, 2016 2023

High Bandwidth GaN-Based Micro-LEDs for Multi-Gb/s Visible Light Communications

Ricardo X. G. Ferreira, Enyuan Xie, Jonathan J. D. McKendry, *Member, IEEE*,
Sujan Rajbhandari, *Member, IEEE*, Hyunchae Chun, Grahame Faulkner, Scott Watson,
Anthony E. Kelly, Erdan Gu, Richard V. Penty, Ian H. White, *Fellow, IEEE*,
Dominic C. O'Brien, *Member, IEEE*, and Martin D. Dawson, *Fellow, IEEE*

***Abstract*— Gallium-nitride (GaN)-based light-emitting diodes (LEDs) are highly efficient sources for general purpose illumination. Visible light communications (VLC) uses these sources to supplement existing wireless communications by offering a large, licence-free region of optical spectrum. Here, we report on progress in the development of micro-scale GaN LEDs (micro-LEDs), optimized for VLC. These blue-emitting micro-LEDs are shown to have very high electrical-to-optical modulation bandwidths, exceeding 800 MHz. The data transmission capabilities of the micro-LEDs are illustrated by demonstrations using ON–OFF-keying, pulse-amplitude modulation, and orthogonal frequency division multiplexing modulation schemes to transmit data over free space at the rates of 1.7, 3.4, and 5 Gb/s, respectively.**

***Index Terms*— Bandwidth, micro light-emitting diodes, GaN, optical communication, visible-light communication, OFDM, PAM.**

I. INTRODUCTION

VISIBLE light communications (VLC) is an emerging technology that has significant potential to supplement existing radio frequency (RF) based wireless communications. VLC opens up a large, licence-free, visible region of the electromagnetic spectrum for wireless communications, and can in principle be integrated into, and work alongside, pre-existing lighting infrastructure. Gallium nitride (GaN) light-emitting diodes (LEDs) are attractive light sources for use in VLC systems. They can be used to generate light across the visible spectrum, including white light, and being semiconductor-based they can be modulated significantly faster than conventional incandescent or fluorescent light sources, as well as being amenable to integration with drive electronics. LED-based VLC typically uses off-the-shelf LEDs, which generally have modest electrical-to-optical modulation bandwidths of the order of 10-20 MHz, although the use of complex modulation schemes, parallel data transmission and equalisation can allow data transmission rates in excess of 1 Gbps [1], [2]. There have been efforts made to develop novel LED epitaxial structure and devices optimised for VLC [3], [4]. For example by reducing the LED active area, and thereby decreasing capacitance and increasing current density, we have previously reported modulation bandwidths in excess of 400 MHz [5]. Such LEDs, with dimensions of 100×100 μm^2 or less, have been used to demonstrate 3 Gbps transmission over free-space [6] and 5 Gbps along a polymer optical fibre (POF) [7]. In this work, we report further advancement of these micro-LED sources. A significant increase in the modulation bandwidth, now exceeding 800 MHz has been obtained. Using single pixels from individually-addressable arrays of these LEDs, with a nominal peak emission wavelength of 450 nm, we demonstrate data transmission over free-space using on-off keying (OOK), pulse-amplitude modulation (PAM) and orthogonal frequency division multiplexing (OFDM) modulation schemes at data rates of 1.7, 3.4 and 5 Gbps, respectively. These modulation bandwidths and data transmission rates represent, to the best of our knowledge, the highest yet reported for GaN LEDs.

II. DEVICES

Two segmented geometries of micro-LEDs were fabricated for this work which we designate A and B, with active areas of 435 and 1369 μm^2, respectively. These areas are equivalent to disk shape micro-LEDs with diameters of 24 μm for LED A and 42 μm for LED B. Fig. 1 shows large concentric arrays of these LEDs designed primarily for use with POF. The chosen micro-LEDs are single elements of these arrays, as shown in Fig. 1 (a) for LED A and Fig. 1 (b) for LED B.

Manuscript received February 19, 2016; revised April 14, 2016; accepted June 10, 2016. Date of publication June 15, 2016; date of current version July 21, 2016. This work was supported by the Engineering and Physical Sciences Research Council through the Program Ultra-Parallel Visible Light Communications under Grant EP/K00042X/1.

R. X. G. Ferreira, E. Xie, J. J. D. McKendry, E. Gu, and M. D. Dawson are with the Department of Physics, Institute of Photonics, University of Strathclyde, Glasgow G1 1RD, U.K. (e-mail: ricardo.ferreira@strath.ac.uk; enyuan.xie@strath.ac.uk; jonathan.mckendry@strath.ac.uk; m.dawson@strath.ac.uk).

S. Rajbhandari is with the School of Computing, Electronics and Maths, Coventry University, Coventry CV1 5FB, U.K. (e-mail: ac1378@coventry.ac.uk).

H. Chun, G. Faulkner, and D. C. O'Brien are with the Department of Engineering, University of Oxford, Oxford OX1 3PJ, U.K. (e-mail: hyunchae.chun@some.ox.ac.uk; grahame.faulkner@eng.ox.ac.uk; dominic.obrien@eng.ox.ac.uk).

S. Watson and A. E. Kelly are with the School of Engineering, University of Glasgow, Glasgow G12 8LT, U.K. (e-mail: s.watson.2@research.gla.ac.uk; anthony.kelly@glasgow.ac.uk).

R. V. Penty and I. H. White are with the Electrical Engineering Division, Centre for Photonic Systems, Department of Engineering, University of Cambridge, Cambridge CB2 1TN, U.K. (e-mail: rvp11@cam.ac.uk; ihw3@cam.ac.uk).

Color versions of one or more of the figures in this letter are available online at http://ieeexplore.ieee.org.

Digital Object Identifier 10.1109/LPT.2016.2581318

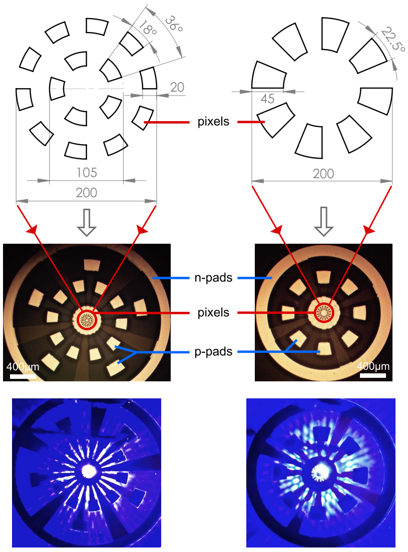

(a) (b)

Fig. 1. Micro-LED designs in concentric multiple element geometries. LED A is a single element of (a) and LED B is a single element of (b), dimensions are given in micrometers. The upper diagrams correspond to the pixels which are located at center of the photographs.

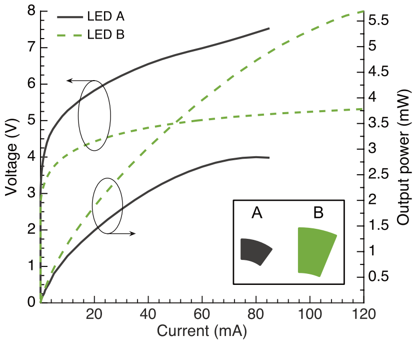

Fig. 2. Voltage-current-optical power characteristics of LED A and B with respective maximum optical power densities of 655 and 415 W/cm^2 at current densities of 19.5 and 8.7 kA/cm^2, respectively. Inset shows the relative size and shape of the micro-LEDs.

A direct comparison of relative size and shape of LED A and B can be found in the inset of Fig. 2.

The micro-LEDs had flip-chip configurations (substrate emitting) and were fabricated from a commercial 450 nm GaN-based LED wafer grown on a c-plane sapphire substrate. Basic details of the fabrication process for these devices can be found in our previous reports [5]. However, here we have changed the p-contact metal and etching depth. We use palladium (Pd) for the p-contact, thermally annealed to form a metal contact with high reflectivity ($>$ 50%) and low contact resistance [8]. In addition, the mesa is etched down to the sapphire substrate, confining the n-GaN to match the LED active area, thus reducing the capacitance of each pixel.

These two changes in fabrication combined with a change of LED shape and layout are the key factors to which we attribute the improvements in performance that are shown in the following sections. Note that the chips are not on a heat-sink.

III. PERFORMANCE

A. I-V and L-I Characteristics

Fig. 2 presents the current-voltage (I-V) and output power-current (L-I) characteristics of the micro-LEDs. The DC current densities are up to 19.5 kA/cm^2 for device A and 8.7 kA/cm^2 for device B. The optical power is 2.7 mW for LED A and 5.7 mW for LED B, corresponding to optical power densities of 655 W/cm^2 and 415 W/cm^2 for LED A and B, respectively. This corresponds to an increase in optical power of three times compared with our previous reports for devices of comparable size [5]. We note that these powers are measured in the forward direction only, without an integrating sphere.

The high current density capability is characteristic of flip-chip micro-LEDs and is attributed to improved thermal management and reduced current crowding [9]. Higher series resistance is common for small active areas and increases with the decrease of area [10], [11]. In these devices the improved p-contact with Pd results in a lower contact resistance in comparison to our previous report using Ni/Au [5]. The lower resistance reduces the Joule heating, thus contributing to a lower junction temperature. In addition, the shape of the pixel is designed to increase the surface-to-active-area ratio, which enables a more efficient thermal dissipation. As such, in comparison with our previous report for equivalent areas, these devices show an increase by a factor of 2 in the current densities at which the roll-over point occurs [5].

B. Modulation Bandwidth

The small signal electrical-to-optical (E-O) modulation bandwidth was measured in similar fashion to our previous reports [5], [12], [13]. The micro-LEDs were directly probed on chip using a high-speed micro-probe. The input signal consists of a constant bias current from a power supply combined with a small modulation voltage (few mV) from a network analyser. The modulated light is then received by a high-speed photodiode (bandwidth = 1.4 GHz) and sent to the network analyser.

Fig. 3 presents the (E-O) bandwidth as a function of the injected current density for LEDs A and B. These devices achieve high current densities as described in III A, enabling modulation bandwidths up to ≈830 MHz for LED A and 400 MHz for LED B. We have previously shown that increasing the current densities in the active region decreases the differential carrier lifetime [5], [14]. The differential carrier

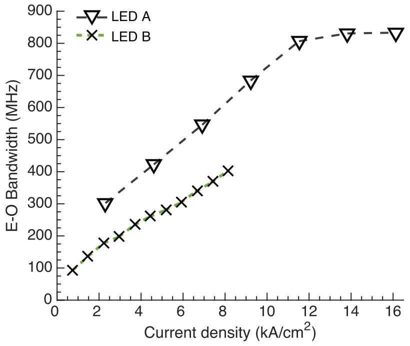

Fig. 3. E-O bandwidth as function of the injected current density for micro-LEDs A and B. The maximum bandwidths are 833 MHz and 397 MHz, respectively. Note that these current densities correspond to a DC bias range of 10–70 mA for LED A and 10–110 mA for LED B.

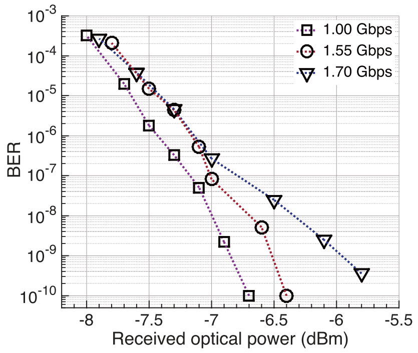

Fig. 4. Bit-error-rate as function of received optical power for LED A in free-space with OOK.

lifetimes are calculated here to be 0.19 ns (at 19.5 $kA/cm2$) for LED A and 0.40 ns (at 8.7 $kA/cm2$) for B, which we attribute to a combined effect of high carrier densities. As a comparison, the micro-LEDs reported in [5] had differential carrier lifetimes down to 0.37 ns at $< 10\, kA/cm2$, which suggests that the high current densities possible from LED A, in particular, are key in enabling the high modulation bandwidths shown here. Lower capacitance due to the etch process down to the substrate may have also reduced parasitic capacitance that might otherwise have affected the modulation response of the LEDs.

In addition, at the same injected current densities the observed bandwidths are higher for LED A than B. This effect differs from our previous reports with 450 nm devices [5]. This difference may be attributed to improved current spreading across the active area of the small pixel and an associated reduction in the junction temperature [15]. Furthermore, temperature differences at the same current densities may contribute to this effect.

IV. DATA TRANSMISSION

The next two sections present free-space data transmission with OOK, PAM and DC biased optical OFDM (DCO-OFDM) modulation formats.

A. OOK

Free-space data transmission using OOK was performed over an optical link distance of approximately 0.5 m using a bit-error ratio test (BERT) system. The various LED chips were directly probed as in section III B with a high-speed micro-probe and the light focused onto the photodiode (Femto HSA-X-S-1G4-SI, bandwidth of 1.4 GHz). Data rates ranging from 155 Mbps up to 1.7 Gbps were investigated for the different devices. In Fig. 4 the BER for LED A versus received optical power is shown for data rates from 1 Gbps to 1.7 Gbps.

A BER of 10^{-9} was achieved for 1.7 Gbps at a received optical power of -6 dBm. Note that no equalisation was applied here and at 1.7 Gbps the system is limited by the bandwidth of the photodetector (1.4 GHz).

B. PAM and OFDM

This section describes the maximum data rates achieved using PAM and OFDM schemes. The experimental set-up was similar to that previously reported [6]. An analogue signal (OFDM or PAM) from an arbitrary waveform generator (AWG, Keysight 81180B) was combined with a 5 V DC bias, using a bias-tee. The output from the micro-LED was collimated and imaged onto a Si photodetector (New Focus 1601, bandwidth of 1 GHz) using a singlet aspheric lens. The micro-LED and photodetector were in this case approximately 0.75 m apart. The received signal was captured by a digital oscilloscope (Keysight, MSO8104A) and processed offline in MATLAB®.

A PAM-*L* signal was generated using a pseudo-random bit sequence (PRBS) of $2^{14} - 1$ and transmitted via the micro-LED. Due to the limited bandwidth of the micro-LED, an adaptive decision feedback equaliser (DFE) was adopted at the receiver. The data rate versus BER for a PAM-4 scheme is shown in Fig. 5 (a). The achievable data rate below the forward error correction (FEC) floor of 3.8×10^{-3} is ~3.8 Gbps, which corresponds to a net data rate of 3.5 Gbps, after applying a 7% FEC overhead reduction. Higher order PAM schemes were also tested, however the data rates achieved were below this value. Although OOK offered BER of 10^{-5} at 3 Gbps with a DFE, it was not possible to test higher data rates due to the limited sampling rate of the AWG.

The spectrally efficient DCO-OFDM scheme was also tested for the same link setup. DCO-OFDM signal generation and decoding is described in detail in [6] and we have adopted a similar approach. The DCO-OFDM parameters used for the experiments were: Fast Fourier Transform (FFT) size of $N_{fft} = 512$; cyclic prefix length = 5; clipping level = $\pm 4\sigma$, where σ is the standard deviation of the time-domain OFDM signal. Fig. 5 (a) presents the data rate versus BER for DCO-OFDM and PAM-4 schemes. Fig. 5 (b) presents the

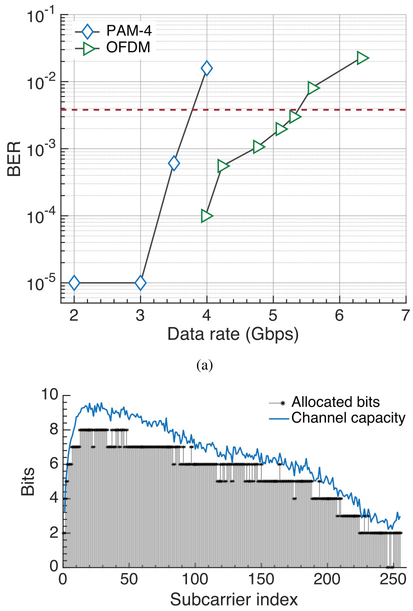

(a)

(b)

Fig. 5. In (a) is the BER as function of the data rate for LED B in free-space with PAM-4 and DCO-OFDM. In (b) is the bit loading per subcarrier index for the OFDM signal.

adaptive bit loading for the DCO-OFDM. Also shown in the figure are the allocated bits for different subcarriers. A maximum data rate of 5.37 Gbps was achieved at a FEC BER floor of 3.8×10^{-3}. Taking into account the 7% FEC overhead, the data becomes 5 Gbps. This compares to 3 Gbps over 5 cm reported in [6], and represents, to the best of the authors' knowledge, the fastest single link wireless VLC data rate demonstrated using a single wavelength.

V. CONCLUSION

We present two new micro-LED designs for VLC and polymer optical fibre systems. We demonstrate record modulation bandwidths and data transmission with both PAM and OFDM. The devices sustain very high current densities producing higher optical power densities than comparable commercial devices while retaining multi-mW optical powers. Bandwidths in excess of 800 MHz were obtained and data rates of 3.5 Gbps using PAM-4 and 5 Gbps using adaptive DCO-OFDM. At this stage in our own studies, the performance achieved by these micro-LEDs is attributed to three factors: deep etch of the mesa down to substrate; improved metallisation of the *Pd* p-contact and the shaping of the active area. The individual contributions of these factors are part of on-going work to be reported shortly. Other future investigations include the influence of design in the thermal and bandwidth performance, and its impacts on the radiative and non-radiative recombination.

REFERENCES

[1] A. M. Khalid, G. Cossu, R. Corsini, P. Choudhury, and E. Ciaramella, "1-Gb/s transmission over a phosphorescent white led by using rate-adaptive discrete multitone modulation," *IEEE Photon. J.*, vol. 4, no. 5, pp. 1465–1473, Oct. 2012.

[2] A. Azhar, T. Tran, and D. O'Brien, "A Gigabit/s indoor wireless transmission using MIMO-OFDM visible-light communications," *IEEE Photon. Technol. Lett.*, vol. 25, no. 2, pp. 171–174, Jan. 15, 2013.

[3] J.-W. Shi, H.-Y. Huang, J. Sheu, C.-H. Chen, Y.-S. Wu, and W. Lai, "The improvement in modulation speed of GaN-based green light-emitting diode (LED) by use of n-type barrier doping for plastic optical fiber (POF) communication," *IEEE Photon. Technol. Lett.*, vol. 18, no. 15, pp. 1636–1638, Aug. 1, 2006.

[4] C. L. Liao, Y. F. Chang, C. L. Ho, and M. C. Wu, "High-speed GaN-based blue light-emitting diodes with gallium-doped ZnO current spreading layer," *IEEE Electron. Device Lett.*, vol. 34, no. 5, pp. 611–613, May 2013.

[5] J. J. D. McKendry *et al.*, "Visible-light communications using a CMOS-controlled micro-light- emitting-diode array," *J. Lightw. Technol.*, vol. 30, no. 1, pp. 61–67, Jan. 1, 2012.

[6] D. Tsonev *et al.*, "A 3-Gb/s single-LED OFDM-based wireless VLC link using a gallium nitride μ LED," *IEEE Photon. Technol. Lett.*, vol. 26, no. 7, pp. 637–640, Apr. 1, 2014.

[7] X. Li *et al.*, "μ LED-based single-wavelength bi-directional POF link with 10 Gb/s aggregate data rate," *J. Lightw. Technol.*, vol. 33, no. 17, pp. 3571–3576, Sep. 1, 2015.

[8] T. V. Blank and Y. A. Gol'dberg, "Mechanisms of current flow in metal-semiconductor ohmic contacts," *Semiconductors*, vol. 41, no. 11, pp. 1263–1292, 2007.

[9] T. Kim *et al.*, "High-efficiency, microscale GaN light-emitting diodes and their thermal properties on unusual substrates," *Small*, vol. 8, no. 11, pp. 1643–1649, 2012.

[10] H. W. Choi, C. W. Jeon, M. D. Dawson, P. R. Edwards, and R. W. Martin, "Fabrication and performance of parallel-addressed InGaN micro-LED arrays," *IEEE Photon. Technol. Lett.*, vol. 15, no. 4, pp. 510–512, Apr. 4, 2003.

[11] H. Xu, J. Zhang, K. M. Davitt, Y. K. Song, and A. V. Nurmikko, "Application of blue–green and ultraviolet micro-LEDs to biological imaging and detection," *J. Phys. D, Appl. Phys.*, vol. 41, no. 9, p. 094013, 2008.

[12] J. J. D. McKendry *et al.*, "High-speed visible light communications using individual pixels in a micro light-emitting diode array," *IEEE Photon. Technol. Lett.*, vol. 22, no. 18, pp. 1346–1348, Sep. 15, 2010.

[13] R. P. Green, J. J. D. McKendry, D. Massoubre, E. Gu, M. D. Dawson, and A. E. Kelly, "Modulation bandwidth studies of recombination processes in blue and green InGaN quantum well micro-light-emitting diodes," *Appl. Phys. Lett.*, vol. 102, no. 9, p. 091103, 2013.

[14] E. F. Schubert, *Light-Emitting Diodes*. Cambridge, U.K.: Cambridge Univ. Press, 2006.

[15] Z. Gong *et al.*, "Size-dependent light output, spectral shift, and self-heating of 400 nm InGaN light-emitting diodes," *J. Appl. Phys.*, vol. 107, no. 1, p. 013103, 2010.

JOURNAL OF LIGHTWAVE TECHNOLOGY, VOL. 34, NO. 8, APRIL 15, 2016 2049

Wireless Visible Light Communications Employing Feed-Forward Pre-Equalization and PAM-4 Modulation

X. Li, N. Bamiedakis, X. Guo, J. J. D. McKendry, E. Xie, R. Ferreira, E. Gu, M. D. Dawson,
R. V. Penty, and I. H. White

(Top-Scored)

***Abstract*—In this paper, feed-forward pre-equalization in conjunction with a PAM modulation scheme are proposed for use in wireless visible light communication (VLC) systems in order to enable the transmission of data rates >1 Gb/s. Simulation results demonstrate that simple few-tap feed-forward pre-equalization is able to remove the intersymbol interference caused by the limited link bandwidth of a line of sight VLC link, providing up to 5 dB better receiver sensitivity compared with postequalization. The pre-equalization scheme is implemented for a free-space VLC link using a PAM modulation scheme, which provides an enhanced spectral efficiency compared to NRZ modulation. Micropixelated LEDs (μLEDs) are used as the transmitter in this study, as they exhibit higher modulation bandwidth than conventional large-diameter LEDs. An avalanche photodiode is used at the receiver to provide an enhanced link power budget. Error-free (BER $<10^{-12}$) 2 Gb/s free-space VLC transmission over 0.6 m is demonstrated experimentally using a simple 3-tap feed-forward pre-equalizer and a PAM-4 modulation scheme. The results show that feed-forward pre-equalization with only a few taps can improve the μLED-based link performance greatly, providing a simple and cost-effective solution for high-speed VLC links.**

***Index Terms*—APD, feed-forward equalization, micro-LED, pre-equalization, pulse amplitude modulation, visible light communication.**

I. INTRODUCTION

THE demand for high speed wireless transmission is growing exponentially with the rapid development of mobile digital devices and wireless network cloud services. Optical wireless communications, with wavelength ranging from infrared to ultraviolet using light-emitting diodes (LEDs) or laser diodes, has been proposed and investigated intensively as a promising complementary technology to traditional radio frequency (RF) transmission systems, as these are currently facing the challenge of an overcrowded RF spectrum and the resulting capacity bottleneck [1]–[5]. Wireless visible light communication (VLC) systems have been proposed based on the deployment of light sources that can provide illumination as well as data transmission, such as Gallium Nitride (GaN) LEDs. These systems can benefit from the use of the increasing deployment of solid state LED lighting technology. LED sources provide significant advantages over conventional lighting sources, namely lower power consumption, longer lifetimes and color rendering capabilities [2]. Moreover, they exhibit modulation bandwidths of the order of tens of MHz and can therefore be efficiently modulated providing data transmission capability as well as their main illumination function. The use of such LED-based communication systems enables the exploitation of the large (hundreds of THz) un-regulated visible spectrum, thus overcoming the current spectrum crunch in the RF and millimetre wave range [2]. Moreover, the use of visible light in indoor wireless communications provides important advantages including cost and energy efficiency [3] as well as enhanced security owing to the light confinement within the walls of a room, and the potential for a high degree of spatial reuse. As a result, atto-cell optical wireless communication systems can be implemented providing important capacity enhancements [6].

VLC links typically deploy intensity modulation and direct detection (IM/DD) techniques owing to their simple implementation, which matches well the low cost character of the LED technology. However, the maximum data rate achieved in such systems is typically constrained by the limited modulation bandwidth of the LEDs (typically in the low MHz range) [7]. As a result, various techniques have been proposed and investigated in order to compensate the LED bandwidth limitation and improve the achievable data rates: (i) advanced modulation formats, (ii) multi-channel communication systems and (iii) equalization techniques. Advanced modulation formats can offer high spectral efficiency, therefore enhancing the channel capacity. Orthogonal frequency division multiplexing (OFDM) [8], [9], carrierless amplitude and phase modulation (CAP) [10] and pulse amplitude modulation (PAM) [7], [11] have been studied in the context of LED-based links and implemented in VLC system demonstrators. In [8], a 3 Gb/s single-LED OFDM-based wireless VLC link using a GaN micro-pixelated LED (μLED) was implemented. An aggregate data rate of 4.5 Gb/s was achieved over a red-green-blue (RGB) LED-based WDM system using a CAP-64 modulation in [10]. A bi-directional

---

Manuscript received October 26, 2015; revised December 27, 2015; accepted January 18, 2016. Date of publication January 21, 2016; date of current version March 3, 2016. This work was supported by the U.K. EPSRC via the Ultra Parallel Visible Light Communication (UPVLC) project. Additional data related to this publication is available at the data repository https://www.repository.cam.ac.uk/handle/1810/251457.

X. Li, N. Bamiedakis, X. Guo, R. V. Penty, and I. H. White are with the Centre for Photonic Systems, Electrical Engineering Division, Department of Engineering, University of Cambridge, Cambridge CB3 0FA, U.K. (e-mail: xl336@cam.ac.uk; nb301@cam.ac.uk; xg218@cam.ac.uk; rvp11@cam.ac.uk; ihw3@cam.ac.uk).

J. J. D. McKendry, E. Xie, R. Ferreira, E. Gu, and M. D. Dawson are with the Institute of Photonics, University of Strathclyde, Glasgow G1 1RD, U.K. (e-mail: jonathan.mckendry@strath.ac.uk; enyuan.xie@strath.ac.uk; ricardo.ferreira@strath.ac.uk; erdan.gu@strath.ac.uk; m.dawson@strath.ac.uk).

Color versions of one or more of the figures in this paper are available online at http://ieeexplore.ieee.org.

Digital Object Identifier 10.1109/JLT.2016.2520503

μLED-based guided-wave VLC system was also realized in [12] with an aggregated data rate of 10 Gb/s achieved over 10 m of plastic optical fiber using a PAM-32 modulation. To realize even higher transmission capacities, multi-channel communication techniques, including multiple-input multiple-output (MIMO) systems [13], [14], wavelength division multiplexing (WDM) [10], [15] and optical spatial modulation (OSM) [16], [17], have also been deployed in VLC free-space links. An imaging-MIMO VLC system using four parallel channels has been demonstrated, achieving an aggregate data rate of 920 Mb/s [14]. Experimental proof-of-concept demonstration of optical spatial modulation OFDM using μLEDs was also realized, with a maximum data rate of 1.34 Gb/s achieved [17].

Equalization is another approach to mitigate the inter symbol interference (ISI) in such links and improve the achievable transmission data rates. Equalization schemes implemented at both the transmitter (pre-equalization) and receiver (post-equalization) side of the link have been proposed [18]–[20]. In [18], a multiple-resonant equalizer has been implemented at the transmitter, achieving 80 Mb/s data transmission with a bit-error-rate (BER) $<10^{-6}$ using a white LED and non-return-to-zero (NRZ) modulation. VLC post-equalization circuits, which reshape the channel response at the receiver side, have also been investigated, achieving NRZ data transmission up to 340 Mb/s [19]. Moreover, the use of an adaptive equalization system using a decision feedback equalizer has been proposed and simulation studies have demonstrated the potential to achieve 1 Gb/s data transmission using 4 feed-forward taps and 2 decision feedback taps using NRZ modulation [20].

In this work, we propose the use of feed-forward equalization (FFE) at the transmitter (pre-equalization) in conjunction with a PAM modulation scheme in order to achieve high data rates of >1 Gb/s in μLED-based VLC links. It is the first time that the feed-forward pre-equalization and post-equalization are compared for a free space VLC system using a PAM scheme. FFE has already been investigated for use in high-speed optical links in order to mitigate ISI and extend the transmission capability [21]–[23]. Significant performance improvements can be achieved using a small number of equalizer taps, which can be implemented using relatively simple electronic circuitry and adaptive control algorithms [21]. For example, 55 Gb/s transmission was demonstrated using a directly-modulated vertical-cavity surface-emitting laser (VCSEL), NRZ modulation scheme and feed-forward equalization [24]. In this work, it is shown that similar benefits can be obtained in LED-based optical links by deploying low-complexity few-tap equalizers. Moreover, pre-equalization is compared with post-equalization for such links and it is demonstrated that pre-equalization can offer ~5 dB better receiver sensitivity compared with post-equalization. Furthermore, PAM modulation is employed in the VLC links studied, as it provides an enhanced spectral efficiency over NRZ modulation and requires a simpler implementation than OFDM without significant digital processing requirements. Herein, simulation and experimental studies are presented on wireless VLC links using GaN μLEDs, APD receivers, feed-forward pre-equalization and PAM modulation schemes and it is demonstrated that multi-gigabit transmission over such low-cost links can be achieved using simple adaptive electronic circuitry. Error-free (BER $<10^{-12}$) 2 Gb/s transmission is achieved over a free-space VLC link, using a simple 3-tap feed-forward pre-equalizer and a PAM-4 modulation scheme. In the sections that follow, the details of the VLC links studied are described (Section II.A), the details of the feed-forward equalization are illustrated (Section II.B) and the related simulation studies are presented (Section II.C). The experimental setups along with the high-speed data transmission experiments are reported in Section III. Finally, Section IV presents the conclusions.

II. VLC LINK AND SIMULATION STUDIES

A. VLC link

The wireless VLC links studied in this work are based on the use of GaN μLEDs and APD receivers. μLEDs typically have, diameters in the range of 20 to 100 μm and can provide moderate output powers ~1 mW and relatively large modulation bandwidths in excess of 100 MHz [25]. Their enhanced bandwidth performance over conventional large size LEDs is due to their small pixel size which reduces the capacitance limitation of conventional larger-size LEDs and which also enables much larger current densities through the devices [25]. Bandwidths of 450 MHz have been demonstrated from 20 μm in diameter 450 nm μLEDs while 1 Gb/s NRZ data transmission has reported [26]. For this work 20 μm diameter 450 nm μLEDs are employed. The μLEDs are modulated with PAM signals in order to improve the spectral efficiency of the link and extend its transmission capability. Low-order PAM schemes, such as PAM-4 and PAM-8, are studied for the VLC links as they are easy to implement in practice with low-cost encoders and decoders.

At the receiver side, APD-based detectors are employed. The advantage of using an APD receiver over a PIN-based receiver in VLC link has already been demonstrated [12], [27]. The reported studies indicate that APDs can provide a larger power budget in such links and offer an improved sensitivity enabling higher data rates or longer reaches [12], [27]. Therefore, an APD receiver with a LNA is employed in this work. For the simulation and experimental studies in this work, an 800 μm diameter Si APD is considered, as it exhibits reasonable responsivity in the visible wavelength range (0.28 A/W) and adequate bandwidth (650 MHz) for gigabit data transmission. The gain and noise performance of the APD detector are experimentally measured and are employed in the link simulations presented below.

The transmission channel is a line-of-sight (LOS) free-space link implemented in the experimental work with optical lenses. This LOS VLC link emulates directly-illuminated configurations such as workspace desks, meeting rooms or work benches while its beam characteristics (coverage, field of view) can be adjusted by employing appropriate beam shaping elements. For the simulations, the LOS channel is assumed to have a time delayed delta impulse response [28]. No multi-path reflections are assumed in the model, in order to simplify the analysis and demonstrate the benefits of the equalization technique on the basic link by mitigating the limited LED bandwidth.

B. Feed-Forward Equalization

As indicated in the introduction, equalization is used to overcome the bandwidth limitation of the LEDs and mitigate the ISI in the VLC link. Equalization has been widely investigated for use in radio communication as well as in fibre optic systems [21], [29]. A feed-forward (FF) equalizer is a linear system whose output is the sum of a set of input signals which are appropriately delayed and weighted by the tap

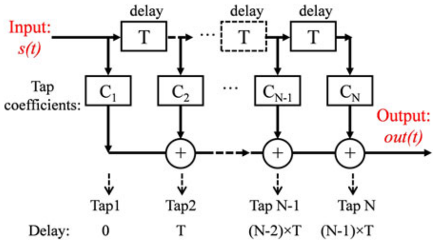

Fig. 1. Schematic of a feed-forward equalizer.

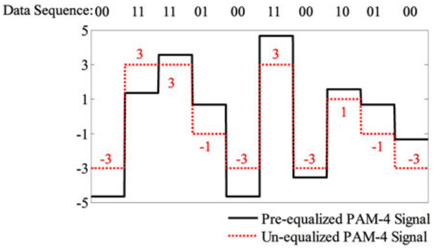

Fig. 2. Waveform of an un-equalized (solid line) and a pre-equalized (dotted line) PAM-4 modulating signal for an example data sequence for a 2-tap feed-forward equalizer with tap coefficients of (1 −0.55).

TABLE I
PARAMETERS USED IN LINK SIMULATION STUDIES

Component	Response	Parameter
μLED	Exponential	Bandwidth: 150 MHz Emission Power: 0 dBm Wavelength: 450 nm
APD	Raised-Cosine	Responsivity: 0.275 A/W Bandwidth: 650 MHz
Modulation scheme	NRZ	2 Gb/s
	PAM-4	1 Gbaud (2 Gb/s) 1.5 Gbaud (3 Gb/s)
	PAM-8	1 Gbaud (3 Gb/s)

coefficients:

$$out(t) = \sum_{n=1}^{N} C_n \times s\left[t-(n-1)T\right]$$

where *out(t)* and *s(t)* are the equalizer output and input signal respectively, C_n ($n = 1, 2 \ldots N$) are the tap coefficients, T is the tap delay and N is the number of taps. Fig. 1 shows the schematic of such a system while Fig. 2 shows an example of a PAM-4 waveform before and after the use of a 2-tap feed-forward equalizer. A feed-forward equalizer can be easily implemented with simple electronic components or a transversal filter [30], [31]. High-speed transversal filters with adjustable tap coefficients have already been developed [30]. For VLC systems, owing to the use of moderate symbol rates (in comparison to laser-based optical links), the electronic implementation of such equalizer circuits becomes straightforward. In this work, we propose the use of a FF equalizer at the transmitter side of the link with a small number of taps (2 to 5) and a tap delay T that matches the symbol period.

C. Simulation studies

Fig. 3 shows the basic link model used in the simulation studies. The performance of the free-space LOS VLC link is evaluated when a few-tap feed-forward pre-equalizer and PAM schemes are applied [Fig. 3 (a)]. As indicated above, the key parameters of link components, matching the values of the components employed in the experiments, are listed in Table I. For comparison, the performance of a similar link is also investigated when feed-forward post-equalization is applied at the receiver [Fig. 3 (b)] and also when NRZ modulation is employed. The waveforms of the received signals in each link configuration are recorded and processed in order to estimate bit-error-rate (BER) performance in each case, employing the BER estimation method described in [32], [33].

To illustrate the operation of the pre- and post- equalized VLC links, Fig. 4 shows the simulated eye diagrams generated at each stage of the link for both configurations when the same feed-forward equalizer is used. The VLC link is assumed to operate at 1.6 Gb/s using 0.8 Gbaud PAM-4 modulation. It employs a 2-tap feed-forward pre- or post- equalizer [Fig. 4 (a)]. For the post-equalized link, an un-distorted PAM-4 signal [Fig. 4 (b)] modulates the LED, while the eye diagram of the detected signal at the APD is completely closed due to ISI [Fig. 4 (c)]. Using the 2-tap feed-forward post-equalizer, the ISI is removed yielding open eye diagrams [Fig. 4 (d)] and therefore the transmitted data can be successfully recovered at the receiver. For the pre-equalized link, the PAM-4 modulating signal is pre-distorted using the same FFE equalizer at the transmitter side of the link and is used to drive the LED [Fig. 4 (e)]. The optimum coefficients of the equalizers are determined using the minimum-mean-square-error (MMSE) adaption algorithm [34]. The eye diagram of the signal at the APD is shown in Fig. 4 (f). The received eye-diagram is open with 4 clear distinguishable levels indicating that the transmitted data can be detected directly without any further equalization. The BER performance of each link can be estimated by analysing the received waveforms and taking into account the noise at the receiver.

Simulations for the free-space VLC link are carried out for 2 Gb/s transmission using NRZ and PAM-4 modulation, whilst varying the number of FFE taps from 2 to 5 and the BER performance of each link configuration is obtained (Fig. 5). These results are obtained using optimized tap coefficients for each link. For NRZ based links, the feed-forward equalizers require at least 4 taps to recover the transmitted signal at 2 Gb/s; while simple 2-tap equalizers can be used for the PAM-4 based links. Similar BER performance can be achieved for both NRZ and PAM-4 links using pre-equalization. The simulation results demonstrate that pre-equalization outperforms post-equalization for all the VLC links studied. 3 dB and 5.5 dB improvements in receiver sensitivity are obtained for the 2 Gb/s PAM-4 and NRZ links respectively. This is due to the noise enhancement penalty induced in the link by the post-equalization process, as the feed-forward post-equalizer amplifies both the received signal and the noise, resulting in a degradation of the signal-to-noise ratio (SNR) at the receiver. Such a noise enhancement penalty does not exist in the pre-equalized link as the

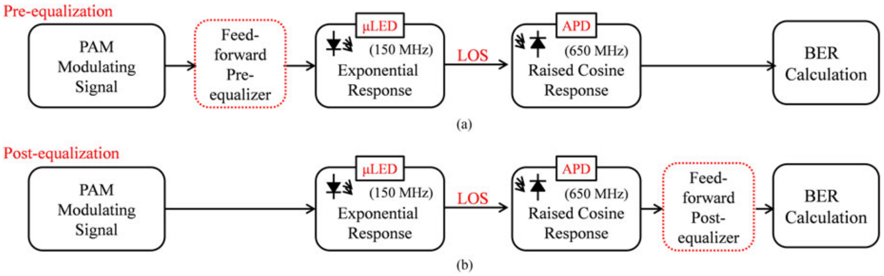

Fig. 3. Schematic of the (a) pre-equalized and (b) post-equalized free-space VLC system using PAM-4 modulation.

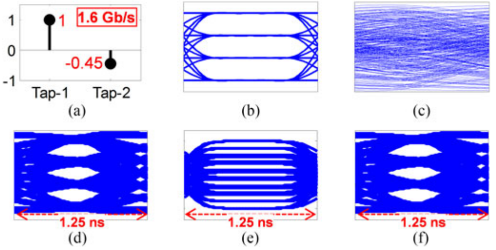

Fig. 4. (a) Tap-coefficients of the feed-forward equalizer; simulated eye-diagram of (b) ideal PAM-4 signal, (c) APD detected signal before post-equalization, (d) post-equalized PAM-4 signal, (e) pre-equalized PAM-4 signal and (f) received PAM-4 signal using pre-equalization.

feed-forward equalizer is implemented at the transmitter side of the link. For NRZ based links, the receiver sensitivity is 2.5 dB larger compared with the PAM-4 based links as the equalizers have larger tap coefficients to remove more ISI, resulting in a larger noise enhancement penalty for the post-equalized link.

Further simulations are carried out on the free-space VLC link comparing the performance of a 1.5 Gbaud PAM-4 and 1 Gbaud PAM-8 transmission, which both provide the same 3 Gb/s data rate. NRZ modulation would not be able to support such high data rate transmission even with a larger number of equalization taps. 3 to 5 taps are considered for the PAM-4 and PAM-8 based links due to the increased symbol rate. Again the BER performance of both the pre- and post-equalized links is extracted and compared (Fig. 6). The BER results indicate a 5 dB improved receiver sensitivity for the pre-equalized link over the respective post-equalized link. Moreover, it is found that PAM-4 modulation outperforms PAM-8 and that error-free (BER $<10^{-12}$) 3 Gb/s transmission can be achieved with a 3-tap and 5-tap FFE pre-equalizer with a receiver sensitivity of -9.4 and -11.8 dBm respectively. The improved performance of PAM-4 over PAM-8 modulation for these links is explained by the increased multi-level penalty that PAM-8 exhibits.

The simulated receiver sensitivity for a 10^{-12} BER for the pre-equalized VLC link as a function of the number of taps is found for the different modulation schemes (NRZ, PAM-4 and PAM-8) and data rates (1.6 to 3 Gb/s) and is shown in Fig. 7. An improvement in the receiver sensitivity (up to 2 dB) can be achieved with a larger number of pre-equalizer taps. However, it can be noticed that beyond a certain number of taps no further improvement is achieved. Higher symbol rates require a larger number of the equalization taps as larger ISI occurs in the link. As a result, a PAM scheme would require fewer tap than the equivalent NRZ link due to the lower required symbol rate. The simulation results indicate that for a particular link the optimum modulation and number of taps can be selected.

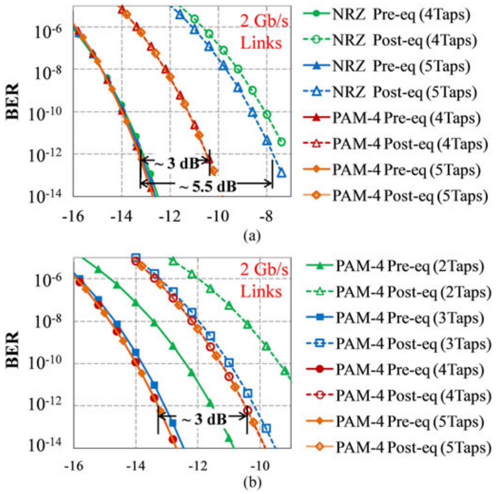

Fig. 5. Simulated BER performance of (a) NRZ and PAM-4 VLC links and (b) PAM-4-based VLC links at 2 Gb/s using pre- and post-equalization with varying number of taps.

In this work, a 2^9–1 PRBS is used to generate the PAM-4 modulation signal. In order to assess the link performance for a longer pattern which would generate more transitions, the use of a longer 2^{15}–1 PRBS pattern is also studied with the same link model. The simulated received eye diagram for a 2^{15}–1 PRBS and for a 2 Gb/s PAM-4 based VLC link using a 4 tap equalizer is shown in Fig. 8 (a). The simulated received eye diagram for a 2^9–1 PRBS pattern is also illustrated for comparison [Fig. 8 (b)]. The obtained BER performance for the two PRBS with different lengths (2^9–1 and 2^{15}–1) are compared in Fig. 8 (c) and it is shown that a small power penalty < 0.5 dB is induced

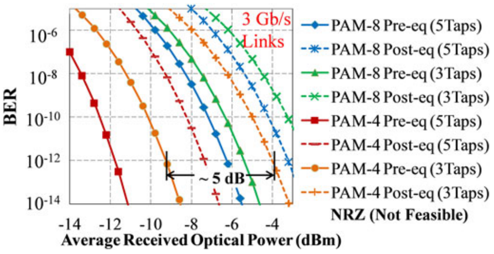

Fig. 6. Simulated BER performance of 3 Gb/s VLC links for different PAM schemes using pre-/ post-equalization with varying number of taps.

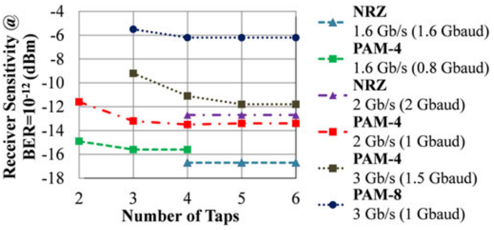

Fig. 7. The receiver sensitivity versus the number of taps of the feed forward pre-equalizer for various modulation schemes.

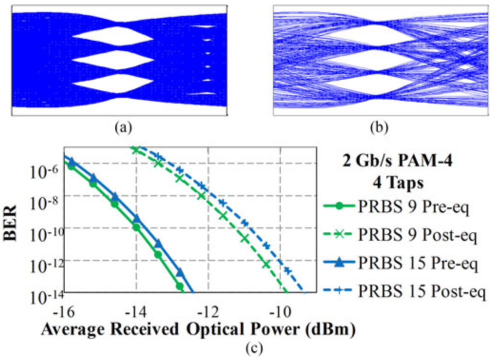

Fig 8. Simulation results of (a) received eye-diagram using a 2^{15}–1 PRBS; (b) received eye-diagram using a 2^9–1 PRBS and (c) BER results using a 2^9–1 and 2^{15}–1 PRBS for a 2 Gb/s PAM-4 based VLC link using 4 taps.

for a BER of 10^{-12}. The use of the 2^9–1 PRBS pattern in the experiments therefore is not expected to result in a significant difference in obtained link performance.

III. EXPERIMENTAL RESULTS

Fig. 9 shows the experimental setup used for the data transmission experiments on the pre-equalized free-space LOS VLC link. An arbitrary waveform generator (AWG) is used to generate the PAM modulating signals and implement the feed-forward pre-equalizer at the transmitter side using its built-in functions. The generated PAM signal is amplified to appropriate voltage levels via an RF amplifier (SHF-826H) and modulates a square 20×20 μm^2 450 nm μLED. The μLED is biased at a DC voltage of 5 V while the modulating signal has a 2 V peak-to-peak amplitude. The optical output is collected using an aspheric lens (Edmund #87–161) with a numerical aperture (NA) of 0.64. At the receiver side, an aspheric lens (Edmund #66–013) is used as a light concentrator focusing the light onto the APD receiver (First Sensor AD800–11). The received electrical signal is amplified using a low noise amplifier (LNA, ZFL-1000LN+) and the obtained waveforms and eye diagrams are captured using a digital storage oscilloscope. The BER performance of the link is calculated offline based on the captured waveforms and the measured receiver noise characteristics. It should be noted that the free-space distance used in the data transmission experiments is 0.6 m and is limited by the size of the optical bench. Transmission over larger distances of ~5 m is feasible as the output beam has a small divergence. In real applications, the maximum free-space distance over which the VLC link will be operated successfully depends on the required coverage, field-of-view and LED output power.

The VLC link is initially tested using a NRZ modulating signal. Fig. 10 shows the received eye diagrams at the data rates of 0.5 Gb/s, 0.6 Gb/s and 0.7 Gb/s with a received optical power of -14.2 dBm. The obtained eye diagram at 0.5 Gb/s is open (Fig 10 (a)), albeit with a very large ISI, while the received eye diagram at 0.7 Gb/s is closed due to the limited μLED bandwidth. As expected, NRZ modulation cannot support data rates > 1 Gb/s over the VLC link. In order to achieve this, a 2-tap FFE pre-equalizer is implemented at the transmitter. The μLED is modulated by the pre-equalized PAM-4 signal at 0.8 Gbaud, providing a data rate of 1.6 Gb/s. Fig. 11 shows the eye diagram of the PAM-4 signal at the transmitter and receiver side of the link for different values of the 2$^{\text{nd}}$ tap coefficient with a received optical power of -14.2 dBm [Fig. 11 (a)]. Fig. 11 (b) shows the corresponding pre-equalized PAM-4 modulating signals while Fig. 11 (c) are the respective eye diagrams recorded at the receiver. The eye diagrams obtained for an un-equalized PAM-4 modulating signal are also illustrated for comparison.

As expected, the uncompensated PAM-4 VLC link fails; the received eye diagram is completely closed and therefore the transmitted data cannot be directly recovered at the receiver. On the other hand, the received eye diagrams for the pre-equalized 1.6 Gb/s PAM-4 links are open and the 4 signal levels are clearly distinguishable. As a result, the transmitted data can be recovered directly at the receiver without any further signal processing. The BER performance of the each pre-equalized 1.6 Gb/s link is calculated for the different tap coefficients studied and the results are shown in Fig. 12. Based on the obtained BER performance, the optimum value and tolerance for the second tap coefficient in this link are obtained. Fig. 13 shows the receiver sensitivity for a 10^{-12} BER as a function of the value of the second tap coefficient as obtained from the simulations and experiments. For a particular target receiver sensitivity, the range of values satisfying this requirement can be identified. For example if a receiver sensitivity of -13 dBm is required in the link, a large tolerance is obtained, with suitable values within the range $[-0.65\ -0.5]$ for the experiment and $[-0.6\ -0.38]$ for the simulation. The experimental results follow the same trend as the simulation results but with a small shift

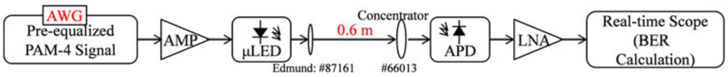

Fig. 9. Experimental setup of the free-space VLC using pre-equalization

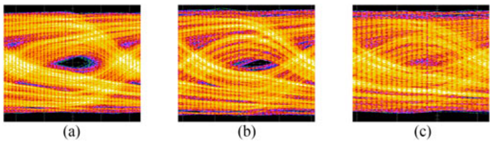

Fig. 10. Received NRZ eye-diagrams of the VLC link at (a) 0.5 Gb/s, (b) 0.6 Gb/s and (c) 0.7 Gb/s

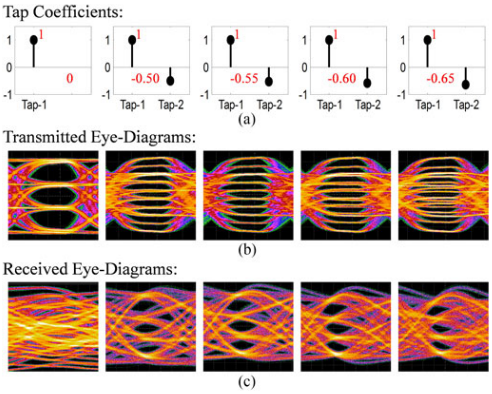

Fig. 11. (a) Tap coefficients and eye-diagrams of the (b) pre-equalized PAM-4 modulating and (c) respective received signal for the 1.6 Gb/s VLC link.

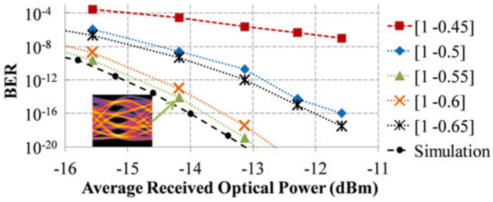

Fig. 12. BER plots for the 1.6 Gb/s pre-equalized PAM-4 link over 0.6 m for various tap coefficients.

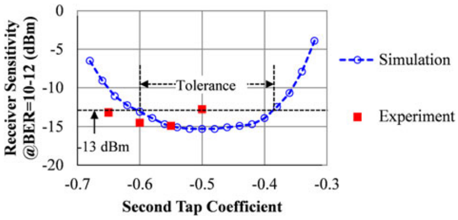

Fig. 13. The receiver sensitivity versus the second tap coefficient for the 1.6 Gb/s PAM-4 VLC link using a 2-tap pre-equalizer.

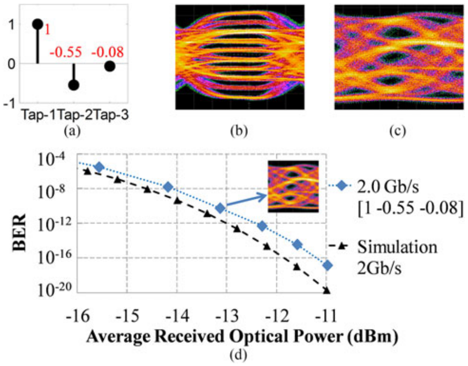

Fig. 14. (a) Optimized tap coefficients of the 3-tap FF pre-equalizer, eye-diagram of (b) the pre-equalized and (c) received PAM-4 signal; (d) BER plots for the optimized 2 Gb/s PAM-4 free-space VLC link.

in values. This difference can be attributed to the slightly different values for link bandwidth between the real link and simulation model and the non-linearities which are not taken into account in the simulation (such as the APD non-linearity). The tap coefficients of [1 -0.55] provide the best BER performance and the corresponding receiver sensitivity for a BER$<10^{-12}$ is found to be -15 dBm. In practice, the optimum equalizer coefficients can be determined experimentally using a training sequence and a feedback mechanism. Communications in VLC systems are expected to be bi-directional so the real-world implementation of such equalization schemes can be incorporated in the higher-level communication protocols.

A 2 Gb/s PAM-4 free-space VLC link is also implemented using the same experimental setup and a 3-tap feed-forward pre-equalizer. The optimum tap coefficients are adaptively adjusted so as to maximize the eye opening of the received PAM-4 signal and optimize the link BER performance. Fig. 14 shows the optimized tap coefficients [Fig. 14 (a)], the corresponding eye diagrams of the pre-equalized PAM-4 modulating signal [Fig. 14 (b)] and the received signal with a received optical power of -14.2 dBm [Fig. 14 (c)]. It can be noticed that the eye diagram of the received PAM-4 signal is open and that the 4 signal levels are clearly distinguishable. The estimated BER performance of the link is shown in Fig. 14 (d) along with the respective simulated BER performance. Error-free (BER$<10^{-12}$) 2 Gb/s transmission is achieved for an average received optical power larger than -12.2 dBm, while good agreement is obtained again between experimental and simulation results.

IV. CONCLUSION

Feed-forward pre-equalization is proposed for use in wireless VLC systems in conjunction with PAM modulation schemes in order to overcome the limited bandwidth of LEDs and achieve multi-gigabit ($>$1 Gb/s) transmission using low-complexity electronic circuitry. The proposed VLC links are based on the deployment of few-tap simple feed-forward equalizers, μLEDs, APD receivers and low-order PAM schemes. Both simulation studies and experimental results demonstrate that such schemes can effectively remove the ISI caused by the limited bandwidth of the link without using any complex digital signal processing. The simulation results indicate 3 Gb/s PAM-4 VLC links are feasible using only 3 to 5 taps in the equalizer and further show that improved receiver sensitivities of up to 5 dB can be achieved by employing pre-equalization over post-equalization. Error-free (BER $<10^{-12}$) 1.6 Gb/s and 2 Gb/s PAM-4 data transmission are achieved over a free-space VLC link using a 2-tap and 3-tap feed-forward pre-equalizer respectively, a 450 nm μLED transmitter and a Si APD receiver. The results showcase the potential benefits of pre-equalization in high-speed VLC systems, providing a cost-effective, energy-efficient and low-complexity approach to overcome the bandwidth limitation.

REFERENCES

[1] T. Komine and M. Nakagawa, "Fundamental analysis for visible-light communication system using LED lights," *IEEE Trans. Consum. Electron.*, vol. 50, no. 1, pp. 100–107, Feb. 2004.

[2] A. Jovicic, J. Li, and T. Richardson, "Visible light communication: Opportunities, challenges and the path to market," *IEEE Commun. Mag.*, vol. 51, no. 12, pp. 26–32, Dec. 2013.

[3] H. Elgala, R. Mesleh, and H. Haas, "Indoor optical wireless communication: Potential and state-of-the-art," *IEEE Commun. Mag.*, vol. 49, no. 9, pp. 56–62, Sep. 2011.

[4] J. M. Kahn and J. R. Barry, "Wireless infrared communications," *Proc. IEEE*, vol. 85, no. 2, pp. 265–298, Feb. 1997.

[5] C. Y. Ying, C. Y. Li, H. H. Lu, C. H. Chang, J. H. Chen, and J. R. Zheng, "A hybrid WDM lightwave transport system based on fiber-wireless and fiber-VLLC convergences," *IEEE Photon. J.*, vol. 6, no. 6, pp. 1–9, Dec. 2014.

[6] C. Cheng, M. Ijaz, D. Tsonev, and H. Haas, "Analysis of downlink transmission in DCO-OFDM-based optical attocell networks," in *Proc. IEEE Global Commun. Conf.*, Dec. 2014, pp. 2072–2077.

[7] C. G. Xi, A. Mirvakili, and V. J. Koomson, "A visible light communication system demonstration based on 16-level pulse amplitude modulation of an LED array," in *Proc. Symp. Photon. Optoelectron.*, May 2012, pp. 1–4.

[8] D. Tsonev, H. C. Chun, S. Rajbhandari, J. J. D. McKendry, S. Videv, E. Gu, M. Haji, S. Watson, A. E. Kelly, G. Faulkner, M. D. Dawson, H. Haas, and D. O'Brien, "A 3-Gb/s single-LED OFDM-based wireless VLC link using a gallium nitride μLED," *IEEE Photon. Technol. Lett.*, vol. 26, no. 7, pp. 637–640, Apr. 2014.

[9] F. M. Wu, C. T. Lin, C. C. Wei, C. W. Chen, Z. Y. Chen, H. T. Huang, and C. Sien, "Performance comparison of OFDM signal and CAP signal over high capacity RGB-LED-based WDM visible light communication," *IEEE Photon. J.*, vol. 5, no. 4, pp. 1–7, Aug. 2013.

[10] Y. G. Wang, L. Tao, X. X. Huang, J. Y. Shi, and N. Chi, "Enhanced performance of a high-speed WDM CAP64 VLC system employing volterra series-based nonlinear equalizer," *IEEE Photon. J.*, vol. 7, no. 3, pp. 1–7, Jun. 2015.

[11] D. J. F. Barros, S. K. Wilson, and J. M. Kahn, "Comparison of orthogonal frequency-division multiplexing and pulse-amplitude modulation in indoor optical wireless links," *IEEE Trans. Commun.*, vol. 60, no. 1, pp. 153–163, Jan. 2012.

[12] X. Li, N. Bamiedakis, J. L. Wei, J. J. D. McKendry, E. Y. Xie, R. Ferreira, E. Gu, M. D. Dawson, R. V. Penty, and I. H. White, "μLED-based single-wavelength bi-directional POF link with 10 Gb/s aggregate data rate," *J. Lightw. Technol.*, vol. 33, no. 17, pp. 3571–3576, Sep. 2015.

[13] A. H. Azhar, T. A. Tran, and D. O'Brien, "Demonstration of high-speed data transmission using MIMO-OFDM visible light communications," in *Proc. IEEE GLOBECOM Workshops*, Dec. 2010, pp. 1052–1056.

[14] S. Rajbhandari, H. Chun, G. Faulkner, K. Cameron, A. V. N. Jalajakumari, R. Henderson, D. Tsonev, M. Ijaz, Z. Chen, H. Haas, E. Xie, J. J. D. McKendry, J. Herrnsdorf, E. Gu, M. D. Dawson, and D. O'Brien, "Imaging-MIMO visible light communication system using μLEDs and integrated receiver," in *Proc. GLOBECOM Workshops*, Dec. 2014, pp. 536–540.

[15] F. M. Wu, C. T. Lin, C. C. Wei, C. W. Chen, Z Y. Chen, and H. T. Huang, "3.22-Gb/s WDM visible light communication of a single RGB LED employing carrier-less amplitude and phase modulation," in *Proc. Opt. Fiber Commun. Conf. Expo./Nat. Fiber Opt. Eng. Conf.*, Mar. 2013, pp. 1–3.

[16] R. Mesleh, H. Elgala, and H. Haas, "Optical spatial modulation," *IEEE J. Opt. Commun. Netw.*, vol. 3, no. 3, pp. 234–244, Mar. 2011.

[17] M. Ijaz, D. Tsonev, J. J. D. McKendry, E. Xie, S. Rajbhandari, H. Chun, G. Faulkner, E. Gu, M. D. Dawson, D. O'Brien, and H. Haas, "Experimental proof-of-concept of optical spatial modulation OFDM using micro LEDs," in *Proc. IEEE Int. Conf. Commun. Workshop*, Jun. 2015, pp. 1338–1343.

[18] H. Le Minh, D. O'Brien, G. Faulkner, L. Zeng, K. Lee, D. Jung, and Y. Oh, "80 Mbit/s visible light communications using pre-equalized white LED," in *Proc. 34th Eur. Conf. Opt. Commun.*, Sep. 2008, pp. 1–2.

[19] H. L. Li, X. B. Chen, B. J. Huang, D. Y. Tang, and H. D. Chen, "High bandwidth visible light communications based on a post-equalization circuit," *IEEE Photon. Technol. Lett.*, vol. 26, no. 2, pp. 119–122, Jan. 2014.

[20] T. Komine, J. H. Lee, S. Haruyama, and M. Nakagawa, "Adaptive equalization system for visible light wireless communication utilizing multiple white LED lighting equipment," *IEEE Trans. Wireless Commun.*, vol. 8, no. 6, pp. 2892–2900, Jun. 2009.

[21] B. L. Kasper, "Equalization of multimode optical fiber systems," *Bell Syst. Tech. J.*, vol. 61, no. 7, pp. 1367–1388, Sep. 1982.

[22] K. Azadet, E. F. Haratsch, H. Kim, F. Saibi, J. H. Saunders, M. Shaffer, L. L. Song, and M. L. Yu, "Equalization and FEC techniques for optical transceivers," *IEEE J. Solid-State Circuits*, vol. 37, no. 3, pp. 317–327, Mar. 2002.

[23] M. Maeng, F. Bien, Y. Hur, H. Kim, S. Chandramouli, E. Gebara, and J. Laskar, "0.18-μm CMOS equalization techniques for 10-Gb/s fiber optical communication links," *IEEE Trans. Microw. Theory Techniques*, vol. 53, no. 11, pp. 3509–3519, Nov. 2005.

[24] D. M. Kuchta, A. V. Rylyakov, C. L. Schow, J. E. Proesel, C. Baks, C. Kocot, L. Graham, R. Johnson, G. Landry, E. Shaw, A. MacInnes, and J. Tatum, "A 55Gb/s directly modulated 850nm VCSEL-based optical link," in *Proc. IEEE Photon. Conf.*, Sep. 2012, pp. 1–2.

[25] J. J. D. McKendry, D. Massoubre, S. Zhang, B. R. Rae, R. P. Green, E. Gu, R. K. Henderson, A. E. Kelly, and M. D. Dawson, "Visible-light communications using a CMOS-controlled micro-light- emitting-diode array," *J. Lightw. Technol.*, vol. 30, no. 1, pp. 61–67, Jan. 2012.

[26] J. J. D. McKendry, R. P. Green, A. E. Kelly, G. Zheng, B. Guilhabert, D. Massoubre, E. Gu, and M. D. Dawson, "High-speed visible light communications using individual pixels in a micro light-emitting diode array," *IEEE Photon. Technol. Lett.*, vol. 22, no. 18, pp. 1346–1348, Sep. 2010.

[27] X. Li, J.L. Wei, N. Bamiedakis, R. V. Penty, and I. H. White, "Avalanche photodiode enhanced PAM-32 5 Gb/s LED-POF link," in *Proc. Eur. Conf. Opt. Commun.*, Sep. 2014, pp. 1–3.

[28] K. Y. Cui, G. Chen, Z. Y. Xu, and R. D. Roberts, "Line-of-sight visible light communication system design and demonstration," in *Proc. Int. Symp. Commun. Syst. Networks Digital Signal Processing*, Jul. 2010, pp. 621–625.

[29] T. S. Rappaport, *Wireless Communications: Principles and Practice*, 2nd ed. Englewood Cliffs, NJ, USA: Prentice Hall, 2002.

[30] H. Wu, J. A. Tierno, P. Pepeljugoski, J. Schaub, S. Gowda, J. A. Kash, and A. Hajimiri, "Integrated transversal equalizers in high-speed fiber-optic systems," *IEEE J. Solid-State Circuits*, vol. 38, no. 12, pp. 2131–2137, Dec. 2003.

[31] J. Sewter and A. C. Carusone, "A 40 Gb/s transversal filter in 0.18 /spl mu/m CMOS using distributed amplifiers," in *Proc. IEEE Custom Integr. Circuits Conf.*, Sep. 2005, pp. 417–420.

[32] J. G. Proakis and M. Salehi, *Digital Communications*, 5th ed. New York, NY, USA: McGraw Hill, 2008.

[33] K. Szczerba, P. Westbergh, J. Karout, J. S. Gustavsson, A. Haglund, M. Karlsson, P. A. Andrekson, E. Agrell, and A. Larsson, "4-PAM for high-speed short-range optical communications," *IEEE J. Opt. Commun. Netw.*, vol. 4, no. 11, pp. 885–894, Nov. 2012.

[34] M. Tuchler, A. C. Singer, and R. Koetter, "Minimum mean squared error equalization using a priori information," *IEEE Trans. Signal Process.*, vol. 50, no. 3, pp. 673–683, Mar. 2002.

Authors' biographies not available at the time of publication.

1918 IEEE TRANSACTIONS ON ELECTRON DEVICES, VOL. 62, NO. 6, JUNE 2015

Active-Matrix GaN Micro Light-Emitting Diode Display With Unprecedented Brightness

Johannes Herrnsdorf, Jonathan J. D. McKendry, *Member, IEEE*, Shuailong Zhang, Enyuan Xie,
Ricardo Ferreira, David Massoubre, Ahmad Mahmood Zuhdi, Robert K. Henderson,
Ian Underwood, Scott Watson, Anthony E. Kelly, Erdan Gu,
and Martin D. Dawson, *Fellow, IEEE*

***Abstract*— Displays based on microsized gallium nitride light-emitting diodes possess extraordinary brightness. It is demonstrated here both theoretically and experimentally that the layout of the n-contact in these devices is important for the best device performance. We highlight, in particular, the significance of a nonthermal increase of differential resistance upon multipixel operation. These findings underpin the realization of a blue microdisplay with a luminance of 10^6 cd/m^2.**

***Index Terms*— CMOS integrated circuits, displays, flip-chip devices, integrated optoelectronics, light-emitting diodes (LEDs).**

I. Introduction

GALLIUM nitride-based light-emitting diodes (GaN LEDs) not only hold great promise for lighting but also can be fabricated into arrays of microscale LEDs integrated with CMOS control electronics [1], [2]. Such devices can serve as miniature displays [3], multisite excitation sources [4], and manipulation tools [5], [6] in the life sciences. LEDs with a size of 100 × 100 μm^2 or less (here referred to as micro-LEDs) can be driven at significantly higher current and optical power density than conventional large-area LEDs [7]. Consequently, they are promising for applications requiring, or benefitting from, high intensity, e.g., displays in high brightness environments (sunlight), projection [8], optoelectronic tweezers [5], [6], or pumping of organic lasers [9]. A further consequence of high current density operation is a reduction of the carrier lifetime [10], making micro-LEDs attractive candidates for high-speed data transmission using visible light [11]. CMOS control of multiple micro-LEDs has the potential to enhance the capabilities of such a communications system [12].

In recent years, matrix-addressed and individually addressed CMOS-controlled GaN microdisplays with a luminance on the order of 10^4 cd/m^2 have been demonstrated [3], [13]. This is already one order of magnitude higher than alternative technologies, such as organic LED displays [3]. A single micropixel can provide an optical power density >150 W/cm^2 yielding luminance in excess of 10^7 cd/m^2. However, scaling this single-pixel performance up to an entire high-brightness display is very challenging. The work reported here is based on CMOS driver electronics and LED arrays specifically designed to tackle this challenge.

We investigate the limitations and issues in high current density operation of flip-chip micro-LED arrays bump-bonded to a CMOS driver chip where several pixels are switched ON at the same time. It is found that in arrays with high LED fill-factor (i.e., the ratio of light-emitting area to total pixel area) a brightness drop occurs which we refer to as the multipixel droop. In the previous study, high current density operation in micro-LEDs was linked to improved thermal management of the small pixels [7]. Therefore, a drop in brightness due to device heating is expected when operating high fill-factor arrays. Interestingly, it is found here that, while thermal issues play a role, a severe limitation for multipixel operation is a nonthermal increase of differential resistance, which may be linked to current crowding. Current crowding will always cause additional device heating, but we demonstrate that the multipixel droop occurs in pulsed and moderate current continuous wave operating regimes where such heating is insignificant. It is, therefore, an electrical crosstalk that occurs in both pulsed and dc operation. This effect can be mitigated by careful layout of the n-contact, possibly sacrificing LED fill-factor. The importance of the n-contact layout has recently been highlighted in [14]

Manuscript received January 20, 2015; revised March 14, 2015; accepted March 21, 2015. Date of publication April 10, 2015; date of current version May 18, 2015. This work was supported by the Engineering and Physical Sciences Research Council through HYPIX Project under Grant EP/F05999X/1 and UltraParallel Visible Light Communications Project under Grant UP-VLC EP/K00042X/1. The review of this paper was arranged by Editor K. J. Chen.

J. Herrnsdorf, J. J. D. McKendry, E. Xie, R. Ferreira, E. Gu, and M. D. Dawson are with the Institute of Photonics, University of Strathclyde, Glasgow G4 0NW, U.K. (e-mail: johannes.herrnsdorf@strath.ac.uk; jonathan.mckendry@strath.ac.uk; enyuan.xie@strath.ac.uk; ricardo.ferreira@strath.ac.uk; erdan.gu@strath.ac.uk; m.dawson@strath.ac.uk).

S. Zhang is with the Institute of Photonics, University of Strathclyde, Glasgow G4 0NW, U.K., and also with the School of Engineering, University of Glasgow, Glasgow G12 8LT, U.K. (e-mail: shuailong.zhang@strath.ac.uk).

D. Massoubre was with the Institute of Photonics, University of Strathclyde, Glasgow G4 0NW, U.K. He is now with the Queensland Micro- and Nanotechnology Centre, Griffith University, Nathan QLD 4111, Australia (e-mail: d.massoubre@griffith.edu.au).

A. M. Zuhdi, R. K. Henderson, and I. Underwood are with the Joint Research Institute for Integrated Systems, Institute for Micro and Nano Systems, School of Engineering, University of Edinburgh, Edinburgh EH93JL, U.K. (e-mail: a.w.mahmood-zuhdi@ed.ac.uk; robert.henderson@ed.ac.uk; ian.underwood@ed.ac.uk).

S. Watson and A. E. Kelly are with the School of Engineering, University of Glasgow, Glasgow G12 8LT, U.K. (e-mail: s.watson.2@research.gla.ac.uk; anthony.kelly@glasgow.ac.uk).

Color versions of one or more of the figures in this paper are available online at http://ieeexplore.ieee.org.

Digital Object Identifier 10.1109/TED.2015.2416915

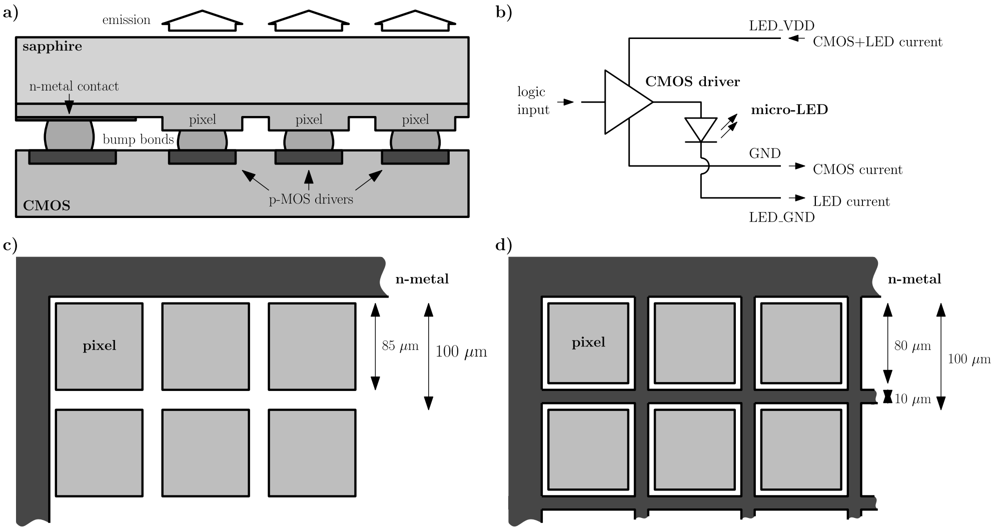

Fig. 1. Schematic of the devices for experimental investigation. (a) Cross section showing the integration of the LED arrays with the CMOS-chip. (b) Electric circuit. (c) Layout A. (d) Layout B.

and here we present a more in-depth study of the underlying physics and performance limitations. As a result of these investigations, we demonstrate a CMOS-integrated blue microdisplay with a display luminance of 10^6 cd/m^2 (12 W/cm^2), exceeding current commercial displays by a factor of 10^3.

II. Experimental Results

A range of factors influences the brightness achievable with micro-LED displays, including the quality of the epitaxial material, the layout of LEDs and CMOS, as well as thermal management. In this paper, we focus on the LED and CMOS layout. The epitaxial structures used are commercial sapphire-grown InGaN/GaN multiquantum-well structures emitting at 450 nm. The LEDs were fabricated as reported earlier [1] using Pd as the p-contact metal [15]. To the best of our knowledge, the epitaxial layer thicknesses and electrical properties are similar to those in Section III. All results reported here were obtained from a single wafer (and, where possible, from the same die) in order to allow the best comparison.

TABLE I
Comparison of the Generation 1 and Generation 2 CMOS Driver

	Generation 1	Generation 2
Array dimensions	16×16	10×40
Pixel pitch	100 μm	100 μm
Bond pad size	50×50 μm^2	100×100 μm^2
Number of power rails connected to one pixel	2	4
Power rail width LED_VDD	5.6 μm	40 μm 33 μm
Power rail width GND	4 μm	25 μm 17 μm
Power rail resistance LED_VDD	0.71 Ω	0.21 Ω 0.17 Ω
Power rail resistance GND	1 Ω	0.40 Ω 0.28 Ω
DC Driving current per pixel	200 mA	400 mA
Electronics underneath bond pad	No	Yes
Fraction of pixel area used by drive transistors	36 %	90 %

A. CMOS Layout

Each micro-LED array was bump-bonded directly on top of a CMOS driver chip fabricated in a 0.35-μm process containing a pitch-matched array of drive circuits [Fig. 1(a)]. These were designed with the aim of driving the highest possible current per pixel while also allowing switching on a nanosecond timescale. To enable LED drive voltages beyond the operating voltage of the CMOS, the driver chip was implemented with three voltage terminals, LED_VDD, GND, and LED_GND, which are shown in Fig. 1(b). LED operating voltages up to 8.3 V are possible by supplying a CMOS compatible voltage of 3.3 V (with respect to GND) on the LED_VDD terminal and −5 V on the LED_GND terminal. Note that the CMOS driver reported here is the latest development in a series of driver chips specifically designed for driving micro-LED pixel arrays [1], [10], [16]–[18]. In this section, we compare the present driver (generation 2) to the previous one (generation 1) [10], [18]. We highlight the changes that were made to enable high-power display operation. A synopsis of both generations is given in Table I.

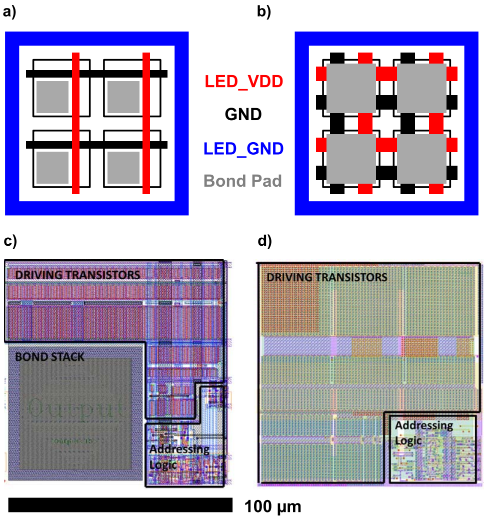

Fig. 2. Schematic of the design changes between (a) and (c) generation 1 CMOS driver and (b) and (d) generation 2 CMOS driver. (a) and (b) Power rail configuration. (c) and (d) Layout of an individual pixel. Note that in (d), the bond stack covers the entire pixel.

The voltage uniformity across the pixel array was improved by reducing the voltage drop along the power rails of the chip due to their resistance. This was minimized by making the power rails supplying each pixel as wide as possible. Furthermore, they were laid out in a grid arrangement, which compares with a linear arrangement in generation 1 [Fig. 2(a) and (b)]. Values for the rail width and resistance in both generations are given in Table I. Both the LED_VDD and the GND rails have a factor 3 and 4 lower rail resistance in generation 2 compared with generation 1. Furthermore, the power rails are each routed through ten dedicated bonding pads.

The integration by bump-bonding requires each pixel to have a bond pad. An important difference between the two CMOS driver generations is that in generation 1, the bond pad area was prohibited to active circuitry in order to avoid fusion with the lower level metals during the bump-bonding process, thus short-circuiting the circuitry underneath [16]. In generation 2, the bond pad was placed on top of the drive circuit so that both could utilize the full pixel area, as shown in Fig. 2(d). This was enabled by making the top metal layer thick and mechanically strong so that it can withstand the forces applied during bonding. The resulting area increase of the driving transistors is clearly visible in Fig. 2(c) and (d). In generation 2, 90% of the pixel area was occupied by the driving transistors, which compares with 36% for generation 1. This increase of transistor size enhances the current handling capability of each driver element.

As a result of these improvements, the generation 2 driver can handle up to 400-mA dc per pixel, which is twice the value of the generation 1 device. A single pixel current of ~300 mA (limited by the LED) has been realized, and a 10 × 10 section of the array (1 × 1 mm^2 area) has been operated at a total current of 900 mA.

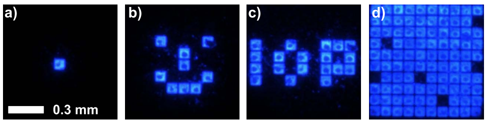

Fig. 3. Patterns displayed on device B at 10^6 cd/m^2 (~7.7 mA/pixel). (a) Single pixel. (b) Smiley. (c) Letters IOP. (d) Full array with a few defects. The voltage was 3.6 V and the camera settings were kept identical for all micrographs.

B. LED Layout

We illustrate the multipixel droop on the basis of two 10 × 10 LED arrays, labeled A and B. These correspond to Fig. 1(c) and (d), respectively. Both were implemented in flip-chip format on the same wafer die and bonded to the same CMOS chip allowing optimal comparison. Note that six other layouts have been fabricated as well and confirm the trends outlined here. These further results are not shown here for brevity and clarity.

Array A is similar to previously reported micro-displays [3], [18] and serves as a reference. It consists of 85 × 85 μm^2 mesas at 100-μm pitch, forming a 10 × 10 array. The n-contact metal surrounds the array and there is no n-metal between the mesas. It is, therefore, similar to devices A1 and A2 in Section III.

Array B is a 10 × 10 array of 80 × 80 μm^2 mesas at 100-μm pitch. In this case, the surrounding n-metal contact is supplemented by 10-μm wide n-metal tracks running through the gaps between each mesa. It is, therefore, similar to device B in Section III.

Both array types are part of a larger 10 × 40 array on a single die, which was bump-bonded to a CMOS chip, as shown in Fig. 1(a). Therefore, both device types have undergone exactly the same fabrication steps at the same time. Fig. 3 shows micrographs of representative displayed patterns. Even though the bump-bonding causes a dark region in the center of the pixels, the optical output power of the individual pixels differs minimally from that prior to bonding the device measured by needle probing. At an operating voltage of 3.3 V, the individual pixels draw a uniform current with <10% pixel-to-pixel variation. This is particularly relevant because in Section II-C it will be shown that the multipixel droop manifests in the current–voltage (I–V) characteristics.

C. Limitation of Display Luminance

At a given LED voltage and resulting LED current, the optical power was measured using a silicon photodetector, which was placed at 3-cm distance from the device. The collection efficiency in this configuration was estimated by assuming a Lambertian emission pattern [9] and the conversion of optical power to luminous intensity was also based on the assumption of a Lambertian emission pattern. Note that the optical power

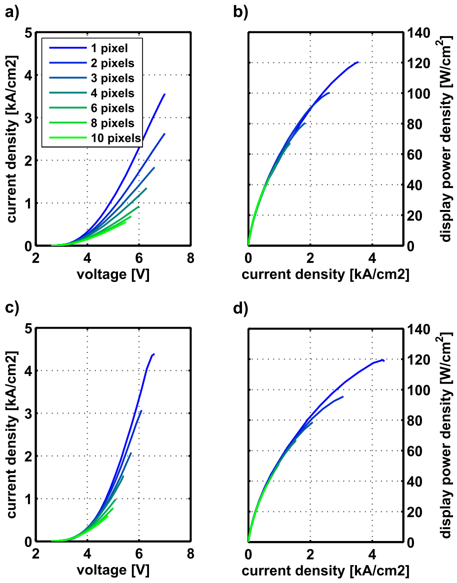

Fig. 4. (a) I–V and (b) L–I of layout A. (c) I–V and (d) L–I of layout B.

and luminous intensity are normalized to the pixel area as a direct measure of display brightness. The current, on the other hand, is normalized to the active area because in the light of earlier investigations [7], [10], [19] this allows the best comparison between the slightly differently sized mesas of layouts A and B.

Earlier studies investigated the dependence of the (I–V) and luminance–current (L–I) characteristics of GaN LEDs as a function of LED size [7] and showed significant variation. Similarly, the I–V and L–I characteristics of a densely packed LED array both vary with the number of pixels that are switched ON, as shown in Fig. 4. Interestingly, the L–I curves are almost identical and the major difference is due to the slightly different LED fill-factor of the two devices. This is discussed in Section II-D. However, clear differences can be seen in the I–V curves.

In both layouts, the I–V shows a higher resistance per pixel the more pixels are switched ON. This multipixel droop depends on both the pixel number and the operating voltage. Close to turn ON, the I–V is independent of the pixel number. However, at voltages that significantly exceed turn ON, a large number of pixels will draw a smaller current density than a small number of pixels, i.e., there is a crosstalk between the pixels that reduces the current per pixel.

By comparing Fig. 4(a) and (c), we see that the multipixel droop is less severe in layout B, indicating that a suitable layout of the n-contact can alleviate the multipixel droop. This finding is well-aligned with an observation in [20] that the n-contact layout is generally important for high performance of lateral-injection LEDs.

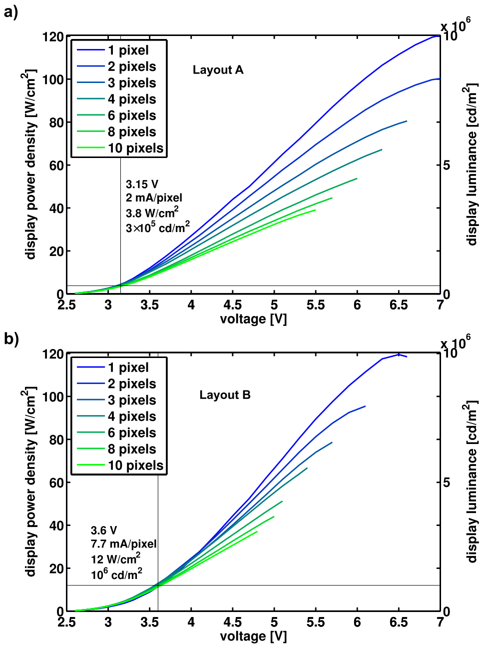

Fig. 5. L–V characteristics of (a) layout A and (b) layout B. Left y-axis: optical output power density normalized to the pixel area (100 × 100 μm^2). Right y-axis: equivalent display luminance for an emission wavelength of 450 nm and a Lambertian emission profile.

The impact of this phenomenon on the display performance shows up in the luminance–voltage (L–V) characteristics shown in Fig. 5. At low voltages, the L–V curves overlap but at higher values they fan-out significantly. This means that above a certain drive voltage the brightness changes upon switching ON and OFF pixels are too large for useful display operation. As indicated in Fig. 5, this operating point for maximal brightness has approximately three times higher optical output power in device B than in device A despite the slightly lower LED fill-factor.

Patterns with larger pixel numbers are compared in Fig. 6 at a constant operating voltage, showing clear multipixel droop. Layout B has generally higher brightness and the relative droop is less severe (54% for layout A and 45% for layout B when switching on a 10 × 10 array). When the full array is switched ON, the power density has dropped to 8.8 W/cm^2. Notably, by raising the voltage from 3.6 to 3.8 V, the brightness of the full array was raised to 11.5 W/cm^2, i.e., only moderate adjustments to the operating voltage are needed to maintain good uniformity.

D. Thermal Effects

The influence of device heating on the multipixel droop can be assessed indirectly from the L–I characteristics and

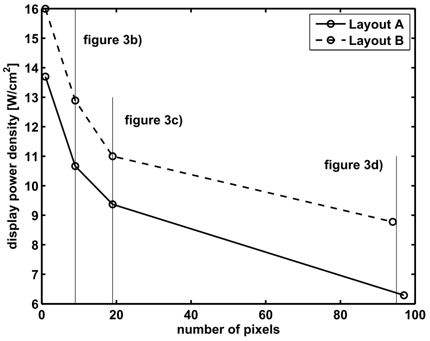

Fig. 6. Optical output power of the display at a constant drive voltage of 3.6 V as a function of pixel number up to a large scale. Note that the power is normalized to the pixel area (100 × 100 μm^2) and not to the active area (85 × 85 μm^2 for device A and 80 × 80 μm^2 for device B). Vertical lines: pixel numbers corresponding to the patterns are shown in Fig. 3.

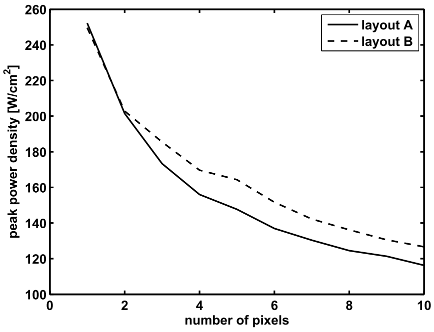

Fig. 7. Peak optical power normalized to pixel area of 10-ns pulses at 8.3 V and 100-Hz repetition rate as a function of pixel number.

directly by thermal imaging. At high currents, heating causes thermal rollover of the optical output power. It can be noted though that rollover occurs at lower current densities, the more pixels are switched ON. This means that cumulative heating has an impact on the device performance and will need to be addressed when pushing display brightness toward and beyond the 10^7 cd/m^2 mark.

Interestingly though, we find that the observed multipixel droop is not entirely of a thermal nature. A first evidence for this is given by nanosecond pulsed operation at low duty cycle, where virtually no cumulative heating occurs. Fig. 7 shows the optical output power when operating with pulses of 10-ns duration (achieved by switching the CMOS transistors with an external clock signal) at a duty cycle of 10^{-6}. In this configuration, no device heating will occur, yet a significant (factor 2) multipixel droop is observed. Note that layout B performs slightly better in pulsed operation, which is remarkable considering the different LED fill-factor.

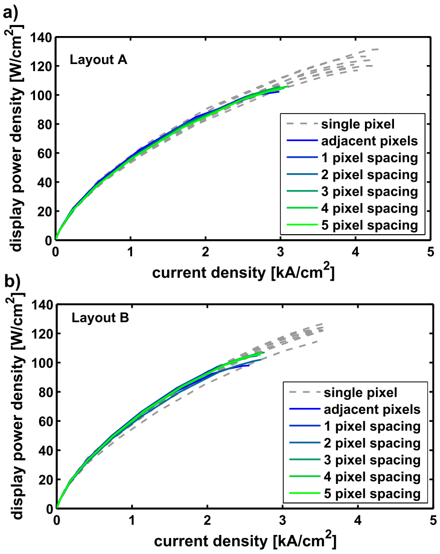

Fig. 8. *L–I* characteristics of two pixels at different relative position in (a) layout A and (b) layout B. Dashed gray curves: single pixel *L–I* characteristics of all the individual pixels involved in this measurement.

Further evidence is obtained in dc operation. Fig. 8 compares the *L–I* characteristics of two pixels switched ON simultaneously and the two pixels are either adjacent to each other or separated by some distance. When the two pixels are adjacent to each other, thermal rollover occurs at ~75% of the current density at which the single pixels rollover. However, when the two operated pixels are several hundred micrometers apart, the thermal rollover is not changed. First of all, this indicates that heat is efficiently spread across the die. Notably though, this behavior is identical for both layouts. This indicates that the thermal property is not responsible for the different multipixel-droop behavior of the two layouts.

To gain better insight into the temperature distribution in the device, we used a thermal infrared camera. Fig. 9(a) presents the junction temperature of a single pixel as a function of current density (kept below rollover). There is no significant difference between layouts A and B. Device B has marginally lower temperatures due to the lower LED fill-factor. Note that the observed junction temperatures are lower than usually reported for GaN-based LEDs under similar driving conditions [21]. We attribute this to improved heat sinking via the bump bonds to the CMOS chip and the small size of the LED pixels.

An example of a thermal image of the device with two pixels switched ON is given in Fig. 9(b). In this case, the pixels have a temperature of ~35 °C and the whole die is heated up to 32 °C. Here, the device was operated at a voltage

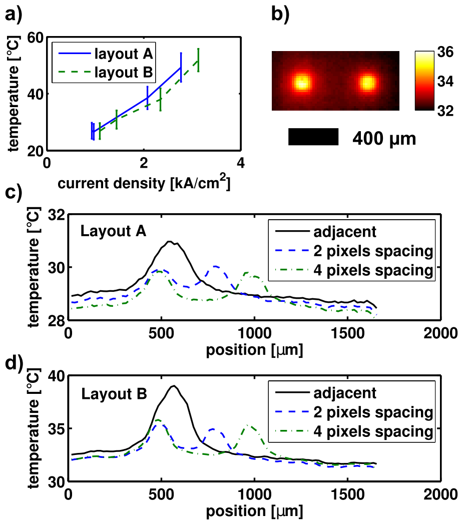

Fig. 9. Thermal performance analyzed by IR imaging. (a) Junction temperature for a single pixel. (b) Image of two pixels switched ON simultaneously (layout B, four pixels spacing). (c) and (d) Temperature profiles of two pixels with different spacing operated at 4.8 V for (c) layout A at 0.78 kA/cm^2 and (d) layout B at 1.28 kA/cm^2.

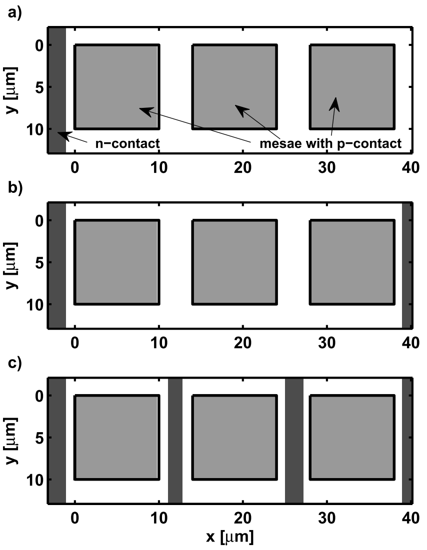

Fig. 10. Schematic of the modeled devices. (a) Layout A1. (b) Layout A2. (c) Layout B. Light gray: mesa area. Dark gray: area covered by n-metal.

of 4.8 V and a current density of 1.28 kA/cm^2, which is well below thermal rollover. For a better quantitative comparison, Fig. 9(c) and (d) shows the temperature profile along a cross section through the centers of both pixels for different pixel spacing. The voltage was kept constant at 4.8 V and, therefore, layout A operated at 60% of the current density of layout B and consequently it had a lower temperature. If the pixels are spaced apart by 100-μm separation or more, their temperature is independent of the pixel spacing. In this case, the mutual heating of the pixels is enabled by the uniform widespread heating across the whole die. Only for directly adjacent pixels, a rise in junction temperature can be seen by thermal imaging. Even then, the temperature of the whole die is the same as for any other pixel spacing.

III. THEORETICAL INVESTIGATION OF THE CURRENT DISTRIBUTION

The experimental results indicate that the current distribution within the n-layer of the devices is important. Therefore, the current density was calculated from a finite-difference model implemented in MATLAB [22], [23]. Here, thermal effects are neglected, highlighting the impact of the n-contact layout on the current distribution in the structure. The following material parameters were used:

$$n_n = 5 \times 10^{18}\ \text{cm}^{-3} \qquad n_p = 10^{17}\ \text{cm}^{-3} \tag{1a}$$

$$\mu_n = 200\ \text{cm}^2/\text{Vs} \qquad \mu_p = 1\ \text{cm}^2/\text{Vs} \tag{1b}$$

$$\rho_{c,n} = 10^{-5}\ \Omega\text{cm}^2 \qquad \rho_{c,p} = 10^{-5}\ \Omega\text{cm}^2 \tag{1c}$$

where n_n and n_p are the electron and hole concentrations in the n- and p-doped regions, μ_n and μ_p are the corresponding carrier mobilities, and $\rho_{c,n}$ and $\rho_{c,p}$ are the contact resistivities of the metal contacts to the n- and p-doped semiconductor regions. The junction was described as an ideal diode with saturation current $j_{\text{sat}} = 10^{-9}$ A/cm^2, ideality factor $n = 5$, and room temperature Boltzmann factor $kT = 27$ meV.

Fig. 10 shows the schematic of the three modeled devices, labeled A1, A2, and B for easy comparison with the devices in Section II. All of them consist of three $10 \times 10\ \mu\text{m}^2$ mesas with a mesa height of 1 μm and a total semiconductor thickness of 3 μm, of which 200 nm are p-doped and the rest n-doped GaN. These devices are smaller than the LEDs in the experimental section in order to reduce the computational effort. The difference between the devices is the layout of the n-contact. Layouts A1 and A2 have no n-contact in between the mesas, whereas layout B has a metal stripe between each mesa. Design A1 has a single n-contact on one side of the device. This is known to cause current crowding effects at high current densities [24], [25]. In layout A2, the pixel group has n-metal contacts on both sides, which is typical for high LED fill-factor arrays and provides good uniformity at low current densities [3]. Finally, design B has n-contacts surrounding each mesa individually.

We look first at the operation of a single pixel at a bias voltage of 4.5 V. Under these conditions, a relatively uniform (<10% variation) current density of ~700 A/cm^2 passes through the junction of the biased pixel. Fig. 11 maps the current density distribution along a cross section through

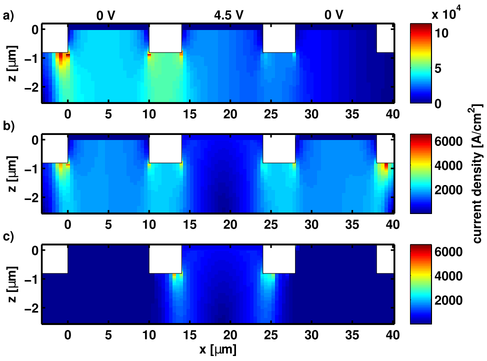

Fig. 11. Current density distribution in the devices shown in Fig. 10 when a voltage of 4.5 V is applied to the center pixel and the side pixels are left at 0 V. (a) Cross-sectional view at $y = 5$ μm through the device A1 shown in Fig. 10(a). (b) and (c) Correspond to layouts A2 [Fig. 10(b)] and B [Fig. 10(c)], respectively.

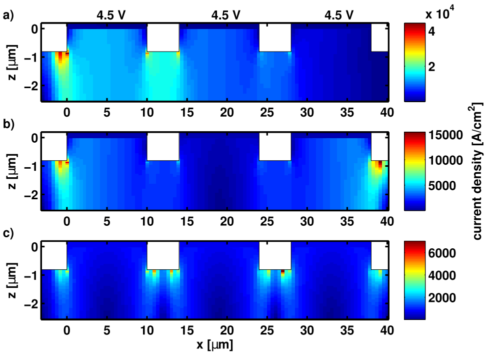

Fig. 12. Similar to Fig. 11, current density cross sections through the devices in Fig. 10. A bias voltage of 4.5 V is applied to all three pixels.

the device. It can be seen that the asymmetric n-layout (device A1) suffers from significant current crowding toward the single n-contact. In the symmetric layouts, the current injected into the center pixel is evenly distributed to the two closest n-contacts, giving similar peak current densities. Note also that in layouts A1 and A2 high lateral currents flow underneath pixels with 0 V bias. Even though there is no vertically injected current in these pixels, the current density in the n-layer is still large due to the current injected at adjacent pixels.

Fig. 12 shows the current density distribution when all pixels are operated simultaneously. It can be seen that current crowding effects at the mesa edges and n-contact edges are only minimized when each mesa is surrounded by its own n-contact regions [layout B, Figs. 10(c) and 12(c)]. Furthermore, the asymmetric n-contact [Fig. 12(a)] leads to current crowding toward the n-contact [24].

Section II-C demonstrates that the multipixel droop is an effect of increased parasitic differential resistance upon switching ON several pixels. It was shown in Section II-D that this differential resistance cannot solely be attributed to device heating and that the n-contact layout has an influence on this effect. The simulation confirms that a major difference between the layouts is the current density distribution. This suggests that there may be a link between current crowding and the multipixel droop. For example, the n-GaN conductivity may change nonthermally as a function of current density. This interpretation is in line with earlier observations that the drift velocity of electrons in semiconductors rolls over at high electric field strength [26], i.e., effectively the electron mobility μ_n decreases at high current density.

IV. CONCLUSION

High brightness CMOS-controlled microdisplays can be made on the basis of GaN flip-chip micro-LEDs. Limiting factors to the achievable luminance include the current handling capability of the control electronics, the current distribution within the LED structure and thermal management. In particular, it is demonstrated that careful LED design toward optimal current distribution in the n-GaN layer is crucial for obtaining the highest possible display luminance. These design considerations may have impact on the fill-factor, pixel size, and resolution. Furthermore, we show that in high-brightness dc and pulsed operation an electrical crosstalk occurs, which is caused by a nonthermal increase of differential resistance and may be linked to current crowding.

REFERENCES

[1] J. J. D. McKendry *et al.*, "Individually addressable AlInGaN micro-LED arrays with CMOS control and subnanosecond output pulses," *IEEE Photon. Technol. Lett.*, vol. 21, no. 12, pp. 811–813, Jun. 15, 2009.

[2] Z. J. Liu, K. M. Wong, C. W. Keung, C. W. Tang, and K. M. Lau, "Monolithic LED microdisplay on active matrix substrate using flip-chip technology," *IEEE J. Sel. Topics Quantum Electron.*, vol. 15, no. 4, pp. 1298–1302, Jul./Aug. 2009.

[3] J. Day, J. Li, D. Y. C. Lie, C. Bradford, J. Y. Lin, and H. X. Jiang, "III-nitride full-scale high-resolution microdisplays," *Appl. Phys. Lett.*, vol. 99, no. 3, p. 031116, 2011.

[4] N. Grossman *et al.*, "Multi-site optical excitation using ChR2 and micro-LED array," *J. Neural Eng.*, vol. 7, no. 1, p. 016004, 2010.

[5] A. Zarowna-Dabrowska *et al.*, "Miniaturized optoelectronic tweezers controlled by GaN micro-pixel light emitting diode arrays," *Opt. Exp.*, vol. 19, no. 3, pp. 2720–2728, 2011.

[6] A. H. Jeorett *et al.*, "Optoelectronic tweezers system for single cell manipulation and fluorescence imaging of live immune cells," *Opt. Exp.*, vol. 22, no. 2, pp. 1372–1380, 2014.

[7] Z. Gong *et al.*, "Size-dependent light output, spectral shift, and self-heating of 400 nm InGaN light-emitting diodes," *J. Appl. Phys.*, vol. 107, no. 1, p. 013103, 2010.

[8] Z. J. Liu, W. C. Chong, K. M. Wong, K. H. Tam, and K. M. Lau, "A novel BLU-free full-color LED projector using LED on silicon micro-displays," *IEEE Photon. Technol. Lett.*, vol. 25, no. 23, pp. 2267–2270, Dec. 1, 2013.

[9] J. Herrnsdorf *et al.*, "Micro-LED pumped polymer laser: A discussion of future pump sources for organic lasers," *Laser Photon. Rev.*, vol. 7, no. 6, pp. 1065–1078, 2013.

[10] J. J. D. McKendry *et al.*, "Visible-light communications using a CMOS-controlled micro-light-emitting-diode array," *J. Lightw. Technol.*, vol. 30, no. 1, pp. 61–67, Jan. 1, 2012.

[11] D. Tsonev *et al.*, "A 3-Gb/s single-LED OFDM-based wireless VLC link using a gallium nitride μLED," *IEEE Photon. Technol. Lett.*, vol. 26, no. 7, pp. 637–640, Apr. 1, 2014.

[12] S. Zhang *et al.*, "1.5 Gbit/s multi-channel visible light communications using CMOS-controlled GaN-based LEDs," *J. Lightw. Technol.*, vol. 31, no. 8, pp. 1211–1216, Apr. 15, 2013.

[13] Z. Gong *et al.*, "Matrix-addressable micropixellated InGaN light-emitting diodes with uniform emission and increased light output," *IEEE Trans. Electron Devices*, vol. 54, no. 10, pp. 2650–2658, Oct. 2007.

[14] Z. J. Liu, W. C. Chong, K. M. Wong, C. W. Keung, and K. M. Lau, "Investigation of forward voltage uniformity in monolithic light-emitting diode arrays," *IEEE Photon. Technol. Lett.*, vol. 25, no. 13, pp. 1290–1293, Jul. 1, 2013.

[15] J.-L. Lee *et al.*, "Ohmic contact formation mechanism of nonalloyed Pd contacts to *p*-type GaN observed by positron annihilation spectroscopy," *Appl. Phys. Lett.*, vol. 74, no. 16, pp. 2289–2291, 1999.

[16] B. R. Rae, "Micro-systems for time-resolved fluorescence analysis using CMOS single-photon avalanche diodes and micro-LEDs," Ph.D. dissertation, School Eng., Univ. Edinburgh, Edinburgh, U.K., 2009.

[17] B. R. Rae *et al.*, "A CMOS time-resolved fluorescence lifetime analysis micro-system," *Sensors*, vol. 9, no. 11, pp. 9255–9274, 2009.

[18] S. Zhang *et al.*, "CMOS-controlled color-tunable smart display," *IEEE Photon. J.*, vol. 4, no. 5, pp. 1639–1646, Oct. 2012.

[19] W. Yang *et al.*, "Size-dependent capacitance study on InGaN-based micro-light-emitting diodes," *J. Appl. Phys.*, vol. 116, no. 4, p. 044512, 2014.

[20] X. Guo, Y.-L. Li, and E. F. Schubert, "Efficiency of GaN/InGaN light-emitting diodes with interdigitated mesa geometry," *Appl. Phys. Lett.*, vol. 79, no. 13, pp. 1936–1938, 2001.

[21] S. Chhajed, Y. Xi, Y.-L. Li, T. Gessmann, and E. F. Schubert, "Influence of junction temperature on chromaticity and color-rendering properties of trichromatic white-light sources based on light-emitting diodes," *J. Appl. Phys.*, vol. 97, no. 5, p. 054506, 2005. [Online]. Available: http://scitation.aip.org/content/aip/journal/jap/97/5/10.1063/1.1852073

[22] J. Herrnsdorf, E. Xie, I. M. Watson, N. Laurand, and M. D. Dawson, "Planar micro- and nano-patterning of GaN light-emitting diodes: Guidelines and limitations," *J. Appl. Phys.*, vol. 115, no. 8, p. 084503, 2014.

[23] M. V. Bogdanov, K. A. Bulashevich, I. Y. Evstratov, A. I. Zhmakin, and S. Y. Karpov, "Coupled modeling of current spreading, thermal effects and light extraction in III-nitride light-emitting diodes," *Semicond. Sci. Technol.*, vol. 23, no. 12, p. 125023, 2008.

[24] X. Guo and E. F. Schubert, "Current crowding and optical saturation effects in GaInN/GaN light-emitting diodes grown on insulating substrates," *Appl. Phys. Lett.*, vol. 78, no. 21, pp. 3337–3339, 2001.

[25] A. E. Chernyakov, K. A. Bulashevich, S. Y. Karpov, and A. L. Zakgeim, "Experimental and theoretical study of electrical, thermal, and optical characteristics of InGaN/GaN high-power flip-chip LEDs," *Phys. Status Solidi A*, vol. 210, no. 3, pp. 466–469, 2013.

[26] H. Okumura, "Present status and future prospect of widegap semiconductor high-power devices," *Jpn. J. Appl. Phys.*, vol. 45, no. 10A, pp. 7565–7586, 2006.

Johannes Herrnsdorf received the Ph.D. degree in physics from the University of Strathclyde, Glasgow, U.K., in 2012.

He is involved in GaN micro-LEDs.

Jonathan J. D. McKendry (M'13) received the Ph.D. degree in physics from the University of Strathclyde, Glasgow, U.K., in 2011.

He is involved in GaN micro-LEDs.

Shuailong Zhang received the Ph.D. degree in physics from the University of Strathclyde, Glasgow, U.K., in 2015.

He is currently with the University of Glasgow, Glasgow.

Enyuan Xie received the Ph.D. degree in physics from the University of Strathclyde, Glasgow, U.K., in 2013.

He is involved in fabrication of GaN LEDs.

Ricardo Ferreira received the M.Sc. degree in engineering physics from the University of Aveiro, Aveiro, Portugal. He is currently pursuing the Ph.D. degree in visible light communications with the University of Strathclyde, Glasgow, U.K.

David Massoubre received the Ph.D. degree in physics from the University of Paris-Sud, Orsay, France, in 2006.

He was with the University of Strathclyde, Glasgow, U.K. He is currently with Griffith University, Nathan, QLD, Australia, where he is involved in SiC/Si for photonics and GaN devices.

Ahmad Mahmood Zuhdi received the M.Eng. degree in electrical and electronics engineering from the University of Edinburgh, Edinburgh, U.K., in 2008, where he is currently pursuing the Ph.D. degree in displays and sensors with feedback.

Robert K. Henderson received the Ph.D. degree from the University of Glasgow, Glasgow, U.K., in 1990.

He was with the Swiss Centre for Microelectronics, Neuchatel, U.K., VLSI Vision Ltd., Edinburgh, U.K., and the University of Edinburgh, Edinburgh. His current research interests include CMOS electronics.

Ian Underwood received the Ph.D. degree in physics from the University of Edinburgh, Edinburgh, U.K., in 1987.

He was involved in the development of liquid crystal on Si technology with the University of Edinburgh, and the University of Colorado, Boulder, CO, USA. He has been a Professor since 2004, and currently leads the Institute for Integrated Micro and Nano Systems.

Scott Watson received the B.Eng. degree in electronics with music from the University of Glasgow, Glasgow, U.K., where he is currently pursuing the Ph.D. degree in visible light communications.

Anthony E. Kelly received the Ph.D. degree from the University of Strathclyde, Glasgow, U.K., in 1999.

He was with the Corning Research Centre, U.K., and Amphotonix Ltd., U.K. He is currently a Senior Lecturer with the University of Glasgow, Glasgow. His current research interests include optical communications.

Erdan Gu received the Ph.D. degree in physics from the University of Aberdeen, Aberdeen, U.K., in 1992.

He was with the Cavendish Laboratory, Cambridge, U.K., Oxford Instruments plc, Abingdon, U.K., and the University of Strathclyde, Glasgow, U.K. He is currently an Associate Director with the Institute of Photonics.

Martin D. Dawson (M'85–SM'98–F'09) received the Ph.D. degree in physics from Imperial College London, London, U.K., in 1985.

He was with the University of North Texas, Denton, TX, USA, the University of Iowa City, Iowa, IA, USA, SLE Oxford, and the University of Strathclyde, Glasgow, where he is currently a Professor. He is also the Director of Research with the Institute of Photonics and the Fraunhofer Center for Applied Photonics.

JOURNAL OF LIGHTWAVE TECHNOLOGY, VOL. 33, NO. 17, SEPTEMBER 1, 2015 3571

μLED-Based Single-Wavelength Bi-directional POF Link With 10 Gb/s Aggregate Data Rate

Xin Li, Nikolaos Bamiedakis, Jinlong Wei, Jonathan J. D. McKendry, Enyuan Xie, Ricardo Ferreira, Erdan Gu,
Martin D. Dawson, Richard V. Penty, and Ian H. White

***Abstract*—We report record 10 Gb/s bi-directional data transmission over a single 10 m SI-POF, by employing blue microlight-emitting diodes (μLEDs) at a single wavelength, APD receivers, and a PAM-32 modulation scheme. The implementation of 10 Gb/s LED-POF links takes advantage of the bi-directional configuration, which doubles the overall channel capacity, and APDs, which provide an enhanced link power budget owing to their improved sensitivity compared with conventional p-i-n photodiodes. Moreover, the high spectral efficiency of the PAM-32 modulation scheme employed, together with equalization techniques, enable the full utilization of the link bandwidth and the transmission of data rates higher than those obtained with conventional on–off keying. Simulation and experimental results demonstrate the feasibility of such a bi-directional link, and simultaneous 5 Gb/s data transmission is realized in each direction, achieving an aggregate data rate of 10 Gb/s with a BER $< 10^{-3}$. The crosstalk penalty between the two directions of the link is measured to be less than 0.5 dB.**

***Index Terms*—APD, bi-directional communication, micro-LED, plastic optical fiber (POF), pulse amplitude modulation (PAM).**

I. INTRODUCTION

In recent years, there has been much research interest in the deployment of step-index plastic optical fiber (SI-POF) in low-cost short-reach communication links, such as those employed in in-home and automotive networks. These applications can fully exploit the mechanical and cost advantages provided by SI-POF, namely, ease of installation, high flexibility, resilience to bending, shock and vibration, and cost-efficiency [1], [2]. Moreover, it has been shown that POF links, apart from higher interconnection data rates, can also provide cost and power advantages over common copper-based technologies [3], [4]. Light-emitting diodes (LEDs) appear to be especially attractive for use in such low cost SI-POF links as they are compatible with the large core diameter of POF, eye-safe, and cost- and energy-efficient. However, the increasing network traffic foreseen in such environments (e.g., the interconnected house, 3-DTV, HDTV, multi-sensor automotive data networks) will require high transmission data rates of >1 Gb/s over such optical links [5]. The high speed performance of LED-POF links is typically limited by the low bandwidth of the POF (200 MHz × 50 m), the RCLEDs typically employed (∼100 MHz), and the relatively high attenuation coefficient of SI-POF (e.g., 0.16 dB/m at 650 nm) [5]. As a result, various schemes which enable an improvement in the achievable data rates over LED-POF links, such as advanced modulation formats, multiplexing techniques, such as wavelength-division multiplexing (WDM) and bi-directional (BiDi) transmission, and the use of avalanche photodiodes (APDs) have attracted considerable research interest. The use of spectrally efficient modulation formats, such as multi-level and multi-carrier modulation, has been proposed and demonstrated in such links. A 5 Gb/s data transmission rate over 25 m of a RCLED-POF link has been realised using 32-level pulse amplitude modulation (PAM-32) with a bit-error ratio (BER) $<10^{-12}$ [6]. A 5.5 Gb/s transmission over 1 m SI-POF is achieved employing GaN LEDs and a PAM-4 modulation scheme [7]. Discrete multi-tone modulation has also been demonstrated using an LED transmitter, achieving 1.5 Gb/s over 50 m of POF with a BER $< 10^{-3}$ [8]. Moreover, WDM has been implemented over SI-POF links using six laser diodes and achieving an aggregate data rate of 21.4 Gb/s [9]. A 1 Gb/s real-time BiDi transmission over a single SI-POF is achieved using red lasers and a passive 1 × 2 POF splitter [10]. Finally, recent studies have demonstrated that APDs can offer improved sensitivity in such links enabling higher data rates or longer reaches [6].

In this work, we propose the use of BiDi transmission over LED-POF links in order to double the channel capacity and we report record single-wavelength 10 Gb/s BiDi data transmission. The link employs 20 μm-diameter, 450 nm μLEDs, 800 μm-diameter APDs and PAM-32 modulation in order to achieve 5 Gb/s in each link direction. Such μLEDs, with diameters $\leq$100 μm, can demonstrate higher modulation bandwidths [11]. Moreover, μLEDs emitting in the blue wavelength range match very well the low attenuation window of POF and the attenuation coefficient is lower than that for red wavelength. It also offers high coupling efficiency owing to their small dimension in comparison to the POF core size (1 mm in diameter). 6.25 Gb/s data transmission over 10 m of POF using 4 μLEDs and a PAM-16 modulation has been experimentally demonstrated with a BER $< 10^{-3}$ [12]. Simulation studies on the BiDi μLED-POF link are presented indicating the feasibility of such link and highlighting the importance of the use of APD-based receivers. The BiDi optical link is implemented and data transmission

---

Manuscript received March 16, 2015; revised May 8, 2015; accepted May 13, 2015. Date of publication June 16, 2015; date of current version August 3, 2015. This work was supported by the UK EPSRC via the Ultra Parallel Visible Light Communication Project. Additional data related to this publication is available at the data repository https://www.repository.cam.ac.uk/handle/1810/247990.

X. Li, N. Bamiedakis, J. Wei, R. V. Penty, and I. H. White are with the Centre for Photonic Systems, Electrical Engineering Division, Department of Engineering, University of Cambridge, Cambridge CB2 1TN, U.K. (e-mail: xl336@cam.ac.uk; nb301@cam.ac.uk; jw748@cam.ac.uk; rvp11@cam.ac.uk; ihw3@cam.ac.uk).

J. J. D. McKendry, E. Xie, R. Ferreira, E. Gu, and M. D. Dawson are with the Institute of Photonics, University of Strathclyde, Glasgow G1 1XQ, U.K. (e-mail: jonathan.mckendry@strath.ac.uk; enyuan.xie@strath.ac.uk; ricardo.ferreira@strath.ac.uk; erdan.gu@strath.ac.uk; m.dawson@strath.ac.uk).

Color versions of one or more of the figures in this paper are available online at http://ieeexplore.ieee.org.

Digital Object Identifier 10.1109/JLT.2015.2443984

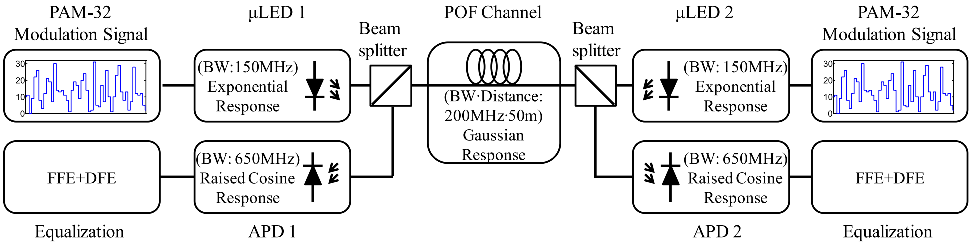

Fig. 1. BiDi link model with noted bandwidth (BW) for the optoelectronic components.

TABLE I
SIMULATION MODELS AND SPECIFICATION

Component	Response	Parameter
μLEDs	Exponential	Bandwidth: 150 MHz Emission Power: 0 dBm Wavelength: 450 nm
POF	Gaussian	Bandwidth distance product: 200 MHz $\times$ 50 m Attenuation:0.2 dB/m at 450 nm
APD	Raised-Cosine	Responsivity: 0.275 A/W Bandwidth: 650 MHz

experiments are carried out to investigate the link performance. A gross aggregate data rate of 10 Gb/s is achieved over 10 m of POF with a BER $< 10^{-3}$ for both directions, which is within forward-error correction (FEC) limits. The 10 Gb/s gross data rate includes the required FEC overhead. The crosstalk penalty for each link direction is measured to be less than 0.5 dB. The reported results constitute, to the best of our knowledge, a record aggregate data rate performance for LED-POF links at a single wavelength and demonstrate the potential to achieve relatively large capacity in short-reach optical links using such low-cost components.

The remainder of the paper is organized as follows. Section II describes the link model used for the simulation studies and presents the obtained results. The link implementation and data transmission experiments are reported in Section III, while Section IV provides the conclusions.

II. SYSTEM MODEL AND SIMULATION RESULTS

A link model is developed to study the performance of the BiDi LED-POF link (see Fig. 1). The characteristics of the components employed in the simulations are based on the actual components used in the link demonstration. Table I summarises the important parameters and the type of response assumed for the different components in the link. Separate component studies have been carried out to determine some of the μLED, POF and APD characteristics, while the value of the remaining parameters required are based on their datasheets. The impulse response of LEDs in fiber optic systems has been studied [13] and an exponential response is proposed. Moreover, the light-voltage (L–V) characteristic of the μLEDs is measured and is incorporated in the model in order to take into account the effect of their non-linear behaviour on the link performance. The frequency response of a SI-POF can be accurately modelled using a Gaussian filter [13]. The employed value for the POF loss coefficient at 450 nm (0.2 dB/m) is based on the measured value of the particular SI-POF (Eska-Mega) used in the experimental demonstration. The obtained loss value is larger than the 0.12 dB/m value used in the datasheet, as this includes bending losses and facets imperfections. The APD receiver is modelled as having a raised cosine frequency response [13] with a bandwidth of 650 MHz, as found by related measurements on the receivers used in the link implementation. The value for the APD responsivity used in the simulations is based on the datasheet of the APD employed in the experiments (First Sensor AD800-11). The value used is 0.275 A/W for M = 1. The receiver noise performance and APD avalanche gain (M) used in the simulation model are based on experimentally-determined values. The beam splitter is assumed to introduce a 3 dB coupling loss in each link direction.

In order to evaluate the effect of the use of the APD in the link, a similar link model is setup using a p-i-n-based receiver instead of the APD. The p-i-n receiver is modelled to have similar bandwidth and noise performance as the APD but with a unity avalanche gain (M = 1). The responsivity used for the p-i-n detector is chosen to be the same as the APD receiver without any gain (0.275 A/W) in order to provide a like-for-like comparison for the link power budget. The typical responsivity for a p-i-n detector at this wavelength range is of similar range (e.g. the commercially-available p-i-n receiver (Femto HAS-X-S-1G4-SI) has a responsivity of 0.19 A/W at 450 nm).

The PAM-32 signal is generated using a 2^9–1 pseudo random binary sequence (PRBS), emulating the short run length codes used in data communications (e.g., 8B10). Every 5 bits of the binary data sequence are combined to form the corresponding PAM-32 symbol. A 1 Gsample/s PAM-32 modulating signal is employed, giving rise to a gross data rate of 5 Gb/s in each direction. Due to the limited bandwidth of the link, the received PAM-32 waveform is severely distorted [see Fig. 2(a)] and the corresponding eye diagram is completely closed [see Fig. 2(b)]. As a result, feed-forward (FFE) and decision-feedback equalization (DFE) are used at the receiver to overcome the link bandwidth limitation and fully recover the transmitted signals [see Fig. 2(c)]. The obtained equalised eye diagrams are open and the 32 levels are clearly distinguishable, indicating that the transmitted data can be successfully recovered at the receiver.

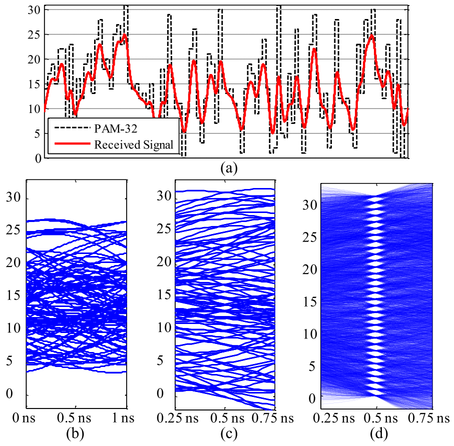

Fig. 2. Simulation results for (a) the transmitted ideal PAM-32 signal and received 5 Gb/s PAM-32 waveform after transmission over 25 m of POF, (b) received eye diagram in one link direction, (c) respective eye-diagram after equalization and (d) equalized eye-diagram generated using a 2^{15}–1 PRBS sequence at 5 Gb/s.

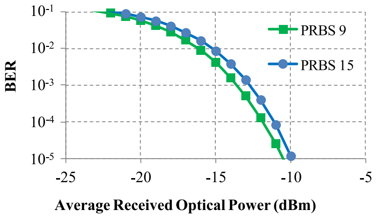

Fig. 3. Simulated BER results for the 5 Gb/s PAM-32 link using 2^{15}–1 PRBS and 2^9–1 PRBS pattern.

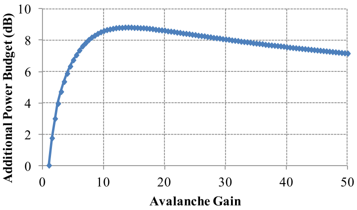

Fig. 4. Additional power budget in the μLED-POF link obtained with the APD receiver as a function of the APD avalanche gain.

It should be noted that the use of the relatively short pattern length (2^9–1 PRBS) results in the absence of some amplitude transitions in the transmitted PAM signal. In order to assess the link performance for a longer pattern which would generate more transitions, a longer 2^{15}–1 PRBS is also studied using the same link model. The simulated received eye diagram after equalization for a 2^{15}–1 PRBS pattern is obtained [see Fig. 2(d)] and the respective BER performance is calculated (see Fig. 3). The obtained eye diagrams are open and the levels are clearly distinguishable. The comparison of the BER curves obtained for a 2^{15}–1 PRBS and a 2^9–1 PRBS pattern indicates a small power penalty <0.5 dB at BER $= 10^{-3}$.

A power budget analysis is used to evaluate the link performance and compare the APD- and p-i-n-based link configurations. The APD exhibits higher sensitivity than the p-i-n and therefore provides a larger power budget. Fig. 4 shows the additional power budget obtained as a function of the APD avalanche gain M. The additional power budget increases as M increases due to the larger APD sensitivity until it reaches an optimum value $M_{\rm opt}$. Further increase in the gain M results in a performance deterioration due to the excess noise factor of the APD. For this particular device, the optimum APD avalanche gain $M_{\rm opt}$ is found to be 12 while the resulting power budget improvement over the p-i-n is ~9 dB. For the simulations, the μLED emitted power is assumed to be 0 dBm while the APD is assumed to operate at the optimum avalanche gain ($M_{\rm opt} = 12$), yielding a sensitivity of -33.7 dBm for a BER of 10^{-3} at 100 Mb/s. For comparison, the sensitivity of the respective p-i-n receiver is -24.5 dBm for the same 10^{-3} BER at 100 Mb/s.

The power penalties considered in the link budget analysis include the multilevel, noise enhancement, residual inter-symbol interference (ISI), extinction ratio, non-linearity, attenuation and beamsplitter loss penalties. The multilevel penalty is introduced by the multilevel modulation scheme due to the reduction in the amplitude between two adjacent levels of the PAM signal [14]. The higher the order of the PAM scheme, the larger is the multilevel penalty. For the PAM-32 scheme, the multilevel penalty is found to be 14.9 dB. The noise enhancement penalty is introduced by the FFE process as, apart from the received signal, the noise is also amplified. Its magnitude depends on the values of the tap coefficients used in FFE process. The residual ISI penalty represents the signal degradation due to the limited link bandwidth that cannot be mitigated through the equalization process. The extinction ratio power penalty is caused by the non-zero power level for the symbol “0,” while the non-linearity penalty is due to the signal distortion induced by the non-linear response of the μLED. The non-linearity penalty is obtained by comparing the BER performance of a link using a μLED with a linear and a non-linear *L–V* characteristic. For different POF lengths, the link bandwidth is different and therefore different tap coefficients are employed in the equalizers to optimise the link performance. As a result, the “linear” and “non-linear” links exhibit different eye closure for the different link lengths and therefore, different values for the respective non-linearity power penalty. The attenuation penalty represents the optical loss in the system due to the transmission over the POF and depends on the link length. To enable BiDi transmission in the link two beam splitters are used in the optical path resulting in additional optical loss in the system. For the simulations, each beamsplitter is assumed to introduce a loss of 3 dB in the link. Finally, a

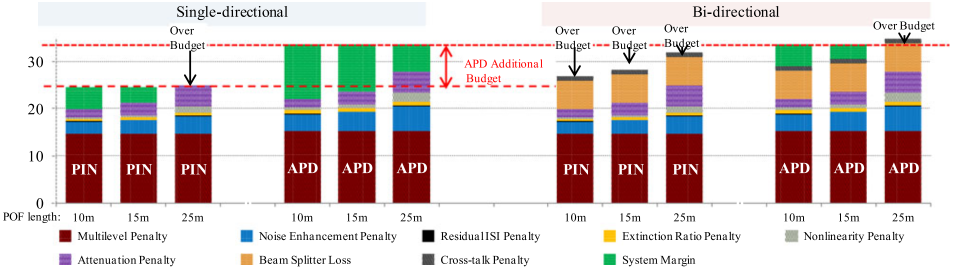

Fig. 5. Simulation results of power budget analysis.

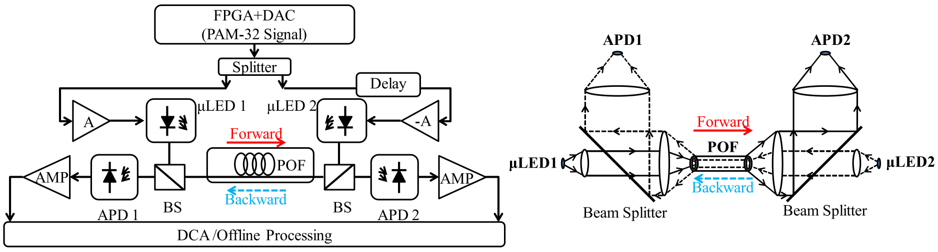

(a) (b)

Fig. 6. (a) Experimental setup for implementing the BiDi SI-POF link; (b) optical coupling scheme at each POF end.

crosstalk penalty of 1 dB is assumed in the BiDi link simulations to account for the effect of the use of the second μLED.

Fig. 5 shows in detail the link power budget of the single-directional (SiDi) and BiDi μLED-POF links implemented with both p-i-n and APD receivers for different POF lengths: 10, 15 and 25 m. The simulation results show that there is no system margin available for the p-i-n-based link to support 10 Gb/s BiDi data transmission for any of the POF lengths studied. However, the APD-based link is able to support 10 Gb/s BiDi transmission up to 15 m of SI-POF due to the larger power budget provided by the APD. The link power margins are found to be 5.7 dB and 4.5 dB for 10 and 15 m of POF, respectively. The simulation results clearly demonstrate the advantage of using APDs in SI-POF links and indicate the feasibility of achieving a 10 Gb/s BiDi link over SI-POF using μLEDs and a PAM-32 modulation scheme.

The link reach is limited by the optical losses in the system: POF attenuation, optical coupling loss at the μLEDs-POF and POF-APD interfaces and the 6 dB optical loss due to the use of the two beamsplitters in the optical path. Longer POF lengths therefore could be potentially supported by employing higher efficiency optical coupling schemes, such as in [15], where a monolithically-integrated transceiver chip is fabricated consisting of p-i-n PDs and top-emitting vertical cavity surface-emitting lasers.

III. EXPERIMENTAL SETUP AND RESULTS

An APD-based 10 Gb/s BiDi LED-POF link is implemented [see Fig. 6(a)]. Two 450 μm GaN μLEDs, each with a 20 μm diameter, are used as the transmitters and two 800 μm-diameter APD as the receivers. For the purposes of this demonstration, discrete optical coupling components are used to combine and split the two optical streams at the input and output of the POF respectively. The emitted light from the μLED is coupled into the POF using a pair of aspheric lenses while a beam splitter is introduced in the optical path at each POF end to enable BiDi link transmission [see Fig. 6(b)]. The light transmitted over the POF is focused on the APD using a pair of aspherical lenses. The input coupling loss (μLED-POF coupling) is measured to be $\sim$2.8 dB, while the output coupling loss (POF-APD coupling) is found to be $\sim$2.4 dB. A slight difference in the obtained coupling loss values is observed in each link direction due to the alignment of the coupling elements. The BiDi coupling scheme can be implemented with miniaturized components integrated with the source and receiver. Work towards this is currently underway to demonstrate a similar POF-link that could find application in real-world low-cost optical systems.

The 5 Gb/s PAM-32 modulation signal is generated using an FPGA and a 16-bit 1 GSamples/s DAC. The modulation signal is split into two PAM-32 signals, which are subsequently delayed

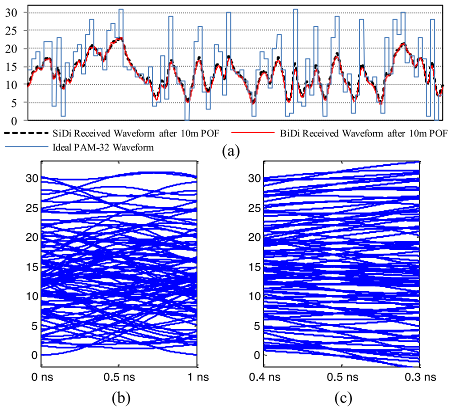

Fig. 7. (a) Received waveforms for SiDi and BiDi transmission; (b) received 5 Gb/s eye-diagram in one link direction after transmission over 10 m of POF and (c) respective eye-diagram after equalization.

with respect to each other to generate two quasi-decorrelated data streams and which are then amplified (SHF-826 H, BW: 70 kHz–25 GHz) in order to drive the two μLEDs. At the APD receiver end, the received electrical signals are amplified using a low noise amplifier (LNA, ZFL-1000L N+, BW: 0.1–1000 MHz, noise figure: 2.9 dB) and are captured using a digital communication analyzer for offline processing. The performance of the SiDi link is obtained using the same setup but by operating one μLED at a time.

The received electrical PAM-32 waveforms for the SiDi and BiDi link operation are shown in Fig. 7(a). The received waveform in the BiDi link is slightly more distorted than the one obtained from the SiDi link operation due to optical crosstalk induced by the operation of the second link channel. This optical crosstalk can be mainly attributed to reflections from the optical interfaces in the link (surfaces of the optical lenses, beam splitters, POF facets as well as APD and μLED dies). After equalization, the transmitted signals are successfully recovered in BiDi link operation and 32 clear signal levels can be observed in the equalised eye-diagram [see Fig. 7(c)]. The BER performance of the link is calculated using the equalised waveforms and the measured APD receiver noise.

In order to optimise the BiDi link performance, the optimum APD gain is investigated for this link configuration. Fig. 8 shows the obtained BER for the optical back-to-back (B2B, short POF patch cord) link under different APD gains. The optimum APD gain is found to be M = 14. The excess noise factor of the APD with M = 14 is 1.49. This yields a sensitivity of -16.8 dBm for a BER of 10^{-3}.

The BER performance of the BiDi link in each direction (forward and backward) is obtained for the optimum APD operating point [see Fig. 9(a) and (b)]. The BER curves obtained for SiDi data transmission over the same setup are also plotted for comparison. The plots demonstrate that BiDi 10 Gb/s transmission can be achieved over 10 m of POF with a BER $< 10^{-3}$. The average optical power required at the receiver end to achieve an aggregate 10 Gb/s over 10 m of SI-POF is –13.8 and –14.4 dBm for the forward and backward direction, respectively. The reverse link direction exhibits slightly improved performance over the forward link by ~0.7 dB, owing to the slightly larger bandwidth of the μLED used in this direction. The power penalty due to optical crosstalk can be found by comparing the BER curves for the SiDi and BiDi links. This is found to be 0.5 and 0.3 dB for the forward and backward channel respectively. The obtained value is small indicating that the BiDi link, and therefore link capacity doubling, is feasible with very small degradation in the performance of each link direction.

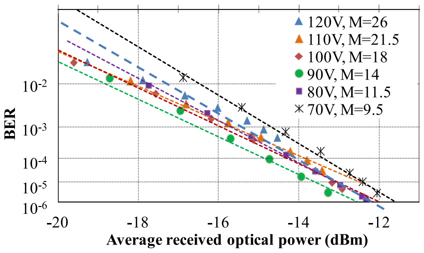

Fig. 8. Experimental BER results for the optical B2B link for different APD gains (M).

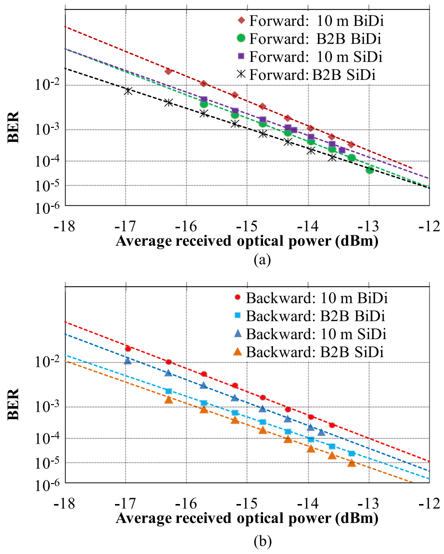

Fig. 9. Experimental BER results for (a) the forward and (b) backward channels in the BiDi link.

IV. CONCLUSION

In this work, we have proposed the use of a BiDi μLED-based single wavelength optical link over SI-POF in conjunction with PAM-32 modulation and APD receivers in order to achieve a record high aggregate SI-POF link capacity. Simulation and experimental studies are presented on a 10 Gb/s BiDi SI-POF link employing 450 nm μLEDs and APDs indicating the feasibility of such links and demonstrating their potential for use in low-cost communication links such as in-home and automotive environments.

The presented simulation studies based on power budget analysis highlight the importance of the use of APD in such links and indicate that a 10 Gb/s BiDi PAM-32 transmission is feasible over 10 m of POF with an 5.3 dB power margin. Longer reaches can be realised by improving the employed optical coupling scheme. A proof-of-principle demonstration is implemented using discrete free-space optical components (lenses, beamsplitters), two 20 μm-diameter μLEDs and two APD receivers. 10 Gb/s BiDi data transmission is achieved over 10 m of SI-POF with a BER $< 10^{-3}$. The receiver sensitivity is found to be –13.8 and –14.4 dBm for the forward and backward link direction respectively, while a small power penalty ($\leq$0.5 dB) is observed in the link due to optical crosstalk. The reported results constitute, to the best to our knowledge, record data rate transmission in LED-based POF links.

REFERENCES

[1] O. Ziemman, J. Krauser, P. E. Zamzow, and W. Daum, *POF Handbook: Optical Short Range Transmission Systems*. New York, NY, USA: Springer-Verlag, 2008

[2] M. Atef, R. Swoboda, and H. Zimmermann, “A gigabit fully integrated plastic optical fiber receiver for a RC-LED source,” in *Proc. IEEE 15th Des. Diagn. Electro. Circuits Syst. Int. Symp.*, Apr. 18–20, 2012, pp. 74–78.

[3] A. M. J. Koonen, H. P. A. Van Den Boom, E. O. Martinez, P. Guignard, and E. Tangdiongga, “Cost optimization of optical in-building networks,” presented at the Eur. Conf. Exhib. Opt. Commun., Geneva, Switzerland, Sep. 18–22, 2011.

[4] A. M. J. Koonen and E. Tangdiongga, “Photonic home area networks,” *J. Lightw. Technol.*, vol. 32, no. 4, pp. 591–604, Feb. 15, 2014.

[5] Y. Dong and K. W. Martin, “Gigabit communications over plastic optical fiber,” *IEEE Solid-State Circuits Mag.*, vol. 3, no. 1, pp. 60–69, Winter 2011.

[6] X. Li, J. L. Wei, N. Bamiedakis, R. V. Penty, and I. H. White, “Avalanche photodiode enhanced PAM-32 5 Gb/s LED-POF link,” presented at the Eur. Conf. Opt. Commun., Cannes, France, Sep. 21–25, 2014.

[7] J. Vinogradov, R. Kruglov, K. L. Chi, J. W. Shi, M. Bloos, S. Loquai, and O. Ziemann, “GaN light-emitting diodes for up to 5.5-Gb/s short-reach data transmission over SI-POF,” *IEEE Photon. Technol. Lett.*, vol. 26, no. 24, pp. 2473–2475, Dec. 15, 2014.

[8] L. Peng, M. Helard, S. Haese, M. Liu, and J. F. Helard, “Hybrid PN-ZP-DMT scheme for spectrum-efficient optical communications and its application to SI-POF,” *J. Lightw. Technol.*, vol. 32, no. 18, pp. 3149–3160, Sep. 15, 2014.

[9] R. Kruglov, J. Vinogradov, S. Loquai, O. Ziemann, C. A. Bunge, T. Hager, and U. Strauss, “21.4 Gb/s discrete multitone transmission over 50-m SI-POF employing 6-channel WDM,” presented at the Opt. Fiber Commun. Conf. Exhib., San Francisco, CA, USA, Mar. 9–13, 2014.

[10] A. Antonino, S. Straullu, S. Abrate, A. Nespola, P. Savio, D. Zeolla, J. R. Molina, R. Gaudino, S. Loquai, and J. Vinogradov, “Real-time gigabit ethernet bidirectional transmission over a single SI-POF up to 75 meters,” presented at the Opt. Fiber Commun. Conf/Nat. Fiber Opt. Eng. Conf., Los Angeles, CA, USA, Mar. 6–10, 2011.

[11] J. J. D. McKendry, D. Massoubre, S. Zhang, B. R. Rae, R. P. Green, E. Gu, R. K. Henderson, A. E. Kelly, and M. D. Dawson, “Visible-light communications using a CMOS-controlled micro-light-emitting-diode array,” *J. Lightw. Technol.*, vol. 30, no. 1, pp. 61–67, Jan. 1, 2012.

[12] X. Li, N. Bamiedakis, J. L. Wei, J. J. D. McKendry, E. Xie, R. Ferreira, E. Gu, M. D. Dawson, R. V. Penty, and I. H. White, “6.25 Gb/s POF link using GaN μLED arrays and optically generated pulse amplitude modulation,” presented at the Conf. Lasers Electro.-Opt., San Jose, CA, USA, May 10–15, 2015.

[13] G. D. Brown, “Bandwidth and rise time calculations for digital multimode fiber-optic data links,” *J. Lightw. Technol.*, vol. 10, no. 5, pp. 672–678, May 1992.

[14] L. Geng, J. L. Wei, R. V. Penty, I. H. White, and D. G. Cunningham, “3 Gbit/s LED-based step index plastic optical fiber link using multilevel pulse amplitude modulation,” presented at the Opt. Fiber Commun. Conf. Expo./Nat. Fiber Opt. Eng. Conf., Anaheim, CA, USA, Mar. 17–21, 2013.

[15] A. Kern, A. Al-Samaneh, D. Wahl, and R. Michalzik, “Monolithic VCSEL—PIN photodiode integration for bi-directional optical data transmission,” *IEEE J. Sel. Topics Quantum Electron.*, vol. 19, no. 4, pp. 1–13, Jul./Aug. 2013.

Authors’ biographies not available at the time of publication.

Heterogeneous integration of gallium nitride light-emitting diodes on diamond and silica by transfer printing

A. J. Trindade,[1,*] B. Guilhabert,[1] E. Y. Xie,[1] R. Ferreira,[1] J. J. D. McKendry,[1] D. Zhu,[2,3] N. Laurand,[1] E. Gu,[1] D. J. Wallis,[2,3] I. M. Watson,[1] C. J. Humphreys,[2] and M. D. Dawson[1]

[1] *Institute of Photonics, SUPA, University of Strathclyde, 106 Rottenrow, Glasgow G4 0NW, UK*
[2] *Department of Materials Science and Metallurgy, University of Cambridge, 27 Charles Babbage Road, Cambridge CB3 0FS, UK*
[3] *Plessey Semiconductors Ltd, Tamerton Road, Roborough, Plymouth, Devon, PL6 7BQ, UK*
[*] *antonio.trindade@strath.ac.uk*

Abstract: We report the transfer printing of blue-emitting micron-scale light-emitting diodes (micro-LEDs) onto fused silica and diamond substrates without the use of intermediary adhesion layers. A consistent Van der Waals bond was achieved via liquid capillary action, despite curvature of the LED membranes following release from their native silicon growth substrates. The excellence of diamond as a heat-spreader allowed the printed membrane LEDs to achieve optical power output density of 10 W/cm^2 when operated at a current density of 254 A/cm^2. This high-current-density operation enabled optical data transmission from the LEDs at 400 Mbit/s.

OCIS codes: (250.0250) Optoelectronics; (120.6810) Thermal effects; (060.4510) Optical communications.

References and links

1. H. S. Kim, E. Brueckner, J. Song, Y. Li, S. Kim, C. Lu, J. Sulkin, K. Choquette, Y. Huang, R. G. Nuzzo, and J. A. Rogers, "Unusual strategies for using indium gallium nitride grown on silicon (111) for solid-state lighting," Proc. Natl. Acad. Sci. U.S.A. **108**(25), 10072–10077 (2011).
2. T. Kim, S. Hyun Lee, Y. Li, Y. Shi, G. Shin, S. Dan Lee, Y. Huang, J. A. Rogers, and J. Su Yu, "Temperature- and size-dependent characteristics in ultrathin inorganic light-emitting diodes assembled by transfer printing," Appl. Phys. Lett. **104**(5), 051901 (2014).
3. J. Senawiratne, A. Chatterjee, T. Detchprohm, W. Zhao, Y. Li, M. Zhu, Y. Xia, X. Li, J. Plawsky, and C. Wetzel, "Junction temperature, spectral shift, and efficiency in GaInN-based blue and green light emitting diodes," Thin Solid Films **518**(6), 1732–1736 (2010).
4. Z. G. Ju, S. T. Tan, Z.-H. Zhang, Y. Ji, Z. Kyaw, Y. Dikme, X. W. Sun, and H. V. Demir, "On the origin of the redshift in the emission wavelength of InGaN/GaN blue light emitting diodes grown with a higher temperature interlayer," Appl. Phys. Lett. **100**(12), 123503 (2012).
5. Z. Gong, S. Jin, Y. Chen, J. McKendry, D. Massoubre, I. M. Watson, E. Gu, and M. D. Dawson, "Size-dependent light output, spectral shift, and self-heating of 400 nm InGaN light-emitting diodes," J. Appl. Phys. **107**(1), 013103 (2010).
6. S. Kim, J. Wu, A. Carlson, S. H. Jin, A. Kovalsky, P. Glass, Z. Liu, N. Ahmed, S. L. Elgan, W. Chen, P. M. Ferreira, M. Sitti, Y. Huang, and J. A. Rogers, "Microstructured elastomeric surfaces with reversible adhesion and examples of their use in deterministic assembly by transfer printing," Proc. Natl. Acad. Sci. U.S.A. **107**(40), 17095–17100 (2010).
7. E. James, Mark, Polymer Data Handbook, (Oxford University, 1999), pp. 424.
8. Z. L. Liau, "Semiconductor wafer bonding via liquid capillarity," Appl. Phys. Lett. **77**(5), 651 (2000).
9. D. Zhu, C. McAleese, K. K. McLaughlin, M. Häberlen, C. O. Salcianu, E. J. Thrush, M. J. Kappers, W. A. Phillips, P. Lane, D. J. Wallis, T. Martin, M. Astles, S. Thomas, A. Pakes, M. Heuken, and C. J. Humphreys, "GaN-based LEDs grown on 6-inch diameter Si (111) substrates by MOVPE," Proc. SPIE **7231**, 723118 (2009).
10. D. Zhu, C. McAleese, M. Haberlen, C. Salcianu, T. Thrush, M. Kappers, A. Phillips, P. Lane, M. Kane, D. Wallis, T. Martin, M. Astles, N. Hylton, P. Dawson, and C. Humphreys, "Efficiency measurement of GaN-based

#235263 - $15.00 USD Received 26 Feb 2015; revised 30 Mar 2015; accepted 30 Mar 2015; published 2 Apr 2015
(C) 2015 OSA 6 Apr 2015 | Vol. 23, No. 7 | DOI:10.1364/OE.23.009329 | OPTICS EXPRESS 9329

quantum well and light-emitting diode structures grown on silicon substrates," J. Appl. Phys. **109**(1), 014502 (2011).
11. H. R. Shanks, P. D. Maycock, P. H. Sidles, and G. C. Danielson, "Thermal conductivity of Silicon from 300 to 1400°K," Phys. Rev. **130**(5), 1743–1748 (1963).
12. A. J. Trindade, B. Guilhabert, D. Massoubre, D. Zhu, N. Laurand, E. Gu, I. M. Watson, C. J. Humphreys, and M. D. Dawson, "Nanoscale-accuracy transfer printing of ultra-thin AlInGaN light-emitting diodes onto mechanically flexible substrates," Appl. Phys. Lett. **103**(25), 253302 (2013).
13. Y. Li, Y. Shi, J. Song, C. Lu, T. Kim, J. A. Rogers, and Y. Huang, "Thermal properties of microscale inorganic light-emitting diodes in a pulsed operation," J. Appl. Phys. **113**(14), 144505 (2013).
14. R. P. Mildren and J. R. Rabeau, Optical Engineering of Diamond, (Wiley-VCH, 2013), Ch. 2 and 11.
15. C. Kittel, "Interpretation of the thermal conductivity of glasses," Phys. Rev. **75**(6), 972–974 (1949).
16. J. J. D. McKendry, D. Massoubre, S. Zhang, B. R. Rae, R. P. Green, E. Gu, R. K. Henderson, A. E. Kelly, and M. D. Dawson, "Visible-light communications using a CMOS-controlled micro-light-emitting-diode array," J. Lightwave Technol. **30**(1), 61–67 (2012).
17. P. Tian, J. J. D. McKendry, Z. Gong, S. Zhang, S. Watson, D. Zhu, I. M. Watson, E. Gu, A. E. Kelly, C. J. Humphreys, and M. D. Dawson, "Characteristics and applications of micro-pixelated GaN-based light emitting diodes on Si substrates," J. Appl. Phys. **115**(3), 033112 (2014).
18. X. A. Cao, S. F. LeBoeuf, and T. E. Stecher, "Temperature-dependent electroluminescence of AlGaN-based UV LEDs," IEEE Electron Device Lett. **27**(5), 329–331 (2006).
19. MicroChem SU-8 Photoresists datasheet", http://www.microchem.com

1. Introduction

Transfer printing (TP) is a rapidly emerging technique for heterogeneous integration in electronics and optoelectronics [1–5]. In TP, soft elastomeric stamps are typically used to 'pick and place' device structures from their native growth substrate to a dissimilar receiving substrate, allowing the creation of novel hybrid device technologies. An important example of the application of this approach is in printing inorganic light-emitting diodes (LEDs), where pre-fabricated LED membrane devices can for example be transferred onto receiving substrates such as those based on polymers, enabling new forms of flexible displays [6]. As the technique matures and is optimized, thin membranes of suspended LED materials can be achieved in various ways, most commonly by directional wet etching of the growth substrate, here termed under-etching [1], or by laser lift-off [2]. However, a general issue for devices based on epitaxial multilayers is that removal of the substrate eliminates a natural heat-sink retained in conventional fabrication. This issue is severe for the important case of gallium nitride (GaN) based LEDs, in which, despite continuing efficiency improvements, most electrical input energy is dissipated as heat. Even for conventional devices in thermal contact with the growth substrate, operation under direct-current (dc) bias results in undesired thermal effects on the electroluminescence (EL), namely red spectral shifts and reduced optical output power (T-droop effect), while irreversible degradation of devices may also occur [3,4]. Reduction of the die size provides systematic improvement in heat dissipation, but does not eliminate these problems [5]. Heat dissipation from transfer-printed GaN-LEDs becomes a more pronounced issue when flexible polymeric materials are used as the receiver substrate, because these have lower thermal conductivities than inorganic materials used as the native growth substrate. Thermal effects in such a situation have been studied previously [2]. Regardless of the choice of receiver substrate in TP, the process flows normally feature adhesion-enhancement layers on the receiving substrates to aid the release of the LEDs from the transporting stamps [6]. Conventionally, these layers are organic materials, with poor thermal conductivities, κ (e.g. for polydimethylsiloxane (PDMS), κ ~0.15 W/m.K [7]). Therefore adhesion-enhancement layers impede heat dissipation from operating devices even if the underlying substrate has a relatively high thermal conductivity.

The attractive alternative to the use of a conventional adhesion-enhancement layer, which we report in this paper, is to use a transient layer of a volatile liquid [8]. The liquid film aids release of devices from the transporting stamps, as in a conventional process. Subsequently, capillary forces during evaporation of the liquid enable formation of a robust Van der Waals bond between the transferred devices and receiving substrate, with no permanent intermediate layer to add thermal resistance, or changes in refractive index, at the interfaces. This study utilized high-performance GaN LED epistructures on Si (111) substrates [9,10]. While Si can act as a reasonably effective heat-sinking material in conventional devices (κ ~149 W/m.K [11]), this material is removed during the under-etching fabrication step, using potassium hydroxide (KOH) solution, needed in the TP process flow [12]. We compared two receiver substrates with thermal conductivities much higher and much lower than that of the GaN-based LED die (κ ~160 W/m.K for GaN [13]), namely diamond (κ ~2200 W/m.K [14]) and optical-grade silica glass (κ ~1.42 W/m.K [15]). The benefits of diamond as a heat spreader were investigated by comparing the dc characteristics of LEDs on these two receiver substrates. This part of our study included the use of thermal imaging to infer device operating temperatures, and to observe the transient heating effects under increasing dc drive currents. The ability of LEDs to operate at high dc current densities is also relevant to the emerging application of visible light communications (VLC) with LED sources [16]. In a typical situation where the data signal is superposed on a dc component, the modulation bandwidth of an LED increases with dc current up to a critical point [16,17]. As it is clearly of interest to see how transfer printed devices perform for VLC applications, we undertook comparison of the modulation bandwidths and data transmission characteristics of devices on diamond and silica.

2. Experimental results

We report the TP in array formats of 100x100 μm^2 LEDs (micro-LEDs) emitting around 465 nm onto single-crystal diamond platelets [14] (200 µm thick) and fused silica substrates (500 µm thick). We concentrate on LEDs of such small dimensions here by reason of applications described later in the paper, but note that scaling to larger areas [2] should in principle be possible if strain compensation issues specific to GaN/Si are addressed. The GaN micro-LED structures and process flow, together with the mechanical transfer system and PDMS stamps, are as described previously [12]. Here, however, capillary bonding was achieved by introducing an intermediate step to the TP process, in which the backside of the devices being transferred is wetted with a suitable liquid as shown in Fig. 1.

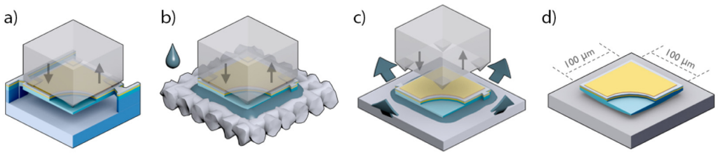

Fig. 1. Schematic of transfer printing using capillary bonding. The left-hand figure represents the pick-up of a suspended device using an elastomeric stamp (a). Upon pick-up, LEDs are compressed against an acetone-wetted cloth (b) and released when the backside contacts receiving substrate (c). The excess of liquid aids the positioning and release of the LED from the transporting stamp. After thermal curing, the LED is bonded to the new substrate (d).

After pick-up from the donor wafer as per Fig. 1(a), the backside is wetted on an acetone-impregnated standard cleanroom wipe as shown in Fig. 1(b). Quick retraction of the stamp removes the LED die from the wipe with its backside still wet, and it is then deposited onto the receiver substrate, shown in Fig. 1(c). The transparency of the stamps allows the TP process to be followed visually, and Fig. 2(a) confirms overflow of excess liquid to the sides of the LED die when it is compressed against the receiving substrate. Slow retraction of the stamp causes the liquid to partially reflow back underneath the die, and provide initial adhesion between the die and the receiving substrate, through liquid capillarity. This stage is shown in Fig. 2 (b). Subsequent evaporation of liquid proceeds from the outside of the die, and during this step the forces at the retreating meniscus bring the two surfaces into intimate contact [8]. While no specific tests have been performed at this time to assess the placement accuracy in detail, the LEDs are printed using the same mechanical system we have previously shown to be capable of sub-micrometer placement [12], and we note that the printed dies hold their positioning during slow stamp retraction and later after the solvent has been evaporated.

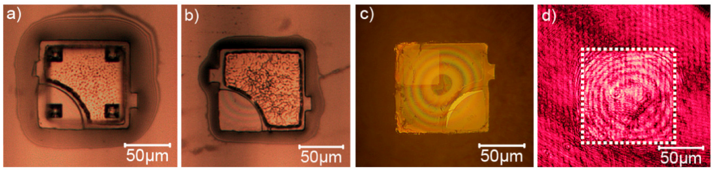

Fig. 2. Images illustrating the process of capillary bonding of individual LEDs onto rigid substrates. Parts (a) and (b) are optical microscope views through the transparent stamp at successive stages: (a) after wetting of the LED backside, contact is made with the receiving substrate; (b) stamp retraction allows the liquid to reflow underneath the LED. Parts (c) and (d) are views through the substrate showing interference effects from an air gap left round after liquid evaporation and bonding in the central region: (c) colored fringes visible under white light; (d) fringes observed under laser light.

After moderate heating to 50°C to evaporate any remaining liquid, the devices are left bonded by Van der Waals forces over the contact area with the receiving substrate. Both combinations of surfaces brought into contact (i.e. diamond or silica substrates, and the micro-LED backside) display similar root-mean-square roughness values of ~1 nm as measured by atomic force microscopy (AFM). We have previously attributed the smoothness of the micro-LED bonding surface to a protective SiN_x layer formed between the Si substrate and the AlN growth initiation layer [17]. This layer can largely protect the underside of the III-nitride die from attack by the KOH etch solution used to remove the Si substrate. Such low roughness results in two tightly-bonded surfaces robust to mechanical disturbance, and surviving multiple wet-processing steps necessary to complete the device fabrication. However, imaging of the devices through the back of the receiving substrate reveals a pattern of interference rings associated with an air gap as shown in Fig. 2(c) and 2(d). This observation correlates with curvature of the LED dies, which limits contact to the central region of the LED. Such curvature is reasonable to expect after removal of the Si substrate beneath the LED epistuctures. The epistructures are engineered such that the total epi-layer/Si substrate system is approximately strain balanced. This requires compressive strain to be introduced into the AlGaN buffer layers using lattice mismatch to counteract the tensile strain introduced by the thermal expansion difference between the nitride layers and the Si substrate on cooling from the growth temperature. After removal of the Si substrate this residual compressive strain in the AlGaN buffer layers then induces the concave curvature seen, as it acts against the topmost GaN layers in the LED stack.

The method to investigate the observed curvature of the LED dies after deposition used the imaged interference rings under monochromatic and coherent (653nm-emitting laser diode) light, exemplified in Fig. 2(d), and standard analysis of optical interference. The height of the die-substrate air gap was spatially reconstructed, allowing visualization of the backplane curvature over a full die as illustrated in Fig. 3(a). Essential information regarding the die positioning and tilting can be obtained from such measurements. The effective contact area, corresponding to the colorless mesh in Fig. 3(a), in the central region of a sample LED was found to be 14 ± 2% of the total die area and a radius of curvature averaging 2 mm per die (assuming a spherical curvature).

#235263 - $15.00 USD Received 26 Feb 2015; revised 30 Mar 2015; accepted 30 Mar 2015; published 2 Apr 2015

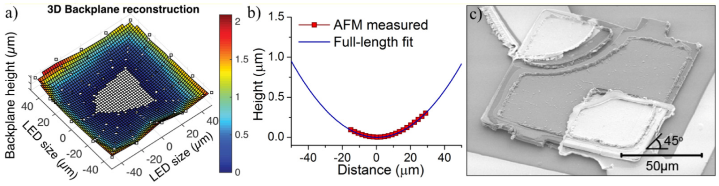

Fig. 3. Backplane curvature measurements. In (a), the calculated height of the air gap between a bonded LED and the substrate is represented as a mesh reconstructed by the photographed interference pattern. The colorless central area indicates where contact is assumed to occur. In part (b), an AFM line scan over the central area of an unbonded LED die is shown and extrapolated with a parabolic fit. Part (c) shows an SEM image of a micro-LED transfer printed onto a rigid substrate (at 45° tilt), and connected to Ti/Au metal tracks.

To further analyze the backplane curvature, an AFM profile scan was performed (45µm in length) on a flipped-over die where the central area was measured and fitted over the entire lateral size of the die as shown in Fig. 3(b). By zeroing the measurement to the minimum height as the center of the backplane curvature, the AFM height scan matches the interference rings height reconstruction for the area surrounding the center of the die (with ± 2 µm lateral fluctuations). However - towards the edges of the reconstructed backplane - higher curvature zones can be seen as per Fig. 3(a), indicating that the radius of curvature is not constant. SEM imaging provided a qualitative assessment of the height at the extremities of ~2.5 µm closely matching the values attained by the interference-based measurements.

To act as an electrical insulation layer and encapsulation for the devices on diamond and silica receiver substrates, an SU-8 epoxy photoresist layer of 10 µm post-cure thickness was deposited and patterned. Metal tracks, comprising 200 nm of Au above 50 nm of Ti, were deposited next, contacting the LED through localized apertures in the SU-8. The media surrounding LED dies in such a situation are shown in the right-hand part of Fig. 4(a).

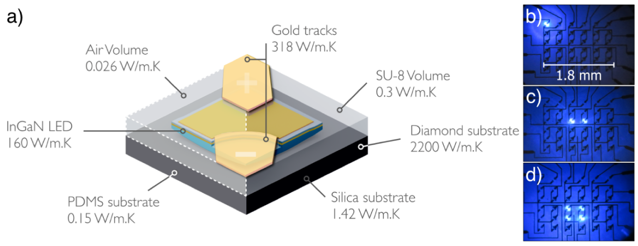

Fig. 4. Thermal conductivities of media surrounding the respective transfer-printed LEDs (a): The left half-section of the device illustrates the air-exposed baseline devices deposited on PDMS adhesion enhancement layers. The right half-section represents the case of the better performing substrates (diamond and silica) with improved heat dissipation and volumetric SU-8 (κ ~0.3 W/m.K [19]) encapsulation on top. Full device arrays can be seen in the microscope images in parts (b), (c) and (d) with configurations of 1, 2 and 4 active LEDs respectively.

As well as introducing the capillary-assisted TP of LEDs onto diamond and silica, we also fabricated for reference identical device structures onto PDMS/polyethylene terephthalate (PET) flexible substrates as previously demonstrated [17]. The media surrounding dies in this case are shown in the left-hand part of Fig. 4(a). 6x6 device arrays were assembled onto each substrate with alternative LED driving configurations as pictured in Fig. 4(b)-(d).

#235263 - $15.00 USD Received 26 Feb 2015; revised 30 Mar 2015; accepted 30 Mar 2015; published 2 Apr 2015

Figure 5 shows the operating voltage (*V*) and the optical output power density (*L*) of three representative LEDs as a function of the current density (*J*). *L-J* curves were acquired with the devices in direct contact with a calibrated Si photodiode detector, capturing only the light going through the supporting substrate. Characteristics of a reference micro-LED bonded to a PET polymer substrate with a 20-µm PDMS intermediate adhesion layer are included for comparison with those of the devices on diamond and bulk silica substrates. The devices on the PDMS/PET substrates were in direct thermal contact with air on one side, while those bonded to the inorganic receiver substrates were encapsulated with SU-8 epoxy as described above. The reference devices operated at a maximum drive current density of 30 A/cm^2, producing an optical output power density of 55 mW/cm^2 before permanent damage was observed. This limited performance is attributable to a poor environment for heat dissipation. The media on opposite sides of the LED dies, air and PDMS, both have lower thermal conductivities than their counterparts in the encapsulated devices bonded to inorganic substrates. LEDs on all three substrates display similar turn-on voltages (~4.5 V), indicating good ohmic contacts, and effective performance from the thin metal current-spreading layer over the p-GaN. A maximum current density of 255 A/cm^2 was measured without significant thermal roll-over on diamond substrates, representing a major improvement when compared to similar devices on soft intermediate layers (~30 A/cm^2) [2,12] .

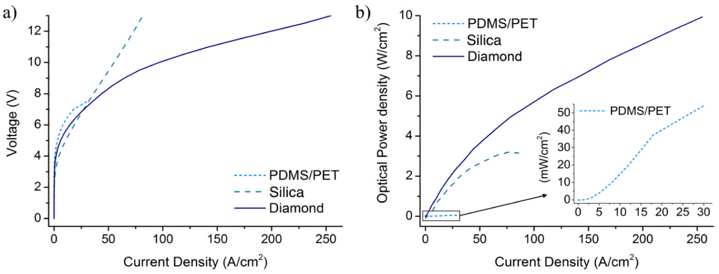

Fig. 5. Characteristics of an individual LED in operation on different substrates. In (a), *J-V* curves for individual LEDs on PDMS/PET, silica and diamond substrates, respectively. In (b) the corresponding *L-J* with the inset showing a magnification of the device emission on the PDMS/PET substrates used as a baseline comparison achieving a maximum optical power density of 55 mW/cm^2.

The maximum values for optical power density in Fig. 5 for devices on inorganic receiver substrates were 10 W/cm^2 at 255 A/cm^2 ($I = 20$ mA) and 3.2 W/cm^2 at 77 A/cm^2 ($I = 6$ mA) for devices on diamond and silica respectively. LEDs on silica gave a maximum optical power inferior to their counterparts on diamond, and started to reach saturation from thermal rollover after 78 A/cm^2. However, repeated drives up to 80 A/cm^2 showed no damage to the LEDs, in contrast to the irreversible damage suffered by devices on PDMS/PET above 30 A/cm^2. LEDs on diamond consistently outperformed those on the other substrates, due to its orders of magnitude higher thermal conductivity. The maximum optical power density *per* LED (10 W/cm^2) was nearly three times higher than that obtained from devices on silica. This represents a significant advance, outperforming previously reported transfer-printed devices with an equal die size by a factor of 10 [2].

To better understand how the two very different thermal conductivities of diamond and silica affected the device performance, the temperature distribution across LED arrays was measured with a calibrated thermal infrared camera, viewing through the substrate [Fig. 6(a)] and focusing on the plane of the LEDs. The camera acquisitions accounted for the emissivity of the GaN in the wavelength range of 1.5 to 5µm and the false-color representation of temperature is referenced to the emissivity of GaN. The images show semi-quantitatively the much greater effectiveness of heat spreading in the array on diamond. At the highest current density no hot spots are evident, in contrast to the hot spot around the powered LED on glass, and there is a comparable temperature rise across the full diameter (3 mm) of the diamond substrate.

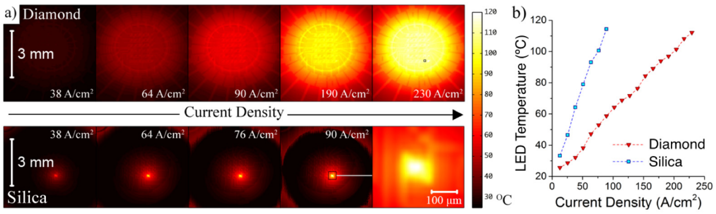

Fig. 6. (a) Thermal imaging of LED arrays with a single device powered on diamond (top) and silica (bottom). The emitting LED is identified in the last diamond frame as a black dot. The last frame of the silica-substrate row shows a magnified view of the die and its metal interconnection tracks. The captured images show the measured temperature corrected for the LED material (GaN); the rest of the image should be interpreted as a relative comparison. Part (b) shows the dependence of LED temperature on the injected current density (see Media 1).

Figure 6(a) also suggests the apparently enhanced temperature rise along the metal interconnection tracks. This is considered to be mainly an artifact arising from the metal emissivity and the calibration procedure, although a significant role for aluminum interconnection tracks in lateral heat transport in similar LED arrays has been proposed and simulated previously [1]. Figure 6(b) shows estimates of the temperature of the powered LED die as a function of drive current density for the two substrates, and shows an approximate linear dependence in each case. Devices are estimated to reach a maximum operating temperature of ~115°C. This is reached by devices on silica at an injection current density of 90 A/cm^2. LEDs on diamond attain a similar temperature only at 230 A/cm^2, a current density 2.5x higher. Representative heat-propagation visualization is available (see Media 1) showing real-time heat propagation with 1mA current increments on both substrates.

The very different heat-spreading properties of diamond and silica are expected to affect the spectral shifts shown by LEDs operating at different dc drive currents. Therefore electroluminescence spectra were recorded with a fiber-coupled spectrometer. Figure 7 shows how the peak EL wavelength shifted, and the inset illustrates typical spectra at relatively low current density. The peak EL emission of the transfer-printed devices shifted over a full range of 464 to 455 nm ($\Delta\lambda$ = 9 nm) and of 463 to 459 nm ($\Delta\lambda$ = 4 nm) on diamond and silica, respectively. The corresponding injected current densities ranged from 12 to 100 A/cm^2 for silica, and to a maximum of 256 A/cm^2 for diamond. In the case of LEDs on silica, the peak wavelength blue-shifts initially, with a reversal to a red shift above 50 A/cm^2 as similar to other reports of InGaN/GaN based LEDs [8]. The blue shift in polar (0001)-oriented device structures, as used here, are usually attributed to carrier screening by piezoelectric fields in the quantum well (QW) active region. Localized heating meanwhile causes strong competitive red shift effects - including bandgap shrinkage - which become dominant at higher injected current densities [8] and due to the devices own self-heating effects [10].

#235263 - $15.00 USD Received 26 Feb 2015; revised 30 Mar 2015; accepted 30 Mar 2015; published 2 Apr 2015

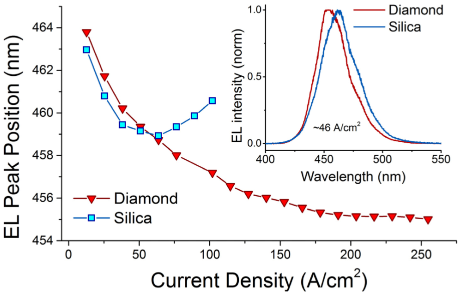

Fig. 7. EL peak shift of a representative single LEDs as a function of increasing injected current on diamond (red triangles) and silica (blue squares). The inset shows representative EL spectra at 46 A/cm2 for both substrates.

In the case of LEDs on diamond, a continuous blue shift is the net observable trend. Because these devices reached similar temperatures to those on silica at the highest current densities, the bandgap shrinkage contribution will be similar. It is likely that strain effects in the QWs, associated with thermal expansion mismatches between the III-nitride dies and underlying substrate, play a role in the markedly different spectral shift behavior [9]. The transition observed from initial blue shifts to red shifts parallels several previously published reports, which discuss contributing mechanisms in more depth, and their investigation with a wide range of techniques [2–4,18].

The combination of LED die sizes 10-100 times smaller in area than those of typical commercial GaN-based devices, and the ability to sustain high dc current densities through effective heat dissipation on diamond, motivated further fast-modulation measurements relevant to visible light communications (VLC) applications. A key parameter for VLC is the electrical-to-optical (E-O) modulation bandwidth (BW), which is conventionally measured using a −3 dB criterion. A small LED size naturally enhances BW by minimization of capacitive contributions, but a decrease in the differential carrier lifetime in GaN-based QWs as carrier density rises also gives a significant increase in BW with current density [16]. BW measurements on transfer-printed devices were acquired in a similar fashion to that reported elsewhere, applying a modulation signal on a constant dc bias [16]. Figure 8 shows the expected initial increase of BW with current density for devices on both diamond and silica.

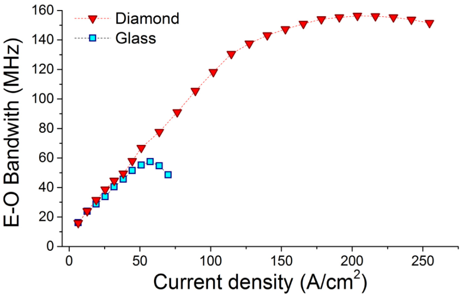

Fig. 8. E-O bandwidths as a function of dc drive current density of representative LEDs deposited onto diamond and silica.

Devices on both silica and diamond displayed similar performance for current densities under 50 A/cm^2. Above this point roll-over became evident for devices on silica, which are thus limited to a maximum BW of ~55 MHz. The BW of devices on diamond continued to increase at much higher current densities, and to plateau at 200 A/cm^2, corresponding to a maximum BW of 154 MHz. These maximum observed BW values, which establish a performance benchmark for transfer printed devices for optical communications, that could be further improved by fabricating smaller LEDs for use in the TP process. Interesting comparisons can also be made between the results in Fig. 8, and previous BW measurements on micro-LEDs fabricated from similar epitaxial material, but tested on the Si growth substrate [17]. These were circular in shape, and of 45 µm diameter. The previous non-transferred devices attained BWs of 190 MHz at relatively low current densities around 6 A/cm^2. However, they displayed an unusual temporary saturation of bandwidth increase in this current density range, before moderate further BW increases at higher current densities attributed to heating effects, and associated lowering of series resistance [17]. The smoother initial BW increase with current density shown by the transfer-printed devices resembles typical results from conventional GaN-on-sapphire devices [16]. These observations suggest that alteration of the strain state of QWs by removal of the Si substrate may influence the recombination dynamics of carriers significantly.

To further demonstrate the potential of the transfer-printed devices for VLC, tests were made of the optical transmission of data in a back-to-back configuration. The resulting eye diagrams are shown in Fig. 9. A simple on-off keying modulation scheme was used with a dc bias for the device on diamond of 10.5 V, and of 5.7 V for the device on the silica. A peak-to-peak modulation of 2 V was used in both configurations, and pseudo-random sequences of 2^7-1 bits were employed, as in previous work [16].

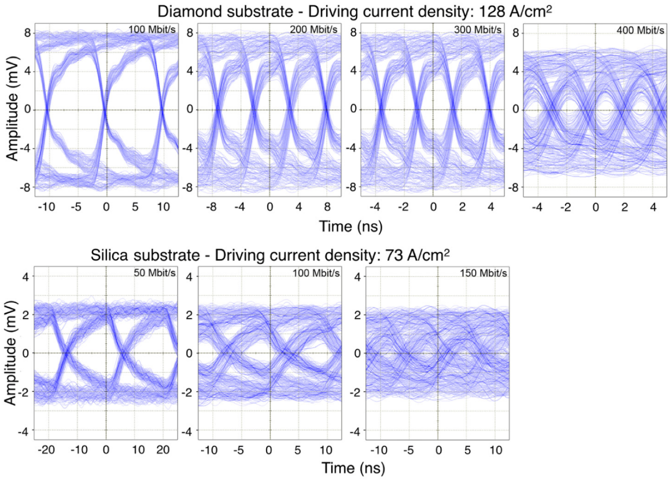

Fig. 9. Data-transmission measurements from representative LEDs deposited onto diamond (top row) and silica (lower row). The eye diagrams were acquired with the same dc applied current throughout.

Devices on diamond displayed open eye diagrams at data-rates up to 400 Mbit/s, correlating with error-free data transmission. In contrast, devices on silica showed eye closure above 100 Mbit/s, which was virtually complete at 150 Mbit/s. The superior performance of the devices on diamond is again ultimately attributable to this material's effectiveness as a heat spreader, allowing operation of the LEDs at higher dc current densities.

3. Summary

Micro-transfer printing combined with liquid capillary bonding is demonstrated as a technique to directly integrate active device membranes to novel rigid substrates without adhesive interlayers. The technique retains the scalability and potentially nanometer positioning accuracy we have demonstrated previously [12], but brings additional benefits in direct contact to functional substrates including those possessing high thermal conductivity. As an important example of the use of this technique, the electrical and optical characteristics of 100 x 100 μm^2 blue-emitting GaN LEDs transfer printed in array format onto diamond and silica receiver substrates are compared, and demonstrate the major benefits of diamond as a heat-spreading material. Devices on diamond were driven at dc current densities up to 254 A/cm^2 without reaching thermal roll-over, or suffering permanent damage. A maximum optical output power density of 10 W/cm^2 was recorded from devices on diamond substrate, which is more than three times the optical power density of counterpart devices on silica (3.2 W/cm^2). The response of the devices to fast modulation, involving superposition of a data signal on a dc offset, was also studied, motivated by applications in optical data transmission. The effective heat dissipation offered by diamond allowed devices to attain maximum electrical-to-optical modulation bandwidths of 154 MHz at dc current densities of ~200 A/cm^2. The same devices achieved a highly competitive back-to-back data transmission rate of 400 Mbit/s at a dc current density of 128 A/cm^2.

The LED structures used in this study were optimized for conventional large-area LED fabrication, where the wafer-scale properties are most important. In future studies we will investigate how the strain profile in the layer stack can be modified to reduce the curvature of the micro-LEDs and improve the contact area, which should bring further benefits to the optoelectronic performance of the devices. We note finally that our technique of LED transfer printing onto diamond has the potential to take advantage of commercial-scale polycrystalline diamond substrates or the cost-economies to be expected from scaled up single-crystal CVD growth of diamond.

Acknowledgments

The authors thank Dr. P.R. Edwards, University of Strathclyde Department of Physics, for his assistance in the SEM imaging acquisition, and Dr. Anthony Kelly and Scott Watson, University of Glasgow, for support in the data transmission and bandwidth measurements. This work was supported by EPSRC grants EP/K00042X/1, EP/I029141/1, EP/F05999X/1, and EP/I012591/1.

APPLIED PHYSICS LETTERS **105**, 171107 (2014)

Temperature-dependent efficiency droop of blue InGaN micro-light emitting diodes

Pengfei Tian,[1] Jonathan J. D. McKendry,[1] Johannes Herrnsdorf,[1] Scott Watson,[2]
Ricardo Ferreira,[1] Ian M. Watson,[1] Erdan Gu,[1,a)] Anthony E. Kelly,[2] and Martin D. Dawson[1]
[1]*Institute of Photonics, University of Strathclyde, 106 Rottenrow, Glasgow G4 0NW, United Kingdom*
[2]*School of Engineering, University of Glasgow, James Watt South Building, Glasgow G12 8LT, United Kingdom*

(Received 30 June 2014; accepted 21 October 2014; published online 29 October 2014)

Temperature-dependent trends in radiative and Auger recombination coefficients have been determined at different injection carrier concentrations using InGaN micro-light emitting diodes 40 μm in diameter. The differential lifetime was obtained first from the measured modulation bandwidth and was then employed to calculate the carrier concentration in the quantum well active region. When the temperature increases, the carrier concentration increases, but both the radiative and Auger recombination coefficients decrease. In addition, the temperature dependence of radiative and Auger recombination coefficients is weaker at a higher injection carrier concentration, which is strongly related to phase space filling. © *2014 AIP Publishing LLC*.
[http://dx.doi.org/10.1063/1.4900865]

Significant progress has been achieved in the application and physical understanding of GaN-based light emitting diodes (LEDs). However, their external quantum efficiency (EQE) shows a non-thermal reduction at high injection current density, known as efficiency droop, which appears to be a barrier for the wide application of LEDs in general lighting.[1,2] This phenomenon is generally studied under pulsed current conditions, which allows analysis of the effects of current density, independent of the heating. However, in many LED applications, such as automotive headlights, the ambient temperature is much higher than normal room temperature, and therefore, the study of temperature-dependent LED efficiency droop is necessary.

Recently, the issue of temperature-dependent reductions in EQE, known as thermal droop, has received more attention.[3] For example, a major reduction in EQE by about 30% has been observed from 300 K to 450 K.[3] Several groups have reported that at a fixed high current density of hundreds of A/cm^2, EQEs first increase and then decrease with increasing temperature, the detailed variation depending largely on the LED design.[4–7] Different mechanisms have been proposed to explain the temperature-dependent efficiency droop, which is interdependent with current-dependent efficiency droop. The proposed current-dependent efficiency droop mechanisms include Auger recombination, electron leakage, and carrier delocalization.[1,2] Recent significant experimental contributions include claims of direct observations of Auger electron emission under current injection[8,9] or photoluminescence.[10] Within the framework of an *ABC* recombination model, the temperature dependence of carrier recombination coefficients has often been investigated experimentally by fitting the temperature-dependent internal quantum efficiency (IQE) curves without considering electron leakage.[11,12] With the increase in temperature, the defect-related Shockley-Read-Hall (SRH) recombination coefficient *A* increases and the radiative recombination coefficient *B* decreases. However, inconsistent temperature-dependent trends in the third-order coefficient *C* (assumed hereon for concreteness to correspond to Auger recombination) have been reported, including a monotonous increase with increasing temperature[11] and little variation at temperatures higher than 200 K.[12] In these studies, current-independent *B* and *C* coefficients have been assumed, and their variations with injection current density/carrier concentration due to phase space filling effects have not been considered. Similar controversy also exists in the theoretical work based on direct/indirect Auger recombination calculations.[13–16] Theoretical work has indicated that the temperature dependence of *B* and *C* coefficients varies at different carrier concentration in quantum wells (QWs) with different carrier confinement conditions;[13] however, experimental verification of such predictions has not yet been achieved.

In this study, we experimentally determine temperature-dependent trends in carrier recombination coefficients, in particular the Auger coefficient, as a function of carrier concentration, through measurements of the experimental modulation bandwidth and EQE of blue-emitting InGaN micro-LEDs. Due to their excellent current spreading and heat dissipation ability, micro-LEDs can be operated at current densities up to several kA/cm^2 with little self-heating, as emphasized in previous publications.[17,18] At such high injection current densities, the phase space filling effect is significant and its effect on the temperature-dependent *B* and *C* coefficients has been demonstrated here. In addition, the excellent current spreading of micro-LEDs helps to alleviate the effect of current crowding on carrier recombination at different current densities and temperatures. Furthermore, we use temperature-dependent modulation bandwidth for carrier recombination analysis. These bandwidth measurements follow methodologies developed in recent studies on the emerging application of visible light communications (VLC).[19,20] While VLC using GaN-based LEDs operating at different temperatures has been demonstrated,[21] the temperature-dependent mechanisms affecting performance

---

[a)] Electronic mail: erdan.gu@strath.ac.uk.

in this application require further investigation to complement understanding of efficiency droop effects, commonly considered in a direct current (DC) drive context.

Individually addressable top-emission (through the *p*-contact) micro-LEDs on *c*-plane sapphire substrates with a diameter of 40 μm and emission wavelength ~445 nm were fabricated from a commercial wafer. The epistructure consists of an *n*-GaN layer, an InGaN/GaN multiple quantum well (MQW) active region, an AlGaN current blocking layer, and a *p*-GaN layer. The micro-LED fabrication processes are similar to those in Ref. 22.

A previous study on micro-LEDs of comparable design shows that the junction temperature of a 40 μm micro-LED differs insignificantly from the ambient temperature even under high injection DC, due to highly effective current spreading and heat dissipation.[17,18] To confirm this observation, the light output power of the micro-LED was compared under pulsed current with low duty cycle (pulse width: 25 μs; pulse period: 525 μs) and DC. No difference of light output power was found up to a current of 35 mA (~2800 A/cm^2). Also, for a 40 μm micro-LED from Ref. 17, the junction temperature shows little change until current density ~2800 A/cm^2. Thus, the self heating can be neglected here at DC 35 mA or less for the measurements of light output power and bandwidth in this work.[17,18] In addition, potential effects of the temperature on current spreading as reported by Kudryk *et al.*[23] are neglected due to the more uniform current spreading in micro-LEDs compared to broad-area LEDs.

The ambient temperature of the micro-LEDs was adjusted by placing the devices on a hotplate, and the temperature was monitored by bonding a thermocouple to the device. The optical −3 dB modulation bandwidth was measured by combining a DC bias from a power source and a small-signal modulation of fixed amplitude from an HP8753ES network analyzer using a bias-tee. Then the light emission from the micro-LED was collected using a 1.4 GHz bandwidth photoreceiver, and the frequency response was recorded by a network analyzer. To calculate the EQE, the light output power as a function of current under different temperatures was measured by a Si detector at a fixed distance from the sample. Detector response changes due to micro-LED spectral changes at different currents/temperatures were further considered to correct the measured light output power. Then, the light output power measured in an integrating sphere at room temperature (~300 K) was used to calibrate the fraction of the light captured by the detector during the variable-temperature measurements.

Fig. 1(a) shows the temperature-dependent EQE versus current density characteristics on a semi-logarithmic scale with device temperature varied from 300 to 500 K in 25 K increments. It can be seen that with the increase in temperature, the EQE peak shifts towards higher current densities and the peak EQE decreases. At low current densities, less than 10 A/cm^2, the EQEs drop with increasing temperature. At high current densities, the variation is complicated. For example, at 1000 A/cm^2, from a close inspection of the data, we found that the EQE increases from 300 to 375 K and decreases from 375 to 500 K. The electrical-to-optical bandwidths of the micro-LED are shown in Fig. 1(b). The bandwidths from 300 to 425 K demonstrate a clear trend. For example, at 500 A/cm^2, the bandwidth decreases, and, at 2500 A/cm^2, the bandwidth increases with the increase in temperature. The bandwidths from 450 K to 500 K show large fluctuations and are not shown here. It should be noted that three randomly selected micro-LEDs have been measured and the results confirm that the obtained temperature-dependent trends in EQE and bandwidth are experimentally repeatable.

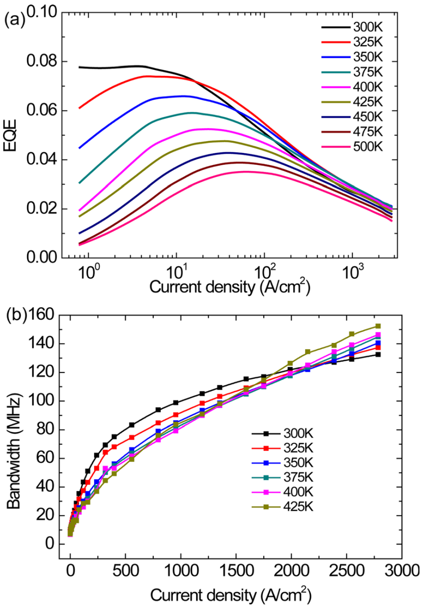

FIG. 1. (a) EQE versus current density from 300 to 500 K with 25 K temperature increments on a semi-logarithmic scale. (b) Bandwidth versus current from 300 to 425 K to show the trend with temperature. The bandwidths from 450 K to 500 K show large fluctuations and are not shown here.

The carrier concentration *n* can be determined from the bandwidth measurement by equation[19,24]

$$n = \frac{1}{qV_{active}} \int_0^I \eta_{inj}(I')\tau(I')dI', \qquad (1)$$

where q is the electron charge, V_{active} is the effective volume of QWs in the active region, I is the current, η_{inj} is the carrier injection efficiency affected by electron leakage, and τ is the differential lifetime calculated from the −3 dB bandwidth, i.e., $f_{3dB} = \sqrt{3}/2\pi\tau$. V_{active} may change under different currents/temperatures due to carrier distribution in more QWs, indium fluctuation, and more possible factors.[25–27] However, due to the lack of sufficient recombination volume information from available data,[25–27] an accurate correction for different currents and temperatures is very challenging. Our analysis follows the common assumption,[28,29] supported by many simulation studies,[30,31] that only the QW closest to the *p*-GaN is heavily populated with carriers. Therefore, in this

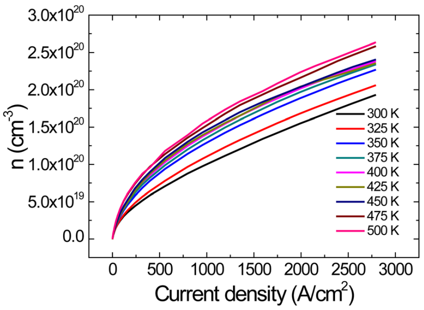

FIG. 2. Carrier concentration n versus current density from 300 to 500 K.

work, one QW with a thickness of 2.8 nm is used to estimate V_{active}. In addition, carrier injection efficiency η_{inj} is assumed to be 1 for all temperatures.[11,12] The electron leakage has little effect at low current densities (roughly before the EQE peak), but may affect LED efficiency at high current densities (roughly after the EQE peak).[1] The latter determined temperature-dependent trend in carrier recombination coefficients is consistent in the whole current density range, so we consider that the effect of electron leakage on our results can be neglected. The calculated carrier concentrations n at different temperatures are shown in Fig. 2. Generally, n keeps increasing from 300 to 500 K, which is consistent with the reduced recombination coefficients in the following text.

In the framework of the *ABC*-approximation, the EQE of the micro-LED is expressed by the following equation:[1]

$$EQE = EXE \times IQE = EXE \times \frac{Bn^2}{An + Bn^2 + Cn^3}, \qquad (2)$$

where EXE is the LED light extraction efficiency. Following Refs. 19 and 32, a constant EXE value of ∼18% has been assumed here, for all current densities and temperatures in this work.[11,12] In addition, a slightly different EXE value will not affect the trends in the *ABC* coefficients. In Eq. (2), the B and C coefficients are only constant at low current densities owing to phase space filling effect.[33,34] The B and C coefficients can be described by the empirical formulas $B = B_0/(1 + n/N^*)$ and $C = C_0/(1 + n/N^*)$, respectively.[14,34] Here, N^* is the phase space filling parameter, and B_0 and C_0 represent B and C at very low n, respectively. From the experimental EQE and IQE, the carrier recombination rates can be obtained. The total carrier recombination rate is expressed as $R_{recom} = I/qV_{active}$, which is the sum of radiative recombination rate $R_r = R_{recom}IQE$ and nonradiative recombination rate $R_{nr} = R_{recom}(1\text{-}IQE)$. Then, from $R_{nr}/n = A + Cn^2$, the A coefficient is obtained at low n (e.g., $n = 1 \times 10^{18}\,\text{cm}^{-3}$); from $R_r/n^2 = B$, the B coefficient is calculated; through $R_{nr}/n^3 = A/n^2 + C$, the C coefficient is available at high n (e.g., $n = 2 \times 10^{20}\,\text{cm}^{-3}$).[34,35] By fitting these curves as shown in Figs. 3(a) and 3(b), the parameters A, B_0, C_0, and N^* can be obtained at different temperatures, as shown in Table I. The physical mechanisms underlying the trends in the fitted parameters are discussed as follows.

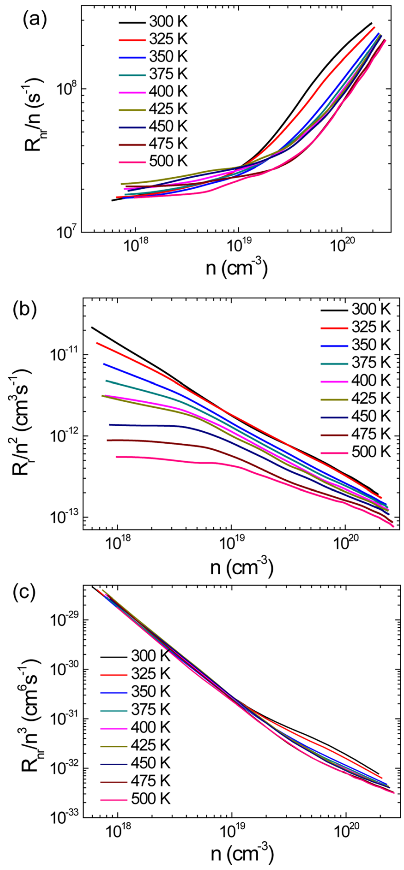

FIG. 3. The experimental variation of (a) R_{nr}/n, (b) R_r/n^2, (c) R_{nr}/n^3 with temperature from 300 to 500 K.

At low current densities, the SRH recombination coefficient A in Table I, as determined from Fig. 3(a), shows a general increasing trend with increasing temperature, consistent with published results.[28,36] However, scatter from the overall

TABLE I. Summary of fitted parameters A, B_0, C_0, and N^* from 300 to 500 K.

T (K)	A (s^{-1})	B_0 (cm^{3}s^{-1})	C_0 (cm^{6}s^{-1})	N^* (cm^{-3})
300	1.74×10^7	8.76×10^{-11}	7.85×10^{-30}	1.94×10^{17}
325	1.78×10^7	2.72×10^{-11}	1.90×10^{-30}	6.72×10^{17}
350	1.76×10^7	1.15×10^{-11}	6.96×10^{-31}	1.42×10^{18}
375	1.86×10^7	5.97×10^{-12}	3.19×10^{-31}	2.86×10^{18}
400	2.03×10^7	3.65×10^{-12}	1.82×10^{-31}	4.75×10^{18}
425	2.21×10^7	3.52×10^{-12}	1.97×10^{-31}	4.34×10^{18}
450	2.03×10^7	1.57×10^{-12}	7.50×10^{-32}	1.17×10^{19}
475	2.09×10^7	9.53×10^{-13}	5.05×10^{-32}	1.55×10^{19}
500	1.77×10^7	5.51×10^{-13}	2.60×10^{-32}	3.18×10^{19}

trend exists, which may come from measurement errors in the -3 dB bandwidths at very low currents. The possible reasons are the relatively large modulation signal compared to the DC component, as well as the noises of optical frequency response. Subsequent analysis has also shown that the temperature dependence of A is relatively weak compared to those of B and C.

In Fig. 3(b), the B coefficient (R_r/n^2) decreases with increasing temperature at all carrier concentrations. This is induced by phase space filling, i.e., the carrier distribution is approximately described by Maxwell-Boltzmann statistics at low carrier concentration and by Fermi-Dirac carrier distribution at high carrier concentration.[14,23,33] As more carriers occupy states in higher sub-bands at higher temperatures, the carrier number per d$\boldsymbol{k}$ interval in $\boldsymbol{k}$-space decreases with increasing temperature, leading to a reduced B coefficient at higher temperatures. In addition, N^* increases with increasing temperature as shown in Table I, i.e., phase-space filling occurs at a higher injection level at a higher temperature, which agrees with the theoretical and experimental trends in other publications[14,23,33] but shows a stronger temperature dependence. The phase space filling effect in Ref. 14 and 33 was estimated by extracting the theoretical data of B versus n. This can be understood by noting that at higher temperatures the thermal distribution already leads to a significant occupation of high-$\boldsymbol{k}$ states. Therefore, a significant change in the occupation of high-$\boldsymbol{k}$ states requires a higher carrier concentration than at lower temperatures.

Figs. 4(a) and 4(b) show the temperature variation of B coefficient at $n = 2 \times 10^{18}\,\mathrm{cm}^{-3}$ and $n = 1 \times 10^{20}\,\mathrm{cm}^{-3}$, respectively. A strong decrease in B with increasing temperature has been found at the low carrier concentration $n = 2 \times 10^{18}\,\mathrm{cm}^{-3}$, empirically scaling as $B \propto 1/T^4$. However, at the high carrier concentration $n = 1 \times 10^{20}\,\mathrm{cm}^{-3}$, a weaker temperature dependence of $B \propto 1/T^{3/2}$ appears. This observation agrees with the theoretical calculation very well[13] and is explained as follows. At a low injection carrier concentration ($2 \times 10^{18}\,\mathrm{cm}^{-3}$), a fraction of carriers, close to the Fermi level and in the high energy tail of the occupation function, is strongly influenced by temperature; at a high carrier concentration ($1 \times 10^{20}\,\mathrm{cm}^{-3}$), the carrier states close to the bandgap are filled, so most carriers are at energies below the Fermi level, leading to less temperature dependence.[13] Other experimental and theoretical work reported weak dependences of B on T,[11,14] which agrees with our results at high carrier concentrations.

The temperature-dependent C coefficients as shown in Fig. 5(a) were calculated from the values of C_0 and N^* in Table I. At all carrier concentrations, the C coefficient decreases with the increase in temperature. In addition, similar to the case of radiative recombination, a weaker temperature dependence is obtained with increasing carrier concentration, which is again related to the phase space filling effect. The temperature dependence of C at a carrier concentration of $1 \times 10^{20}\,\mathrm{cm}^{-3}$ is shown in Fig. 5(b) and empirically follows $C \propto 1/T^2$. The temperature dependence of the C coefficient in this work is contrary to most theoretical and experimental trends in the literature,[11,14–16] but agrees with one design in theoretical result with relatively weak carrier confinement in the QWs.[13]

In summary, the temperature dependence of the recombination coefficients in blue-emitting InGaN/GaN MQW LEDs has been investigated experimentally. With increasing temperature, the radiative and Auger recombination coefficients decrease. It is also found that the temperature dependence of radiative and Auger recombination coefficients becomes weaker at higher carrier concentrations. The phase space filling effect is proposed to contribute significantly to the variation of temperature-dependent radiative and Auger recombination coefficients. This work not only provides further insight into efficiency droop, but also helps to elucidate

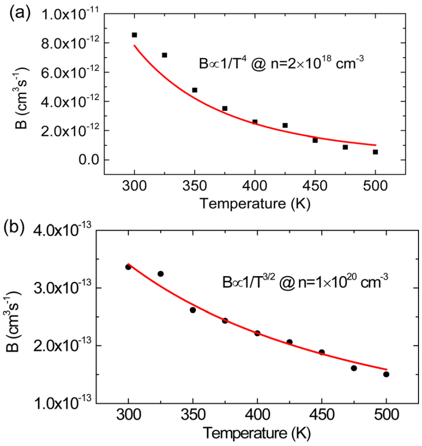

FIG. 4. B coefficient variation with temperature (a) at $n = 2 \times 10^{18}\,\mathrm{cm}^{-3}$ ($B \propto 1/T^4$) and (b) at $n = 1 \times 10^{20}\,\mathrm{cm}^{-3}$ ($B \propto 1/T^{3/2}$). The red lines are fits to the experimental data (black symbols).

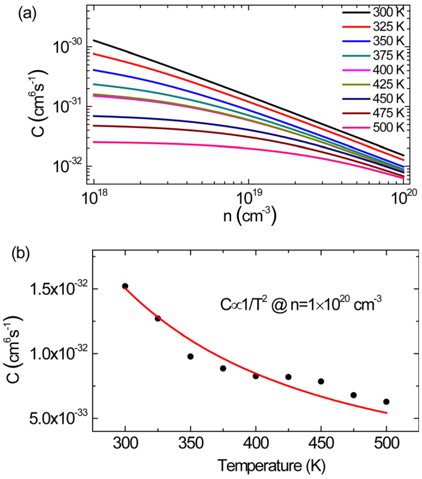

FIG. 5. (a) Calculated C coefficient versus n at different temperatures. (b) C coefficient variation with temperature at $n = 1 \times 10^{20}\,\mathrm{cm}^{-3}$ ($C \propto 1/T$). The red line is a fit to the calculated data (black symbols).

trends in the small-signal modulation bandwidth relevant to the application of LEDs in VLC.

We acknowledge support from Scottish Universities Physics Alliance, China Scholarship Council, Overseas Research Students Awards Scheme, University of Strathclyde, and Engineering and Physical Sciences Research Council Grant EP/K00042X/1. We thank Michael Wallace, Strathclyde University Department of Physics, for his help with the integrating sphere test.

[1] J. Piprek, Phys. Status Solidi A **207**, 2217 (2010).
[2] G. Verzellesi, D. Saguatti, M. Meneghini, F. Bertazzi, M. Goano, G. Meneghesso, and E. Zanoni, J. Appl. Phys. **114**, 071101 (2013).
[3] D. S. Meyaard, Q. Shan, J. Cho, E. F. Schubert, S.-H. Han, M.-H. Kim, C. Sone, S. J. Oh, and J. K. Kim, Appl. Phys. Lett. **100**, 081106 (2012).
[4] H. Masui, T. Ive, M. C. Schmidt, N. N. Fellows, H. Sato, H. Asamizu, S. Nakamura, and S. P. DenBaars, Jpn. J. Appl. Phys., Part 1 **47**, 2112 (2008).
[5] D.-S. Shin, D.-P. Han, J.-Y. Oh, and J.-I. Shim, Appl. Phys. Lett. **100**, 153506 (2012).
[6] D. S. Meyaard, G.-B. Lin, J. Cho, E. F. Schubert, H. Shim, S.-H. Han, M.-H. Kim, C. Sone, and Y. S. Kim, Appl. Phys. Lett. **102**, 251114 (2013).
[7] C. H. Wang, J. R. Chen, C. H. Chiu, H. C. Kuo, Y.-L. Li, T. C. Lu, and S. C. Wang, IEEE Photonics Technol. Lett. **22**, 236 (2010).
[8] J. Iveland, L. Martinelli, J. Peretti, J. S. Speck, and C. Weisbuch, Phys. Rev. Lett. **110**, 177406 (2013).
[9] J. Iveland, M. Piccardo, L. Martinelli, J. Peretti, J. W. Choi, N. Young, S. Nakamura, J. S. Speck, and C. Weisbuch, Appl. Phys. Lett. **105**, 052103 (2014).
[10] M. Binder, A. Nirschl, R. Zeisel, T. Hager, H.-J. Lugauer, M. Sabathil, D. Bougeard, J. Wagner, and B. Galler, Appl. Phys. Lett. **103**, 071108 (2013).
[11] B. Galler, P. Drechsel, R. Monnard, P. Rode, P. Stauss, S. Froehlich, W. Bergbauer, M. Binder, M. Sabathil, B. Hahn, and J. Wagner, Appl. Phys. Lett. **101**, 131111 (2012).
[12] S. Y. Karpov, Phys. Status Solidi RRL **4**, 320 (2010).
[13] J. Hader, J. V. Moloney, and S. W. Koch, IEEE J. Quantum Electron. **44**,185 (2008).
[14] E. Kioupakis, Q. Yan, D. Steiauf, and C. G. Van de Walle, New J. Phys. **15**, 125006 (2013).
[15] E. Kioupakis, P. Rinke, K. T. Delaney, and C. G. Van de Walle, Appl. Phys. Lett. **98**, 161107 (2011).
[16] F. Bertazzi, M. Goano, and E. Bellotti, Appl. Phys. Lett. **101**, 011111 (2012).
[17] Z. Gong, S. Jin, Y. Chen, J. McKendry, D. Massoubre, I. M. Watson, E. Gu, and M. D. Dawson, J. Appl. Phys. **107**, 013103 (2010).
[18] P. Tian, J. J. D. McKendry, Z. Gong, B. Guilhabert, I. M. Watson, E. Gu, Z. Chen, G. Zhang, and M. D. Dawson, Appl. Phys. Lett. **101**, 231110 (2012).
[19] R. P. Green, J. J. D. McKendry, D. Massoubre, E. Gu, M. D. Dawson, and A. E. Kelly, Appl. Phys. Lett. **102**, 091103 (2013).
[20] J. J. D. McKendry, D. Massoubre, S. Zhang, B. R. Rae, R. P. Green, E. Gu, R. K. Henderson, A. E. Kelly, and M. D. Dawson, IEEE J. Lightwave Technol. **30**, 61 (2012).
[21] J.-W. Shi, H.-W. Huang, F.-M. Kuo, J.-K. Sheu, W.-C. Lai, and M. L. Lee, IEEE Photonics Technol. Lett. **22**, 1033 (2010).
[22] P. Tian, J. J. D. McKendry, Z. Gong, S. Zhang, S. Watson, D. Zhu, I. M. Watson, E. Gu, A. E. Kelly, C. J. Humphreys, and M. D. Dawson, J. Appl. Phys. **115**, 033112 (2014).
[23] Y. Y. Kudryk, A. K. Tkachenko, and A. V. Zinovchuk, Semicond. Sci. Technol. **27**, 055013 (2012).
[24] R. Olshansky, C. Su, J. Manning, and W. Powazinik, IEEE J. Quantum Electron. **20**, 838 (1984).
[25] B. Galler, A. Laubsch, A. Wojcik, H. Lugauer, A. Gomez-Iglesias, M. Sabathil, and B. Hahn, Physica Status Solidi C **8**, 2372 (2011).
[26] Y.-R. Wu, R. Shivaraman, K.-C. Wang, and J. S. Speck, Appl. Phys. Lett. **101**, 083505 (2012).
[27] H.-Y. Ryu, D.-S. Shin, and J.-I. Shim, Appl. Phys. Lett. **100**, 131109 (2012).
[28] D. S. Meyaard, Q. Shan, Q. Dai, J. Cho, E. F. Schubert, M.-H. Kim, and C. Sone, Appl. Phys. Lett. **99**, 041112 (2011).
[29] Q. Dai, Q. Shan, J. Wang, S. Chhajed, J. Cho, E. F. Schubert, M. H. Crawford, D. D. Koleske, M.-H. Kim, and Y. Park, Appl. Phys. Lett. **97**, 133507 (2010).
[30] J. R. Chen, Y. C. Wu, S. C. Ling, T. S. Ko, T. C. Lu, H. C. Kuo, Y. K. Kuo, and S. C. Wang, Appl. Phys. B **98**, 779 (2010).
[31] Y.-K. Kuo, T.-H. Wang, J.-Y. Chang, and M.-C. Tsai, Appl. Phys. Lett. **99**, 091107 (2011).
[32] T.-X. Lee, K. Gao, W.-T. Chien, and C.-C. Sun, Opt. Express **15**, 6670 (2007).
[33] J. Hader, J. V. Moloney, and S. W. Koch, Appl. Phys. Lett. **87**, 201112 (2005).
[34] A. David and M. J. Grundmann, Appl. Phys. Lett. **96**, 103504 (2010).
[35] A. David and M. J. Grundmann, Appl. Phys. Lett. **97**, 033501 (2010).
[36] H. P. T. Nguyen, M. Djavid, K. Cui, and Z. Mi, Nanotechnology **23**, 194012 (2012).

Appendix 1

Micro-LED design process

The following figures are early stage handmade sketches to explore the concepts of pixel shape on current distribution, self heating, mutual heating, addressing metal tracks and optical coupling for fibre optics geometries.

Figure. 6.3 is an early draft of what became the design of segmented micro–LEDs. Here, the initials concerns were to increase the optical power via a multi-pixel array and to meet the fibre geometry for an uniform optical coupling. Initial thoughts about using transfer-printing technology to create a transceiver module with no optics using an APD as receiver. At that stage it was concluded that with the dimensions of such transceiver didn't meet the maximum diameter for POF applications. However, this exercise allowed to further develop the concept of multi-pixel arrays considering the following aspects: the influence of the track length on the pixel-to-pixel variation of series resistance, and consequently, output optical power; the thermal management of the mutual and self heating effects; and the active area compensation for the optical out-coupling of outer pixels. These concepts were implemented in the final version of the segmented micro–LEDs, as presented in 4.3.

Figure 6.4 shows considerations of the optical coupling for applications with POF. Light from the chip travels to refractive index matching liquid and into the POF. The initial calculations had further defined the a small area difference between inner and outer pixels of the segmented micro–LEDs to compensate for the coupling loss.

Figure 6.5 shows an initial draft of a cluster for application in POF. The idea here was to centralise the p-pad for a direct wire bond. In principle, this detail should improve two aspects:

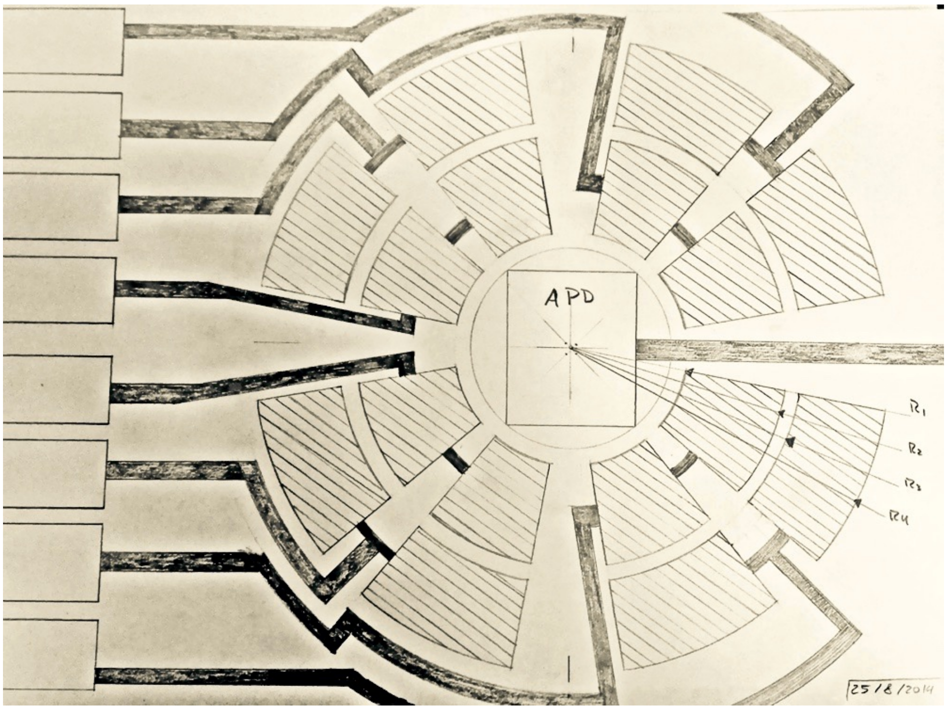

Figure 6.3: Draft sketch for a segmented device for integration of a avalanche photodiode.

to create a more uniform current distribution for all pixels of the cluster, a typical problem in cluster format of micro–LEDs; and to force the launch of the optical in an equidistant ring to the fibre to reduce the high-order ray dispersion inside the fibre core, which may slightly increase the bandwidth of the fibre. This device was not realised.

Figure 6.6 is an early draft of what became the design of the broad-area LEDs, ring and half-ring shaped micro–LEDs. The initial thoughts here were to improve the performance of single pixel micro-LEDs. The two main aspects considered were current crowding and thermal management. Starting with the typical circular-shaped pixel, a ring-shaped geometry allows to remove the highest temperature zone. To compensate for the loss in active area, a larger diameter and wall width could be used and at simultaneously, larger diameters would reduce heat transfer between opposite side of the ring, effectively reducing junction temperature. The concept as shown in the figure 6.6 was broken down in steps and firstly implemented in broad-area for further study, see figure 4.3; and the micro-LED implementation followed in form of ring and half-ring shapes, see figure 4.13.

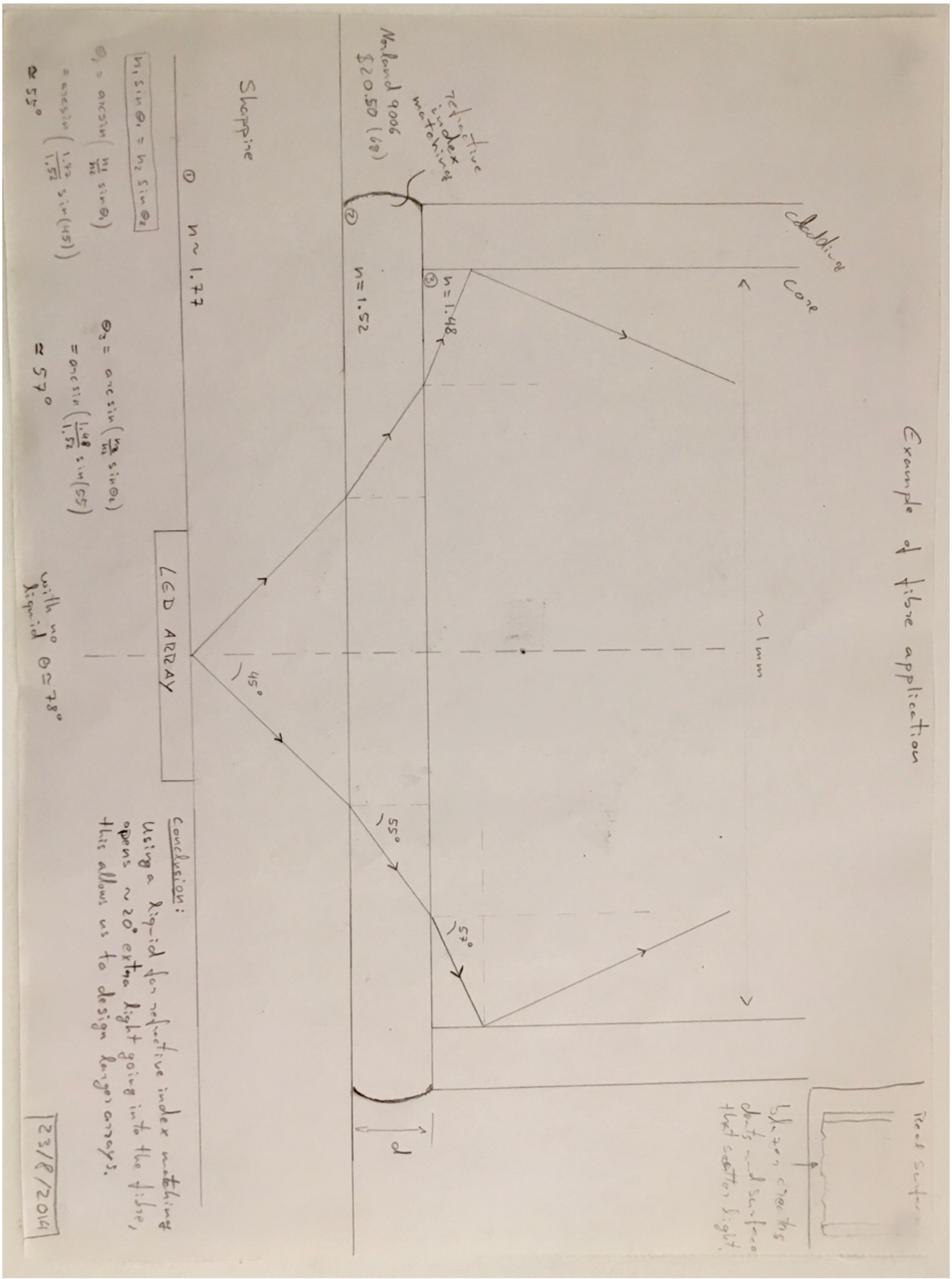

Figure 6.4: Considerations of the optical coupling for integration with plastic optical fibre.

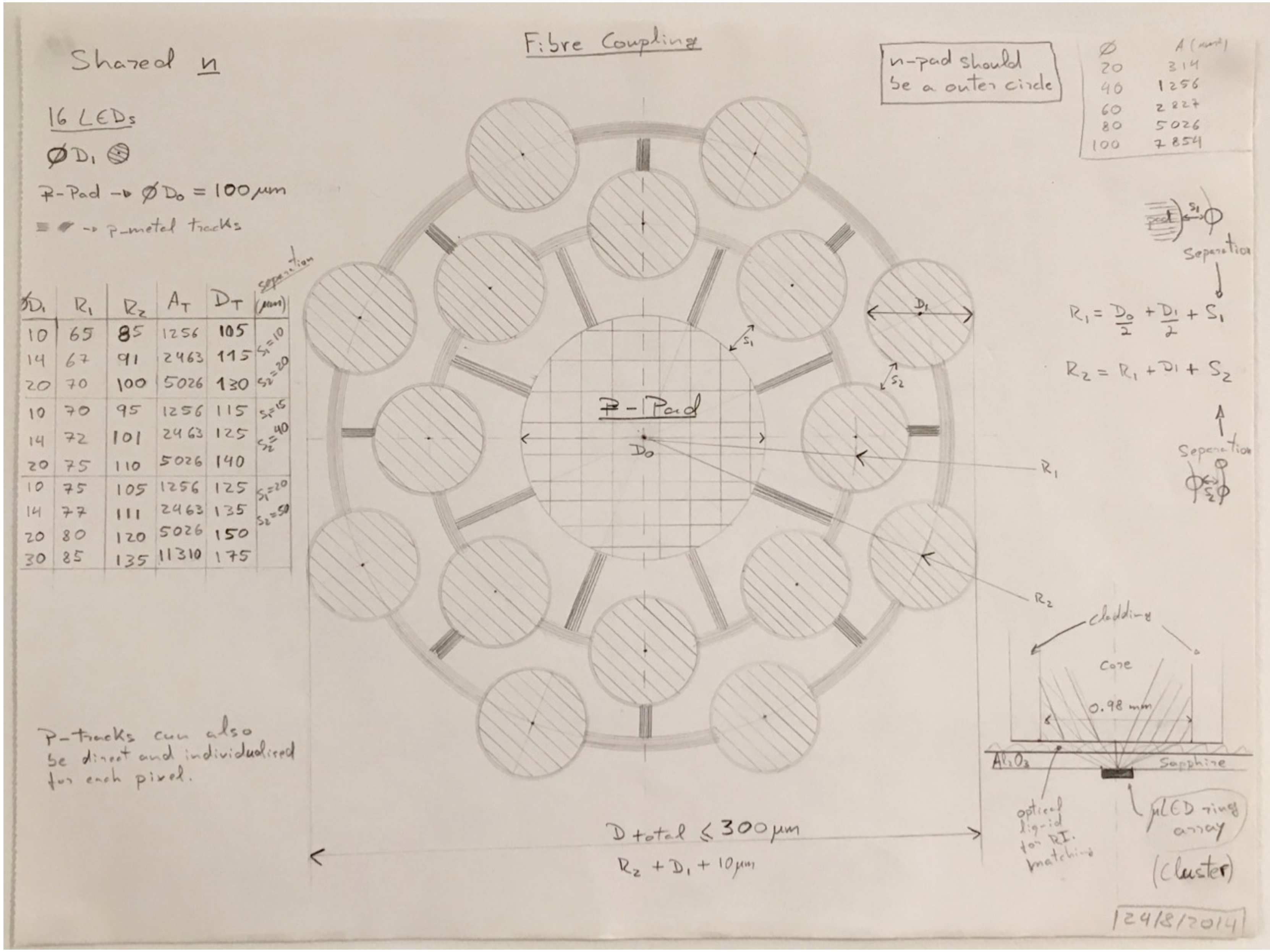

Shared n

16 LEDs

ØD_1

P-Pad → ØD_0 = 100 μm

→ p-metal tracks

ØD_1	R_1	R_2	A_T	D_T	separation (μm)
10	65	85	1256	105	$S_1=10$ $S_2=20$
14	67	91	2463	115	
20	70	100	5026	130	
10	70	95	1256	115	$S_1=15$ $S_2=40$
14	72	101	2463	125	
20	75	110	5026	140	
10	75	105	1256	125	$S_1=20$ $S_2=50$
14	77	111	2463	135	
20	80	120	5026	150	
30	85	135	11310	175	

P-tracks can also be direct and individualised for each pixel.

n-pad should be a outer circle

Ø	A (μm²)
20	314
40	1256
60	2827
80	5026
100	7854

$$R_1 = \frac{D_0}{2} + \frac{D_1}{2} + S_1$$

$$R_2 = R_1 + D_1 + S_2$$

D total ≤ 300 μm

$R_2 + D_1 + 10\,\mu m$

24/8/2014

Figure 6.5: Draft sketch of a cluster for integration with plastic optical fibre.

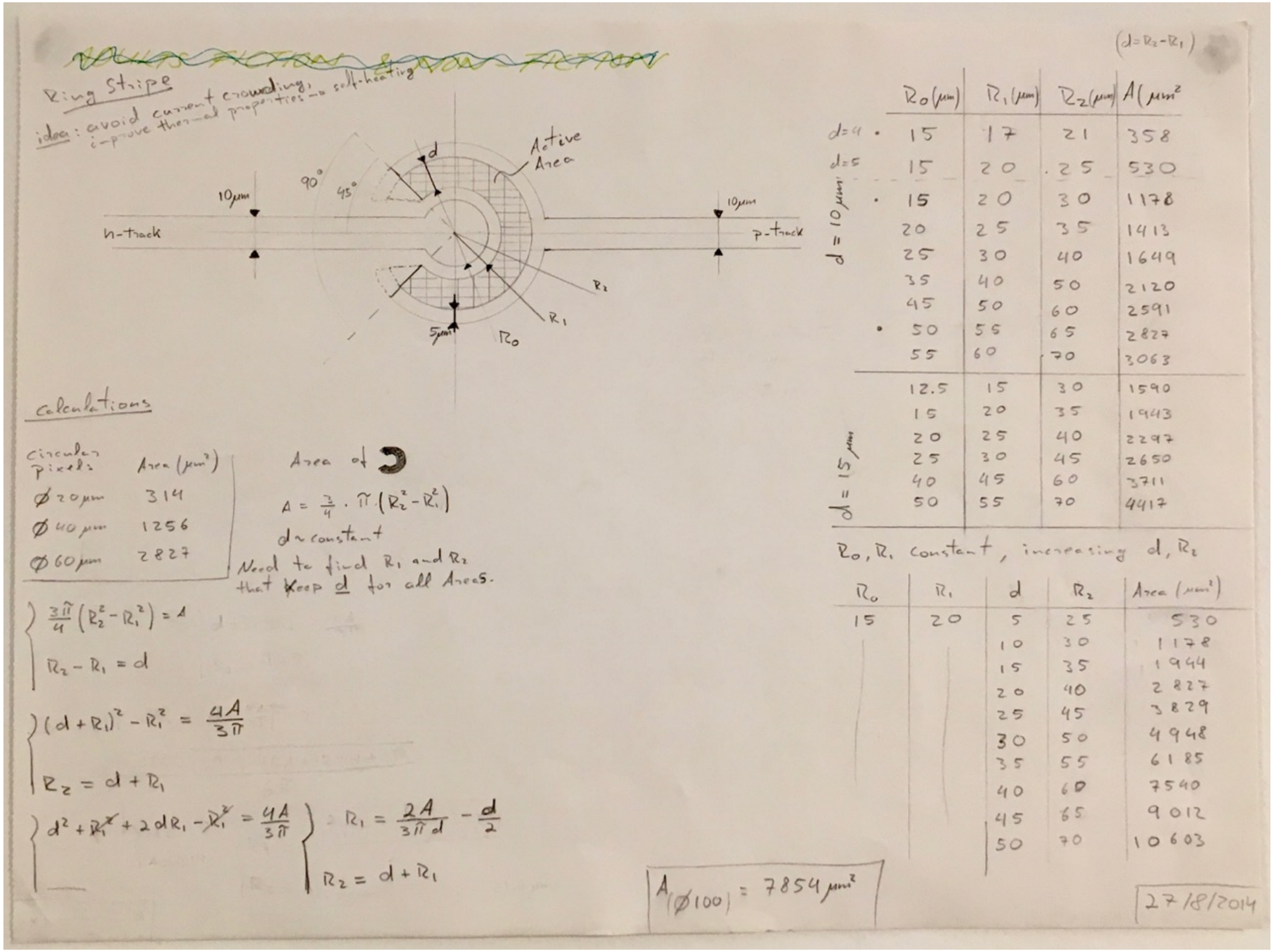

[redacted]

Ring Stripe

idea: avoid current crowding,
improve thermal properties → self-heating

Calculations

Circular pixels	Area (μm^2)
∅ 20μm	314
∅ 40μm	1256
∅ 60μm	2827

Area of ◖

$A = \frac{3}{4} \cdot \pi \cdot (R_2^2 - R_1^2)$

$d \sim$ constant

Need to find R_1 and R_2 that ~~K~~keep <u>d</u> for all Areas.

$$\begin{cases} \frac{3\pi}{4}\left(R_2^2 - R_1^2\right) = A \\ R_2 - R_1 = d \end{cases}$$

$$\begin{cases} (d + R_1)^2 - R_1^2 = \frac{4A}{3\pi} \\ R_2 = d + R_1 \end{cases}$$

$$\begin{cases} d^2 + \cancel{R_1^2} + 2dR_1 - \cancel{R_1^2} = \frac{4A}{3\pi} \\ \end{cases} \quad \begin{cases} R_1 = \frac{2A}{3\pi d} - \frac{d}{2} \\ R_2 = d + R_1 \end{cases}$$

$A_{(\varnothing 100)} = 7854 \mu m^2$

$(d = R_2 - R_1)$

	R_0 (μm)	R_1 (μm)	R_2 (μm)	A (μm^2)
d=4 •	15	17	21	358
d=5	15	20	25	530
d = 10 μm •	15	20	30	1178
	20	25	35	1413
	25	30	40	1649
	35	40	50	2120
	45	50	60	2591
•	50	55	65	2827
	55	60	70	3063
d = 15 μm	12.5	15	30	1590
	15	20	35	1943
	20	25	40	2297
	25	30	45	2650
	40	45	60	3711
	50	55	70	4417

R_0, R_1 constant, increasing d, R_2

R_0	R_1	d	R_2	Area (μm^2)
15	20	5	25	530
		10	30	1178
		15	35	1944
		20	40	2827
		25	45	3829
		30	50	4948
		35	55	6185
		40	60	7540
		45	65	9012
		50	70	10603

27/8/2014

Figure 6.6: Draft sketch for a semi-ring shaped micro-LED.

Appendix 2

Matlab^{TM} applications

This section presents various software applications developed during the course of the PhD. Although these applications did not contribute directly to results, they did provide significant time savings and consistency in the analysis.

These applications have been used by LED group at the Institute of Photonics and the University of Glasgow. Their use was crucial to fix bugs, improving features and adapt the software to real needs. One feature that is present is a help button with usage instructions for users not familiar with the application. In addition, for the Bandwidth application, a full user manual was written, which includes details of how the application was programmed and data management for datasets.

I–V & L–I

Measurement of the I–V and L–I characteristics were all taken with the assistance of a computerised setup controlled via Labview^{TM}. The output data comes in the form of text files which require further processing in order to plot the respective I–V and L–I curves. Fig. 6.7 presents a software application developed in Matlab^{TM} to assist with the management, processing and analysis of the I–V and L–I data sets. Analysis with this applications is fast and consistent with any data set. Tools are included to plot various common graphs (I–V, L–I, L–V, IQE, EQE), determine key characteristics of the devices such as driving voltage, series resistance and efficiency, and an option for normalised units is also included.

Spectra

Measurement of the emission spectra from LEDs are done with a spectrometer connected to a computer with acquisition software from the vendor. The typical case is to store a spectrum for each injection current. This data is stored as text files with two columns, one for wavelength and another for the corresponding count number. As such, a full measurement involves a set of currents that explores the whole operating range of the LED, typically ten or more measurements per device. In order to accelerate the process of data analysis, as shown in Fig. 6.8 a Matlab^{TM} application was developed to analyse all the spectra of a device at once. It supports Gaussian and Lorentzian fits from which the central emission peak and the spectral linewidth or FWHM are calculated.

Thermal analysis for FLIR camera

Thermal imaging measurements with the infra-red camera FLIR SC7000 require a calibration to the emissivity of the materials under study. In addition, to correctly determine junction temperature, the mean temperature across the active area must be calculated. Fig. 6.9 presents a software application developed in Matlab^{TM} for the these purposes.

Modulation bandwidth

Measurements of modulation bandwidth were all taken manually with an optical setup (Fig. 3.1) and a network analyser to evaluate the loss or gain between the input and output signals. The network analyser stores frequency response data in a floppy disk which afterwards is transferred to a computer. Fig. 6.10 presents a software developed in Matlab^{TM} to process multiple sets of data of various devices and extract the relevant information with precision.

This software tool allows one to look at the same data set in two distinct ways. Firstly, as shown in Fig. 6.11 (a), it allows one to plot the obtained bandwidth as a function of the injected current for one or multiple LEDs, this is the standard plot to show bandwidth of a device. Secondly, it can re-shape the data set and plot the obtained bandwidth as function of the LED for each injection current, as shown in Fig. 6.11 (b). The latter is especially useful to compare the performance of LEDs with similar properties such as active area, this plot is used in chapters 4 and 5.

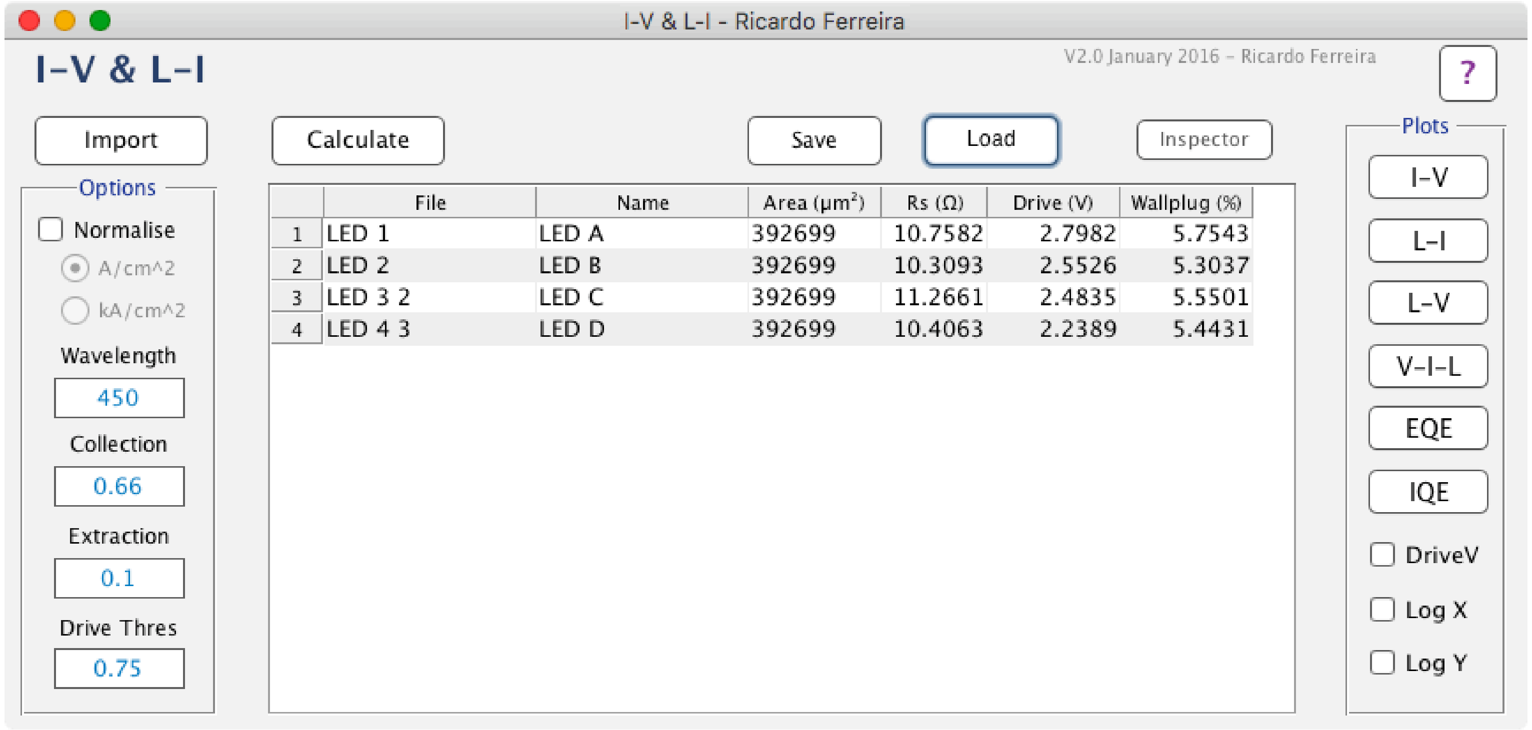

☐ Normalise

● A/cm^2

○ kA/cm^2

Wavelength: 450

Collection: 0.66

Extraction: 0.1

Drive Thres: 0.75

	File	Name	Area (μm²)	Rs (Ω)	Drive (V)	Wallplug (%)
1	LED 1	LED A	392699	10.7582	2.7982	5.7543
2	LED 2	LED B	392699	10.3093	2.5526	5.3037
3	LED 3 2	LED C	392699	11.2661	2.4835	5.5501
4	LED 4 3	LED D	392699	10.4063	2.2389	5.4431

☐ DriveV

☐ Log X

☐ Log Y

Figure 6.7: Software application developed in Matlab for processing the data of the I–V and L–I characteristics.

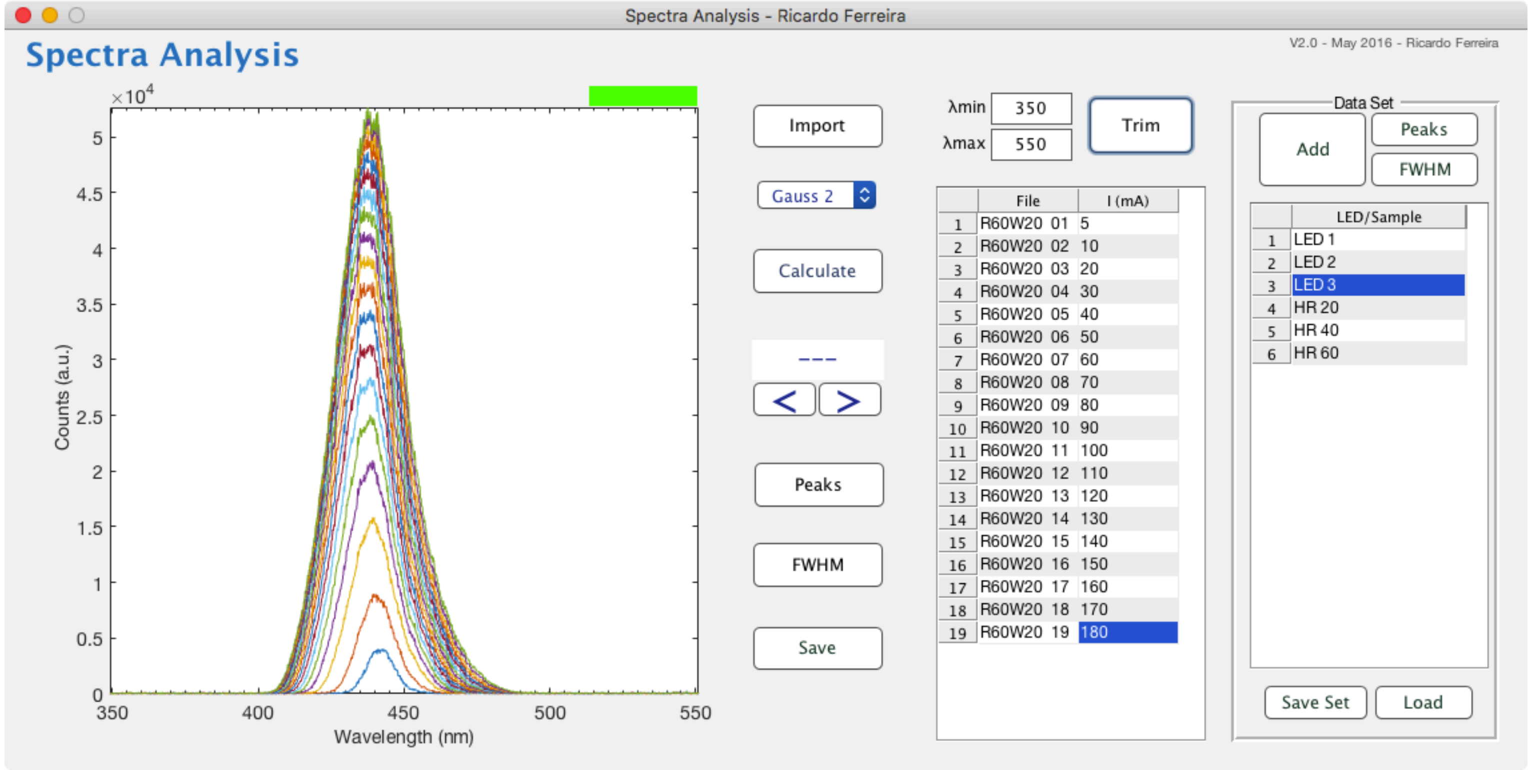

Gauss 2

λmin 350

λmax 550

	File	I (mA)
1	R60W20 01	5
2	R60W20 02	10
3	R60W20 03	20
4	R60W20 04	30
5	R60W20 05	40
6	R60W20 06	50
7	R60W20 07	60
8	R60W20 08	70
9	R60W20 09	80
10	R60W20 10	90
11	R60W20 11	100
12	R60W20 12	110
13	R60W20 13	120
14	R60W20 14	130
15	R60W20 15	140
16	R60W20 16	150
17	R60W20 17	160
18	R60W20 18	170
19	R60W20 19	180

	LED/Sample
1	LED 1
2	LED 2
3	LED 3
4	HR 20
5	HR 40
6	HR 60

Figure 6.8: Software application developed in Matlab for processing emission spectra of LEDs.

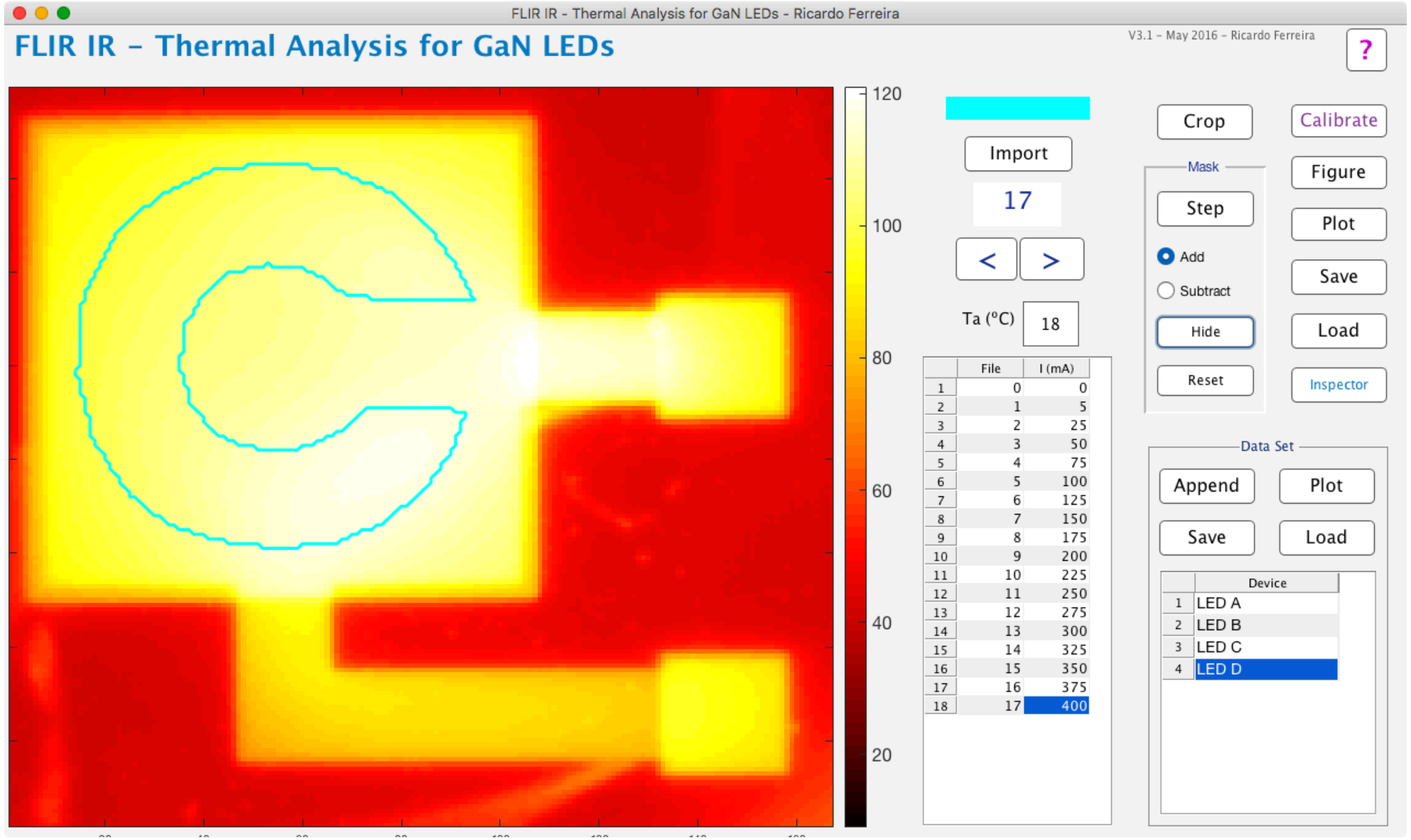

Ta (°C) 18

	File	I (mA)
1	0	0
2	1	5
3	2	25
4	3	50
5	4	75
6	5	100
7	6	125
8	7	150
9	8	175
10	9	200
11	10	225
12	11	250
13	12	275
14	13	300
15	14	325
16	15	350
17	16	375
18	17	400

	Device
1	LED A
2	LED B
3	LED C
4	LED D

Figure 6.9: Software application developed in Matlab to evaluate junction temperature of LEDs. It is used to correct emissivity from infra–red imaging of LEDs based on previous calibration curves; the application shows the mask with the selected zone corresponding to the active area of the device.

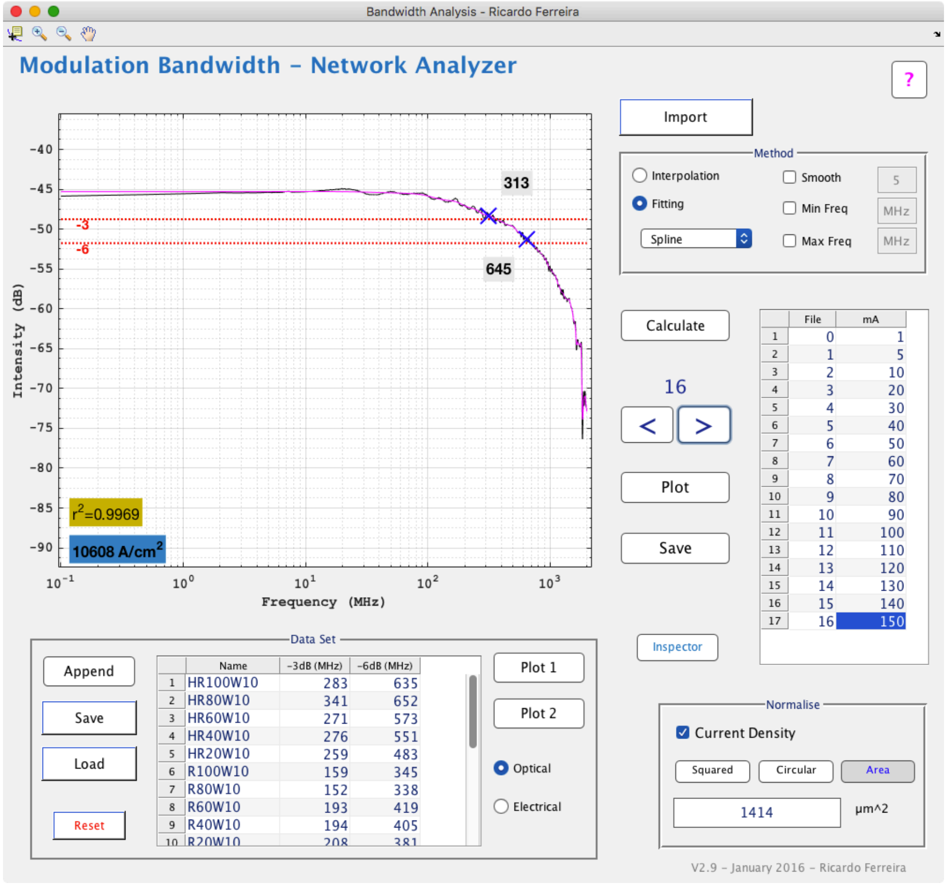

Method
○ Interpolation
● Fitting
Spline
☐ Smooth 5
☐ Min Freq MHz
☐ Max Freq MHz

16

	File	mA
1	0	1
2	1	5
3	2	10
4	3	20
5	4	30
6	5	40
7	6	50
8	7	60
9	8	70
10	9	80
11	10	90
12	11	100
13	12	110
14	13	120
15	14	130
16	15	140
17	16	150

Data Set

	Name	-3dB (MHz)	-6dB (MHz)
1	HR100W10	283	635
2	HR80W10	341	652
3	HR60W10	271	573
4	HR40W10	276	551
5	HR20W10	259	483
6	R100W10	159	345
7	R80W10	152	338
8	R60W10	193	419
9	R40W10	194	405
10	R20W10	208	381

● Optical
○ Electrical

Normalise
☑ Current Density
Squared Circular Area
1414 μm^2

V2.9 – January 2016 – Ricardo Ferreira

Figure 6.10: Main front-end of the software application developed in Matlab for rapid and precise analysis of frequency response curves.

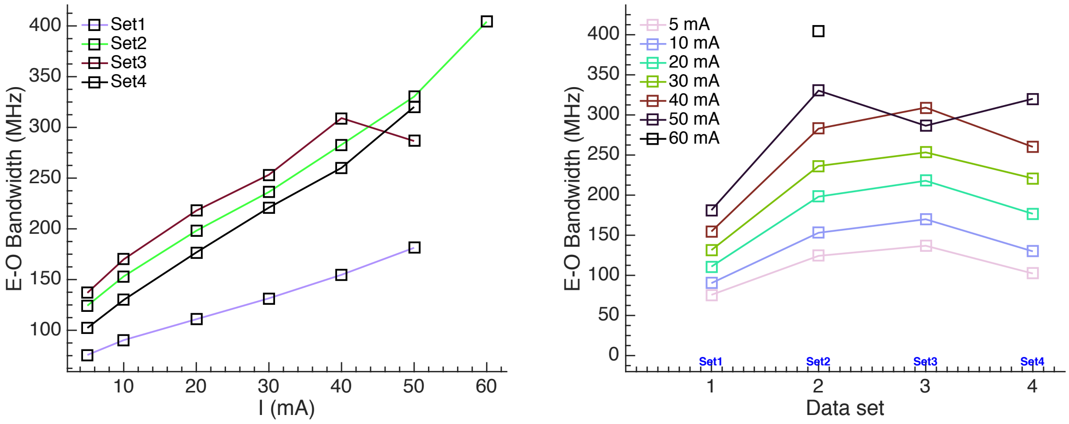

(a) Bandwidth curves as function of current

(b) Bandwidth curves as function of LED

Figure 6.11: In (a) the plot of bandwidth curves as a function of injection current for a set of micro–LEDs, and (b) the plot of bandwidth curves a function of the LED for a set of currents. Note that these graphs are obtained from the same data set, each curve of (a) corresponds to a column of point in (b).

Source code

The source code of these applications is show the next pages for a selection of meaningful code lines of the main function file only for brevity. Note that these applications have a user interface which requires a certain style of programming and this reflected in the code with a large amount of data types conversions. In addition, data storage is kept in the user interface itself, allowing to always be loaded in the random access memory and very fast transition to the processor for calculations. Each application also has a number of extra functions, not shown here, that accomplish standard and repetitive tasks.

I–V & L–I

The total number of code lines of the main file is 1011. Below are shown the 121–255 lines corresponding to the core calculations.

```matlab
function Calculate_Callback(hObject, eventdata, handles)

% Clear previous run
clc;
set(handles.Calculate,'UserData',[]);
set(handles.Calculate,'BackgroundColor','default');
set(handles.IV,'BackgroundColor','default');
set(handles.LI,'BackgroundColor','default');
set(handles.EQE,'BackgroundColor','default');
set(handles.IQE,'BackgroundColor','default');
set(handles.VIL,'BackgroundColor','default');
set(handles.Save,'BackgroundColor','default');
set(handles.Export,'BackgroundColor','default');

% Show busy
set(handles.Calculate,'BackgroundColor','yellow');

% Get Imported Data & TableData
Data = get(handles.Import,'UserData');
TableData = get(handles.Table, 'Data');
Data.Names = TableData(:,2);

% Create colours
Data.ColourSet = varycolor(Data.n);



% --- Rs & Turn-On

% Pre-allocation
Data.X      = cell(Data.n,1);
Data.Yfit   = cell(Data.n,1);
Data.Rs     = zeros(Data.n,1);
Data.DriveV = zeros(Data.n,1);

for i = 1:Data.n,

```

```
    % Find the point to match the Drive Threshold from max current
    idx = find(Data.I{i} ≤ (str2num(get(handles.DriveThreshold,'String'))) * ...
        max(Data.I{i}), 1, 'last');

    % Linear fit:  y=mx+b
    [FitCoeff R2] = LinearFit(Data.V{i}(idx:end), 1E-3 * Data.I{i}(idx:end)); % ...
        includes conversion mA -> A
    m     = FitCoeff(1);
    b     = FitCoeff(2);
    X     = linspace(0, max(cell2mat(Data.V(i))), Data.nn)';
    Yfit  = m * X + b;
    [a aa]           = find( Yfit > 0,1);
    Data.X{i,1}      = X(a:end);
    Data.Yfit{i,1}  = Yfit(a:end);

    % Rs (Ohm)
    Data.Rs(i) = 1 ./ m;  % factor due to I(mA) in the fit

    % Turn-On voltage (V)
    Data.DriveV(i) = abs(b ./ m);
end
clear idx FitCoeff R2 a b m aa




% --- Normalise to Current Density

Data.Area{Data.n,1} = [];

if get(handles.DensityUnits,'Value')

    Area = TableData(:,3);

    % Current Density - J
    for i = 1:numel(Area)
        Data.Area{i,1} = num2str(round(eval(Area{i})));   % um^2
        Data.J{i,1} = 1E5 .* Data.I{i} ./ eval(Area{i});  % A/cm^2
    end

    % Luminescence Density - LD
    for i = 1:numel(Area)
        Data.LD{i,1} = 1E5 .* Data.L{i} ./ eval(Area{i});  % W/cm^2
    end

    TableData(:,3) = Data.Area;
end




% --- EQE, IQE & Wallplug

Data.Wavelength = str2num(get(handles.Wavelength,'String')) * 1E-9;
Data.EQE_factor = 2 - str2num(get(handles.Collection_Eff,'String'));
Data.Extraction_Eff = str2num(get(handles.Extraction_Eff,'String'));

for i = 1:Data.n,

    idx = find(Data.L{i} > 0.1 * max(Data.L{i}),1);

    while Data.V{i}(idx,1) ≤ 0
        idx = idx+1;
    end

    for j = idx:numel(Data.L{i}),

        % EQE
```

```
        Data.EQE{i,1}(j,1) = Data.EQE_factor * ( Data.L{i}(j,1) ./ (6.626E-34 * ...
            (3e8 ./ Data.Wavelength) ) ) ./ ( Data.I{i}(j,1) ./ 1.602E-19 );

        % IQE
        Data.IQE{i,1}(j,1) = Data.EQE{i,1}(j,1) ./ Data.Extraction_Eff;

        % Wallplug efficiency
        WallPlug{i,1}(j,1) = 100 * Data.L{i}(j,1) ./ ( Data.I{i}(j,1) * ...
            Data.V{i}(j,1) ); % Percentage (%)
        if WallPlug{i,1}(j,1) == inf
            WallPlug{i,1}(j,1) = 0;
        end

    end

    Data.WallPlug(i) = max(WallPlug{i}(WallPlug{i}>0));

end
clear i j idx


% --- Fill table
TableData(:,1) = Data.Files;
TableData(:,2) = Data.Names;
TableData(:,4) = num2cell(round(Data.Rs));
TableData(:,5) = num2cell(Data.DriveV);
TableData(:,6) = num2cell(Data.WallPlug);
set(handles.Table, 'Data', TableData);

% Store processed data
set(handles.Calculate,'UserData',Data);

% Show done
set(handles.Calculate,'BackgroundColor','Green');
```

Spectra

The total number of code lines of the main file is 495. Below are shown the 197–277 lines corresponding to the core calculations.

```
% red light - busy or error
set(handles.LED,'BackgroundColor','red');

Table = get(handles.Table,'Data');
if isempty(Table{1,2})
    errordlg('fill the table');
    set(handles.LED,'BackgroundColor','default');
    return
end

% get raw data
Data = get(handles.Import,'UserData');


% read current from table
TableData = get(handles.Table,'Data');
Data.Current = str2double(TableData(:,2));


% Fit
Eq = get(handles.Eq,'Value');
```

```
if numel(Data.Wavelength) < 5E3 && Eq ≠4,
    Data.X      = linspace( Data.Wavelength(1), Data.Wavelength(end), 1E4 )';
    Data.YFit   = zeros(1E4,Data.n);
elseif Eq == 4,
    Data.X      = Data.Wavelength;
    Data.YFit   = zeros(length(Data.Wavelength),Data.n);
end
Data.Peaks = zeros(Data.n,1);
Data.FWHM  = zeros(Data.n,1);
for i = 1:Data.n

    [Fit gof] = CreateFit( Data.Wavelength, Data.Intensity(:,i), Eq);

    if Eq ≠ 4
    Data.YFit(:,i)      = feval(Fit,Data.X);
    Data.FitCoeff(:,i) = coeffvalues(Fit);
    else
        Data.YFit(:,i) = Fit;
    end

    % Calculate emission Peak
    [A, I]  = max(Data.YFit(:,i));
    Data.Peaks(i) = Data.X(I);


    % Calculate full width at half maximum of the raw data using the fit
    Data.FWHM(i,1) = fwhm(Data.X, Data.YFit);
%     a = find(Data.YFit > 1/2*Data.YFit);
%     left  = a(1);
%     right = a(end);
%    FWHM()  = Data.X(a(end)) - Data.X(a(1));

end
Data.Peaks = Data.Peaks(:);
clear i j Fit Spectrum yUp yDown xUp xDown A gof FitCoeff I a


% Clean Axes
cla(handles.Axes);
axes(handles.Axes);
xlabel(handles.Axes,' Wavelength (nm) ');
ylabel(handles.Axes,' Counts (a.u.)');

% plot first graph & fit
Data.Counter = 1;
plot(Data.Wavelength, Data.Intensity(:,Data.Counter),'.b','MarkerSize',8);
hold('on');
plot(Data.X, Data.YFit(:,1),'-r','LineWidth',2);
legend({'data','fit'},'Location','NorthEast','FontSize',14,'Box','off');
axis tight


% Set the FileNumber
set(handles.FileNumber,'String',num2str(Data.Counter));

% save data to handles
set(handles.Calculate,'UserData',Data);

% green light - all good
set(handles.LED,'BackgroundColor','green');
```

Thermal analysis for FLIR cameras

The total number of code lines of the main file is 697. Below are shown the 439–552 lines corresponding to the core calculations.

```matlab
function Calculate_Callback(hObject, eventdata, handles)

set(handles.Calculate,'BackgroundColor', 'yellow');

try
    Data       = get(handles.Import,'UserData');
    Counter    = get(handles.FileNumber,'UserData');
catch ME
    return
end

% Load emissivity calibration (should be in the same folder)
load('EmissivityCorrection.mat');
dE = 0.1;
dT = 0.2;

Ta = str2num(get(handles.Ta,'String'));


%% --- Get currents from table
TableData = get(handles.Table,'Data');
Data.I     = TableData(:,2);


%% --- Emissivity Correction
% Will correct the emissivity from 1.0 to the correct value
% based on the initial temperature of each pixel.

% GaN Emissivity Map
% Getting emissivity of each pixel from the calibration curve
a = GaN_Emissivity.a;
b = GaN_Emissivity.b;
c = GaN_Emissivity.c;
d = GaN_Emissivity.d;

for m = 1:Data.n
    EmissivityMap{m,1} = a.*exp(b.*Data.Thermal{m,1}) + ...
        c.*exp(d.*Data.Thermal{m,1});

    idx = EmissivityMap{m,1} > 1;
    EmissivityMap{m,1}(idx) = 1;
    idx = EmissivityMap{m,1} < 0.25;
    EmissivityMap{m,1}(idx) = 0.25;
end
clear a b c d m index

% Temperature correction
% Uses the Emissivity Map to correct the temperature to the 'real' value
a = Temp_Emissivity.a;
b = Temp_Emissivity.b;
c = Temp_Emissivity.c;
d = Temp_Emissivity.d;

for m = 1:Data.n
    for i = 1:size(Data.Thermal{1,1},1)
        for j =  1:size(Data.Thermal{1,1},2)

            Data.Thermal{m,1}(i,j) = ...
                Data.Thermal{m,1}(i,j)*exp(b*EmissivityMap{m,1}(i,j))...
```

```
                + (Data.Thermal{m,1}(i,j) * 0.7818) * ...
                    exp(d*EmissivityMap{m,1}(i,j));

            if Data.Thermal{m,1}(i,j) < Ta
                Data.Thermal{m,1}(i,j) = Ta;
            end

            %     Temperature Estimation Error - from emissivity & camera focus
            Data.ThermalError{m,1}(i,j) = dE * ( exp(b*EmissivityMap{m,1}(i,j)) ...
               + 0.7818*exp(d*EmissivityMap{m,1}(i,j)) )...
                + dT * Data.Thermal{m,1}(i,j) * (exp(b*EmissivityMap{m,1}(i,j)) ...
                    + 0.7818*exp(d*EmissivityMap{m,1}(i,j)));

        end
    end


    % --- Calculate a mean value of the pixels
    if get(handles.Mask,'UserData') == 1

        %     Tj - mean temperature of each image
        Data.Tmean(m,1) = mean(Data.Thermal{m}(Data.Mask));

        %     Errors of each image
        Data.Error(m,1) = mean(Data.ThermalError{m}(Data.Mask));

    else

        %     Tj - mean temperature of each image
        Data.Tmean(m,1) = mean(Data.Thermal{m}( Data.Thermal{m} > ...
            0.5*max(max(Data.Thermal{m}))));
        % Data.Tmean(m,1) = mean(Data.Thermal{m}( Data.Thermal{m} > ...
            0.5*max(max(Data.Thermal{m}))));

        % Errors of each image
        % ErrorMax(m,1)  = max(max(ThermalError{m,1}));
        % Error(m,1) = mean(mean(ThermalError{m,1}));
        Data.Error(m,1) = mean(Data.ThermalError{m}( Data.Thermal{m} > ...
            0.5*max(max(Data.Thermal{m}))));
    end

end
clear a b c d m i j ThermalError


% New colorbar limits for the area
Data.Tmin = min(min(cell2mat(Data.Thermal)));
Data.Tmax = max(max(cell2mat(Data.Thermal)));


%% --- Save data to handles
set(handles.Import,'UserData',Data);

% Update the image
cla;
imagesc(Data.Thermal{Counter});
caxis([round(Data.Tmin),round(Data.Tmax)]);
colorbar;
colorbar('FontSize',16);
colormap('hot');
drawnow update

set(handles.Calculate,'BackgroundColor', 'green');
```

Modulation bandwidth

The total number of code lines of the main file is 1553. Below are shown the 174–511 lines corresponding to the core calculations.

```
function Calculate_Callback(hObject, eventdata, handles)
% Objective: Calculate the electrical and optical bandwidth points (-3dB & -6dB).
%%%%%%%%%%%%%%% Please be very careful with ANY changes! %%%%%%%%%%%%%%%

set(handles.Calculate,'BackgroundColor', 'yellow'); pause(0.01);
set(handles.Right,'BackgroundColor', 'default');
set(handles.Left,'BackgroundColor', 'default');
set(handles.Save,'BackgroundColor', 'default');

clc
cla(handles.Axes);
axes(handles.Axes);

% Get Data from the Import button
Data        = get(handles.Import,'UserData');
FileName    = Data.FileName;
Amplitudes  = Data.Amplitudes;
Frequencies = Data.Frequencies;
XLimits     = Data.XLimits;
YLimits     = Data.YLimits;
clear Data

% Number of files
n = numel(FileName);
nPoints = 5E3;
% Memory Pre-Allocation for the bandwidth indexes and final values as Columns ...
    (I think in Columns not Rows)
BW_E_Index = zeros(n,1);
BW_O_Index = zeros(n,1);
BW_E       = zeros(n,1);
BW_O       = zeros(n,1);
% Memory Pre-Allocation for the Iterpolation/Fitted variables, big time saver ...
    for large DataSets,
X = zeros(nPoints, n);
Y = zeros(nPoints, n);


%%%%%%%%%%%%%%%  -  Smoothing  -  %%%%%%%%%%%%%%%
if get(handles.Smooth,'Value')
    SmoothPoints = str2double(get(handles.SmoothPoints,'String'));
    for i = 1:1:n
        Amplitudes(:,i) = smooth(Frequencies(:,i), Amplitudes(:,i), ...
            SmoothPoints, 'rlowess');
    end
end


%%%%%%%%%%%%%%%%  -  Trim  -  %%%%%%%%%%%%%%%%
% Trims the Min
if get(handles.MinFrequency,'Value')
    MinFreq     = str2double(get(handles.MinFreq,'String'));
    IndexMin    = find( Frequencies > MinFreq , 1);        % find the indexes ...
        for Max Frequecy admitted
    Frequencies( 1:(IndexMin+1), :) = [];
    Amplitudes(  1:(IndexMin+1), :) = [];
end
% Trims the Max
if get(handles.MaxFrequency,'Value')
```

```
    MaxFreq     = str2double(get(handles.MaxFreq,'String'));
    IndexMax    = find( Frequencies > MaxFreq, 1);        % find the indexes ...
        for Max Frequecy admitted
    Frequencies( (IndexMax-1):end, :) = [];
    Amplitudes(  (IndexMax-1):end, :) = [];
end


%%%%%%%%%%%%%%%  -  Current Density  -  %%%%%%%%%%%%%%%
%   Get Currents from the Table
TableData = get(handles.Table,'Data');
Current   = TableData(:,2);

if get(handles.CurrentDensity,'Value') && get(handles.Circular,'Value')

    Size = str2num(get(handles.Area,'String'));

    if Size == 0,
        errordlg('Size cannot be zero!');
        set(handles.Calculate,'BackgroundColor', 'red');
        return
    end

    Data.Area      = pi*(Size/2)^2;
    CurrentDensity = 1e5 * Current ./ (Data.Area);      % A/cm^2

elseif get(handles.CurrentDensity,'Value') && get(handles.Squared,'Value');

    Size = str2double(get(handles.Area,'String'));

    if Size == 0,
        errordlg('Size cannot be zero!');
        set(handles.Calculate,'BackgroundColor', 'red');
        return
    end

    Data.Area      = Size^2;
    CurrentDensity = 1e5 * Current ./ (Data.Area);     % A/cm^2

elseif get(handles.CurrentDensity,'Value') && get(handles.AreaButton,'Value');

    Data.Area = round(eval(get(handles.Area,'String')));

    if Data.Area == 0,
        errordlg('Area cannot be zero!');
        set(handles.Calculate,'BackgroundColor', 'red');
        return
    end

    CurrentDensity = 1e5 * Current ./ (Data.Area);     % A/cm^2

end
clear Size


%%%%%%%%%%%%%%%  -  Interpolation Method -  %%%%%%%%%%%%%%%
% The interpolation is done with nPoints per File
if get(handles.Interpolation,'Value')
    % Loop for the interpolation of each file separatly
    for i = 1:1:n;
        % Interpolation with nPoints per File  , X-Frequencies, Y-Amplitudes
        X(:,i) = linspace( Frequencies(1,i), Frequencies(end,i), nPoints );
        Y(:,i) = interp1( Frequencies(:,i), Amplitudes(:,i), X(:,i), 'spline');
        % Bandwidth calculation, get the indices I for the vector X that give ...
            the correct values on Y(X(I))
        BW_E_Index(i)   = find( Y(:,i) < (mean(Y(1:20,i)) - 3), 1);
        BW_O_Index(i)   = find( Y(:,i) < (mean(Y(1:20,i)) - 6), 1);
    end
```

```
elseif ¬get(handles.Fitting,'Value')
    set(handles.Calculate,'BackgroundColor', 'red');
    errordlg('Inconsistency with the methods.', 'Error Dialog');
    return
end



%%%%%%%%%%%%%%%%  -  Fitting Method  -  %%%%%%%%%%%%%%%%
% The Fits are done with the function "CreateFit.m"
if get(handles.Fitting,'Value')

    Equation = get(handles.Equation,'Value');

    %     Small interpolation to increase the number of points for the fit
    for i = 1:1:n;
        x(:,i) = linspace( Frequencies(1,i), Frequencies(end,i), 5E3 );
        y(:,i) = interp1( Frequencies(:,i), Amplitudes(:,i), x(:,i), 'spline');
    end
    Frequencies = x;
    Amplitudes  = y;
    clear x y

    %  Fit each File for the chosen Equation
    for i = 1:1:n,

        %         Fits the data and gets the Fitted function
        [f gof] = CreateFit(Frequencies(:,i), Amplitudes(:,i), Equation);

        %         Y evaluates the Fit function on X with 1E6 numbers
        X(:,i)       = linspace( Frequencies(1,i), Frequencies(end,i), nPoints );
        YFit(:,i)    = feval(f,X(:,i));
        R2(i,1)      = gof.rsquare;

        %       Store the Fit parameters and Godness-Of-Fit to export later
        Fit(i,:)       = coeffvalues(f);
        GOF(i,1)       = gof;

        %       Bandwidth calculation, get the indices I for the vector X that ...
            give the correct values on Y(X(I))
        BW_E_Index(i)    = find( YFit(:,i) < (mean(YFit(1:20,i)) - 3), 1);
        BW_O_Index(i)    = find( YFit(:,i) < (mean(YFit(1:20,i)) - 6), 1);
    end

elseif ¬get(handles.Interpolation,'Value')
    set(handles.Calculate,'BackgroundColor', 'red');
    errordlg('Inconsistency with the methods.', 'Error Dialog');
    return
end



% Get the Bandwidth arrays always as columns.
BW_E_Index = BW_E_Index(:);
BW_O_Index = BW_O_Index(:);
% Calcule the Bandwidth with the determined indexes from the previous methods
for i=1:1:n
    BW_E(i,1) = X(BW_E_Index(i),i);  % Eletric Bandwidth Array
    BW_O(i,1) = X(BW_O_Index(i),i);  % Optical Bandwidth Array
end




%%%%%%%%%%%%%%%%  -  Plotting  -  %%%%%%%%%%%%%%%%
cla;
hold('on');
grid('on');
```

```
axis([XLimits YLimits]); % Set the axis limits to the previous used values

% Plot according to the Interpolation or Fitting methods
if get(handles.Interpolation,'Value')

    % Plot the data from the first file in log scale for X-axis
    plot(handles.Axes, X(:,1), Y(:,1), '-k');

    % Crosses for BW points, Electrical and Optical (-3dB & -6dB)
    plot(handles.Axes, X(BW_E_Index(1), 1),  Y(BW_E_Index(1), 1), 'xb', ...
        'MarkerSize', 24, 'LineWidth', 2);
    plot(handles.Axes, X(BW_O_Index(1), 1),  Y(BW_O_Index(1), 1), 'xb', ...
        'MarkerSize', 24, 'LineWidth', 2);

    % Dashed lines for the Electrical and Optical Bandwidth (-3dB & -6dB)
    plot(handles.Axes, [Frequencies(1, 1) Frequencies(end, 1)], [ ...
        (mean(Amplitudes(1:2,1))-3)  (mean(Amplitudes(1:2,1))-3) ], ':r', ...
        'LineWidth', 2);
    plot(handles.Axes, [Frequencies(1, 1) Frequencies(end, 1)], [ ...
        (mean(Amplitudes(1:2,1))-6)  (mean(Amplitudes(1:2,1))-6) ], ':r', ...
        'LineWidth', 2);

    % Show the values of dashed lines
    text( 1.3*min(XLimits), mean(Amplitudes(1:20,1))-3, ' -3 ', 'FontName', ...
        'Arial', 'FontSize', 14,...
        'HorizontalAlignment','left', ...
            'VerticalAlignment','top','FontWeight','bold', 'Color','red');
    text( 1.3*min(XLimits), mean(Amplitudes(1:20,1))-6, ' -6 ', 'FontName', ...
        'Arial', 'FontSize', 14,...
        'HorizontalAlignment','left','VerticalAlignment','top','FontWeight','bold','Color','red'

    % Show Bandwidth Values close the highlighted points
    text( 1.35*X(BW_E_Index(1),1), 0.94*Y(BW_E_Index(1),1), sprintf('%.0f', ...
        X(BW_E_Index(1))),...
        'FontName', 'CourierNew', 'FontSize', 16, 'FontWeight', 'bold', ...
            'Interpreter','tex',...
        'HorizontalAlignment', 'left', 'VerticalAlignment', 'bottom', ...
            'BackgroundColor', [0.9, 0.9, 0.9]);
    text( 0.75*X(BW_O_Index(1),1), 1.05*Y(BW_O_Index(1),1), sprintf('%.0f', ...
        X(BW_O_Index(1),1)),...
        'FontName', 'CourierNew', 'FontSize', 16, 'FontWeight', 'bold', ...
            'Interpreter','tex',...
        'HorizontalAlignment', 'right', 'VerticalAlignment', 'top', ...
            'BackgroundColor', [0.9, 0.9, 0.9]);

elseif get(handles.Fitting,'Value')

    % Plot the Original Imported Data + the Fitted from the first file in log ...
        scale for X-axis
    plot(handles.Axes, Frequencies(:,1), Amplitudes(:,1), '-k');
    plot(handles.Axes, X(:,1), YFit(:,1), '-m');

    % Dashed lines for the Electrical and Optical Bandwidth (-3dB & -6dB)
    plot(handles.Axes, [Frequencies(1, 1) Frequencies(end, 1)], [ ...
        (mean(Amplitudes(1:2,1))-3)  (mean(Amplitudes(1:2,1))-3) ], ':r', ...
        'LineWidth', 2);
    plot(handles.Axes, [Frequencies(1, 1) Frequencies(end, 1)], [ ...
        (mean(Amplitudes(1:2,1))-6)  (mean(Amplitudes(1:2,1))-6) ], ':r', ...
        'LineWidth', 2);

    % Show the values of dashed lines
    text( 1.3*min(XLimits), mean(Amplitudes(1:20,1))-3, ' -3 ', 'FontName', ...
        'Arial', 'FontSize', 14,...
        'HorizontalAlignment','left', ...
            'VerticalAlignment','top','FontWeight','bold', 'Color','red');
```

```
    text( 1.3*min(XLimits), mean(Amplitudes(1:20,1))-6, ' -6 ', 'FontName', ...
        'Arial', 'FontSize', 14,...
        'HorizontalAlignment','left','VerticalAlignment','top','FontWeight','bold','Color','red'

    % Crosses for BW points, Electrical and Optical (-3dB & -6dB)
    plot(handles.Axes, X(BW_E_Index(1), 1),  YFit(BW_E_Index(1), 1), 'xb', ...
        'MarkerSize', 24, 'LineWidth', 2);
    plot(handles.Axes, X(BW_O_Index(1), 1),  YFit(BW_O_Index(1), 1), 'xb', ...
        'MarkerSize', 24, 'LineWidth', 2);

    % Show Bandwidth Values close the highlighted points
    text( 1.35*X(BW_E_Index(1),1), 0.94*YFit(BW_E_Index(1),1), sprintf('%.0f', ...
        X(BW_E_Index(1))),...
        'FontName', 'CourierNew', 'FontSize', 16, 'FontWeight', 'bold', ...
            'Interpreter','tex',...
        'HorizontalAlignment', 'left', 'VerticalAlignment', 'bottom', ...
            'BackgroundColor', [0.9, 0.9, 0.9]);
    text( 0.75*X(BW_O_Index(1),1), 1.05*YFit(BW_O_Index(1),1), sprintf('%.0f', ...
        X(BW_O_Index(1),1)),...
        'FontName', 'CourierNew', 'FontSize', 16, 'FontWeight', 'bold', ...
            'Interpreter','tex',...
        'HorizontalAlignment', 'right', 'VerticalAlignment', 'top', ...
            'BackgroundColor', [0.9, 0.9, 0.9]);

    %     Plot the R^2 value from the fit
    text( 1.3*min(XLimits), 0.91*min(YLimits), strcat('r^2=', ...
        sprintf('%.4f',R2(1)),' '),...
        'FontName', 'CourierNew', 'FontSize', 16, 'Interpreter','tex',...
        'HorizontalAlignment', 'left', 'VerticalAlignment', 'top', ...
            'BackgroundColor', [0.8, 0.7, 0.1]);

else
    errordlg('Unkown issue while plotting, ask god for help!');
end

%  Show value of Current or Current Density
if get(handles.CurrentDensity,'Value')
    text( 1.3*min(XLimits), 0.96*min(YLimits), ...
        strcat(sprintf('%.0f',CurrentDensity(1)),' A/cm^2'),...
        'FontName', 'CourierNew', 'FontSize', 16, 'FontWeight', 'bold', ...
            'Interpreter','tex',...
        'HorizontalAlignment', 'left', 'VerticalAlignment', 'top', ...
            'BackgroundColor', [0.1, 0.5, 0.75]);
else
    text( 1.3*min(XLimits), 0.96*min(YLimits), ...
        strcat(sprintf('%.0f',Current(1)),' mA'),...
        'FontName', 'CourierNew', 'FontSize', 16, 'FontWeight', 'bold', ...
            'Interpreter','tex',...
        'HorizontalAlignment', 'left', 'VerticalAlignment', 'top', ...
            'BackgroundColor', [0.1, 0.5, 0.75]);
end

hold off;

% Set the Left button dark to reflect to the user the first file is already ...
    being displayed
set(handles.Left,'BackgroundColor', 'black');
set(handles.Right,'BackgroundColor', 'default');



%%%%%%%%%%%%%%%%  -  Save Calculated Data  -  %%%%%%%%%%%%%%%%
% Warn the user that data was not saved with a RED button and ERROR dialog
try

    %   Create Data Structure
```

```
    Data.X                = X;
    Data.Y                = Y;
    Data.Frequencies      = Frequencies;
    Data.Amplitudes       = Amplitudes;
    Data.BW_E_Index       = BW_E_Index;
    Data.BW_O_Index       = BW_O_Index;
    Data.BW_E             = BW_E;
    Data.BW_O             = BW_O;
    Data.XLimits          = XLimits;
    Data.YLimits          = YLimits;
    Data.Counter          = 1;      % Counter - first File displayed in this button
    Data.FileName         = FileName;

    %     Get the equation inside the data structure
    if get(handles.Fitting, 'Value')
        switch get(handles.Equation, 'Value')
            case 1
                Data.Equation = 'y = a1*exp(b1*x) + a2*x+b2';
            case 2
                Data.Equation = 'y = a1*exp(b1*x) + a2*exp(b2*x)';
            case 3
                Data.Equation = 'y = a1**x^2 + a2*x + c';
            case 4
                Data.Equation = '- splines -';
        end
    end


    if get(handles.CurrentDensity,'Value')
        Data.CurrentDensity = CurrentDensity;
        if get(handles.AreaButton,'Value')
            set(handles.Area,'String',num2str(Data.Area));
        end
    end


    try Data.MaxFreq    = MaxFreq; end

    try Data.MinFreq    = MinFreq; end

    try Data.Current    = Current; end

    try
        Data.YFit = YFit;
        Data.Fit  = Fit;
        Data.R2   = R2;
        Data.GOF  = GOF;
    end

    %   Send Data Structure to handles
    set(handles.Calculate,'UserData', Data);
    set(handles.FileName,'String', FileName(1));
    set(handles.Calculate,'BackgroundColor', 'green');
    set(handles.PlotBandwidth,'BackgroundColor', 'default');

catch ME
    set(handles.Calculate,'BackgroundColor', 'red');
    %     errordlg('ERROR - Saving the calculated data was not sucesseful!', ...
        'Error Dialog');
    %     return
end
```